UNIVERSIDADE FEDERAL DE PERNAMBUCO
DEPARTAMENTO DE FÍSICA – CCEN
PROGRAMA DE PÓS-GRADUAÇÃO EM FÍSICA

ALBERT STEVENS REYNA OCAS

HIGH-ORDER NONLINEARITIES OF PHOTONICS MATERIALS: FUNDAMENTALS AND APPLICATIONS

Recife
2017

ALBERT STEVENS REYNA OCAS

HIGH-ORDER NONLINEARITIES OF PHOTONICS MATERIALS: FUNDAMENTALS AND APPLICATIONS

Tese apresentada ao Programa de Pós-Graduação em Física da Universidade Federal de Pernambuco, como requisito parcial para a obtenção do título de Doutor em Física.

Orientador:
Prof. Dr. Cid Bartolomeu de Araújo

Recife
2017

Catalogação na fonte
Bibliotecário Joana D'Arc Leão Salvador CRB 4-572

R459h Reyna Ocas, Albert Stevens.
High-order nonlinearities of photonics materials: fundamentals and applications / Albert Stevens Reyna Ocas . – 2017.
235 f.: fig., tab.

Orientador: Cid Bartolomeu de Araújo.
Tese (Doutorado) – Universidade Federal de Pernambuco. CCEN. Física, Recife, 2017.
Inclui referências e apêndices.

1. Ótica não-linear. 2. Materiais fotônicos. 3. Controle da resposta não linear. 4. Nanocompósitos metal-dielétrico. I. Araújo, Cid Bartolomeu de (Orientador). II. Titulo.

535.2 CDD (22. ed.) UFPE-FQ 2017-35

ALBERT STEVENS REYNA OCAS

HIGH-ORDER NONLINEARITIES OF PHOTONICS MATERIALS: FUNDAMENTALS AND APPLICATIONS

Tese apresentada ao Programa de Pós-Graduação em Física da Universidade Federal de Pernambuco, como requisito parcial para a obtenção do título de Doutor em Física.

Aprovada em: 17/01/2017.

BANCA EXAMINADORA

Prof. Dr. Cid Bartolomeu de Araújo
Orientador
Universidade Federal de Pernambuco

Prof. Dr. Edilson Lucena Falcão Filho
Examinador Interno
Universidade Federal de Pernambuco

Prof. Dr. José Roberto Rios Leite
Examinador Interno
Universidade Federal de Pernambuco

Prof. Dr. Jandir Miguel Hickmann
Examinador Externo
Universidade Federal do Rio Grande do Sul

Prof. Dr. Sérgio Carlos Zilio
Examinador Externo
Universidade de São Paulo

A Deus, meus pais Graciela & Luis, meus irmãos Evelyn & Luis, e Talita.
Eu conclui esta jornada com sucesso graças a todos vocês.

Em memória de Kiarita
"Você sempre estará nos meus pensamentos e no meu coração"

Agradecimentos

Após uma longa e satisfatória jornada de esforço e dedicação, que consta de várias horas com os livros e artigos, semanas no computador, meses na mesa óptica e anos no laboratório, um é impulsionado a otourgar-se todos os créditos do trabalho. No entanto, a finalização deste projeto foi alcançado graças ao apoio físico, mental e sobretudo sentimental de muitas pessoas ao meu redor. Por esse motivo, dedico umas breves, porém significativas frases para cada um de vocês, e peço desculpas antecipadamente por não ser capaz de agradecer a todas as pessoas que tem me ajudado ao longo desses 4 anos.

Em princípio, gostaria de agradecer a Deus pelo dom da vida, o bem-estar e a saúde, permitindo-me tentar ser uma pessoa melhor a cada dia; por guiar os meus pasos, fortalecer meu coração, iluminar minha mente e por colocar no meu caminho maravilhosas pessoas que tem sido o meu apoio e companhia durante todo este período.

Agradeço de forma muito especial a minha família: minha mãe Graciela Ocas (*“Chelita*”), meu pai Luis Reyna (*“Viejito*”), minha irmã Evelyn Reyna (*“Feita*”) e meu irmão Luis Reyna (*“Churre*”) pois embora encontrem-se distantes físicamente, sempre senti sua presença, seu amor, compreensão e apoio em cada momento de alegrias e naqueles não tão felizes. Muito obrigado “*my family*”, muito do que eu sou e tenho alcançado é graças a todos vocês. Agradeço também a *“Kiarita”*, e embora não esteja mais conosco, sempre viverá nos meus pensamentos.

Agradeço a Talita Candido pelo seu amor, carisma, respeito e paciência para compartilhar sua vida comigo. Obrigado *“minha Tatá”*, é muito especial saber que conto com alguém como você na minha vida. Agradeço também à família Candido de Oliveira pelo seu carinho: Dona Luzinete, Thyago e Aninha, Nathalie e Daniel, Biel e Joanna = Clarice.

Agradeço ao meus avôs Benito Reyna, Dominga Pinco e Manuel Ocas; tios e primos que participaram direta ou indiretamente na concretização deste objetivo. *“Papá Beno”* hoje eu posso dizer: Promessa cumprida!

Agradeço ao meu orientador, o prof. Cid B. de Araújo, pelos ensinamentos, apoio, confiança e motivação ao longo de todo meu mestrado e doutorado. Obrigado por ser um excelente exemplo para seguir na minha vida profissional e cotidiana. Foi um prazer trabalhar com você e espero que possamos continuar nossas colaborações *“altamente não lineares”*.

Agradeço aos professores do departamento de Física da UFPE, em especial aos professores Edilson Falcão, Anderson Gomes, Lúcio Acioli e Leonardo Menezes pelas frutíferas discussões, essenciais para minha formação profissional e desenvolvimento deste trabalho. Igualmente, agradeço ao prof. Boris Malomed da *Tel Aviv University* pela transferência de conhecimentos teóricos sobre o estudo de solitones espaciais e ao prof. George Boudebs da *Université d'Angers* pelos ensinamentos em técnicas criativas de caracterizações não lineares.

Não posso deixar de agradecer aos meus colegas e amigos de laboratório: Anderson Amaral

(um grande amigo e excelente pessoa para compartilhar a paixão pela ciência), Andréa Ferreira, Felipe Elan, André Moura, Hans García, Gemima Barros, Renato Silva, Manoel, Sandra Carreño, Rudson, Maxwell, Oscar, Edison Rosero, Whualkuer Lozano e companheiros do OSA Student Chapter-Recife, pela amizade, por compartilhar discussões acadêmicas e os momentos de folga, e por tornar o laboratório um excelente lugar para trabalhar em harmonia. Também gostaría de agradecer à familia Machado Moura por seu carinho e atenção.

Aos técnicos do Departamento de Física da UFPE: Marcos Aurélio e Daniel (Oficina de Eletrônica) por seus ensinamentos para construir circuitos eletrônicos que otimizem os resultados experimentais, e a Maria Virgínia (Lab. de Química) por suas contribuições na caracterização dos materiais usados nesta tese.

Finalmente, agradeço ao CNPq pela bolsa de estudos, indispensável para realizar meu doutorado. A OSA e o Student-Chapter pela experiência na organização do “X Simpósio de Lasers e suas Aplicações” e pelo suporte financeiro para participar de eventos internacionais como *Frontiers in Optics*, *Latin America Optics & Photonics* e *The Siegman International School on Laser*.

If I have seen further it is by standing on the shoulders of Giants
—ISAAC NEWTON

Abstract

The nonlinear (NL) optical response of matter to optical fields is described by expressing the induced polarization by a power series of the electric field with NL susceptibilities as coefficients of the series. In the majority of cases reported, the NL behavior of photonic materials is described by the lowest-order susceptibility (second-order in noncentrosymmetric media and third-order in centrosymmetric media). However, even at moderate intensities, the contributions of high-order nonlinearities (HON) are important and their understanding allows the exploitation of new NL effects. This thesis presents a comprehensive study on the origin, fundamentals and measurement procedures of the HON in photonic materials with inversion symmetry. A metal-dielectric nanocomposite (MDNC) and a highly NL solvent, viz. carbon disulfide (CS_2) , were chosen to represent self-defocusing (SDF) and self-focusing (SF) NL media, respectively, both exhibiting HON contributions. For MDNCs, its NL response presents contributions of third- (cubic nonlinearity), fifth- (quintic nonlinearity) and seventh-order (septimal nonlinearity), depending on the properties of the material (volume fraction, environment, size and shape of the nanoparticles) and the incident laser (wavelength, intensity, pulse duration and repetition rate). Based on this statement, it was developed a simple, but effective, nonlinearity management (NM) procedure which enables to control the magnitude and phase of the different high-order susceptibilities by adjusting the light intensity and the volume fraction occupied by the nanoparticles. The NM procedure allowed us to conduct experimental studies of NL effects induced by HON. Experiments based on transverse phenomena such as spatial self- and cross-phase modulation and spatial modulation instability in media with HON, as well as stable propagation of two-dimensional fundamental and vortex solitons, which is only possible in materials with specific HON, are reported in this thesis by using the NM procedure applied to MDNCs. On the other hand, a detailed study of a well-known solvent (liquid CS_2) shows an unusual NL behavior depending on the incident pulse duration. In the picoseconds regime, CS_2 behaves as a saturable SF medium, while in the femtoseconds regime, it behaves like a cubic-quintic (focusing-defocusing) medium. Characterization, analysis and understanding of both types of NL response allowed to perform important contributions in the field of the optical vortex solitons with attractive applications in all-optical devices and manipulation of light-by-light. All experiments were corroborated by theoretical models and numerical simulations based on the NL Schrödinger equation properly modified to include contributions of HON.

Keywords: High-order nonlinearities. Photonic materials. Metal-dielectric nanocomposites. Nonlinearity management. Nonlinear Schrödinger equation.

Resumo

A resposta não linear (NL) da matéria frente aos campos ópticos é descrita expressando a polarização induzida como uma série de potências do campo elétrico, onde as susceptibilidades NLs representam os coeficientes da expansão. Na maioria dos casos reportados, o comportamento NL dos materiais fotônicos é descrito pela susceptibilidade de menor ordem (segunda ou terceira ordem em materiais não centrossimétricos ou centrossimétricos, respectivamente). No entanto, inclusive em intensidades moderadas, as contribuições das não linearidades de altas ordens são importantes e seu entendimento permite a exploração de novos efeitos NLs. Esta tese apresenta um estudo abrangente sobre a origem, fundamentos e procedimentos de medição das não linearidades de altas ordens em materiais fotônicos com simetria de inversão. Um nanocompósito metal-dielétrico (MDNC) e um solvente altamente NL (dissulfeto de carbono-CS_2) foram escolhidos para representar meios NL autodesfocalizadores e autofocalizadores, respectivamente, ambos apresentando contribuições de não linearidades de altas ordens. A resposta NL dos MDNCs apresentam contribuições de terceira, quinta e sétima ordem, dependendo das propriedades do material (fração volumétrica, solvente, tamanho e forma das nanopartículas) e do laser incidente (comprimento de onda, intensidade, duração do pulso e taxa de repetição). Com base nessa afirmação, foi desenvolvido um procedimento simples, porém eficaz, de controlar a resposta NL de MDNCs, permitindo manipular a magnitude e a fase das diferentes susceptibilidades de altas ordens ajustando a intensidade da luz e a fração volumétrica ocupada pelas nanopartículas. O procedimento de controle da resposta NL permitiu conduzir estudos experimentais de efeitos NL sendo induzidos pelas susceptibilidades de altas ordens. Experimentos baseados em fenômenos transversais, tais como automodulação de fase, modulação de fase cruzada e instabilidade da modulação espacial em meios com não linearidades de altas ordens, bem como a propagação estável de solitons fundamentais e solitons vorticais foram estudados nesta tese usando o procedimento de controle da resposta NL aplicado a MDNCs. Por outro lado, um estudo detalhado de um bem conhecido solvente NL (CS_2 líquido) mostra uma resposta NL exótica a qual depende diretamente do tempo de duração do pulso incidente e do regime de intensidades utilizado. No regime de picosegundos, CS_2 se comporta como um meio autofocalizador saturável, enquanto que no regime de fentosegundos apresenta não linearidades de terceira e quinta ordem, simultaneamente. A caracterização, análise e compreensão de ambos tipos de resposta NL permitiram introduzir importantes contribuições no campo dos solitons vorticais, com possíveis aplicações em dispositivos totalmente ópticos e procedimentos de manipulação de luz por luz. Todos os experimentos foram corroborados por modelos teóricos e simulações numéricas baseadas na equação de Schrödinger NL adequadamente modificada para incluir as contribuições de altas ordens.

Palavras-chave:

Não linearidades de altas ordens. Materiais fotônicos. Nanocompósitos metal-dielétrico. Controle da resposta não linear. Equação de Schrödinger não linear.

List of Figures

List of Tables

Nomenclature

2PA	Two-photon absorption
3PA	Three-photon absorption
Ag	Silver
AOD	All-optical devices
AOS	All-optical switches
C-NLSE	Cubic nonlinear Schrödinger equation
CA	Closed-aperture
CCD	Charge-coupled device
CFD	Compact finite difference
CID	Chemical interface damping
CQ-NLSE	Cubic-quintic nonlinear Schrödinger equation
CQS-NLSE	Cubic-quintic-septimal nonlinear Schrödinger equation
DDPG	Digital delay and pulse generator
DFWM	Degenerate four-wave mixing
DLS	Dynamic Ligth Scattering
DOVS	Delocalized optical vortex soliton
EMF	Electromagnetic field
ET	Energy transfer
FWHM	Full width at half maximum
FWM	Four-wave mixing
LSP-DT	Localized surface plasmon dephasing times

LSP	Localized surface plasmons
LSPR	Llocalized surface plasmon resonance
MI	Modulational instability
NLSE	Nonlinear Schrödinger equation
OAM	Orbital angular momentum
OA	Open-aperture
OV	Optical vortex
OVS	Optical vortex soliton
PVA	Polyvinyl acetate
PVP	Polivinilpirrolidona
Q-NLSE	Quintic nonlinear Schrödinger equation
RK2	Second-order Runge-Kutta
RSA	Reverse saturable absorption
SHG	Second-harmonic generation
SiO_2	Silicon dioxide or Silica
SLIM	Scattered light imaging method
SMI	Spatial modulation instability
SPM	Self-phase modulation
SPR	Surface plasmon resonance
SSPM	Spatial self-phase modulation
SVEA	Slowly varying envelope approximation
SXPM	Spatial cross-phase modulation
TEM	Transmission electron microscope
TE	Transverse electric
TIR	Total internal reflection
TMI	Temporal-modulation instability

TM	Transverse magnetic
VA	Variational approximation
VK	Vakhitov-Kolokolov
VPP	Vortex phase plate

Contents

1 INTRODUCTION

The field of "Optics and Photonics" ranges from the understanding of the light propagation and light-matter interaction to the design and fabrication of optical devices based on the generation, control and detection of photons. Nowadays, photonics is emerging as a multidisciplinary frontier of science and technology due to the potential applications in many areas of present and future information [1, 2] and image processing technologies [3]. Some classic devices such as: cameras, telescopes, microscopes and others most commonly used devices as barcode readers, CD players, LCD TVs, datashows, chemical and biochemical sensors, laser pointers, among others, combine electronics with photonics (optoelectronic systems) and these are considered as transition systems to a generation of future photonic devices. Numerous advantages arise with the photonic applications, essentially in the telecommunications field, being the main one the significant increase of the transfer rate, detection and processing of information over long distances [4, 5]. To achieve this goal, several studies are necessary to construct very efficient data transfer devices such as photonic-crystal fibers [6, 7], highly sensitive detectors such as photonic sensors [8] and all-optical modulators [9, 10] coupled in photonic integrated circuits [11, 12] for high-speed data processing. Despite the excellent results obtained so far, various research groups, around the world, continue conducting extensive studies to optimize the performance of all-optical devices.

Nonlinear optics plays an important role in the development of scientific and technological advances obtained in photonic technology, since it is responsible for increasing the strength of light-matter interaction. From the first observation of second harmonic generation (SHG) in a quartz crystal, reported by Franken *et al.* [13], considered as the beggining of NL optics, different NL processes have been reported in a wide variety of materials. Examples of NL phenomena that are useful in photonic applications include the ability to modulate the light frequency [14], inducing self-action effects [15, 16], and manipulate light-by-light such as: amplification of one light source induced by another source [17], switching processes [18, 19], wave mixing processes [20], among others.

In the last years, the evolution of photonics has intensified research activities on searching for new materials that display unusual and interesting NL optical properties. In this way, materials with fast NL response and large NL susceptibility are attractive for potential applications in photonic technology. In general, changes in the absorption, refraction and light scattering properties are signatures of NL optical effects [21]. Commonly, these NL phenomena are properly described by the lower-order nonlinearity (second-order in noncentrosymmetric media and third-order in centrosymmetric media). However, there is a large number of materials exhibiting strong contributions of HON that can be detected even using low intensity lasers [22]. Such contributions of HON have the ability to change the NL effects induced by the lower-order nonlinearity, as well as originate new NL phenomena that depend on high power of electric field, as presented in this thesis. The rapid development of laser and materials technology has led to many studies of NL phenomena in light-matter interactions. The discovery of different types of materials exhibiting HON and their applications in various fields of science and technology made the NL optics a fascinating field of research and developments.

The origin of HON depends strongly on the type of material and contributions to its optical, electrical and magnetic properties can be very relevant. This thesis focuses on the study of two types of materials: a metal-dielectric nanocomposite (MDNC), represented by silver colloids, and liquid carbon disulfide (CS_2), which is a highly NL solvent. Previous works reported the presence of HON, in both photonic materials, for peak intensities of few GW/cm^2, in the picoseconds and femtoseconds regimes [23, 24, 25]. In the case of MDNCs, HON have been attributed to direct NL processes (intrinsic effects of NPs) or cascade processes, which consist of a sequence of low-order interactions to build a high-order response. In both process, large enhancement of the HON was obtained when the optical frequency is in near-resonance with the localized-surface-plasmon frequencies associated to the NPs, due to the increased local field in the vicinities of the NPs [23, 24]. In particular, MDNCs were chosen due to their fast response and high NL susceptibility, which are essential characteristics for applications in a certain class of photonic devices. Also, liquid CS_2 was chosen by its large NL response and because this liquid is the most popular material for applications in NL optics, being frequently used as a standard reference for measurements of NL parameters. However, only few studies shows detailed NL characterization of CS_2 for high intensities, when HON are significant. In principle, NL behavior such as saturable self-focusing (SF) nonlinearity [26] and cubic-quintic nonlinearity[1] [25] were identified in the CS_2 which are dependent of the time duration of the incident laser. Also, processes of two-photon absorption (2PA) [27] and three-photon absorption (3PA) [25, 26] were observed depending on the wavelength analyzed. These different NL behaviors of CS_2 are related to the nature of their nonlinearity, which can be of thermal origin (nanoseconds regime), molecular reorientation (picoseconds regime) or electronic origin (femtoseconds regime). However, in either case the HON are relevant to the detailed NL characterization and understanding of the optical properties of the material. In principle, from the fundamental point of view, HON are important to understand phenomena such as: light condensates [28], rogue waves [29], solitons formation [30], and harmonic generation [31]. In turn, great efforts are being developed with the goal of bringing knowledge of HON for possible applications in photonics technology, as performed in this thesis.

1.1 THESIS OBJECTIVES

This thesis is intended to provide a study on the origin, fundamentals, measurement procedures and control of HON in photonic materials. At the same time, demonstrate the importance of their contributions in optical phenomena previously studied for the low-order nonlinearity, but this time induced by HON, such as: spatial self- and cross-phase modulation, spatial modulation instability and nonlinear polarization rotation; as well as in NL phenomena which are possible to be observed only with contributions from HON such as: spatial fundamental

---

[1] cubic nonlinearity refers to third-order nonlinearity $\left(\chi^{(3)}\right)$, while quintic nonlinearity corresponds to fifth-order nonlinearity $\left(\chi^{(5)}\right)$

and vortex solitons. From the technological point of view, this thesis aims to show efficient processes for controlling the NL response of MDNCs, with the goal of demonstrate their applications in the construction of all-optical devices and in situations that require the manipulation of light-by-light.

1.2 OUTLINE OF THE THESIS

This thesis is organized in the following manner:

- Chapter 2 discusses the basic aspects of NL optics for the understanding of the experiments performed in this thesis. The fundamental concepts of light-matter interaction are discussed through of the description of the NL polarization and NL susceptibilities, which are related to processes of NL refraction and NL absorption. In addition, NL optical effects based on the third-order nonlinearity are discussed, with emphasis to the effects induced by the modulation of NL refractive index. Finally, basic notions of HON are presented as introduction to the theory developed in this thesis.

- Chapter 3 gives a basic introduction on MDNCs, by describing some of their linear and NL optical properties. Special attention is given to the influence of local field effects, as well as to the characteristic of the composites (size, shape and environment) on the effective nonlinearity. The origin and the measurements procedure to characterize the HON are discussed and analyzed based on a generalization of the Maxwell-Garnet model.

- Chapter 4 describes a method for controlling the NL response of MDNCs. Applications of the NM procedure for observation of NL optical phenomena induced by HON are presented and analyzed by using the generalized Maxwell-Garnet model, described in the previous chapter.

- Chapter 5 discusses the theory necessary for description of the light propagation in NL media exhibiting HON. The behavior of the laser beam propagation in MDNCs and liquid CS_2 was described by introducing new terms in the standard NL Schrödinger equation (NLSE). In addition, the theory of NL birefringence in optical fibers was extended to describe the polarization rotation in capillaries with the core filled with MDNCs.

- Chapter 6 discusses two experiments concerning the stable propagation of fundamental solitons. The first one corresponds to a theoretical work that aims to identify the stable and unstable propagation regions of one-dimensional solitons in cubic-quintic-septimal media [2] by using the variational approximation method. The second one shows the stable propagation of two transverse dimensional spatial solitons due to competition between quintic and septimal nonlinearities. Both results are modeled by the cubic-quintic-septimal NLSE modified to include losses.

---

[2] septimal nonlinearity corresponds to seventh-order nonlinearity $\left(\chi^{(7)}\right)$

- Chapter 7 discusses the formation and stable propagation of optical vortex solitons (OVSs) in SF and SDF media. In CS_2 (saturable self-focusing medium) the OVS should be unstable. However in the section 7.2 it is shown experimentally and numerically that there is a stability region for the OVSs. Nevertheless, instability regions in CS_2 were also identified and the azimuthal symmetry breaking is observed. Section 7.3 discusses the procedure to control the emerging beams after the split of an OVS, which can be applied to the construction of all-optical devices. In addition, processes of guiding and confinement of light induced by OVSs are discussed in a self-defocusing MDNC.
- Chapter 8 discusses the effects of NL polarization instability in a hollow capillary filled with cubic-quintic MDNC. The experimental results shown here are corroborated with the theoretical model developed in section 5.5.
- Finally, Chapter 9 presents the conclusions and perspectives for future works.

The experiments and theories presented in this thesis are original contributions to the study of HON in photonic materials. The NL effects induced by HON, reported here, would not have been observed without proper understanding, characterization and control of the NL response of materials. Contributions such as the NM procedure open new horizons for the study of novel NL phenomena, as well as technological applications that require highly NL materials with adequate control of their NL response. On the other hand, the recent observations of fundamental solitons and OVSs and their applications in switching, confinement and guiding of light may favor the developement of new devices based on the light-by-light manipulation.

1.3 REVIEW OF PREVIOUS WORKS

Previous works that directly motivated the study of the topics investigated in this thesis are briefly described below.

1.3.1 High-Order Nonlinearities of MDNCs

Metal-dielectric nanocomposites (MDNCs) present large NL response because to the contribution of surface plasmon resonance (SPR) responsible for enhancement of the local field effects. It is considered that the electric field inside of each NP is different from that of the applied field due to the difference in the dielectric functions of the metal and the host. The local fields may be larger than the average field and thus an enhancement of the optical response occurs. Therefore, it is expected the observation of effective HON in the macroscopic behavior of the MDNCs. In a previous work, Falcão-Filho *et al.* measure the values of third-, fifth-, seventh- and ninth-order susceptibilities in a colloid containing silver NPs suspended in water, for peak intensity of few GW/cm^2 [23]. The experiments were performed by exploiting the large sensitivity of the Z-scan technique, using a laser beam at 532 nm delivering single 80 ps pulses at low repetition rate. Here, because the excitation of the samples was made with photons of 2.34 eV, the interband transitions of silver are negligible and the mechanism that contribute to the NL optical response was assigned mainly to the contribution of hot electrons.

However, the HON were attributed to local field effects due to the mismatch between the dielectric function of the silver NP and the host. Fig. 1.1 illustrates the linear behavior of the third- and fifth-order nonlinearity as a function of the NPs filling factor. The experimental results were corroborated by using an effective-medium theory [32], which enabled the understanding of the origin and the relative magnitude of the effective NL high-order susceptibilities.

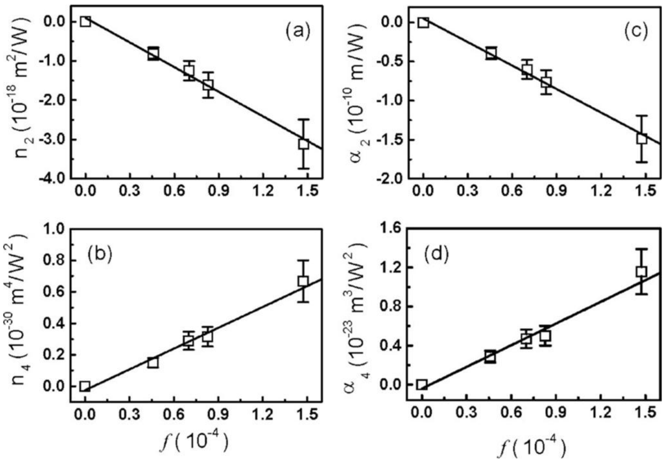

Figure 1.1 Dependence of the third- and fifth-order nonlinearity with the NP volume fraction; (a), (b) refractive indices and (c), (d) absorption coefficients (Reprinted from [23])

Moreover, Jayabalan measured the time dependence of the third-, fifth-, and seventh-order NL absorption coefficients of silver nanoplatelets suspended in water, by using a 190 fs laser in 778 nm [33]. Fig. 1.2 shows the experimental and theoretical measured time dependence of HON absorption coefficients for intensity of hundreds of MW/cm^2. By comparing the experimental results with the model of thermalized electrons developed in [33], it has been shown that the HON have a strong contribution due to the hot electrons in the metal NPs.

Then, he concluded that HON in MDNCs have contributions of hot electrons when these are analyzed with pulses widths higher than the electron thermalization time (few hundreds of femtoseconds). For pulses with shorter pulses widths, HON are of electronic origin. Therefore, the origin of the HON in MDNCs depends on the properties of NL material and the characteristics of the light source.

1.3.2 Nonlinear Behavior of CS_2 in the Picosecond and Femtosecond Regimes

CS_2 is a NL material per excellence. Its linear and NL properties have been extensively studied by different techniques and research groups. Particularly, important is the work developed by Sheik-Bahae *et al.* [27], where the Z-scan technique was discussed in details. In that study the third-order NL refractive index of CS_2 was measured by using lasers with 300 ns pulses at 1064 nm and 27 ps pulses at 532 nm, both with peak intensities around of units of GW/cm^2. Fig. 1.3 illustrates the *closed-aperture* (CA) Z-scan curves, in the two temporal regimes, where it is clearly seen a sign reversal of the NL refractive index because the nonlin-

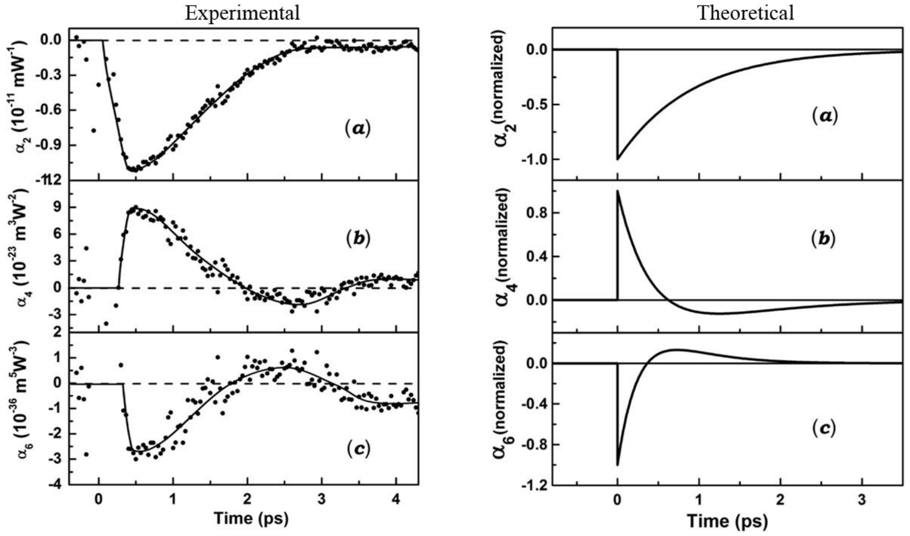

Figure 1.2 Experimental and theoretical time dependence of (a) third-, (b) fifth-, and (c) seventh-order absorption coefficients of silver nanoplatelets in water. (Reprinted from [33]).

earity origin changes from thermal SDF (nanoseconds regime) to SF molecular reorientation (picoseconds regime).

The NL absorption of CS_2 was also studied by Ganeev *et al.* who measured the 2PA and 3PA coefficients by using femtoseconds lasers with low repetition rate in 795 nm and 1054 nm, respectively [34]. Fig. 1.4(a) shows the $open-aperture$ (OA) Z-scan curves obtained at 795 nm, 110 fs and 10 Hz, for intensities between 4 and 380 GW/cm^2. The solid lines correspond to the fit considering contribution of two-photon absorption (2PA) . Similarly, Fig. 1.4(b) displays the experimental data obtained in 1054 nm, 475 fs and 1 Hz, for intensities of hundred of GW/cm^2. Here, it is possible to observe that the fit corresponding to contribution of 3PA (solid line) is more suitable than the fit corresponding to 2PA (dashed line). It means that the multiphoton contributions are heavily dependent on the laser wavelength used.

Despite the study conducted by Sheik-Bahae be highly reliable and quite cited in the liter-

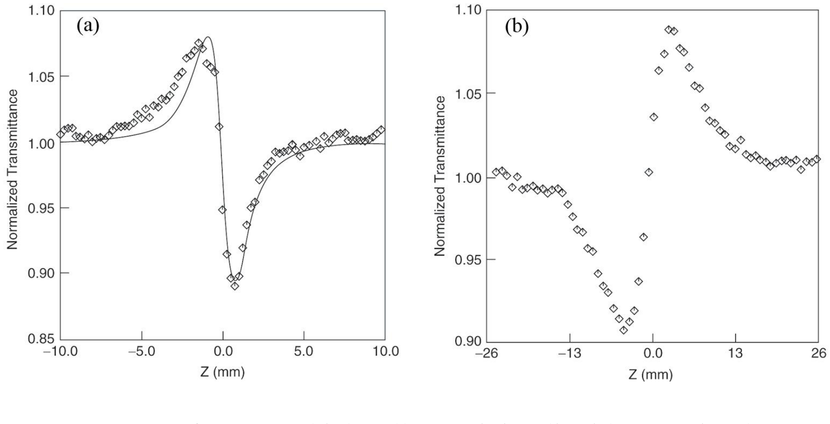

Figure 1.3 CA Z-scan curves of a 1 mm thick cell containing liquid CS_2 using lasers with (a) 300 ns at λ = 1064 nm and (b) 27 ps at λ = 532 nm. (Reprinted from [27]).

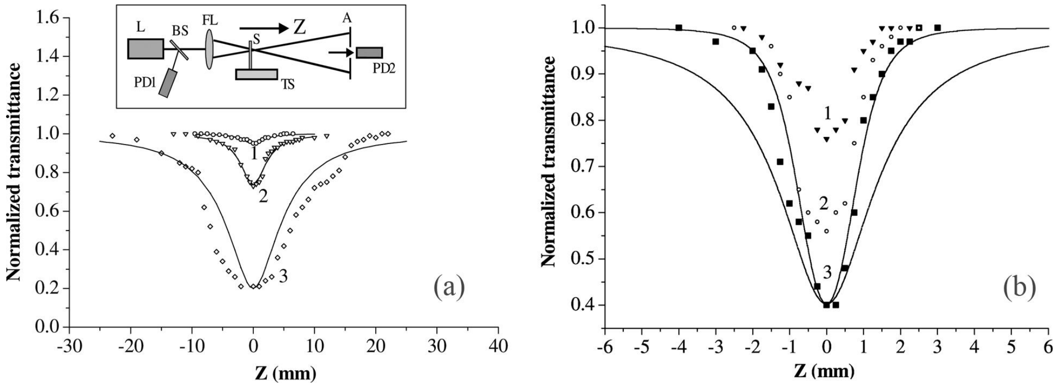

Figure 1.4 OA Z-scan curves for CS_2 in: (a) 795 nm with intensities of (1) 4, (2) 22 and (c) 380 GW/cm^2; (b) 1054 nm with intensities of (1) 220, (2) 320 and (c) 400 GW/cm^2. The solid lines correspond to fit considering contribution of (a) 2PA; (b) 3PA (solid line) and 2PA (dashed line). (Reprinted from [34]).

ature, this is limited to low intensities, losing information on possible contributions of HON. An analysis at high intensities (532 nm and 12-ps-long pulses) was carried out by Besse *et al.* by using the D4σ method [26]. Fig. 1.5(a) shows a nonpolynomial behavior of the effective NL refractive index as a function of the incident intensity, for peak intensities up to hundred of GW/cm^2. The experimental results were fitted by an empirical expression that simulates a saturated-like Kerr behavior. In addition, Besse *et al.* performed measurements of NL absorption noting that CS_2 has contributions of 3PA in 532 nm. Fig. 1.5(b) shows the OA Z-scan curve for intensity of 25 GW/cm^2. The numerical fit shows that the NL absorption behavior is best described by considering 3PA (red line) in comparison to 2PA (blue line).

The empirical expression proposed in [26] was used to reproduce the formation of filaments observed experimentally in high intensities.

In the femtoseconds regime, Kong *et al.* again used the Z-scan technique to characterize the NL parameters of CS_2 in 800 nm, but broaching a broad intensity range [25]. They observed

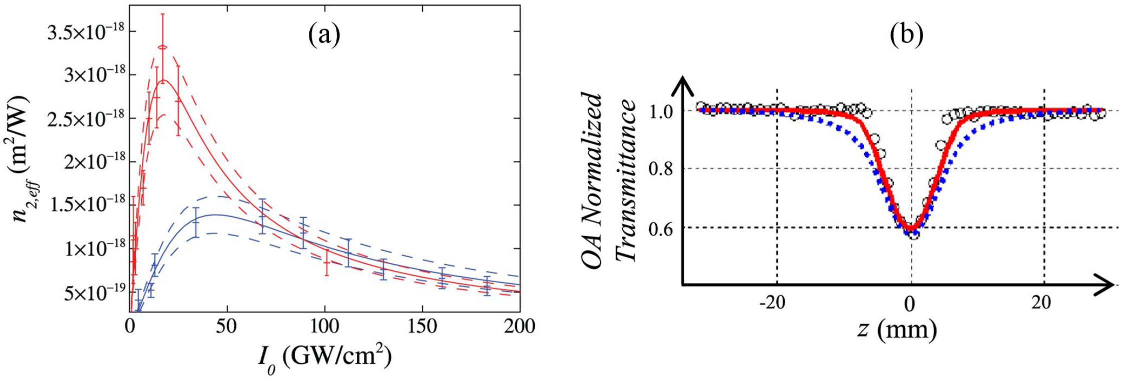

Figure 1.5 (a) Effective NL refractive index of CS_2 for picoseconds regime in 532 nm (red points) and 1064 nm (blue points). The solid lines correspond to the best fit obtained from empirical model. (b) OA Z-scan curve of CS2 in 532 nm, for intensity of 25 GW/cm^2. The red (blue) line corresponds to fit considering 3PA (2PA). (Reprinted from [26]).

that for intensities smaller than 75 GW/cm^2, the NL refraction is mainly governed by the third-order process, as previously reported in other works [27, 35]. However, for intensities between 75 and 220 GW/cm^2, Kong *et al.* demostrated that the third- and fifth-order nonlinearities are relevant. Fig. 1.6(a) illustrates the transmittance variation between peak and valley of CA Z-scan curves as a function of incident intensity. The parabolic behavior observed indicates the existence of HON contributions; otherwise the behavior should be linear.

In analogy to the study carried out by Ganeev, measurements of NL absorption were performed using the OA Z-scan technique, as shown in Fig. 1.6(b). Again the absorptive behavior was attributed to the 3PA process.

It is possible to note that despite the CS_2 be a reference material widely used for NL experiments for long time, their NL parameters vary abruptly depending on the conditions used for incidents lasers.

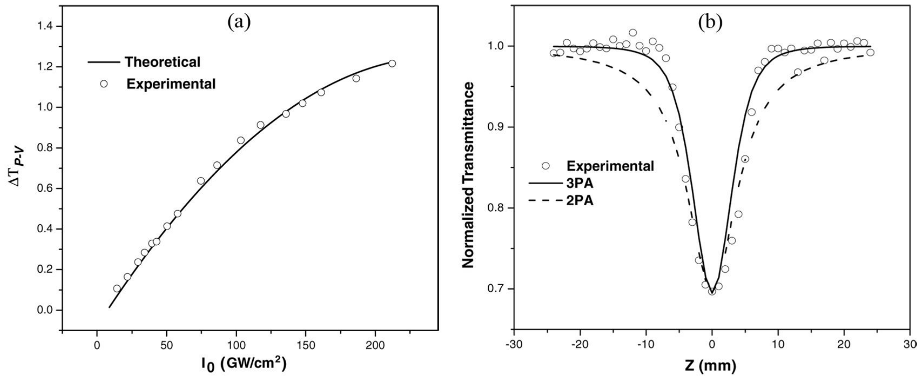

Figure 1.6 Intensity dependence of $|\Delta T_{p\text{-}v}|$ for NL refraction of CS_2 in femtoseconds regime. (b) OA Z-scan curve for 146 GW/cm^2. Laser wavelength: 800 nm (Reprinted from [25]).

1.3.3 Two Dimensional Fundamental Solitons in Cubic-Quintic Media

A spatial soliton is considered as a solitary wave that travels without suffering spatial deformation (i.e. its shape and size remain constant throughout its propagation). Theoretically, fundamental spatial solitons appear as an exact solution for the NL Schrödinger equation (NLSE) with focusing cubic nonlinearity. The first observation of one-dimensional spatial solitons was reported in a planar waveguide filled with liquid CS_2, where the NL response was dominated by cubic SF nonlinearity [36], and their behavior is described by the cubic NLSE. Shortly thereafter, theoretical studies predicted that two-dimensional spatial solitons can not propagate in media with instantaneous cubic nonlinearity, because catastrophic beam collapse occurs at high powers [37]. From that moment, various theoretical studies were conducted with the aim of finding the necessary conditions to obtain the stable solitons propagation in two transverse dimensions. Among such stabilizing phenomena are nonlocality [38], saturation of the nonlinearity [39], photorefractive [40] and thermal effects [41], self-induced transparency [42], and dissipative effects without and with gain [43, 44]. In the case of homogeneous media, one of the most attractive theories suggests the use of saturable nonlinearity to arrest the beam collapse

[39]. The effectiveness of the proposal was corroborated experimentally in heavy-metal- oxide glasses presenting large 3PA cross section [45, 46]. Moreover, saturation of the nonlinearity can be modeled by means of HON. Based on this premise, Fan *et al.* reported the formation and stable propagation of soliton-like filaments in a cubic-quintic medium, where the 3PA plays an important role in preventing the filament collapse induced by the Kerr effect [47]. In a similar way, Falcão-Filho *et al.* observed the successful excitation of two-dimensional fundamental solitons in liquid CS_2 due to the simultaneous contribution of the refractive third- and fifth-order nonlinearities, where the dissipative effects due to the 3PA were considered [30]. Fig. 1.7(a) presents the behavior of the output beam waist as a function of the laser intensity for incident Gaussian beam with waist of 16 and 28 μm. It was possible to observe that for high intensity the beam waist remains constant, indicating the region of stable propagation of two-dimensional soliton. Because the experience was performed at 920 nm in resonance with a 3PA transition and femtoseconds regime, the NL behavior of CS_2 corresponds to cubic nonlinearity at low intensities and cubic-quintic nonlinearity, at high intensities. In this case, the Gaussian beam diverges due to linear diffraction effect, at low intensities [Fig. 1.7(b)]. However, at high intensities, the soliton-like behavior is well reproduced by the NLSE when the cubic and quintic nonlinearities are taken into account, as shown in Fig. 1.7(c). Measurements performed with cells of thickness 10 and 20 mm show that the fundamental soliton propagates stably for more than 10 Rayleigh lengths.

The realization of this kind of experiment reveals the importance of HON for the observation of new NL optical phenomena.

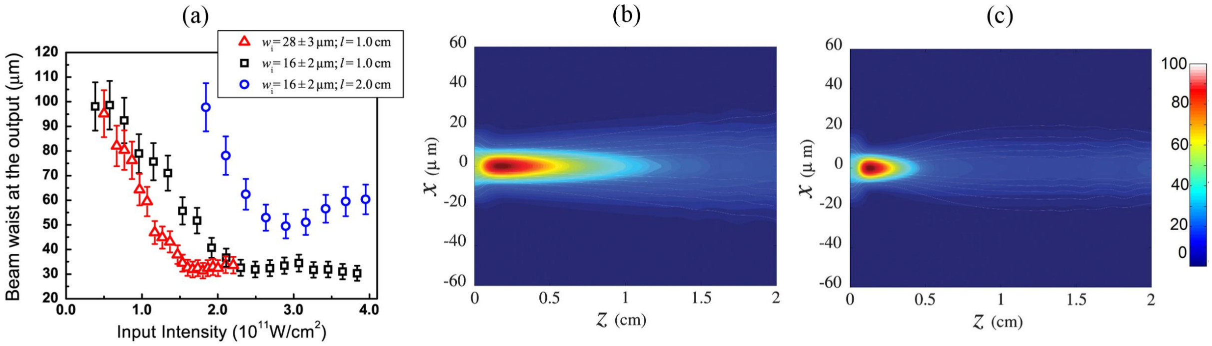

Figure 1.7 (a) Beam waist at the exit face of the cell as a function of the input intensity. Numerical simulation of the beam profile evolution in liquid CS_2 for (b) 80 GW/cm^2 and (c) 160 GW/cm^2. In (b) and (c) x-axis and z-axis represent a transverse and longitudinal (propagation direction) dimensions, respectively; while the color scale represents the beam intensity (Reprinted from [30]).

1.3.4 Spatial Optical Vortex Solitons in Self-focusing Media

Optical Vortex Solitons (OVSs) are light waves with orbital angular momentum (OAM) and zero amplitude in the center of the transverse profile, which travel without suffering deformation. This type of structured light presents stable propagation in defocusing NL optical media [48], but it is unstable in focusing NL media. The effect that produces the instability is called of modulational instability (MI) and will be explained later. The first theoretical work that studies the MI in OVSs was conducted by Firth *et al.* [49]. In that work, numerical simulations of the optical vortex beam propagation in a saturable self-focusing medium show the split of the vortex into filaments that become in fundamental solitons, as shown in Fig. 1.8. The filaments fly out tangentially from the initial ring, like free Newtonian particles, due to conservation of the OAM. In addition, the number of filaments is strongly dependent on the input OAM.

Since Firth's work was published, several experimental and theoretical studies showing instabilities in SF media were reported. On the contrary, there are no experimental reports showing the stable propagation of OVS in cubic SF. Nevertheless, there are several theoretical works that suggest the use of HON to arrest the instabilities, in analogy with the fundamental soliton behavior [50].

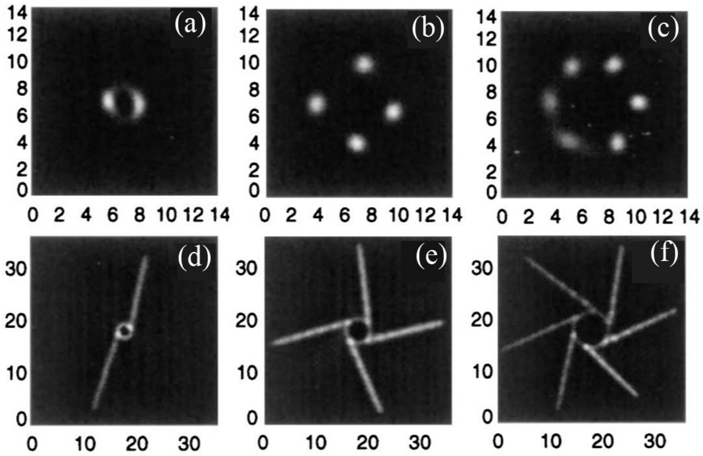

Figure 1.8 (a-c) Splitting of OVSs and (d-f) trajectory of the filaments in saturable SF media, for beams with OAM per photon: (a, d) $\hbar$, (b, e) $2\hbar$ and (c,f) $3\hbar$ (Reprinted from [49]).

To understand a science it is necessary to know its history
- AUGUSTE COMTE

2 NONLINEAR OPTICS

2.1 INTRODUCTION

In the area of optics the interest is concentrated on the study of the properties of light, as well as on the light propagation and its interaction with matter. At relatively low light intensities, the optical properties of materials are essentially independent of the illumination intensity. This is called the linear optical regime. However, when the illumination is sufficiently intense, the optical properties become dependent on the intensity of the light and NL optics comes into play, with its own selection rules and criteria, opening up a completely new and fascinating field of optical phenomena and applications.

In order to induce NL effects, very strong electromagnetic fields (EMFs), typically produced by lasers, are needed. However, the NL optical behavior is not observed when light travels in free space. Rather, the nonlinearity resides in the medium through which the light travels [51]. In this sense, the role of the EMF impressed on the medium is to modify the wave-functions of the atomic electrons, which originate a polarization in the medium. If the EMF is weak compared with the intra-atomic field, the electron wave-functions are slightly perturbed. Therefore, the resulting polarization effect is, to a good approximation, a linear function of the field. Nevertheless, for stronger EMF, the electron wave-functions are modified to a significant degree, producing a NL response of the medium [21].

In the history of NL optics, there are some disagreements on its origin. While some authors agree that an early demonstration of NL optics goes back to 1928, when it was reported scattering of light through mutual interaction of two frequencies with phonons, known as Raman effect [52]. Others may argue that the beginning of NL optics was marked by the first observation of second-harmonic generation in a quartz crystal, by Franken *et al.* [13], which took place shortly after the demonstration of the first working laser built by Maiman in 1960. Although the experiment which gave birth to the NL optics continues being debated, it is generally accepted that both were crucial to the evolution and understanding of the different NL phenomena known so far.

On the other hand, the pioneer studies in NL optics were not based only on observation of new phenomena. Few years after the work of Franken, Bloembergen and co-workers developed the full theory describing the propagation of electromagnetic waves through NL optical active media [53, 54]. Both works connect the intrinsic NL properties of electrons and ions bound in atoms, molecules, and dense media with the macroscopic properties of Maxwell's field quantities in NL media, as well as at a plane interface between a linear and NL medium. For instance, in the classical domain, Maxwell's theory was extended to include high-order interactions between light and matter in terms of NL susceptibilities. In the quantum domain, perturbation theory of the atomic wave function was used to obtain the NL optical susceptibilities. The development and interpretation of these theories allowed the understanding of the different NL optical phenomena observed experimentally, as well as predict new NL effects.

Nonlinear optics is divided into three regimes depending on the amplitude of the incident electric field and the internal electric field that keeps electrons bound to the atomic nucleus. The regime of the **perturbative NL optics** occurs for field amplitudes lower than the intra-atomic fields. Here, the incident field disturbs the atomic levels in non-resonant excitation conditions. Therefore, energy levels suffer only a small displacement, proportional to the intensity due to Stark displacement [55]. If the field amplitudes become comparable, or larger, than the intra-atomic fields experienced by the outermost electrons, there is a large probability that an electron escape of its bound state, causing the ionization of an atom or molecule. The range of field intensities which causes this process is referred to as **strong-field regime of the NL optics** [56]. Finally, the **relativistic regime** occurs when free electrons are accelerated to relativistic velocities, that is, when the electron-nucleus interaction is negligible in comparison with interaction energy between the light field and the atom. Here, the electron trajectory is governed by the equations of relativistic motion [55]. The work in this thesis is related only to the non-relativistic regimes.

This chapter is focused on the fundamentals of the NL polarization and NL susceptibility of materials with inversion symmetry. Some effects induced by the third-order susceptibility are described, mainly due to the effects of NL refraction and NL absorption. In addition, these previous concepts are extended to discuss the origin and properties of HON.

2.2 NONLINEAR POLARIZATION

Light is an electromagnetic wave formed by an electric field $\vec{E}$ and a magnetic field $\vec{H}$, both rapidly varying in time. The fields are related by Maxwell's equations, and because the interaction with the magnetic field is very small, the optical wave can be characterized by defining only its electric field. The wave equation derived from the Maxwell's equations, describing the wave propagation of an electric field vector in an electrically neutral and nonconductive dielectric medium without macroscopic magnetization is expressed by [57]:

$$\vec{\nabla} \times \vec{\nabla} \times \vec{E}(\vec{r},t) + \frac{1}{c^2}\frac{\partial^2 \vec{E}(\vec{r},t)}{\partial t^2} = -\frac{1}{\varepsilon_0 c^2}\frac{\partial^2 \vec{P}(\vec{r},t)}{\partial t^2}, \tag{2.1}$$

where $\vec{E}(\vec{r},t)$ is the incident electric field, $\vec{P}(\vec{r},t)$ is the induced polarization, ε_0 and c is the electrical permittivity and the light speed in the vacuum, respectively.

To complete the description of the light propagation in a dielectric medium, it is necessary to define the relationship between $\vec{E}(\vec{r},t)$ and $\vec{P}(\vec{r},t)$. In this way, from the microscopic point of view, a material can be considered essentially as a system composed of positively charged particles (ionic nuclei) and negative (electrons). When a light wave passes through a material, it acts through its electric and magnetic fields on the charges present in this medium. Commonly, this interaction induces a charge displacement: the positive charges follow the direction of the incident field, while the negative charges travel in the opposite direction. These processes vary considerably from one material to another. For example, in a conductive medium, electrons create an electric current due to their movement when subjected to an incident field. In the case of a dielectric material, the particles join together to form an "elastic". Thus, its instantaneous displacements induces electric dipole moments which oscillate at the same frequency of electric field. The emergence of dipole moments gives rise to the phenomenon known as polarization.

In principle, $\overrightarrow{P}(\overrightarrow{r},t)$ is defined as the average of dipoles moments, $\langle\overrightarrow{\mu}(\overrightarrow{r},t)\rangle$, per unit volume

$$\overrightarrow{P}(\overrightarrow{r},t) = N\langle\overrightarrow{\mu}(\overrightarrow{r},t)\rangle, \tag{2.2}$$

where N is the number of microscopic dipoles per unit volume.

In order to understand the fundamentals of the optical nonlinearity, we must start with the use of constitutive equations , i.e. those that relate the induced polarization with the incident electric field. In general, $\tilde{P}$ is a function of the electric field $\tilde{E}$ which completely describes the response of the medium to the applied field. For simplicity, we consider here that $\tilde{E}$ and $\tilde{P}$ are scalar quantities[1]. Besides, the effect of the magnetic field are much smaller than the electric field and can be neglected. If it is assumed that the incident field is weak, the radiation acts as a small perturbation and the charges within of the medium behave as harmonic oscillators. For the case of a material that displays a purely linear response, the relationship between $\tilde{P}$ and $\tilde{E}$ can be expressed by:

$$\tilde{P}(\overrightarrow{r},t) = \varepsilon_0 \int_0^\infty R^{(1)}\left(\overrightarrow{r}',t'\right)\tilde{E}\left(\overrightarrow{r}-\overrightarrow{r}',t-t'\right)dr'dt', \tag{2.3}$$

where ε_0 is the permittivity of free space and $R^{(1)}$ is the linear response function, which gives the contribution to the polarization produced at time t by an electric field applied at the earlier time $t-t'$. It is important to note that the effective range of integration in Eq. 2.3 is from 0 to ∞ only, because causality requires, $R^{(1)}(\overrightarrow{r}',t') = 0$ for $t' < 0$. This condition defines that $\tilde{P}(\overrightarrow{r},t)$ depends only on past and not on future values of the electric field. Then, eq. 2.3 can be transformed to the $\left(\overrightarrow{k},\omega\right)$ domain by introducing the Fourier transforms $\tilde{E}(\overrightarrow{r},t) = \int_{-\infty}^{\infty} E\left(\overrightarrow{k},\omega\right) exp\left[i\left(\overrightarrow{k}\cdot\overrightarrow{r}-\omega t\right)\right] dkd\omega$.

$$\tilde{P}(\overrightarrow{r},t) = \varepsilon_0 \int_0^\infty dkd\omega\chi^{(1)}\left(\overrightarrow{k},\omega\right)E\left(\overrightarrow{k},\omega\right)exp\left[i\overrightarrow{k}\cdot\overrightarrow{r}-i\omega t\right], \tag{2.4}$$

with $\chi^{(1)}\left(\overrightarrow{k},\omega\right) = \int_{-\infty}^{\infty} R^{(1)}(\overrightarrow{r}',t')exp\left[-i\left(\overrightarrow{k}\cdot\overrightarrow{r}'-\omega t'\right)\right]dr'dt'$ being the linear susceptibility. Furthermore, in the electric dipole approximation, $\chi^{(1)}(\overrightarrow{r},t)$ is independent of $\overrightarrow{r}$, as well as $\chi^{(1)}\left(\overrightarrow{k},\omega\right)$ is independent of $\overrightarrow{k}$. Then, by replacing the left-hand side of eq. 2.4 with $\int\tilde{P}\left(\overrightarrow{k},\omega\right)exp\left(i\overrightarrow{k}\cdot\overrightarrow{r}-i\omega t\right)dkd\omega$, and noting that the equality must be maintained for each frequency ω, we obtain the usual frequency domain description of linear response:

$$\tilde{P}\left(\overrightarrow{k},\omega\right) = \varepsilon_0\chi^{(1)}(\omega)E\left(\overrightarrow{k},\omega\right). \tag{2.5}$$

---

[1] $(\sim)$ is used to denote a quantity that varies rapidly in time

The coefficient $\chi^{(1)}$ is a constant only in the sense of be independent of $\tilde{E}$. However, its magnitude is a function of the frequency of the field used, ω. Eq. 2.3 is valid for the field strength of conventional sources. The linear susceptibility of an isotropic medium, in optical frequencies, is related to the relative dielectric function of the medium , $\varepsilon(\omega)$, by the following relationship:

$$\varepsilon(\omega) = 1 + \chi^{(1)}(\omega), \tag{2.6}$$

with $\tilde{E}(t) = Re\left(Ee^{-i\omega t}\right)$ being the electric field of the incident wave. In addittion, the optical response of a medium can be represented by its complex refractive index

$$n_c^2(\omega) = \varepsilon(\omega) = \left[n(\omega) + i\frac{\alpha(\omega)c}{2\omega}\right]^2, \tag{2.7}$$

where the real part of n_c describes the refractive behavior of the medium, while the absortive behavior is represented by the imaginary part of n_c. In the linear regime, the linear refraction index, n_0, and linear absorption coefficient, α_0, depend on the field frequency, but are independent of the field intensity.

On the other hand, when the laser field is so high as to change the restoring force exerted by the electron on the nucleus, the charges of the medium behave as anharmonic oscillators and $\tilde{P}$ has a NL dependence with $\tilde{E}$. Since the anharmonicity is very small compared with the harmonicity, the polarization can be expanded, in the perturbation limit, as a power series of the electric field

$$\begin{aligned}\tilde{P}(\overrightarrow{r},t) = \varepsilon_0 \Bigg[&\int_{-\infty}^{\infty} R^{(1)}\left(\overrightarrow{r}',t'\right)\tilde{E}\left(\overrightarrow{r}-\overrightarrow{r}',t-t'\right)dr'dt' \\ &+ \int_{-\infty}^{\infty} R^{(2)}(\overrightarrow{r}_1,t_1,\overrightarrow{r}_2,t_2)E(\overrightarrow{r}-\overrightarrow{r}_1,t-t_1)E(\overrightarrow{r}-\overrightarrow{r}_2,t-t_2)dr_1dt_1dr_2dt_2 \\ &+ \int_{-\infty}^{\infty} R^{(3)}(\overrightarrow{r}_1,t_1,\overrightarrow{r}_2,t_2,\overrightarrow{r}_3,t_3)E(\overrightarrow{r}-\overrightarrow{r}_1,t-t_1)E(\overrightarrow{r}-\overrightarrow{r}_2,t-t_2)E(\overrightarrow{r}-\overrightarrow{r}_3,t-t_3) \\ &\times dr_1dt_1dr_2dt_2dr_3dt_3 \Bigg],\end{aligned} \tag{2.8}$$

where the coefficients $R^{(N)}$ $(N = 1, 2, 3, \ldots)$ define the degree of nonlinearity and represent the *N-th* order response function. Eq. 2.8 describes only the NL optical interactions that occur in a medium without loss neither dispersion, being $\chi^{(N)}$ real , scalar and constant. However, by considering the vectorial nature of the fields, as well as the tensorial nature of the susceptibilities, which depends on the electronic and molecular structure of the medium, it is possible to generalize the constitutive relationship between polarization and incident electric field. Thus, Eq. 2.8 can be expressed more generally, in the frequency domain, by applying the Fourier transform, of the form:

$$\tilde{P}\left(\vec{k},\omega\right) = \varepsilon_0 \left[\overline{\chi}^{(1)}(\omega)\cdot\vec{E}\left(\vec{k},\omega\right) + \overline{\chi}^{(2)}(\omega=\omega_1+\omega_2) : \vec{E}\left(\vec{k}_1,\omega_1\right)\vec{E}\left(\vec{k}_2,\omega_2\right) \right.$$
$$\left. + \overline{\chi}^{(3)}(\omega=\omega_1+\omega_2+\omega_3) \vdots \vec{E}\left(\vec{k}_1,\omega_1\right)\vec{E}\left(\vec{k}_2,\omega_2\right)\vec{E}\left(\vec{k}_3,\omega_3\right) + \dots\right], \tag{2.9}$$

where $\overline{\chi}^{(N)}$are $(N+1)$-th order tensor representing the linear $(N=1)$ and NL $(N>1)$ optical susceptibilities.

(a) Linear Terms

The $\overline{\chi}^{(1)}(\omega)$ term in Eq. 2.9 is a tensor with 9 components. However, in an isotropic medium, there is only one nonzero component, and the electric susceptibility or dielectric response is written as a scalar quantity. The linear polarization, $P^{(L)}$, is responsible for the effects of linear refraction, absorption, gain and birefringence. These properties constitute the subject of classical optics, where if there are various waves incident on a material, they do not influence each other.

(b) Second-Order Terms

The $\overline{\chi}^{(2)}(\omega_3=\omega_1+\omega_2;\omega_1,\omega_2)$ term in Eq. 2.8 correspond to second-order effects, which in general can be called three-wave mixing. The second-order NL polarization oscillating at a frequency ω_3 due to the presence of fields oscillating at the frequencies ω_1 and ω_2, with $\omega_3=\omega_1+\omega_2$, is given by [58]:

$$\tilde{P}_i^{(2)}(\omega_3) = \varepsilon_0 \sum_{j,k}\sum_{\omega} D(\omega_3;\omega_1,\omega_2)\,\chi_{ijk}^{(2)}(\omega_3;\omega_1,\omega_2)\,\tilde{E}_j(\omega_1)\,\tilde{E}_k(\omega_2), \tag{2.10}$$

where the first summations over j, k, is simply an explicit way of stating that the Einstein convention of summation over repeated indices holds. The summation sign $\sum_\omega$ serves as a reminder that the expression that follows is to be summed over all distinct sets of ω_1, ω_2. Because of the intrinsic permutation symmetry, the frequency arguments appearing in Eq. 2.10 may be written in arbitrary order. The degeneracy factor for the *n-th* order susceptibility, in the convention of [58], is formally described as

$$D(\omega_{n+1};\omega_1,\dots,\omega_n) = 2^{l+m-n}p, \tag{2.11}$$

where

$$\begin{aligned} p &= \text{the number of distintic permutations of } \omega_1,\dots,\omega_n, \\ n &= \text{the order of the nonlinearity } (n=2), \\ m &= \text{the number of angular frequencies that are zero, and} \\ l &= \begin{cases} 1, & \text{if } \omega_{n+1}\neq 0, \\ 0, & \text{otherwise.} \end{cases} \end{aligned}$$

Each one of the indices i, j and k are related to the Cartesian coordinates (x, y, z). The effects, described by $\chi^{(2)}(\omega_3 = \omega_1 + \omega_2; \omega_1, \omega_2)$, are listed in Table 2.1.

These effects occur only in materials that lack inversion symmetry, since even-order susceptibilities are null in media with such symmetry. In second harmonic generation and parametric mixing the conversion efficiency per unit length, η, is determined by phase matching conditions defined by relation (see Section 2.2.1 of [21]):

$$\eta = \left(\frac{sin(\triangle kL/2)}{\triangle kL/2} \right)^2, \tag{2.12}$$

where $\triangle k = k_{\omega_1} + k_{\omega_2} - k_{\omega_3}$ is the wavevector mismatch of the process and L is the thickness of the NL medium. The process will be more efficient when Eq. 2.12 reaches its maximum value (as close to $\eta = 1$, which occurs when $\triangle k = 0$). It is important to mention that ordinary materials display natural frequency dispersion (frequency dependence of the refractive index). Thus, it is impossible to achieve maximum efficiency in these materials, unless a way is found to phase-match the interaction. One of the most common methods to achieve $\triangle k = 0$ is to use birefringent materials. Angle-tuning of these materials is the technique to modify the refractive indices and tune the phase matching. Other conditions that can be adjusted to increase the conversion efficiency are the use of different light frequencies and variations in the material temperature.

NL Effect	Mixture of frequencies	NL susceptibility
Sum-frequency Generation	$\omega_1, \omega_2, \omega_3 = \omega_1 + \omega_2$	$\chi^{(2)}(\omega_1 + \omega_2; \omega_1, \omega_2)$
Second Harmonic Generation	$\omega_1 = \omega_2 = \omega$, e $\omega_3 = 2\omega$	$\chi^{(2)}(2\omega; \omega, \omega)$
Parametric Mixing	$\omega_1, -\omega_2, \omega_3 = \omega_1 - \omega_2$	$\chi^{(2)}(\omega_1 - \omega_2; \omega_1, -\omega_2)$
Optical Rectification	$\omega_1 = -\omega_2 = \omega$, e $\omega_3 = 0$	$\chi^{(2)}(0; \omega, -\omega)$
Pockels effect	$\omega_1 = 0$, e $\omega_3 = \omega_2 = \omega$	$\chi^{(2)}(\omega; 0, \omega)$

Table 2.1 Effects related to the second-order susceptibility

(c) Third-Order Terms

The $\overline{\chi}^{(3)}(\omega_4 = \omega_1 + \omega_2 + \omega_3; \omega_1, \omega_2, \omega_3)$ term in Eq. 2.8 correspond to third-order effects, that occur independently of whether or not a material possesses inversion symmetry. The relationship between the third-order polarization and the third-order susceptibility is given by [58]:

$$\tilde{P}_i^{(3)}(\omega_4) = \varepsilon_0 \sum_{j,k,l} \sum_{\omega} D(\omega_4; \omega_1, \omega_2, \omega_3) \chi_{ijkl}^{(3)}(\omega_4; \omega_1, \omega_2, \omega_3) \tilde{E}_j(\omega_1) \tilde{E}_k(\omega_2) \tilde{E}_l(\omega_3), \tag{2.13}$$

where $D(\omega_4; \omega_1, \omega_2, \omega_3) = 2^{l+m-n} p$ with $n = 3$. The most common third-order effects are given in Table 2.2.

$\chi^{(3)}_{ijkl}$ is a tensor with 81 components. Since each of the coordinate axes must be equivalent in an isotropic material, the third-order susceptibility possesses the following symmetry properties:

$$\left.\begin{array}{llllll}
\chi^{(3)}_{1111} & = \chi^{(3)}_{2222} & = \chi^{(3)}_{3333}, & & & \\
\chi^{(3)}_{1122} & = \chi^{(3)}_{1133} & = \chi^{(3)}_{2211} & = \chi^{(3)}_{2233} & = \chi^{(3)}_{3311} & = \chi^{(3)}_{3322}, \\
\chi^{(3)}_{1212} & = \chi^{(3)}_{1313} & = \chi^{(3)}_{2323} & = \chi^{(3)}_{2121} & = \chi^{(3)}_{3131} & = \chi^{(3)}_{3232}, \\
\chi^{(3)}_{1221} & = \chi^{(3)}_{1331} & = \chi^{(3)}_{2112} & = \chi^{(3)}_{2332} & = \chi^{(3)}_{3113} & = \chi^{(3)}_{3223},
\end{array}\right\} \tag{2.14}$$

so that only the 21 terms identified above are non-zero. Nevertheless, the elements are related among themselves by (see Section 4.2 of [21]):

$$\chi^{(3)}_{ijkl} = \chi^{(3)}_{1122}\delta_{ij}\delta_{kl} + \chi^{(3)}_{1212}\delta_{ik}\delta_{jl} + \chi^{(3)}_{1221}\delta_{il}\delta_{kj}. \tag{2.15}$$

In particular, for the case of the instantaneous Kerr effect [see table 2.2], which is studied in this thesis, the intrinsic permutation symmetry requires that $\chi^{(3)}_{1122} = \chi^{(3)}_{1212}$. Therefore, Eq. 2.15 is summarized in:

$$\chi^{(3)}_{ijkl} = \chi^{(3)}_{1122}\left(\delta_{ij}\delta_{kl} + \delta_{ik}\delta_{jl}\right) + \chi^{(3)}_{1221}\delta_{il}\delta_{kj}, \tag{2.16}$$

and the third-order polarization for distinguishable fields is given by:

$$\vec{P}^{(3)}(\omega) = 6\varepsilon_0\chi^{(3)}_{1122}\left(\vec{E}\cdot\vec{E}^*\right)\vec{E} + 3\varepsilon_0\chi^{(3)}_{1221}\left(\vec{E}\cdot\vec{E}\right)\vec{E}^*. \tag{2.17}$$

NL Effect	Mixture of frequencies	NL susceptibility
Third Harmonic Generation	$\omega_1, \omega_2, \omega_3 = \omega$, e $\omega_4 = 3\omega$	$\chi^{(3)}(3\omega; \omega, \omega, \omega)$
Non-degenerate Four Wave Mixing	$\omega_1, \omega_2, \pm\omega_3, \omega_4 = \omega_1 + \omega_2 \pm \omega_3$	$\chi^{(3)}(\omega_1 + \omega_2 \pm \omega_3; \omega_1, \omega_2, \pm\omega_3)$
Raman Scattering and Brillouin Scattering	$\omega_1, -\omega_2 = \omega$, e $\omega_3, \omega_4 = \omega \pm \Omega$	$\chi^{(3)}(\omega \pm \Omega; \omega, -\omega; \omega \pm \Omega)$
Instantaneous AC Kerr effect (Degenerate Four Wave Mixing)	$\omega_1, \omega_2, -\omega_3, \omega_4 = \omega$	$\chi^{(3)}(\omega; \omega, \omega, -\omega)$
DC Kerr effect	$\omega_1, \omega_4 = \omega$, e $\omega_2, \omega_3 = 0$	$\chi^{(3)}(\omega; \omega, 0, 0)$
Two Photon Absorption	$\omega_1, -\omega_2, \omega_3, \omega_4 = \omega$	$\chi^{(3)}(\omega; \omega, -\omega, \omega)$
Static electric field induced Second Harmonic Generation	$\omega_1, \omega_2 = \omega$, $\omega_3 = 0$, e $\omega_4 = 2\omega$	$\chi^{(3)}(2\omega; \omega, \omega, 0)$

Table 2.2 Effects related to the third-order susceptibility

All materials in the universe exhibits third-order nonlinearity irrespective of their crystal structure.

(d) High-Order Terms

High-order NL processes are more difficult to be observed, because they require very high intensity fields. However, there are many materials that exhibit this type of behavior. The basis for the HON are discussed at the end of this chapter.

2.3 ORIGIN OF THE NONLINEARITIES

The magnitude of the NL response of a material depends on the physical effects induced by the light field. These effects have different origins, namely, electronic polarization, nuclear response, electrostriction and thermal response. The study of nonlinearities presented in this thesis are related to centrosymmetric materials, i.e. even-order nonlinearities are canceled, and the third-order is the lowest order susceptibility. For this particular case, $\chi^{(3)}$ can be decomposed in a sum of terms corresponding to each contribution

$$\chi^{(3)} = \chi^{(3)}_{elec} + \chi^{(3)}_{nuc} + \chi^{(3)}_{str} + \chi^{(3)}_{th}. \tag{2.18}$$

Depending on the duration of the pulse and the repetition rate of the laser, these phenomena contribute more or less to the nonlinear response.

The Electronic Response

Except near a resonance, the electronic response is quasi -instantaneous, less than one femtosecond. It is due to the spontaneous nonlinear distortion of the electronic distribution around the nuclei and it is independent of the temperature.

Far from any resonance, the different components of the third-order susceptibility tensor [Eq. 2.14] for isotropic materials [58] satisfy:

$$\chi^{(3)}_{1111} = 3\chi^{(3)}_{1122} = 3\chi^{(3)}_{1212} = 3\chi^{(3)}_{1221}. \tag{2.19}$$

Thus, all the components of the $\chi^{(3)}$ tensor can be defined from the knowledge of only one of them. Whatever the duration of the pulse and the repetition rate of the laser, the electronic response is always present. A more detailed description of the electronic nonlinearities is performed in section 2.4. Because the NL response of MDNCs are of electronic origin, Chapters 3, 4, 6 and 8 introduce specifications on the NL response of MDNCs for each condition studied.

The Nuclear Response

The nuclear response depends on the rearrangement of the nuclei position in the modified potential due to the electrons rearrangements. The nuclei motions are much slower than the electronic ones and depend on the temperature. There are different types of nuclear response:

- Molecular reorientation comes from the alignment of the molecules having acquired or possessing naturally a dipolar moment in the direction of the exciting electric field. This process is therefore important in polar molecules.

- Molecular redistribution is particularly present in dense polarizable media. The application of an intense electric field produces interactions between the created dipoles and leads to a redistribution of the molecules which acquire a new equilibrium state by minimization of the energy.

- Vibrations are collective motions of molecules , in the same or opposite directions.

- Librations are vibrations based on a rotational motion of the molecules on sites that prevent overall rotation. They are more descriptively called "rotational vibrations"

The response time of nuclear processes is on the order of several hundreds of femtoseconds to a few picoseconds.

Of special interest is the nonlinearity produced by molecular reorientation, because it corresponds to the nonlinearity of the CS_2, under the conditions studied in this thesis. In particular, the CS_2 molecule has an elongated shape, therefore one can expect that the polarizability in the longest direction of the molecule is greater than in the transverse direction.

Fig. 2.1 shows the polarizability of an elongated molecule, σ, with associated induced dipole, p, with the applied electric field. Thus, the longitudinal (p_L) and transverse (p_T) components of the induced dipole are given by

$$p_L = \sigma_L E_L, \tag{2.20}$$

$$p_T = \sigma_T E_T, \tag{2.21}$$

where E_L and E_T are the projections of the electric field in the longitudinal and transverse directions of the molecule.

In this sense, an incident electric field will produce a reorientation of the molecule to the position of minimum orientational potential energy, U, when the induced dipole is aligned with the incident field. For an arbitrary orientation, corresponding to the angle θ, the potential energy is given by

$$U = -\frac{1}{2}\alpha\sigma_T E^2 - \frac{1}{2}(\sigma_L - \sigma_T) E^2 cos^2\theta. \tag{2.22}$$

If the field is oscillating, as in the case of an incident monochromatic wave, the induced dipole suffers an oscillation, and Eq. 2.22 is valid for the root mean square of the electric field, $|E|^2$. In this case, it can be shown that the NL refractive index caused by the incident field is given by (see Section 4.4 of [21])

$$n_2 = \frac{16\pi^2 N}{45 n_0^2 c}\left(\frac{n_0^2+2}{3}\right)^4 \frac{(\sigma_L - \sigma_T)^2}{k_B T}, \tag{2.23}$$

where N is the number density of molecules, k_B is the Boltzmann constant and T is the temperature. Typical values of n_2 for CS_2 are the order of 10^{-14} cm^2/W.

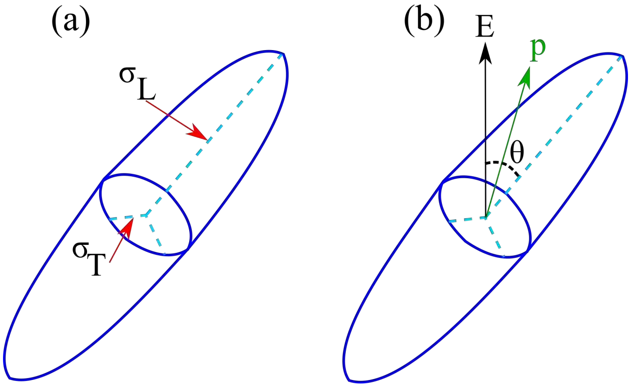

Figure 2.1 (a) Longitudinal and transverse polarizabilities of an elongated molecule. (b) Polarization direction induced by an electric field E, at an angle θ to the longitudinal direction of the molecule.

The Electrostrictive Response

Electrostriction is the process in which the material density increases in response to an applied electric field. The electric field polarizes the molecules which lead to an intermolecular attraction and therefore to a compression of the material. The local increase of the pressure induces an increase of the NL response.

The presence of an optical field within a material produces a pressure given by [59]

$$P_{str} = \frac{\gamma_{str}}{4n_0c}I, \tag{2.24}$$

where I is the intensity, $\gamma_{str} = \rho_0 \left(\frac{\partial\varepsilon}{\partial\rho}\right)_{\rho=\rho_0}$ is known as the electrostrictive constant, with ρ_0 and ε_r being the non-disruptive density and the relative dielectric permittivity, respectively. This parameter can be evaluated using the Lorentz-Lorenz formula [59]

$$\gamma_{str} = \frac{(\varepsilon_{r0}-1)(\varepsilon_{r0}+2)}{3}, \tag{2.25}$$

where ε_{r0} is the non- disrupted relative dielectric permittivity.

For a Gaussian beam with a beam waist w_0, the change in the density will be established in a time $\tau_p \approx w_0/v_s$, where v_s is the sound velocity in the material. The maximal density variation on the optical axis is given by the source term of the acoustic differential equation

$$\triangle\rho_{max} = \frac{\gamma_{str}I}{2n_0cv_s^2}. \tag{2.26}$$

This density variation corresponds to a third-order susceptibility of:

$$\chi^{(3)}_{str} = \frac{\varepsilon_0\gamma^2_{str}}{3\rho_0v_s^2}. \tag{2.27}$$

The electrostrictive effect has a response time of nanoseconds, the typical transit time of an acoustic wave crossing the light beam with $w_0 \cong 10$ µm.

The Thermal Response

The thermal response is due to the absorption of the electric field energy by the material, which is then dissipated in the form of heat. This process induces a change in the NL properties and the response time of thermal effects is on the order of microseconds.

The spatial and temporal temperature change, $T\left(\vec{r},t\right)$, in the material obeys to the differential heat equation with a source term coming from the conversion into heat of part of the energy described by

$$\rho_0 C_p \frac{\partial T}{\partial t} - \kappa \nabla^2 T = \alpha I, \tag{2.28}$$

where ρ_0 is the density of the medium, C_p the heat-capacity at constant pressure, κ the thermal conductivity, α the absorption coefficient and I the irradiance. The term $\kappa\nabla^2 T$ represents the thermal diffusion. The source term αI represents the fraction of the beam power converted into heat by unit of volume.

The transient behavior of thermal diffusion is determined by the thermal diffusivity $D = \frac{\kappa}{\rho_0 C_p}$. For a Gaussian beam with beam waist w_0, the heat will leave the focal region by diffusion in a time $\tau_D \approx \frac{w_0^2}{4D}$. For short pulses, the thermal diffusion has no influence on the beam itself. Therefore, the term $\kappa\nabla^2 T$ in the differential equation 2.28 can be neglected. Thus, Eq. 2.28 can be integrated to determine the temporal evolution of the temperature vaariation on the optical axis at the focal region

$$\triangle T\left(t\right) = T\left(t\right) - T\left(-\infty\right) = \frac{\alpha}{\rho_0 C_p}\int_{-\infty}^{t} I\left(0,\tau\right) d\tau. \tag{2.29}$$

Hence, the variation of the third-order susceptibility associated with the thermal effect can be written as:

$$\chi_{th}^{(3)} = \frac{4\varepsilon_0 n_0^2 c}{3I_0}\frac{\partial n}{\partial T}\triangle T = \frac{\partial \chi^{(3)}}{\partial T}\triangle T, \tag{2.30}$$

where $\frac{\partial n}{\partial T}$ is the thermo-optical coefficient and I_0 the peak irradiance.

2.4 NL REFRACTION AND NL ABSORPTION

It is well known the relationship between the real and imaginary parts of the linear susceptibility, $\chi^{(1)}$, with the corresponding linear refractive index, n_0, and the linear absorption coefficient, α_0, of a material. Here, the real part of the susceptibility leads to a change of the incident wave phase, which is responsible for the refractive index. The imaginary part of the susceptibility represents the part of the induced polarization which is out of phase in 90° with the applied field, producing the attenuation (absorption) of the incident field.

If the material is centrosymmetric, i.e. admits inversion symmetry, the second-order susceptibility vanishes and the most important NL term is the third-order susceptibility, this type of material is called Kerr medium. Similarly to the linear regime, the real and imaginary parts of the third-order susceptibility, $\chi^{(3)}$, are relate to the third-order refractive index, n_2, and third-order absorption coefficient, α_2. This can be understood by analyzing the terms of third-order polarization that oscillate in the same frequency of the incident optical field. For simplicity, it is assumed that the incident electric field oscillates in the frequency ω and is given by:

$$\tilde{E}(t) = E\,e^{-i\omega t} + c.c. \tag{2.31}$$

The total polarization of the system, for a frequency ω , considering the first- and third-order terms is:

$$\tilde{P}(\omega) = \varepsilon_0 \left[\chi^{(1)}(\omega) + \frac{3}{4}\chi^{(3)}(\omega;\omega,-\omega,\omega)\,|E|^2\right] E, \tag{2.32}$$

$$\tilde{P}(\omega) = \varepsilon_0 \left[\chi_{eff}(\omega)\right] E, \tag{2.33}$$

where the effective susceptibility of the medium, $\chi_{eff}(\omega) = \chi^{(1)}(\omega) + \frac{3}{4}\chi^{(3)}(\omega;\omega,-\omega,\omega)\,|E|^2$, may be expressed as a function of the electric field amplitude. The coefficient of the third-order polarization, for the optical Kerr effect, is obtained by considering the degeneracy factor of Eq. 2.11 as $D = 2^{1+0-3}(3) = 3/4$ [58].

By using a constitutive relation between the electric displacement vector, $\overrightarrow{D}$, and the applied electric field, obtained from Maxwell's equations, we have

$$\overrightarrow{D} = \varepsilon_r \overrightarrow{E} = \varepsilon_0 \overrightarrow{E} + \overrightarrow{P}, \tag{2.34}$$

where $\overrightarrow{P} = \varepsilon_0 \chi_{eff} \overrightarrow{E}$ and

$$\varepsilon = \frac{\varepsilon_r}{\varepsilon_0} = 1 + \chi_{eff}, \tag{2.35}$$

$$\varepsilon = 1 + \chi^{(1)}(\omega) + \frac{3}{4}\chi^{(3)}(\omega;\omega,-\omega,\omega)\,|E|^2. \tag{2.36}$$

It is possible to derive the NL refractive index and NL absorption coefficient by comparing Eq. 2.36 with Eq. 2.7, making some small considerations.

NL Refraction

Several mechanisms may contribute to the third-order NL response. Here, it is described the dependence of the refractive index with the incident light intensity, known as NL refraction effect. The NL refraction phenomenon is one of the most explored in the scientific literature and probably the most important effect for building quasi-instantaneous optical switches (see Chapter 2 of [60]). Nevertheless, their theoretical description and its applications depend strongly on the origin of their nonlinearity, as seen in Section 2.3. Here, changes of the refractive index with the intensity, due to electronic polarization, are discussed. Such variations are induced when the frequency of the incident wave is far from the resonance frequencies of the material, but the optical field has a large amplitude, enough to distort its electronic distribution. The origin of the NL refractive index is in the spatial redistribution of the electron cloud.

By comparing the real part of Eq. 2.7 and Eq. 2.36, and assuming that the absorption coefficient is much smaller than the refractive index in such a way that it can be neglected, the refractive index is given by:

$$n(\omega) = \sqrt{1 + Re\left[\chi^{(1)}(\omega)\right] + \frac{3}{4} Re\left[\chi^{(3)}(\omega;\omega,-\omega,\omega)\right] |E|^2}. \tag{2.37}$$

Considering the linear refractive index $n_0 = \sqrt{1 + Re\left[\chi^{(1)}(\omega)\right]}$ and the intensity of the incident wave $I = \frac{1}{2} n_0 \varepsilon_0 c |E|^2$, Eq. 2.37 becomes:

$$n(\omega) = n_0 \sqrt{1 + \frac{3Re\left[\chi^{(3)}(\omega;\omega,-\omega,\omega)\right]}{4n_0^2} \left(\frac{2I}{n_0 \varepsilon_0 c}\right)}. \tag{2.38}$$

Making a binomial expansion, due to the NL term be less than the linear term, the total refractive index is given by:

$$n(\omega) = n_0 + \frac{3Re\left[\chi^{(3)}(\omega;\omega,-\omega,\omega)\right]}{4n_0^2 \varepsilon_0 c} I. \tag{2.39}$$

Eq. 2.39 shows that the variation of the linear refractive index depends linearly with the intensity, where the coefficient is called of third-order refractive index and is proportional to real part of the third-order susceptibility

$$n_2(\omega) = \frac{3Re\left[\chi^{(3)}(\omega;\omega,-\omega,\omega)\right]}{4n_0^2 \varepsilon_0 c}. \tag{2.40}$$

The change in refractive index proportional to the incident intensity is known as the Kerr optical effect, and is responsible for effects such as: self-focusing, self-defocusing, self-phase modulation, among others. The Kerr optical effect is explained in the Section 2.5.1.

NL Absorption

Saturable Absorption

Saturable absorption is a property of materials where the absorption of light decreases with the increasing of light intensity. At sufficiently high incident light intensity, atoms or molecules in an initial state of a saturable absorber material become excited into an upper energy state at such a rate that there is insufficient time for them to decay back to the ground state before the ground state becomes depleted, and the absorption subsequently saturates.

A simple kinetic model can be used when the saturation is considered in terms of depletion of the ground state concentration. Thus, for a two-level system in the steady state,

$$\frac{dN}{dt} = \frac{\sigma I}{h\nu}(N_g - N) - \frac{N}{\tau} = 0, \tag{2.41}$$

where N is the concentration of excited state molecules, N_g is the undepleted ground state concentration, σ is the absorption cross section, hv is the photon energy, and τ is the lifetime of the excited state population. Assuming that the absorption coefficient α is proportional to the ground state population, $\alpha = \sigma(N_g - N)$, we get the following equation describing the saturation,

$$\alpha = \frac{\alpha_0}{1+\frac{I\sigma\tau}{hv}} = \frac{\alpha_0}{1+\frac{I}{I_s}}, \tag{2.42}$$

where $I_s = \frac{hv}{\sigma\tau}$ is the saturation intensity and $\alpha_0 = \sigma N_g$ is the linear absorption coefficient. The case described by the above equation is referred to as homogeneous saturation (see Chapter 1 of [21]).

The main applications of saturable absorbers are in passive mode-locking and Q-switching of lasers, i.e. in the generation of short pulses [61]. The key parameters for a saturable absorber are its wavelength range (where it absorbs), its dynamic response (recovery time), and its saturation intensity and fluence (at what intensity or pulse energy it saturates). Saturable absorbers are also useful for purposes of NL filtering outside laser resonators, e.g., cleaning up pulse shapes, and optical signal processing.

Two-Photon Absorption (2PA)

The transition of a system from the ground state to a higher level by the simultaneous absorption of two photons is termed two-photon absorption. In the degenerate case, two photons of frequency ω of the incident field are simultaneously absorbed by the system to make the transition to a state that is approximately resonant at 2ω . A schematic representation of 2PA can be found in Fig. 2.2.

The intermediate level being virtual, the two photons should be simultaneously absorbed making the process sensitive to the instantaneous optical intensity of the incident radiation. 2PA process is proportional to the square of the input intensity. The propagation of a monocromatic laser light through the system describing the optical loss is given by:

$$\frac{dI}{dz} = -\alpha_0 I - \alpha_2 I^2, \tag{2.43}$$

where α_0 is the linear absorption coefficient (which can be very small), α_2 is the 2PA coefficient

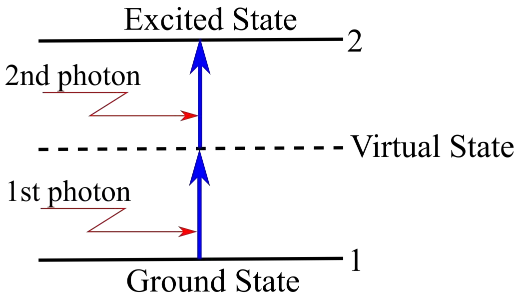

Figure 2.2 Schematic representation of two-photon absorption.

and z is the propagation direction. α_2 is a macroscopic parameter that characterizes the material and is related to the individual molecular 2PA cross section σ_2 through,

$$\sigma_2 = \frac{\hbar\omega\alpha_2}{N}, \tag{2.44}$$

where N is the number density of the molecules in the system and $\hbar$ is the reduced Planck constant. It is the imaginary part of the third-order NL susceptibility of the system that determines the strength of the 2PA. The relation between the 2PA coefficient and $\chi^{(3)}$ of a centrosymmetric system, for linearly polarized incident light, is given by

$$\alpha_2 = \frac{3\omega}{2\varepsilon_0 n_0^2 c^2} Im\left[\chi^{(3)}\right]. \tag{2.45}$$

Reverse Saturable Absorption (RSA)

Reverse saturable absorption is a two-step, sequential one-photon absorption process as shown schematically in Fig. 2.3. In this case the medium has a resonant linear absorption for the incident laser beam, and some of the molecules in the ground state are excited to another excited state of higher energy. For a properly chosen medium, it is possible that the excited molecules make another transition from the excited state 2 to a higher excited state 3 via another one-photon absorption. (In polyatomic molecules in fact a 5-level model may be considered, which involves both singlet and triplet states).

The possibility of this process depends on the number of molecules N_2 at the first excited state 2, the incident intensity I, and the excited state absorption cross section σ_{23}. On the other hand, N_2 is related to N_1 and I by the expression,

$$N_2 \propto \sigma_{12} N_1 I, \tag{2.46}$$

where σ_{12} is the cross-section of the transition from the ground state to state 2. As can be seen from this relation, the number of molecules in state 2 (N_2) continuously grows with the incident intensity I and the one-photon sequential absorption from state 2 to state 3 becomes more significant, provided that the cross section σ_{23} of this transition is considerably larger than σ_{12}. Under the steady-state condition, the intensity change of the laser beam in the NL medium along its propagation direction can be expressed as,

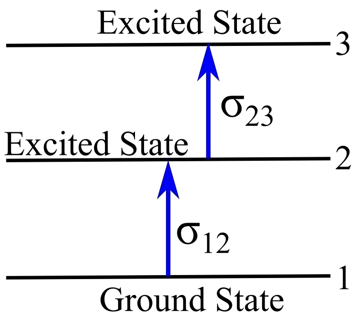

Figure 2.3 Schematic representation of reverse saturable absorption.

$$\frac{dI}{dz} = -\sigma_{12}(N_1 - N_2)I - \sigma_{23}N_2 I. \tag{2.47}$$

In the simplest case, it can be assumed that $N_1 \gg N_2, N_3 = 0$, and $N_1 = N_0$, where N_0 is the number density of the absorbing molecules. Then according to Eq. 2.46, the above equation can be rewritten as

$$\begin{aligned} \frac{dI}{dz} &= -\sigma_{12}N_0 I - b\sigma_{12}\sigma_{23}N_0 I^2, \\ \frac{dI}{dz} &= -\alpha_0 I - \alpha_2' I^2, \end{aligned} \tag{2.48}$$

where b is a proportionality coefficient, and the linear absorption coefficient $\alpha_0 = \sigma_{12}N_0$ and NL absorption coefficient $\alpha_2' = b\sigma_{12}\sigma_{23}N_0$.

2.5 OTHER NL EFFECTS

Below are described some of the most important NL effects associated to the NL refractive index. These NL phenomena will be the basis for studies in HON effects, reported in this thesis.

2.5.1 Optical Kerr Effect

The change in the refractive index of a material in response to the optical intensity is known as the Kerr effect (see Section 4.1 [21]). As a result, a high intensity beam travelling through a Kerr medium will undergo self-phase modulation (SPM), a NL effect in which the refractive index of the medium is changed by a beam of light (Fig. 2.4). Physically the high intensity light beam induces a NL polarization and this alters the optical path length of the light beam, resulting in a phase shift at the exit of the sample. The SPM can drive some interesting NL phenomena, such as self focusing [Fig. 2.4(a)] and self defocusing [Fig. 2.4(b)].

Self-focusing (SF) and self-defocusing (SDF) phenomena are inverse NL effects produced by positive $(\triangle n > 0)$ and negative $(\triangle n < 0)$ NL refractive index, respectively. When passing through a Kerr medium a Gaussian beam with uniform phase will experience SPM in proportion to the intensity of the beam. Thus, a Gaussian beam experience different phase shifts, $\triangle\Phi$, across the profile of the beam, due to the nonuniform intensity. The phase shift is expressed by

$$\triangle\Phi = k(\triangle n)L_{eff}, \tag{2.49}$$

where L_{eff} is the effective length of the medium.

In SF media, the high intensity light of a Gaussian beam causes a local increase in the refractive index, $n = (n_0 + \triangle n) > n_0$, experiencing a positive phase shift. In thin media, this high index region acts as a thin convergent lens, inducing the beam focalization. The opposite effect occurs when the nonlinearity is negative (SDF media), $n = (n_0 + \triangle n) < n_0$. High intensity regions of the beam cause a local decrease in the refractive index which induce a negative phase shift the beam. Therefore the beam diverges, or defocus, faster than it would in a linear regime.

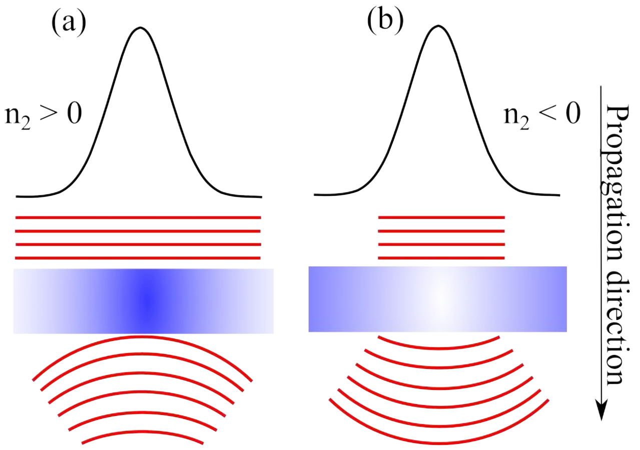

Figure 2.4 (a) Self-focusing and (b) self-defocusing effects of an intense Gaussian beam. The red lines illustrate the evolution of a incident beam with plane wavefront when passing through a Kerr material.

It is clear that the sign of the nonlinearity has a drastic effect on the output beam. When a medium has a positive (negative) nonlinearity, a high intensity beam propagating through it will experience SF (SDF). It's important to mention that the output beam has a higher (lower) peak than the input. However, this does not break any conservation of energy rules because the integrals of both curves (optical power) are in fact identical. Each output has the same integral as the input, as one would expect in a closed system when absorption is neglected.

2.5.2 NL Transverse Effects

As explained above, when an intense light beam propagates in a NL medium, the light-matter interaction modifies the spatial profile of the beam, resulting in various transverse effects. These NL effects can be self-induced or induced by another intense beam. Below, it is briefly described some transverse effects induced by the third-order nonlinearity in isotropic media.

2.5.2.1 Spatial Self-Phase Modulation (SSPM)

When a Gaussian laser beam passes through a NL medium, it may exhibit a characteristic diffraction ring pattern resulting from SSPM effect [62].

Spatial self-phase modulation is a consequence of the difference in NL refractive index at different radial positions of a beam due to its non-uniform spatial intensity profile. The variation of the refractive index not only produces different light speeds leading to self-focusing or self-defocusing, but also induces changes in the optical path of each part of the beam. Since the manifestation of SPM is closely related to the temporal and spatial behavior of a light beam, the analysis of the patterns produced by a thick sample becomes very complicated. This is mainly due to the fact that SPM and SF (or SDF) effects can generally coexist in a thick sample and the theoretical treatment becomes rather complex. For the sake of simplicity, we consider only thin NL samples.

In thin media, SSPM phenomena caused by Gaussian beam can be described as diffraction of light through a circular aperture, which introduces a spatial NL phase shift depending on the local light intensity. The circular aperture corresponds to the beam width on the sample, while the phase shift profile is due to the NL response of the medium. Following the classical theory of Fraunhoffer diffraction [63], the light field in rectangular coordinates can be written as:

$$E_F(p,q) = C\int_A E_I exp\left[-ik\left(p\xi + q\eta\right)\right] d\xi d\eta, \tag{2.50}$$

where (p,q) are the coordinates of a point P in the diffraction pattern, (ξ,η) are the coordinates of a typical point in the aperture and C is a constant [see Fig. 2.5(a)]. E_i is the incident electric field and k is the wave vector of the incident electromagnetic radiation. For a circular aperture, it is more convenient to use polar coordinates to represent the light field. Let (ρ,ϑ) be the polar coordinates of a typical point in the aperture

$$\left.\begin{array}{ll} \rho cos\vartheta & = \xi \\ \rho sin\vartheta & = \eta \end{array}\right\}, \tag{2.51}$$

and (Ω,ψ) be the coordinates of a point P in the diffraction pattern referred to the geometrical image of the source

$$\left.\begin{array}{ll} \Omega cos\psi & = p \\ \Omega sin\psi & = q \end{array}\right\}. \tag{2.52}$$

It follows that $\Omega = \sqrt{p^2+q^2}$ is the sine of the angle which the direction (p,q) makes with the central direction $p = q = 0$. If a is the radius of the circular aperture, the diffraction integral now can be written as,

$$E_F(p,q) = C\int_0^a\int_0^{2\pi} E_I exp\left[-ik\rho\Omega cos\left(\vartheta - \psi\right)\right] d\vartheta d\rho. \tag{2.53}$$

For an incident Gaussian beam, the electric field can be written as

$$E_I = E_0 exp\left[-\left(\frac{\rho^2}{w^2}\right) - \left(\frac{ik\rho^2}{2R}\right)\right], \tag{2.54}$$

where ρ is the radial distance of a point on the wavefront from the center of the beam, w is the beam width, and R is the radius of curvature of the wavefront. Here, it is possible to observe that, for a Gaussian beam, the intensity is a function of ρ. Hence the NL phase shift introduced at the aperture should also be a function of ρ. If this NL phase shift can be represented by $\phi^{NL}(\rho) = \triangle\Phi exp\left[\frac{-2\rho^2}{w^2}\right]$, with $\triangle\Phi$ given by Eq. 2.49, then Eq. 2.53 must be multiplied by a phase factor of $exp\left[-i\phi^{NL}(\rho)\right]$

$$E_F(p,q) = C\int_0^a\int_0^{2\pi} E_I exp\left[-ik\rho\Omega cos\left(\vartheta - \psi\right)\right] exp\left[-i\phi^{NL}(\rho)\right] d\vartheta d\rho. \tag{2.55}$$

By using the standard Bessel functions (see Chapter 3 of [57])

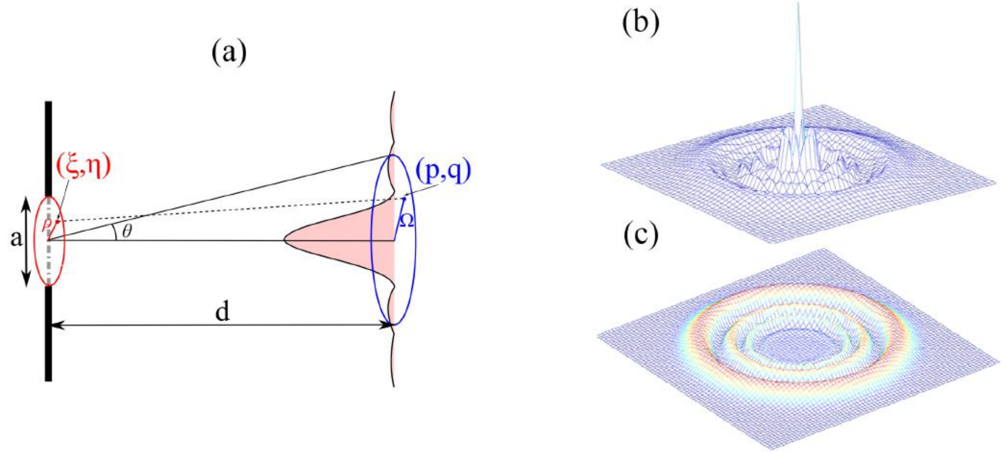

Figure 2.5 (a) Schematic representation used to analyze the SSPM effects with the theory of Fraunhofer diffraction. Typical diffraction patterns of SSPM for cubic (b) self-focusing and (c) self-defocusing media [62].

$$J_n(x) = \frac{i^{-n}}{2\pi} \int_0^{2\pi} exp\left[i\left(xcos\beta\right)\right] exp\left[i\left(n\beta\right)\right] d\beta, \tag{2.56}$$

and assuming that $\Omega \approx \theta$, the diffraction angle; the light field at far-field can be written as

$$E_F(p,q) = 2\pi C E_0 \int_0^a J_0(k\rho\theta)\, exp\left[-\left(\frac{\rho^2}{w^2}\right) - \left(\frac{ik\rho^2}{2R}\right)\right] exp\left[-i\phi^{NL}(\rho)\right] d\rho. \tag{2.57}$$

It can be seen from the above equation that the diffraction ring pattern, obtained by SSPM effect, depends mainly on the NL phase shift $\phi^{NL}(\rho)$ and the curvature radius R [see Fig. 2.5(b) and (c)].

2.5.2.2 Spatial Modulation Instability (SMI)

In NL dynamics, much attention has been devoted to the investigations of modulational instability in the framework of the NL Schrödinger equation (NLSE). Modulational instability is a characteristic feature of a wide class of NL systems and can be classified into three main categories: spatial [64], temporal [65] and spatiotemporal [66]. This thesis focuses the studies of MI in the spatial domain.

SMI occurs due to the interaction between the effects of diffraction and nonlinearity. It is a fundamental NL phenomenon in which a weak perturbation imposed on the input beam grows exponentially, resulting into the breaks up of homogeneous beam into numerous small filaments. Hence SMI is considered as a basic process that classifies the quantitative behavior of modulated waves and may initialize the formation of stable entities such as envelope of spatial solitons. In general, SMI typically occurs in the same parameter region where soliton-like phenomenon occurs and can be loosely considered as a precursor to spatial soliton formation.

SMI plays an important role in many NL phenomenon such as: cross-phase modulation [67], four-wave mixing [68], SHG [69], polarization and birefringence [70] and spatial solitons [71]. In this section, SMI is analyzed due to spatial cross-phase modulation (XPM) effect.

The electric field of two copropagating beams linearly polarized, at frequencies ω_1 e ω_2, is expressed by

$$\vec{E}\left(\vec{r},t\right) = \frac{1}{2}\hat{x}\sum_{j=1}^{2} A_j\left(\vec{r},t\right) exp\left[i\left(k_j z - \omega_j t\right)\right] + c.c., \tag{2.58}$$

where $\hat{x}$ is the polarization unit vector, $k_j = n_{0j}\omega_j/c$ is the wave number and $n_{0j} = n_0\left(\omega_j\right)$ is the linear refractive index, which depends on the frequency due to the chromatic dispersion. By substituting the Eq. 2.58 in the wave equation [Eq. 2.1], considering the total polarization as a sum of linear polarization and third-order polarization [Eq. 2.32], and making the paraxial approximation, the coupled amplitude equations, which describe the propagation of two optical beam, assume the form:

$$\frac{\partial A_1}{\partial z} - \frac{i}{2k_1}\left(\frac{\partial^2 A_1}{\partial x^2} + \frac{\partial^2 A_1}{\partial y^2}\right) = \frac{ik_1 n_2}{n_{01}}\left(\left|A_1\right|^2 + 2\left|A_2\right|^2\right)A_1, \tag{2.59}$$

$$\frac{\partial A_2}{\partial z} - \frac{i}{2k_2}\left(\frac{\partial^2 A_2}{\partial x^2} + \frac{\partial^2 A_2}{\partial y^2}\right) = \frac{ik_2 n_2}{n_{02}}\left(\left|A_2\right|^2 + 2\left|A_1\right|^2\right)A_2, \tag{2.60}$$

where $n_2 \propto Re\left[\chi^{(3)}\right]$ is the third-order refractive index. The first terms of the right-hand sides represent the SSPM effects, while the second terms correspond to the spatial cross-phase modulation (SXPM) effects. A more detailed procedure for obtain Eqs. 2.58 and 2.59, will be specified in Chapter 5.

In order to study the origin of the transverse SMI, the waves are assumed to be plane waves with constant intensity I_j [72], i.e.

$$A_j\left(x,y,z=0\right) = \sqrt{I_j}. \tag{2.61}$$

Thus, the analytical solutions of the coupled equations are:

$$A_j\left(x,y,z\right) = \sqrt{I_j} exp\left[ik_j z\frac{n_2}{n_{0j}}\left(I_j + 2I_{3-j}\right)\right], \tag{2.62}$$

with $j = 1$, 2. The stability of these solutions are analyzed by introducing a small perturbation to the exact solutions, of the form:

$$A'_j\left(x,y,z\right) = A_j\left(x,y,z\right)\left\{1 + u_j\left(z\right)exp\left[i\left(px+qy\right)\right] + v_j^*\left(z\right)exp\left[-i\left(px+qy\right)\right]\right\}, \tag{2.63}$$

where p and q are the components of the spatial frequency associated with the transverse perturbation. Substituting Eq. 2.63 into Eqs. 2.59 and 2.60 and linearizing in terms of u_j and v_j^*, it is obtained a set of equations with nontrivial solution of the form $u_j \propto exp\left(iKz\right)$, where K is the wave number and obey the dispersion relation:

$$\left(K^2 - h_1^2\right)\left(K^2 - h_2^2\right) = C^2, \tag{2.64}$$

with

$$h_j = \frac{S}{2k_j}\left[S^2 - sgn\left(n_2\right)S_{cj}^2\right]^{1/2}, \tag{2.65}$$

$$C = S^2\left(\frac{S_{c1}S_{c2}}{k_1k_2}\right), \tag{2.66}$$

$$S^2 = p^2 + q^2, \tag{2.67}$$

$$S_{cj} = 2k_j\left(\frac{|n_2|I_j}{n_{0j}}\right)^{1/2}. \tag{2.68}$$

The dispersion relation [Eq. 2.64] shows that K becomes imaginary whenever $C > h_1h_2$. This is the necessary condition for transverse modulation instability. Finally, the growth rate of SMI induced by third-order nonlinearity is given by $\Gamma = 2Im\left(K\right)$.

2.5.3 Optical Spatial Solitons

In linear media, localized wavepackets typically spread as they propagate. However, in some NL materials, nonlinearity can under proper conditions stop the spreading, and such wavepackets do not change their shapes at all as they propagate. These wavepackets are then called optical solitons in analogy with solitons in hidrodynamics. In 1834, a Scottish scientist John S. Russell observed a "rounded smooth and well defined heap of water" propagating in a narrow and shallow canal "without change of form or diminution of speed" [73]. This was the first scientifically documented observation of solitons in nature. In the spatial domain, optical solitons are self-trapped light beams that appear due to the balance between the linear diffraction and the nonlinearity. High intensity light locally increases the index of refraction, and then this modulation in the index of refraction acts as a waveguide, guiding the beam that created the modulation itself. In quite a few cases this self-consistent self-trapping also turns out to be stable, and such a beam is called an “optical spatial soliton” [48].

Theoretically, the possibility of soliton formation was first suggested in 1962 by Askar’yan, who predicted that “the effects of the gradient of a strong electromagnetic beam on electrons and atoms can be used to set up waveguide propagation conditions and to eliminate divergence of the beam (self-focusing)" [74]. Shortly after, Chiao, Garmire and Townes computed the profile that exhibits a perfect balance between Kerr nonlinearity and diffraction, known as the (2 + 1)-D (Townes) soliton [75]. However, a year later, Kelley showed that for sufficiently strong powers, the nonlinearity can dominate the diffraction and hence, the (2 + 1)D Kerr solitons collapse [76]. Indeed, it became quickly clear that observation of stable spatial solitons in Kerr media is only possible in planar geometry $(D = 1)$. In addition, it was predicted that stable solitons in bulk $(D \geq 2)$ can form in media with a saturable nonlinearity [39].

The earliest experimental evidence of spatial self-trapping was provided by Bjorkholm and Ashkin in 1974 in bulk vapor of sodium atoms [77]. This self-trapping was accompanied by significant absorption, hence, it was not true solitonic propagation. It tooks 11 years until the first observation of true solitons in CS_2 gas [36] which has a reorientational nonlinearity. In further studies, Kerr solitons have been observed in planar waveguides of glass [78], semiconductors

[79, 80] and polymers [81]. Finally, genuine bulk spatial solitons were observed in polymers with a cubic-quintic nonlinearity [82]. Studies of spatial solitons have made rapid progress since the mid-1990's, when two new soliton-supporting NL optical media became available to experiments [83]. First, generation of solitons in quadratic media which was identified theoretically in the mid-1970's [84], was demonstrated experimentally in a series of works of the group of G. Stegeman. In particular, an effective Kerr coefficient in a quadratic medium was first produced and measured experimentally by De Salvo *et al.* [85]. Then, (2 + 1)D and (1 + 1)D spatial quadratic solitons were generated experimentally by Torruellas *et al.* [86] and Schiek *et al.* [87], respectively. Second, Segev et al. [88] predicted that the saturable nonlinearities of photorefractive materials can support stable soliton propagation. Soon afterwards, a variety of photorefractive solitons, of both (1 + 1)D and (2 + 1)D types and for both focusing and defocusing nonlinearities, have been explored. Vortex soliton dynamics have been theoretically investigated in numerous contexts [89, 90] and the angular momentum and spatial dynamics have been studied experimentally in defocusing Kerr [91], photorefractive [92] and quadratic NL media [90].

Of all the different types of spatial solitons mentioned above, we will focus on the study of Kerr-like solitons, which correspond to the experiences presented in this thesis. To have a preliminary notion of the study of spatial solitons, this section assumes the one-dimensional propagation of an optical beam through a Kerr medium exhibiting only third-order refractive index. A more complete mathematical formalism, including contribution of HON, is developed in Chapter 5.

The evolution of optical fields in NL media can be modeled by using the NLSE, obtained from Maxwell's equations. For simplicity, it will be used the normalized cubic NLSE (C-NLSE) given by:

$$i\frac{\partial u}{\partial z}+\frac{1}{2}\frac{\partial^2 u}{\partial x^2}\pm|u|^2u=0, \tag{2.69}$$

where u is the normalized field amplitude, z and x are the propagation and transverse direction, respectively. The positive (negative) sign corresponds to a SF (SDF) medium. For SF media, one of all solution of Eq. 2.69 is of particular interest:

$$u_{BS}=u_0sech\left[u_0x\right]exp\left[iu_0^2\frac{z}{2}\right], \tag{2.70}$$

where it is possible to note that the intensity of this family of solutions $\left(I_{BS}=|u_{BS}|^2\right)$ is z independent. Therefore, all solution of this type, known as bright solitons, will keep their shape and size invariant along propagation [Fig. 2.6(a)]. However, in order to observe such solitons in nature, it is not enough to have a steady state mathematical solution in hand: one should also check for the stability of this steady state solution to noise and to deviations from ideal initial condition. If the solution exemplifies a state of stationary propagation - only then it can be considered as a soliton. It is important to note that a bright soliton exists when the self-focusing nonlinearity balance the linear diffraction. Thus, a specific power is required for that the diffraction angle be equal to the self-focusing angle. Therefore, the self-trapping ocurrs only if the power contained in the beam has the critical value (see Section 7.1 [21]):

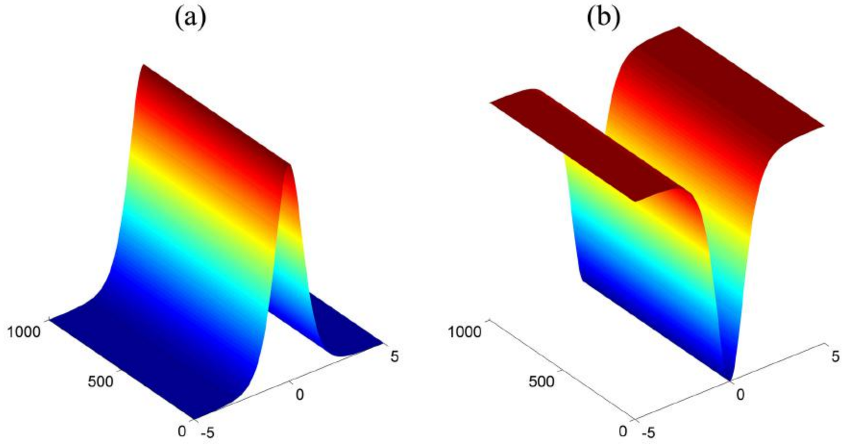

Figure 2.6 One-dimensional (a) bright and (b) dark spatial solitons

$$P_{cr} \approx \frac{\lambda_0^2}{8n_0n_2}. \tag{2.71}$$

Similarly, for SDF media, a solution of Eq. 2.69 has the form:

$$u_{DS} = u_0 tanh\left[u_0x\right] exp\left[iu_0^2z\right]. \tag{2.72}$$

This last equation represents a dark soliton [Fig. 2.6(b)], which propagates without changing its size and shape. Dark solitons are more difficult to handle than bright solitons, but they have shown to be more stable and robust to losses.

2.5.4 Filamentation

A filament is a dynamic optical pulse structure with an intense core that is able to propagate over extended distances much larger than the typical diffraction length while keeping a narrow beam size without the help of any external guiding mechanism [93]. The filamentation regime occurs when the incident beam power is higher than the critical power, P_{cr}, defined in Eq. 2.71, so that self-focusing effects predominate on the linear diffraction, producing the break-up of the original beam [94].

Filamentation can be viewed as a near-forward four-wave mixing process. Figure 2.7(a) displays the interaction schematically. Two on-axis photons from the main beam are annihilated, creating two off-axis photons, with equal but opposite transverse wave vectors. It is generally assumed that the main beam is very strong, while the off-axis modes are initially weak perturbations. In the classical case, these perturbations are slight distortions to the wavefront, while in the quantum case the perturbations are vacuum fluctuations. Making the strong pump approximation, the system can then be analyzed by writing and solving a set of coupled equations for the side modes.

Research into filamentation began soon after the invention of the laser. A detailed theory of filamentation was first developed by Bespalov and Talanov [95]. According to the these theory,

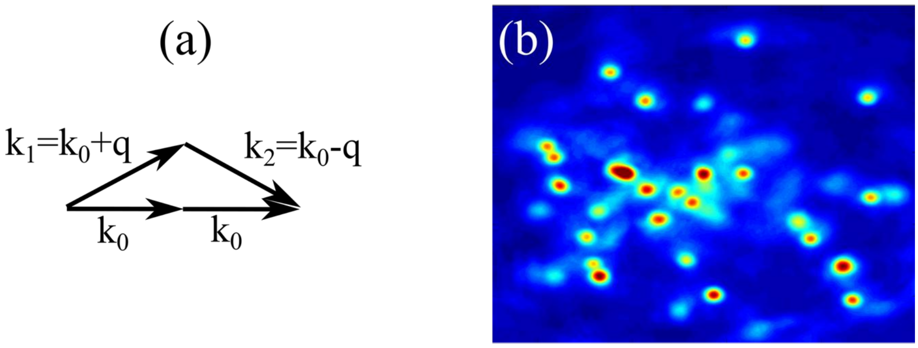

Figure 2.7 (a) Schematic representation of filamentation. (b) Filamentation pattern observed in CS_2 [26]

the size of the generated filaments is given by:

$$\Lambda = \frac{\pi}{k}\sqrt{\frac{n}{2n_2 I}}. \tag{2.73}$$

Each filament is predicted to contain approximately one critical power (P_{cr}). During the formation of each filament, the perturbations are predicted to display exponential growth, where the exponential gain factor for a given mode is

$$g = K\sqrt{\frac{n_2 E^2}{n_0} - \frac{K^2}{4k^2}}, \tag{2.74}$$

where K is the magnitude of the transverse wave vector of a the given mode and E is the root mean square field strength. This equation was corroborated experimentally by illuminating a silicate glass with an intense picosecond laser [96]. Here, molecular excitation is predicted as a dominating mechanism for the filamentation process rather than the electronic Kerr effect for filaments of very small size.

For experimental exploration of the properties of filamentation, the side modes are often purposely populated. This can be achieved by putting a transverse spatial modulation on the beam. As long as the depth of modulation is weak, the above analysis is still correct. Fig. 2.7(b) shows an experimental image of laser filamentation obtained in CS_2, in picosecond regime [26].

During most of the 34 years since the original development in the field of filamentation, the new experiments and theoretical studies have involved attempts to quantify and limit the effects of filamentation. With the recent availability of ultrafast laser systems, filamentation is also being explored in the femtosecond regime [97]. However, the basic theory being applied is the same as in other regimes such as picosecond and nanosecond.

2.6 HIGH-ORDER NONLINEARITIES (HON)

Usually, the NL response of centrosymmetric photonic materials has been described by considering the third-order NL optical contribution, at “relatively” low intensity levels. However, HON may become significant at high intensities (e.g, quintic nonlinearity, $\chi^{(5)}$, and septimal nonlinearity, $\chi^{(7)}$), and have to be included to describe the total NL optical response. In some cases, HON can cause problems (e.g, rapid break-up of a beam even at moderate intensities), especially when no adequate control of their contributions is made. Nevertheless, for several applications HON are desired (e.g, formation of stable multi-dimensional optical solitons). Therefore, a better understanding of HON in materials is then crucial.

Until few decades ago, HON contributions were totally neglected. However, the characterization of materials with intense pico and femtosecond lasers allowed the observation of many phenomena associated to HON. Up to the present, HON have been reported for glasses [98], solvents [25], MDNCs [23], gases [31] and atomic systems [99].

In centrossymetric materials, the total polarization having components along a particular direction μ can be expressed as the sum of linear $\left(\tilde{P}^{L}\right)$ and NL contributions $\left(\tilde{P}^{NL}\right)$:

$$\begin{aligned}\tilde{P}_{\mu}(\omega) &= \tilde{P}_{\mu}^{L}(\omega)+\tilde{P}_{\mu}^{NL}(\omega),\\ &= \tilde{P}_{\mu}^{L}(\omega)+\sum_{N=1}\tilde{P}_{\mu}^{(2N+1)}(\omega).\end{aligned} \tag{2.75}$$

In the perturbation limit, the (2N+1)-th NL polarization in μ-direction, using the notation of [58], can be expressed by:

$$\begin{aligned}\tilde{P}_{\mu}^{(2N+1)}(\omega_{2N+2}) = \varepsilon_0 \sum_{\varsigma_1,\varsigma_2,\ldots,\varsigma_{2N+1}} \sum_{\omega} & D(\omega_{2N+2};\omega_1,\omega_2,\ldots,\omega_{2N+1})\\ &\times \chi_{\mu\varsigma_1,\varsigma_2,\ldots,\varsigma_{2N+1}}^{(2N+1)}(\omega_{2N+2};\omega_1,\omega_2,\ldots,\omega_{2N+1})\\ &\times \tilde{E}_{\varsigma_1}(\omega_1)\tilde{E}_{\varsigma_2}(\omega_2)\ldots\tilde{E}_{\varsigma_{2N+1}}(\omega_{2N+1}),\end{aligned} \tag{2.76}$$

where $\omega_{2N+2}=\omega_1+\omega_2+\ldots+\omega_{2N+1}=\omega$. For simplicity, it was assumed that the incident field is linearly polarized, e.g. in the x-direction. That is, $\tilde{E}_x(\omega)\neq 0$, and null along y- and z-directions. Therefore, Eq. 2.76 is reduced to:

$$\tilde{P}_{x}^{(2N+1)}(\omega) = \varepsilon_0 D \chi_{(2N+2)x}^{(2N+1)}(\omega)\left|\tilde{E}_x(\omega)\right|^{2N}\tilde{E}_x(\omega), \tag{2.77}$$

where $\chi_{(2N+2)x}^{(2N+1)}(\omega)$ with $N=1,2,\ldots$ is the (2N+1)-th NL susceptibility in frequency ω and D is given by Eq. 2.11. However, for Kerr-type nonlinearities, where all frequencies are nonzero ($m=0$ and $l=1$ in Eq. 2.11) and all nonlinearities are of odd-order ($n=2N+1$), it is possible to express the degeneracy factor only by the order of the nonlinearity:

$$D = 2^{1-(2N+1)}p = 2^{-2N}\left[\frac{(2N+1)!}{(N)!\,(N+1)!}\right]. \tag{2.78}$$

Therefore, the total polarization [Eq. 2.75] in the x-direction as a function of electric field is given by:

$$\begin{aligned}\tilde{P}_x(\omega) &= \varepsilon_0\chi_{xx}^{(1)}\tilde{E}_x(\omega)+\varepsilon_0\left[\sum_{N=1}2^{-2N}\frac{(2N+1)!}{(N)!\,(N+1)!}\chi_{(2N+2)x}^{(2N+1)}(\omega)\left|\tilde{E}_x(\omega)\right|^{2N}\right]\tilde{E}_x(\omega),\\ \tilde{P}_x(\omega) &= \varepsilon_0\chi_{eff}\tilde{E}_x(\omega),\end{aligned} \tag{2.79}$$

and the dielectric function is:

$$\begin{aligned}
\varepsilon &= 1 + \chi_{eff}, \\
\varepsilon &= 1 + \chi_{xx}^{(1)} + \sum_{N=1} 2^{-2N} \frac{(2N+1)!}{(N)!\,(N+1)!} \chi_{(2N+2)x}^{(2N+1)}(\omega) \left|\tilde{E}_x(\omega)\right|^{2N}.
\end{aligned} \tag{2.80}$$

Following the procedure described in Section 2.4, it is possible to show that the total refractive index, n, and the total absorption coefficient, α, are expressed by:

$$n = n_0 + \frac{1}{2n_0} \sum_{N=1} \left[2^{-2N} \frac{(2N+1)!}{(N)!\,(N+1)!} Re\left[\chi_{(2N+2)x}^{(2N+1)}(\omega)\right] \left|\tilde{E}_x(\omega)\right|^{2N} \right], \tag{2.81}$$

$$\alpha = \alpha_0 + \frac{\omega}{cn_0} \sum_{N=1} \left[2^{-2N} \frac{(2N+1)!}{(N)!\,(N+1)!} Im\left[\chi_{(2N+2)x}^{(2N+1)}(\omega)\right] \left|\tilde{E}_x(\omega)\right|^{2N} \right]. \tag{2.82}$$

On the other hand, the total refraction and absorption coefficients can be written as a function of the intensity, of form:

$$n = n_0 + \sum_{N=1} n_{2N} I^N, \tag{2.83}$$

$$\alpha = \alpha_0 + \sum_{N=1} \alpha_{2N} I^N. \tag{2.84}$$

Thus, a relationship between the (2N+1)-th NL refraction (absorption) coefficients and the real (imaginary) part of the (2N+1)-th NL susceptibilities can be obtained by using the relationship between the electric field amplitude and intensity $\left(I = \frac{1}{2}\varepsilon_0 n_0 c |E|^2\right)$

$$n_{2N} = \frac{1}{2n_0} \left(\frac{1}{2\varepsilon_0 n_0 c}\right)^N \frac{(2N+1)!}{(N)!\,(N+1)!} Re\left[\chi_{(2N+2)x}^{(2N+1)}(\omega)\right] \tag{2.85}$$

$$\alpha_{2N} = \frac{\omega}{cn_0} \left(\frac{1}{2\varepsilon_0 n_0 c}\right)^N \frac{(2N+1)!}{(N)!\,(N+1)!} Im\left[\chi_{(2N+2)x}^{(2N+1)}(\omega)\right] \tag{2.86}$$

The origin of the HON is also associated to the effects mentioned in Section 2.3, but it will depend on the type of material being studied. Currently, it is known that HON may arise from direct or cascade (microscopic and macroscopic) contributions. These different types of HON contributions are discussed in Section 3.5.2 for the particular case of MDNCs.

In science, when human behavior enters the equation, things go nonlinear.
That's why Physics is easy and Sociology is hard.
- NEIL TYSON

Nature is nonlinear everywhere
- JOSÉ RIOS LEITE

3 METAL-DIELECTRIC NANOCOMPOSITES

3.1 INTRODUCTION

Nanocomposites are materials that combine two or more natural or artificial elements (with different physical or chemical properties), in which at least one of the phases shows dimensions in the nanometer scale. In particular, metal-dielectric nanocomposites (MDNCs) are artificial materials formed by metal NPs hosted in a dielectric medium, so that they may surpass the performances of bulk materials [100]. Generally, the optical properties of MDNCs are described by the effective dielectric constant, as studied in Chapter 2. Metal particles with sizes much smaller than the wavelength of an external applied EMF interact strongly with the EMF, at optical frequencies. The resulting collective oscillations of the free electrons inside the particles induce an enhancement of the effective field that modifies the effective dielectric constant of the MDNC. This effect is called *dielectric* or *classical confinement* [101]. On the other hand, a quantum treatment shows that the optical response of MDNCs is sensitive to particle size, when it is in the quantum size regime (diameter < 10 nm). This effect called *quantum confinement* occurs because the electrons in the NPs are confined to regions much smaller than their mean free path, which is of the order of a few micrometers for the case of bulk noble metals [102]. As a consequence of these confinements, MDNCs exhibit significant improvement and modification in their mechanical, thermal, transport and optical properties over bulk materials.

Of special interest is the improvement of the optical properties of MDNCs, which has generated an enormous evolution in optics and photonics. For instance, it is well known that bulk metals posses high optical linear and NL response. However, it is difficult to take advantage of this optical properties in experiments based on the transmission or light propagation, because light penetrates into metals for only tens of nanometers [101]. On the contrary, much of the light that illuminates a metal is reflected and for that reason metals are widely used in the construction of mirrors. Nevertheless, light can penetrate more deeply into metals when they are combined with dielectric materials. Thus, with recent developments of nanoscience and nanotechnology combined with an increasing knowledge in surface chemistry and functionalization, MDNCs have expanded the applications of metals in the field of optics such as optical limiters [103], optical tweezers [104] and all-optical switches [105].

However, the application of MDNCs are not limited to the exploration of their optical properties. Significant technological advances using MDNCs have been made in medical applications [106], chemical and biological sensing [107], genosensors and immunosensors [108], plasmonic solar cells [109], detection of chemical pollutants [110], forensic science [111], among others.

The present chapter aims to discuss a background on the optical properties of MDNCs, focusing on its NL behavior. In addition, the influence of the local-field effects on the NL susceptibility of MDNCs, as weel as the internal (size, shape) and external factors (environment properties) are studied. These concepts are extended for the HON, discussing their origins and measurement procedures. The Chapter concludes with an analysis of the NL optical properties of MDNCs by introducing a generalized Maxwell-Garnett model, which includes the HON contributions of metal NPs.

3.2 LINEAR OPTICAL PROPERTIES

The interaction between light and metals takes place between the optical electric field and the conduction electrons of the metals. Normally, some light energy can be transferred to the host lattice as heat via electron-phonon collisions. In general, the optical properties of metals can be characterized by two parameters: refractive index, n, and extinction coefficient, K, that result in the complex refractive index, n_c, where:

$$n_c = n + iK. \tag{3.1}$$

The refractive index n is defined as the ratio between the velocity of light in vacuum and the phase velocity of light in the given medium. The extinction coefficient K is related to the exponential decay of the wave as it passes through the medium. Both parameters depend on the wavelength and samples' temperature. The absorption coefficient is related to the extinction coefficient by comparing Eq. 3.1 with Eq. 2.7:

$$\alpha = \frac{2\omega}{c} K. \tag{3.2}$$

In this way, the expression for an electromagnetic wave propagating in an absorbing medium can be expressed as:

$$E = E_0 exp\left[-i\frac{2\pi}{\lambda}(n - iK)x\right] exp\left[-i\omega t\right], \tag{3.3}$$

resulting in the well known Beer's law:

$$I \propto |E|^2 = |E_0|^2 exp\left[-\alpha x\right]. \tag{3.4}$$

Eq. 3.4 indicates that the flux density will drop by a factor of e^{-1} after the wave has propagated a distance $\delta_p = \frac{1}{\alpha}$, which is known as the penetration depth. For a transparent material the penetration depth is larger than its thickness. However, the penetration depth for metals is very small. For instance, silver has a penetration depth of only ~2.5 nm for the light at 532 nm [112].

In solids, the electronic transitions are related to the complex dielectric constant ,$\varepsilon = \varepsilon' + i\varepsilon''$, and according to Chapter 2, these physical quantities are connected by:

$$\varepsilon' = n^2 - K^2, \tag{3.5}$$

$$\varepsilon'' = 2nK. \tag{3.6}$$

Therefore, the first step to understand the linear optical properties of metals and MDNCs is to analyze its optical response by investigating its dielectric function.

(a) In Bulk Metals

Noble metals, in particular Au, Ag and Cu, have similar band structures, which include a set of five valence bands with low dispersion, called d-bands (associated to atomic d-orbitals), and a half-filled sp-band called the conduction band. All the electron bands are therefore either filled or empty, except for the conduction band which is filled up to the Fermi level. Most of the electronic properties in metals involve only a small number of the electron bands, and often even involve only the conduction band states near the Fermi energy. This is the case for the interactions involving the conduction electrons, such as electron-electron and electron-phonon interactions, and for the optical response in the IR to visible spectral range. However, the response of the noble metals to an electromagnetic excitation in the UV- visible range should include the influence of bound electrons in the d-bands.

For the particular case of excitation in the visible regime, the optical properties of metals can be explained by considering the conduction electrons as a gas of free particles, moving around fixed ion cores. This model developed by Drude allows to obtain the dielectric function of a metal, with good accuracy [113]. Drude's model is based on three fundamental assumptions:

- *Free Electron Approximation:* The interaction between the electron gas and the fixed ion cores is modelled by assuming that an electron will occasionally collide with an ion core and change its trajectory. These collisions are instantaneous events that change the velocity of the electrons. Between two successive collisions, the interactions of the electron gas with the ion cores are neglected.

- *Independent Electron Approximation:* Interactions between individual electrons in the gas are neglected.

- *Relaxation Time Approximation:* On average, an electron will travel through the metal for a relaxation time before experiencing a collision. The relaxation time is related to the resistivity of a metal R by the relation $\tau_r = m/(Rnq^2)$, where n, m and q are the number, mass and charge of the electron.

The motion of the free electrons in metal subjected to an external electric field E can be express as:

$$m_0\ddot{r} + m_0\gamma_r\dot{r} = -qE, \tag{3.7}$$

where m_0 is the effective optical mass of the conduction electrons, $\gamma_r = 1/\tau_r$ is the damping coefficient, with the relaxation time of the free electron τ_r in the order of 10^{-4} s, in the room temperature.

Assuming a harmonic time dependence of the electric field, i.e., $E(t) = E_0 exp(-i\omega t)$, a particular solution of this equation describing the oscillation of the electron in x-direction $x(t) = x_0 exp(-i\omega t)$ is:

$$x = \frac{q}{m_0(\omega^2 + i\gamma_r\omega)}E(t). \tag{3.8}$$

The displaced electrons contribute to the macroscopic polarization $P = -Nqx$, explicitly given by

$$P = -\frac{Nq^2}{m_0(\omega^2 + i\gamma_r\omega)}E(t), \tag{3.9}$$

where N is the density of the conduction electrons and the dielectric displacement, $D = \varepsilon_0 E + P$, is

$$D = \varepsilon_0 \left[1 - \frac{\omega_p^2}{\left(\omega^2 + i\gamma_r \omega\right)} \right] E\left(t\right), \tag{3.10}$$

where $\omega_p = \sqrt{Nq^2 / \left(m_0 \varepsilon_0\right)}$ is the plasma frequency of the free electron gas. Therefore the dielectric function is:

$$\varepsilon\left(\omega\right) = 1 - \frac{\omega_p^2}{\left(\omega^2 + i\gamma_r \omega\right)}. \tag{3.11}$$

The real and imaginary components of this complex dielectric function $\varepsilon_m\left(\omega\right) = \varepsilon_m'\left(\omega\right) + i\varepsilon_m''\left(\omega\right)$ are given by

$$\varepsilon_m'\left(\omega\right) = 1 - \frac{\omega_p^2 \tau_r^2}{\omega^2 \tau_r^2 + 1}, \tag{3.12}$$

$$\varepsilon_m''\left(\omega\right) = \frac{\omega_p^2 \tau_r}{\omega\left(\omega^2 \tau_r^2 + 1\right)}. \tag{3.13}$$

It should however, be noted that the Drude model is only an idealization and describes none of the real metals perfectly. The plasma model of metals is valid over a frequency range up to the ultraviolet for alkali metals and to visible frequencies for noble metals (mainly Au and Ag) [113], when interband transitions of electrons begin to occur. In addition, for noble metals at near-infrared frequencies it is possible to consider $\omega \gg 1/\tau_r$ [114]. Therefore:

$$\varepsilon_m'\left(\omega\right) \approx 1 - \frac{\omega_p^2}{\omega^2} = 1 - \frac{\lambda^2}{\lambda_p^2}, \tag{3.14}$$

$$\varepsilon_m''\left(\omega\right) \approx \frac{\omega_p^2}{\omega^3 \tau_r} = \frac{1}{2\pi c \tau_r} \frac{\lambda^3}{\lambda_p^2}, \tag{3.15}$$

where $\lambda_p^{-2} = Nq^2 / \left(4\pi^2 \varepsilon_0 m_0 c^2\right)$. Typical values of m_0 and τ_r for noble metal are given in Table 3.1.

In particular, Johnson *et al.* [114] reported experimental measurements of the refractive indices and absorption coefficients of silver, for different wavelengths. These measurements were fitted by Eqs. 3.5 and 3.6, where the dielectric function are given by Eq. 3.14 and 3.15, as shown in Fig. 3.1. This indicates that the Drude model is reliable mainly for low energies.

Metal	m_0	$\tau_r\ (fs)$
Copper	1.49 ± 0.06	6.9 ± 0.7
Silver	0.96 ± 0.04	31 ± 12
Gold	0.99 ± 0.04	9.3 ± 0.9

Table 3.1 Effective optical masses and relaxation times for noble metals [114]

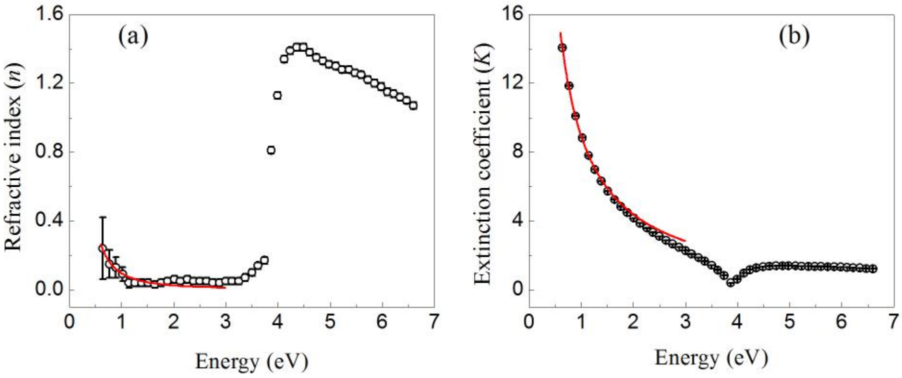

Figure 3.1 (a) Refractive index and (b) extinction coefficient of silver in differents wavelengths [114]. The solid lines correspond to Drude model.

(b) In MDNCs

The fascinating optical properties of the MDNCs originate from the interaction between the nanoparticles and the incident light which results in an electronic oscillatory motion at the interface metal-dielectric. The optical parameters, n and K are effective quantities and have contributions of the host and the volume fraction occupied by the NPs. A well-established model to study the optical properties of MDNCs is the Maxwell-Garnett model [115], which is simple and convenient for modeling due to its linearity. The Maxwell Garnett model is valid for dielectric composites with dilute conductive phases (below the percolation threshold[1]). This is a model that implies the quasistatic approximation and aims to predict the effective optical response of a composite, without calculate the microscopic electric field. Its main features are:

- The mixture is electrodynamically isotropic.
- The mixture is non-parametric, that is, its parameters do not change in time according to some law as a result of external forces (electrical, mechanical, etc.).
- The inclusions are spherical NPs with diameter a separated by distances greater than their characteristic size $(b > a)$.
- The light wavelength λ used to analyze the optical properties, satisfies $\lambda > b > a$.
- If there are conducting inclusions, their concentration should be lower than the percolation threshold.

Under these conditions it is possible to consider that the electric field inside a dielectric sphere, with radius a and dielectric function ε_{NP}, placed in an infinite medium of dielectric constant ε_h, on which is applied a static and uniform electric field E_0 in the z-direction, is given by:

$$E_{ins} = \frac{3\varepsilon_h}{\varepsilon_{NP} + 2\varepsilon_h} E_0. \tag{3.16}$$

---

[1] percolation threshold is the limit in which the conductivity of the medium changes from being dominated by the conductivity of the dielectric component to be dominated by the conductivity of the metallic component.

The derivation of this equation is detailed in Section 3.4. Consequently, the field outside the sphere is given by the electric field E_0 plus the electric field due to a dipole p, at the origin. However, for the topology assumed in the Maxwell-Garnett model, the following approximation is valid

$$E_{out} = E_0. \tag{3.17}$$

The induced polarization, P, per unit volume within the NP is related to the electric field by $P = (\varepsilon_{NP} - \varepsilon_h) E_{ins}$, with an electric dipole moment of the form:

$$p = v_{NP} P = 3\varepsilon_h v_{NP} \left(\frac{\varepsilon_{NP} - \varepsilon_h}{\varepsilon_{NP} + 2\varepsilon_h} \right) E_0, \tag{3.18}$$

where v_{NP} is the volume of the NP.

Because the electromagnetic radiation corresponds to harmonic fields, the electric field of the Maxwell-Garnett model corresponds to an average of the fields inside and outside of the NPs on the volume of the composite. Thus, the effective Maxwell-Garnet field is:

$$E_{MG} = f E_{ins} + (1 - f) E_{out}, \tag{3.19}$$

where f is the volume fraction, which is defined as the ratio between the volume occupied by the NPs and the host. Both electric fields E_{ins} and E_{out} are homogeneous within the medium, independent of the volumetric region analyzed. This is a consequence of the interaction between the particles is not being considered, besides the electric dipole field in the dielectric medium is neglected.

By introducing the Eqs. 3.16 and 3.17 in Eq. 3.19, we have

$$E_{MG} = \left[f \left(\frac{3\varepsilon_h}{\varepsilon_{NP} + 2\varepsilon_h} \right) + (1 - f) \right] E_0. \tag{3.20}$$

Similarly, the polarization in the Maxwell-Garnett model corresponds to an average, on the composite volume and on the polarizations inside and outside of the NPs, given by

$$\begin{aligned} P_{MG} &= \varepsilon_h \left[f (\varepsilon_{NP} - 1) E_{ins} + (1 - f)(\varepsilon_h - 1) E_{out} \right], \\ &= \varepsilon_h \left[3 f \varepsilon_h \left(\frac{\varepsilon_{NP} - 1}{\varepsilon_{NP} + 2\varepsilon_h} \right) + (1 - f)(\varepsilon_h - 1) \right] E_0, \end{aligned} \tag{3.21}$$

and by using the relation $P_{MG} = \varepsilon_h \left(\varepsilon_{eff} - 1 \right) E_{MG}$, it is possible to obtain an expression for the effective dielectric function of the form:

$$\begin{aligned} \varepsilon_{eff} &= \varepsilon_h \frac{\varepsilon_{NP}(1 + 2f) + 2\varepsilon_h (1 - f)}{\varepsilon_{NP}(1 - f) + \varepsilon_h (2 + f)}, \\ \varepsilon_{eff} &= \varepsilon_h \left[1 + \frac{3\Theta f}{1 - \Theta f} \right], \end{aligned} \tag{3.22}$$

with

$$\Theta = \frac{\varepsilon_{NP} - \varepsilon_h}{\varepsilon_{NP} + 2\varepsilon_h}. \tag{3.23}$$

By considering the host dielectric function, ε_h, to be real and the NPs dielectric function as $\varepsilon_{NP} = \varepsilon'_{NP} + i\varepsilon''_{NP}$, the real and imaginary parts of the effective dielectric function, ε'_{eff} and ε''_{eff} respectively, are given by:

$$\varepsilon'_{eff} = \varepsilon_h \left\{ \frac{\left[(\varepsilon'_{NP})^2 + (\varepsilon''_{NP})^2 \right] (1-f)(1+2f) + \varepsilon_h \varepsilon'_{NP} \left(4f^2 + f + 4 \right) + 2\varepsilon_h^2 (1-f)(f+2)}{\left[(\varepsilon'_{NP})^2 + (\varepsilon''_{NP})^2 \right] (1-f)^2 + 2\varepsilon_h \varepsilon'_{NP} (1-f)(f+2) + \varepsilon_h^2 (f+2)^2} \right\}, \tag{3.24}$$

$$\varepsilon''_{NP} = \varepsilon_h \left\{ \frac{9\varepsilon_h^2 \varepsilon''_{NP} f}{\left[(\varepsilon'_{NP})^2 + (\varepsilon''_{NP})^2 \right] (1-f)^2 + 2\varepsilon_h \varepsilon'_{NP} (1-f)(f+2) + \varepsilon_h^2 (f+2)^2} \right\}. \tag{3.25}$$

These equations reveal that incident radiation does not distinguish separately the NPs of the dielectric medium, but the compound as a whole. Therefore, the optical response of the MDNC depends on all components of the composite, where the strength of each contribution is managed by the value of f, for these reasons the dielectric function is called *effective dielectric function* $\left(\varepsilon_{eff}\right)$.

Again, from Eqs. 3.24 and 3.25 is possible to obtain the optical parameters of MDNC such as: effective refractive index, n_{eff}, and the effective extinction coefficient ,K_{eff}, as shown in Fig 3.2. As a demonstration we use CS_2 as the host, where its dielectric constant is given by [116]

$$\begin{aligned} \varepsilon_h(\lambda) &= \left[n_{CS_2}(\lambda) \right]^2, \\ &= \left[1.580826 + \frac{1.52389 \times 10^{-2}}{\lambda^2} + \frac{4.8578 \times 10^{-4}}{\lambda^4} + \frac{8.2863 \times 10^{-5}}{\lambda^6} + \frac{1.4619 \times 10^{-5}}{\lambda^8} \right]^2. \end{aligned} \tag{3.26}$$

Fig. 3.2 shows the variation of the effective refractive index and effective extinction coefficient of MDNC consisting of silver NPs suspended in CS_2, by varying the volume fraction. $f = 0$ represents to pure CS_2 and $f = 1$ is the pure metal (silver).

3.3 SURFACE PLASMON RESONANCE

Plasmon resonances arise from the collective, resonant oscillations of the conduction electrons. In this thesis, only the case of metals will be considered. A discussion on plasmon in semiconductors can be found in [117]. Like all oscillators, the conduction electrons have a characteristic frequency, $\omega_p = \sqrt{Ne^2/m_{eff}\varepsilon_0}$, known as the plasma frequency, which depends on the density of electrons, N, and the effective mass, m_{eff}. Plasmon oscillations can be categorized into three different modes, depending on the applicable boundary conditions: volume, surface, and localized surface (or particle) plasmons, which are all schematically illustrated in Fig. 3.3.

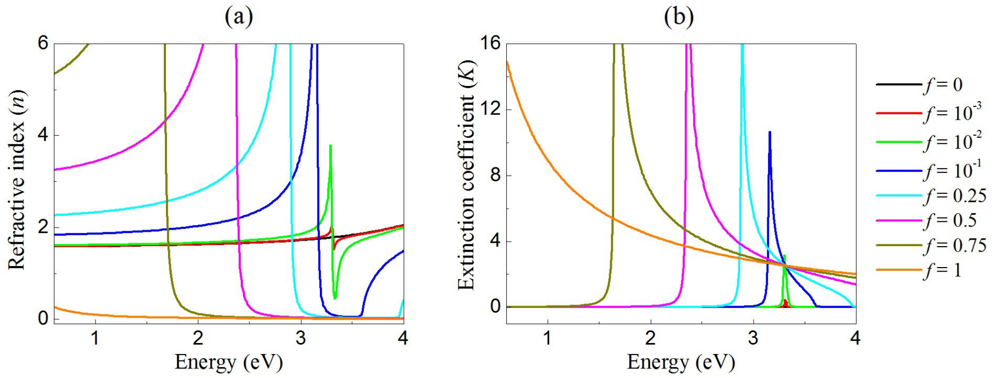

Figure 3.2 Effective (a) refractive index and (b) extinction coefficient of a MDNC consisting of silver NPs suspended in CS_2, for different volume fractions, obtained from Maxwell-Garnett model.

Volume plasmons [Fig. 3.3(a)] are collective oscillations of the conduction electron gas in a bulk metal. These resonances are not confined, and cannot be directly excited with an electromagnetic wave. In bulk metals, the motion of the free conduction electron is similar to a mass being dragged in a viscous fluid, as a consequence appear more than one resonance frequency, which will differ based on whether the electrons can respond quickly enough to the driving force of the incident field. Thus, if the incident light frequency (ω_{in}) is larger than the plasma frequency (ω_p), the electrons will not oscillate and the light will be almost totally transmitted or absorbed in interband transitions. However, if $\omega_{in} < \omega_p$, the electrons will oscillate 180° out of phase with the incident light, causing a strong reflection [118], as shown in Fig 3.3(a).

For the case where the metal is reduced to a thin film, the oscillations only exist at the surface, giving rise to propagating charge waves known as surface plasmon polaritons (SPPs). SPPs occur for example at dielectric-metal interfaces. In essence, these resonances correspond to the oscillations of the longitudinal charge density confined in one dimension. Considering the directional plasmon propagation along metal surfaces, the wave equation yields two possible propagation modes, transverse magnetic (TM) , and transverse electric (TE) . Due to the boundary conditions at the interface between metal and dielectric, only TM modes may excite surface plasmons. Moreover, the only allowed TM modes must fulfill the dispersion relation:

$$k_{SPP}(\omega) = k_0(\omega)\sqrt{\frac{\varepsilon_m(\omega)\,\varepsilon_d(\omega)}{\varepsilon_m(\omega)+\varepsilon_d(\omega)}}, \tag{3.27}$$

where $k_{SP}(\omega)$ is the propagation constant of the surface plasmon, $k_0(\omega)$ is the propagation constant of the applied fundamental field, $\varepsilon_m(\omega)$ is the dielectric function of the metal, and $\varepsilon_d(\omega)$ is the dielectric function of the surrounding dielectric material. The direct consequence of the dispersion relation [Eq. 3.27] is that surface plasmons can only exist for opposite signs of the real parts of $\varepsilon_m(\omega)$ and $\varepsilon_d(\omega)$. For the case of a metal surrounded by a dielectric material, this condition is always satisfied, because $Re\left[\varepsilon_m(\omega)\right]$ has negative values in the visible and near-infrared spectral regions and dielectrics always possess a positive $\varepsilon_d(\omega)$. The above condition also implies that the electric waves decay exponentially perpendicular to the surface.

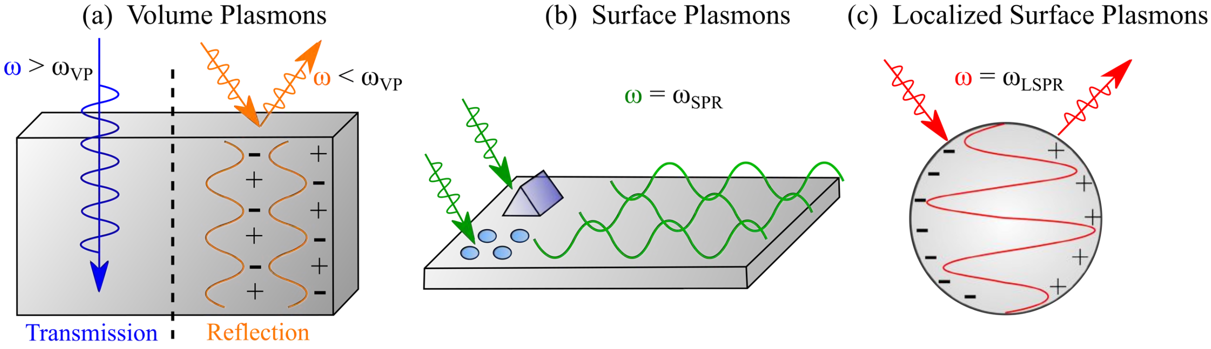

Figure 3.3 Different modes of plasmon resonances in metals: a) volume plasmon (with resonance frequency ω_{VP}), b) surface plasmon (with resonance frequency ω_{SPR}), and c) localized surface plasmon (with resonance frequency ω_{LSPR}) [118].

Moreover, the dispersion relation also implies that the surface plasmon and the excitation field have different wavevectors. Therefore, surface plasmons cannot be excited by light propagating in free space, but special phase-matching techniques, e.g., using a prism (Kretschmann or Otto configuration), or diffraction grating, are needed to effectively couple light to surface plasmons [119]. The dispersion curve in Eq. 3.27 defines an angle for which the grating or the prism can supply the necessary momentum to excite the SPP. At this angle, light will be absorbed (see Fig. 3.3(b)), leading to a dip in the reflection or transmission spectrum [118].

Plasmons may be excited also in metal NPs that are three-dimensional structures whose sizes are of the order of the wavelength of the excitation field or less. The oscillations of the conduction electrons inside such structures are confined in all three dimensions, and are referred to as localized surface plasmons (LSP) or particle plasmons. In comparison to surface plasmon, LSP are non-propagating modes which can be easily excited with direct light illumination, without the use of any special configurations such as prisms or gratings. The interaction of the applied field with a collection of metal NPs can be described as an electromagnetic scattering problem. However, existing analytical solutions are limited to spheres, spheroids, and ellipsoids [120]. The approximated response of the collection of particles much smaller than the wavelength of the optical field can be obtained within the quasi-static approximation, as shown in the previous Section. In such case, the sizes of individual particles and the distance between them are much smaller than the wavelength of the incoming light, which means that the EM field can be treated locally as a constant. Within this approximation, a spherical particle in a static EM field is characterized by a polarizability:

$$\sigma = 4\pi a^3 \left(\frac{\varepsilon_{NP} - \varepsilon_h}{\varepsilon_{NP} + 2\varepsilon_h} \right), \tag{3.28}$$

obtained from Eq. 3.18. When the dielectric functions have opposite signs such that $Re\left[\varepsilon_{NP}\right] = -2\varepsilon_h$, the polarizability is maximum and the optical frequency satisfying this condition is referred as localized surface plasmon resonance (LSPR) , this is the so-called Frohlich condition. This approximation is valid only for particles with sizes smaller than 100 nm. Then, when the MDNC is illuminated, the incident electric field exerts a force resulting in displacement of the conduction electrons inside the NP. The attraction between the positive ions and the electrons acts as an effective restoring force causing the electrons to move back to its equilibrium position. The optical frequency satisfying Frohlich condition can be determined from the Drude model by using Eq. 3.14

$$\omega = \frac{\omega_p}{\sqrt{1+2\varepsilon_h}}, \tag{3.29}$$

which implies that the resonance frequency depends on the dielectric medium surrounding the metal NP. LSPR leads to two very important effects: strong absorption and scattering of the incident light at LSP frequencies as well as strongly enhanced electric fields near the NP surface [121].

3.4 LOCAL FIELD EFFECTS

In dielectric materials, the atoms or molecules experience not only the external applied electric field but also the electric field produced by the dipoles that were oriented in the direction of applied electric field. The electromagnetic field which is responsible for this internal polarization is called local field. Its values is different from the external field and the average field inside the medium. The influence of the local field effects on the optical properties of the medium becomes substantial when the atomic densities of a material system is larger than $\approx 10^{15}$ cm^{-3} [122]. The local field effect results in a modification of the optical properties of the medium and therefore provide some interesting optical phenomena.

In order to account for local-field effects on the optical properties of a material, one needs to apply a proper model relating the local field to its macroscopic counterparts. There are different models for performing local field-corrections depending on the medium of interest, and each one predicts different expressions for the local-field correction factor. For homogeneous media, the Lorentz local field model and the Onsager model, describe the local field effects in solids and polar liquids, respectively. On the other hand, the real-cavity model is used to describe composite materials. In this thesis we are interested in media obeying the geometrical configuration of Maxwell-Garnett constituted by metal NPs suspended in a NL solvent. Therefore the real-cavity model is the most appropriate, but in this Section, we developed both the Lorentz and real-cavity model, in order to note the similarities and differences between the local field effects in MDNCs where the surrounding medium is a solid or a liquid phase. The identification of both models allows us to understand more appropriately the contributions of HON in both classes of materials, as discussed in Section 3.5.2.

The Lorentz local field model (or virtual-cavity model) treats the solid media as a cubic lattice of point dipoles of the same sort. The local field, $\tilde{E}_{loc}$, acting on a specific dipole is obtained by creating an imaginary spherical cavity around the dipole with radius much larger than the distance between the dipoles, and much smaller than the optical wavelength. Here, the contributions from the dipoles situated within the spherical cavity to the local field are accounted individually, while the dipoles outside the cavity are characterized by an average macroscopic polarization. This approach yields the well-known expression:

$$\tilde{E}_{loc} = \tilde{E} + \frac{1}{3\varepsilon_0}\tilde{P}, \tag{3.30}$$

where $\tilde{E}$ and $\tilde{P}$ are the macroscopic average field and polarization.

The dipole moment induced in a typical molecule (or atom) of a losless and dispersionless medium can be expressed by

$$\tilde{p} = \varepsilon_0 \sigma \tilde{E}_{loc}, \tag{3.31}$$

where σ represents the microscopic polarizability. The relationship between the macroscopic polarization and the average field of a material with molecular (or atomic) number density N is

$$\begin{aligned} \tilde{P} &= N\tilde{p}, \\ \tilde{P} &= N\varepsilon_0 \sigma \left[\tilde{E} + \frac{1}{3\varepsilon_0} \tilde{P} \right]. \end{aligned} \tag{3.32}$$

In addition, the macroscopic polarization can be expressed as a sum of linear and NL contributions:

$$\tilde{P} = \tilde{P}^L + \tilde{P}^{NL}. \tag{3.33}$$

When considered only the linear term and the linear polarization, given by Eq. 2.3, it is possible to find a relationship between the linear susceptibility, $\chi^{(1)}$, and the microscopic polarizability, given by

$$\chi^{(1)} = \frac{N\sigma}{1 - \frac{1}{3}N\sigma}. \tag{3.34}$$

However, the linear dielectric constant of the medium, $\varepsilon^{(1)}$, is related to linear susceptibility by Eq. 2.6. Thus, it is possible to obtain the relationship of Lorentz–Lorenz (or Clausius–Mossotti) relation:

$$\frac{1}{3} N\sigma = \frac{\varepsilon^{(1)} - 1}{\varepsilon^{(1)} + 2}, \tag{3.35}$$

and the linear susceptibility can be written as:

$$\chi^{(1)} = \frac{\varepsilon^{(1)} + 2}{3} N\sigma. \tag{3.36}$$

Finally, by substituting Eq. 3.36 in Eq. 2.3, and inserting the result in Eq. 3.32 and then using the relationship 3.31, we obtain the equation relating the local field to the average field:

$$\tilde{E}_{loc} = \frac{\varepsilon^{(1)} + 2}{3} \tilde{E}, \tag{3.37}$$

where

$$L_{Lor} = \frac{\varepsilon^{(1)} + 2}{3}, \tag{3.38}$$

is known as the Lorentz local-field correction factor.

Note that the local field factor defined in Eq. 3.38 differs from the correction factor used in Eq. 3.16 (the factors are reversed). This discrepancy occurs due to the way in which is considered the analysis region. In the Onsager [123] and real-cavity models [124], a molecule (or atom) is treated as being in a real spherical cavity in the medium, i.e. the cavity has the same size of a molecule. While the Lorentz model assumes a large cavity. Therefore, the local field that acts on the molecule is due to the existent field in the center of the real cavity, which is surrounded by a dielectric medium. The mathematical expression for the field inside the spherical cavity , $\tilde{E}_{ins}$, is commonly studied in courses of classical electrodynamics and has the form (see Chapter 4 of [57]):

$$\tilde{E}_{ins} = \frac{3}{\varepsilon + 2}\tilde{E}, \tag{3.39}$$

where $\tilde{E}$ represents the applied macroscopic field. For the special case of MDNCs containing metal NPs suspended in a host $\varepsilon = \varepsilon_{NP}/\varepsilon_h$, with ε_{NP} and ε_h being the dielectric function of the NPs and the host, respectively. In this model, the local-field correction factor is given by:

$$L_{CRM} = \frac{3\varepsilon_h}{\varepsilon_{NP} + 2\varepsilon_h}, \tag{3.40}$$

which it is the same used for the Maxwell-Garnett model [Eq. 3.16]. Although models lead to different local-field correction factors, there are sophisticated theories that reconcile both treatments [125]. Hereafter, the local field factor corresponds to the expression given in Eq. 3.40 and is labeled only as η [2]. It is important to note that when $\varepsilon_{NP} \approx -2\varepsilon_h$, the local field factor increases considerably and as a consequence the local field effects are enhanced.

3.5 NL OPTICAL PROPERTIES

Metal-dielectric nanocomposites have generated considerable interest in NL optics and nanophotonics technology due to its large third-order NL susceptibility, ultrafast response time, tunable surface plasmon resonance (SPR) frequency and considerable enhancement of their effective NL optical response. Such enhancement is due to the local field effects for frequencies near the LSPR. This can be understood by extend the Maxwell-Garnett model, discussed in Section 3.2, considering NL contributions. In this way, Sipe *et al.* developed an expansion of the Maxwell-Garnett model for the case where the metal NPs and the host exhibit third-order nonlinearities [100]. For instance, assuming a centrosymmetry medium interacting with linearly polarized light, it was possible to show that the effective third-order susceptibility $\left(\chi^{(3)}_{eff}\right)$, for small volume fractions (f), is related to the third-order susceptibility of each components by :

$$\chi^{(3)}_{eff} = f\frac{\chi^{(3)}_{NP}}{R^2\left|R\right|^2} + \frac{\chi^{(3)}_h\left\{1 - f\left\{1 - 0.4\left[4\left|\Theta\right|^2\Theta^2 + \left(3\left|\Theta\right|^2\Theta^2 + \Theta^3\right) + 9\left(\left|\Theta\right|^2 + \Theta^2\right)\right]\right\}\right\}}{\left|1 - \Theta f\right|^2\left(1 - \Theta f\right)^2}, \tag{3.41}$$

com

$$R = \left(1 - \Theta f\right)\frac{\varepsilon_{NP} + 2\varepsilon_h}{3\varepsilon_h} = \frac{1 - \Theta f}{\eta}, \tag{3.42}$$

---

[2] In this thesis, η is used instead of the original notation L to avoid confusion with the sample length in the next chapters

where Θ is given by Eq. 3.23, $\chi_{NP}^{(3)}$ and $\chi_{h}^{(3)}$ are the third-order susceptibility of the NPs and host, respectively. Eq. 3.41 reveals the importance of the local field contributions to increase the effective third-order susceptibility, since these depend on a fourth-order power. Deduction of third-order susceptibility [Eq. 3.41] as well as an expansion to higher-order susceptibilities is shown in Section 3.6.

The first report on the optical nonlinearity of the MDNCs was published in 1985 by Ricard *et al.* [126]. Using the optical phase conjugation, under picosecond laser pulse excitation, their experiments showed a resonance enhancement of the order of 10^9 and 10^6 for gold and silver NPs, respectively. They categorize the resonant and non resonant interaction regime in context of local field factor. In an effort to understand the source of the NPs nonlinearity, they invoked three types of NL contributions:

- *Intraband contribution:* This is due to quasi-free electrons in the conduction band and is associated with electron transitions at the Fermi level in incompletely filled bands, or when a filled band overlaps in energy with an empty band. These transitions also provide an absorption mechanism but at lower energies. Electrons at the Fermi level in metals are excited by photons of very small energies, for that reason they are essentially considered as quasi-free electrons. The contribution of the quasi-free electrons to the dielectric function can be described classically via the Drude model [see Section. 3.2]. Intraband contributions is a size dependent contribution arising from the confinement of conduction electrons in the nano-dimension. Correspondingly the contribution is vanishingly small for nanoparticles having sizes of the order of 10 nm.

- *Interband contribution:* This contribution is related to optical transitions between two electronic bands, or interband transitions (from filled bands to states in the conduction band, or from the latter to empty bands of higher energy). By virtue of the Pauli exclusion principle, a d-band electron can only be excited into an unoccupied state of the conduction band, i.e., above the Fermi energy. Thus, there is a minimal photon energy for which the interband transition can occur, corresponding to the excitation of an electron from the top of the valence band to the Fermi level situated in the conduction band. This defines an energy threshold below which the imaginary part of the interband contribution to the dielectric function is zero. In particular, this threshold falls in the UV range for silver (3.9 eV) [127] and in the visible range for gold and copper (at around 2.4 and 2.1 eV, respectively) [127, 128].

- *Hot-electrons contribution:* This contribution results from the heating of conduction electrons induced by a light pulse with duration time shorter than the thermalization time of electrons [33]. When a short light pulse illuminates a MDNCs, part of the energy in the pulse is absorbed by the electrons in the metal, and the energy distribution among the electrons can be highly nonthermal. Subsequent electron-electron scattering results in thermalization of the electrons, which happens during the first few hundreds of femtoseconds. Shortly thereafter, the hot-electron relaxation process occurs on ultrafast timescales due to strong electron-phonon interactions. This ultrafast process allows to modify the metallic dielectric function to a considerable extent.

From these contributions, it is possible to observe that the NL response of MDNCs depends on extrinsic parameters such as: frequency and pulse duration of incident laser. However, the NL optical properties are also heavily dependent on the material parameters, such as: sizes and shape of the NPS, as well as of the surrounding dielectric environment. Proper manipulation of these parameters allows to enhance substantially the NL response of the composite.

3.5.1 Influence of the Size, Shape and Environment on the NPs Nonlinearities

Size and shape dependence

The dependence of LSPR wavelength on the size of the nanoparticles can be clearly seen by the size dependence in the scattering and absorption cross-section, as defined by the Mie theory [129]. Fig. 3.4(a) displays the dependence of LSPR wavelength with the size of spherical silver NPs. The red-shifting of the plasmon resonance for larger particles, in most simple terms, can be attributed to the reduction in the restoring force due to the increasing distance between the conduction electrons and the positive ions. Further increase in the size of the nanoparticles leads also to higher modes of oscillations as the electrons are no longer able to respond homogenously to the applied field due to field retardation across the NP [130].

Variation in the LSPR not only depends on the particle size, but also on the NP shape [131]. Probably, the most exotic example of this can be seen in the case of rod shaped nanostructures. Nanorods can be approximated as nanoparticles elongated along one of its axis. The elongated shape of the nanorod causes the conduction electrons to oscillate in two different directions depending upon the polarization of the incident light. The two LSPRs are termed as either longitudinal or transverse resonances depending on whether the direction of oscillation is along the long or short axis of the nanorod. Besides nanospheres and nanorods, various other nanostructures of different shapes have been designed and fabricated showing different optical properties. Fig. 3.4(b) exhibits the dependence of LSPR wavelength with the shape of different silver NPs.

Therefore, it is possible to conclude that both the size and the shape dependence of the LSPR produce changes on the linear optical properties of the material such as: linear refractive index and linear extinction coefficient [131].

However, since the variation in size and shape of the particles alters the intensity and position of the LSPR, and this in turn modifies the effects of local field, then the NL optical properties are also affected by variations of the intrinsic parameters of MDNCs (size and shape of NPs). Accordingly, Uchida *et al.* reported an increase of two orders of magnitude in the effective third-order susceptibility of cooper-doped glasses (with NP radius between 2.5 nm and 47.7 nm) and silver-doped glasses (with NP radius between 2.1 nm and 15.3 nm), using a degenerate four-wave mixing (DFWM) experiment [134]. Nevertheless, the results show that the third-order susceptibility of the metal is almost independent of the particle size. A proper interpretation of this phenomenon was performed in terms of the increase of the mean free path of the conduction electrons in the metal NPs. Here, the NL response was due to thermo-optic contribution. A similar study was reported in copper nanoclusters [135]. With the evolution

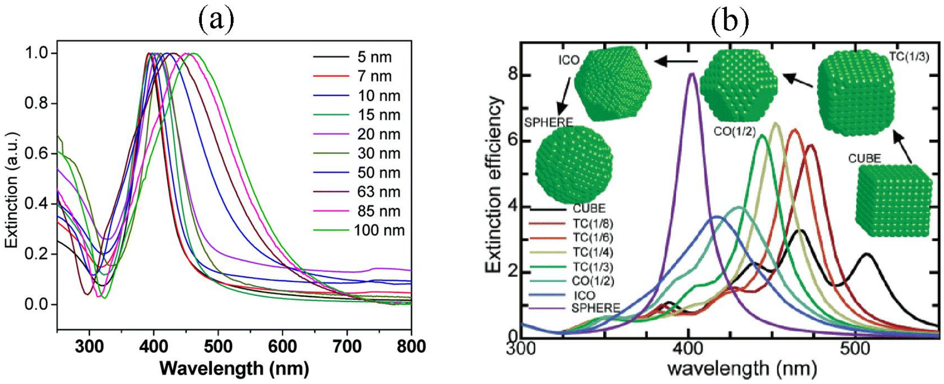

Figure 3.4 (a) Size and (b) shape dependence of the extinction spectra of silver NPs. (Reprinted of [132] and [133])

of the nanotechnology, different types of routines were developed allowing to prepare MDNCs with proper control of the particle size. Thus, several other works showing the size dependence of nonlinearity in MDNCs were reported [136, 137, 138, 139, 140].

Recently, a theoretical and numerical approach predicts the size dependence of the third-order susceptibility of the metal NPs based on quantum finite-size effects of conduction electrons in metal particles [141]. Experimental results that corroborate this theory were performed with silver NPs deposited on a SiO_2 substrate [142]. Here, quantum size effects lead to an increase in the nonlinearity of Ag NPs with size between 3 nm and 16 nm. Fig. 3.5 shows the increase of the real and imaginary part of the third-order susceptibility of Ag with the decrease in the particle size [142].

In analogy, studies of the nonlinearity in MDNCs depending on the NP shape were reported due to changes in the LSPR [143, 144, 145, 139]. In addition, a numerical model based on the effective medium approximation combined with the discrete dipole approximation allows to predict large enhancements of the NL susceptibility by manipulate the size and shape of the metal NPs, in order to tune the LSPR to a desired frequency [140]. Fig. 3.6 shows the varia-

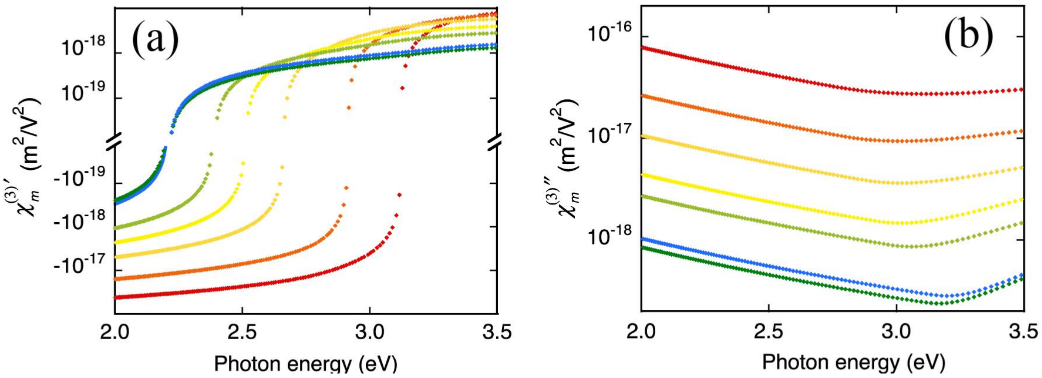

Figure 3.5 Size dependence of (a) real and (b) imaginary components of the third-order susceptibility of Ag particles with diameters ranging from 3.0 to 16 nm. (Reprinted of [142])

tions of the NL susceptibility for three different shapes of Ag NPs (nanosphere, nanorod and nanotriangle) hosted in silica [140]. Here, it is possible to note that thee number of peaks of the NL susceptibility increases for the NPs with many sharp edges, offering the possibility of control their NL properties. Moreover, the amplitude of the resonance peaks of the susceptibility decreases for particles with several sharp edges, but the nonresonant susceptibility in the long-wavelength tail is enhanced for such particles. The field redistribution and enhancement in this case results from excitation of both dipole resonances and quadrupole resonances in each type of NP.

Although most studies associate the shape dependence of nonlinearity with variations in the LSPR, it was also shown that the electron relaxation times varies with the shape of the NPs; as a consequence the contributions of hot-electrons vary the NL response of the MDNC [146].

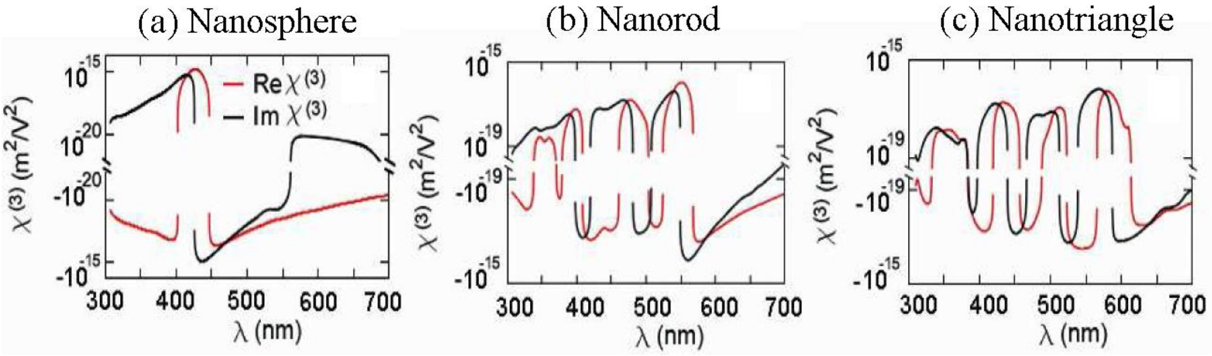

Figure 3.6 Real and imaginary components of third-order susceptibility of silver (a) nanospheres, (b) nanorods and (c) nanotriangles. (Reprinted of [140])

Influence of the Environment/Host

The LSPR wavelength of the metal NPs is also influenced by the dielectric properties of the surrounding media. Higher values of the dielectric function of the surrounding media (ε_h) result in smaller restoring force because more surface charges are compensated by the polarized charges of the surrounding medium. In general, for non-absorbing surroundings, an increase in the index of refraction of the surroundings leads to a red-shifts of the LSPR. The interplay between the substance and the surroundings is critical, and occasionally non-intuitive. Specifically, differences in the wavelength-dependent behavior of the dielectric functions involved can substantially alter both the position and strength of the LSPR.

In MDNCs, the environment usually corresponds to a dielectric host and the stabilizing agents. Both surrounding media can change the NL response of the MDNC. For instance, the dielectric constant of the host acts directly on the effective NL susceptibility, as seen in the Maxwell-Garnett model [Eq. 3.41]. Also a stabilizing agent covering the NPs as a shell, changes the dielectric function of the NP and consequently the effective NL response of the MDNC. Table 3.2 shows the values of the effective third-order susceptibilities for silver colloids stabilized with three different agents, reported by Gómez *et al.* [147]. Changes in the

Samples	$Re\left[\chi_{eff}^{(3)}\right]\ \left(\times 10^{-22}\,m^2/V^2\right)$	$Im\left[\chi_{eff}^{(3)}\right]\ \left(\times 10^{-22}\,m^2/V^2\right)$
Sodium citrate capped Ag NPs	-9.7 ± 1.4	1.8 ± 0.3
PVP capped Ag NPs	-7.8 ± 1.2	4.2 ± 0.6
PVA capped Ag NPs	-15 ± 2.2	4.7 ± 0.7

Table 3.2 Effective third order susceptibility for silver colloids stabilized by different agents [147].

magnitude of the $\chi_{eff}^{(3)}$ of more than 100% illustrate the strong dependence of the NL response of a MDNC with the stabilizing medium and the route of synthesis. The results can be understood as the influence of adsorbed molecules, used as the stabilizing agent, on the NP surface which lead to changes in its dielectric function, being able to increase the NL interaction with electromagnetic field.

Also, Gómez *et al.* [148] reported changes in the effective third-order susceptibilities of silver colloids when suspended in different solvents, as shown in Table 3.3. The interpretation of why the host acts on the nonlinearity of the MDNC is directly observed in Eq. 3.41 from the Maxwell-Garnett model. However, the experimental results also reveal that solvents with molecules presenting large electric dipole moment significantly change the NL response of the MDNC.

On the other hand, it is well known that the NL response of MDNCs is strongly influenced by the local field effects, which in turn is directly related with the time taken by LSP to lose its coherence. Although the local field enhancement is relevant to the NL behavior of MDNCs, it is often neglected because its dephasing time is very short (few femtoseconds) [149]. Almeida *et al.* reported variations in the LSP dephasing (LSP-DTs) in silver colloids depending on the stabilizing agents used in their preparation [150]. The persistent spectral hole burning (PSHB) technique was used to measure LSP-DTs of 3.0, 2.3 and 1.8 fs for silver NPs stabilized by trisodium citrate, PVP and PVA, respectively. The differences between LSP-DTs were attributed to changes in the electronic density of states due to the interaction between the NPs and the capping agents caused mainly by Landau damping and chemical interface damping (CID) effects [150]. Effects of size and shape of the NPs can also vary the LSP-DTs producing changes in the NL response of the MDNCs [151, 152].

Host	$Re\left[\chi_{eff}^{(3)}\right]\ \left(\times 10^{-20}\,m^2/V^2\right)$	$Im\left[\chi_{eff}^{(3)}\right]\ \left(\times 10^{-22}\,m^2/V^2\right)$
Methanol	-1.00	5.32
Water	-0.36	10.6
Acetone	-1.62	3.05
Ethylene glycol	-3.76	6.99

Table 3.3 Effective third order susceptibility for silver colloids suspended in different solvents [148].

3.5.2 Origin of HON in MDNCs

Although the NL behavior of MDNCs is being studied for a long time, only in the last decade it was reported the presence of HON [23, 24]. In principle, HON in MDNC were predicted as a result of the large third-order nonlinearity of the metal NPs, which are enhanced by tuning the LSPR [126]. On this base, theoretical studies show that large third-order nonlinearity can lead to fifth-order NL response in MDNCs [153, 32]. The origin of the quintic nonlinearity can be thought of as an iterative effect, because the field inside the particle depends on the dielectric function of the metal and in the NL regime, the dielectric function itself depends on the applied field. In this sense, HON in MDNCs frequently appear by using intense light pulse with short time duration (of the order of picosecond or femtosecond). However, the strength and origin of the HON vary with the wavelength and pulse duration [23, 154]. Concerning to the wavelength dependence of the nonlinearity, for the special case of silver NPs, it is known that for photon energies smaller than 2 eV the light absorption is dominated by intraband transitions. Moreover, photons of 3eV the optical absorption is dominated by the LSPR, while for photon energies above 4 eV interband transitions dominate the optical response [23]. On the other hand, HON in MDNCs are of electronic origin when the pulse duration is shorter than the electron thermalization time (few hundreds of femtoseconds), and for higher pulse duration their origin is the contribution of hot electrons [33].

One of the first theoretical works that considers the presence of HON in MDNCs, due to large third-order nonlinearity, was developed by Kothari [32]. This model introduced an exact solution to the effective dielectric function of the MDNC, by using the effective-medium theory based on the T-matrix approach, which predicts that the local electric field should be the same in all NPs, independent of the local arrangement inside a composite. Under these conditions, considering the dielectric function of one NP as: $\varepsilon_{NP} + \chi_{NP}^{(3)} |E_L|^2$ and assuming to be a very diluted media $(f \ll 1)$ with a linear host $\left(\chi_h^{(3)} = 0\right)$, it is possible to rewrite the Eq. 3.41 in the form:

$$\chi_{eff}^{(3)} = f \frac{\chi_{NP}^{(3)}}{R'^2 |R'|^2}, \tag{3.43}$$

with $R' = (\varepsilon_{NP} + 2\varepsilon_h)/3\varepsilon_h = \eta^{-1}$. In addition, the total effective dielectric function of the MDNC can be written as a function of local field as [32]:

$$\varepsilon_{total} = \varepsilon_{NP,eff} + \frac{\chi_{NP,eff}^{(3)} |R'|^2 |E_L|^2}{1 + a_0 |E_L|^2}, \tag{3.44}$$

where $\varepsilon_{NP,eff}$ and $\chi_{NP,eff}^{(3)}$ correspond to the contribution of the dielectric functions and third-order susceptibilities of all NPs, respectively. Also,

$$a_0 = \left(\frac{\chi_{NP}^{(3)}}{\varepsilon_{NP} + 2\varepsilon_h} \right), \tag{3.45}$$

and the local field, E_L, is related to the mean macroscopic field E by:

$$E = R' E_L \left(1 + a_0 \left|E_L\right|^2\right). \tag{3.46}$$

For weak fields, Eq. 3.44 can be expanded as a power series in function of the macroscopic field, such that it is possible to express the total dielectric function as:

$$\varepsilon_{total} = \varepsilon_{NP,eff} + \chi^{(3)}_{total}, \tag{3.47}$$

with

$$\chi^{(3)}_{total} = \chi^{(3)}_{NP,eff} + \bar{\chi}^{(5)} \left|E\right|^2 + \bar{\chi}^{(7)} \left|E\right|^4 + \bar{\chi}^{(9)} \left|E\right|^6 + \ldots, \tag{3.48}$$

where

$$\begin{aligned}
\bar{\chi}^{(5)} &= -\,\varsigma_0 \chi^{(3)}_{NP,eff} & \qquad \varsigma_0 &= \frac{2a_0 + a_0^*}{\left|R'\right|^2} \\
\bar{\chi}^{(7)} &= \left(\varsigma_1 + \varsigma_0^2\right) \chi^{(3)}_{NP,eff} & \qquad \varsigma_1 &= \frac{a_0^2 + \left|a_0\right|^2 + \left(a_0^*\right)^2}{\left|R'\right|^4} \\
\bar{\chi}^{(9)} &= -\left(\varsigma_2 + 2\varsigma_1\varsigma_0 + \varsigma_0^3\right) \chi^{(3)}_{NP,eff} & \qquad \varsigma_2 &= \frac{2a_0^3 + 3\left|a_0\right|^2 \left(a_0 + a_0^*\right) + 2\left(a_0^*\right)^3}{\left|R'\right|^6}
\end{aligned} \tag{3.49}$$

From these equations, it is possible to observe that the HON depend only on the third-order nonlinearity, previously obtained in the Maxwell-Garnett model.

A quick interpretation of the Kothari model reveals that the origin of HON is due to cascaded-like contributions of the third-order nonlinearities. However, this model disregards the intrinsic contributions of the HON in MDNCs. For a better understanding of the origin of HON in MDNCs, it is useful to distinguish the different mechanisms that contribute to enhance their magnitude and effects. In recent work, Dolgaleva *et al.* define the concepts and mark the differences between three types of NL contributions in nanocomposites, corresponding to the direct (intrinsic) and the two cascaded contributions (microscopic and macroscopic) [155]. To give rise to a simple interpretation of the NL response in nanocomposites, Dolgaleva treats the medium as a two-level atomic system and analyzes the nature of the fifth-order nonlinearities taking into consideration the local field effects. However, a treatment in atomic scale requires to express the NL response in terms of the NL hyperpolarizability, γ^{NL}. The three NL contributions are briefly discussed below.

Intrinsic Optical Nonlinearities

The third- and fifth-order optical susceptibilities have the direct contributions from the corresponding third- and fifth-order microscopic hyperpolarizabilities, respectively, which are called the intrinsic optical nonlinearities. “Direct contribution” is understood as the linear dependence between $\chi^{(j)}$ and $\gamma^{(j)}_{at}$, when N and L_{Lor} are assumed to be constant. Here, the NL responses are expressed by the local field corrected effective susceptibilities as [156]

$$\chi_{int}^{(3)} = N\gamma_{at}^{(3)} \left|L_{Lor}\right|^2 L_{Lor}^2, \tag{3.50}$$

$$\chi_{int}^{(5)} = N\gamma_{at}^{(5)} \left|L_{Lor}\right|^4 L_{Lor}^2, \tag{3.51}$$

where N is the molecular or atomic density, L_{Lor} is the Lorentz local field correction factor, $\gamma_{at}^{(3)}$ and $\gamma_{at}^{(5)}$ are the third- and fifth-order microscopic hyperpolarizabilities, respectively. It can be seen that the intrinsic contribution has a linear dependence with N.

Microscopic cascaded contribution

Microscopic cascade has a local nature, i.e. the fields acts on individual molecules (or atoms) in the medium and the NL polarization induced can couple with the generated field but the process does not require propagation nor phase matching [157]. If a medium lacks inversion symmetry, the local field effect creates the microscopic cascaded contribution from the second-order hyperpolarizability $\left(\gamma_{at}^{(2)} : \gamma_{at}^{(2)}\right)$ to the third-order nonlinear optical susceptibility $\left(\gamma_{at}^{(3)}\right)$ [157]. In analogy, the third-order hyperpolarizability of a centrosymmetric material, that does not possess the second-order hyperpolarizability, gives rise to the fifth-order NL response by microscopic cascading $\left(\gamma_{at}^{(5)} \propto \gamma_{at}^{(3)} : \gamma_{at}^{(3)}\right)$ [158]. It was shown that the microscopic cascaded contribution to the fifth-order optical nonlinearity $\left(\chi_{micro}^{(5)}\right)$ are also affected by local field effect and can be expressed by [156]:

$$\chi_{micro}^{(5)} = \frac{24\pi}{10} N^2 \left[\gamma_{at}^{(3)}\right]^2 \left|L_{Lor}\right|^4 L_{Lor}^3 + \frac{12\pi}{10} N^2 \left|\gamma_{at}^{(3)}\right|^2 \left|L_{Lor}\right|^6 L_{Lor}. \tag{3.52}$$

Notice that in this case the fifth-order susceptibility has a quadratic dependence with N.

Macroscopic cascaded contribution

Macroscopic cascade process are of nonlocal nature. That is, an intermediate field generated by a lower-order NL process propagates to contribute to a higher-order NL process by nonlinearly interacting with the fundamental field [159]. For instance, the intensity-dependent refractive index, which is a $\chi^{(3)}$ process, can be mimicked by a two-step sequence of the second-harmonic generation $\left[\chi^{(2)}(2\omega;\omega,\omega)\right]$ followed by the difference-frequency generation $\left[\chi^{(2)}(\omega;2\omega,-\omega)\right]$ with a fundamental wave at ω. It was shown that the measured $\chi^{(3)}$ contains contributions proportional to $\left|\chi^{(2)}\right|^2$ for materials having no inversion symmetry [160]. Similarly, the macroscopic contribution to the total electric field generated by the fifth-order nonlinear process $\chi_{macro}^{(5)}$ is proportional to $\left|\chi^{(3)}\right|^2$ for any material and therefore to N^2 [155]. The mathematical expression for this type of contribution strongly depends on the configuration to be studied, because macroscopic cascade process are affected by the propagation and phase matching conditions.

Similar expressions for the high-order susceptibilities of MDNCs, corresponding to intrinsic and microscopic cascaded contributions, are presented in Section 3.6 based on the Maxwell-Garnett model.

3.5.3 Measurement and Analysis of HON

Nowadays, several works are dedicated to the study of HON in different physical systems by using a wide variety of characterization techniques. In special, HON in MDNCs are widely explored by one of the most known NL characterization techniques, called: Z-scan technique [27]. This thesis also makes use of this simple and elegant technique to characterize the NL response of the metal colloids studied here.

The Z-scan technique bases its principle of operation on the self-focusing and self-defocusing effects, discussed in Section 2.5.1. This technique has gained much popularity because it allows to identify the sign and magnitude of the NL parameters with a simple analysis of the transmittance curve. However, it has been demonstrated that the Z-scan technique has a high sensitivity to detect HON [23]. In general, short light pulse with intensities on the order of GW/cm^2 are needed to explore the HON in MDNCs. In order to perform the measurements of NL refraction, a light beam is focused onto a thin cell, containing the NL material, moving along the direction of propagation (z-direction) around the region where the laser beam is focused. The intensity of the transmitted light is detected after passing through a small aperture placed in front of a photodetector in the far-field. For this reason, this configuration is called *closed-aperture* (CA) Z-scan scheme. For focusing (defocusing) media, corresponding to $n_{NL} > 0$ ($n_{NL} < 0$), the Z-scan transmittance curve shows a valley (peak) followed by a peak (valley) to displacement of the sample from before to after the focal plane of the laser. Further details on the Z-scan technique are given in Appendix A. Changes of the transmittance in far-field are related to the phase-shift experienced by a beam when it passes through a material with NL refractive index n_{NL}. The NL phase obtained from the Z-scan experiments considering HON terms can be expressed by [23]:

$$\triangle\Phi_{NL} = \sum_{N=1} \triangle\Phi_0^{(2N+1)}, \tag{3.53}$$

with

$$\triangle\Phi_0^{(2N+1)} = kn_{2N}I^N \left[\frac{1-exp\left(-N\alpha_0 L\right)}{N\alpha_0}\right], \tag{3.54}$$

where $\triangle\Phi_0^{(2N+1)}$ is the $(2N+1)$th-order phase-shift, I is the incident intensity, L is the sample length, $k = 2\pi n_0/\lambda$, λ is the laser wavelength, n_0 and α_0 are the linear refraction index and linear absorption coefficient, respectively. By using the Gaussian decomposition method [27], it is possible to obtain an expression for the normalized transmittance at far-field, given by [23]:

$$T\left(z, \triangle\Phi_{NL}\right) \cong 1 + \sum_{N=1} \frac{(4N)\,\triangle\Phi_0^{(2N+1)}\,(z/z_0)}{\left[(z/z_0)^2 + (2N+1)^2\right]\left[(z/z_0)^2+1\right]^N}, \tag{3.55}$$

where z_0 is the Rayleigh length of the focused beam. Eq. 3.55 is the general expression for the CA Z-scan transmittance curves as a function of the propagation distance around the focal plane. However, for the characterization of the HON there are a large number of parameters that must be fitted to the experimental results, leading to significant errors in the calculation of NL coefficients. In order to improve the fit procedure, a better way is to express the peak-valley transmittance variation, $\triangle T_{p,v}$, as a function of the incident intensity of the form [23]:

$$\triangle T_{p,v} \cong 0.406\triangle\Phi_0^{(3)} + 0.210\triangle\Phi_0^{(5)} + 0.130\triangle\Phi_0^{(7)} + 0.087\triangle\Phi_0^{(9)} + \ldots, \tag{3.56}$$

where the coefficients were obtained by considering the mean peak–valley separation $\triangle z_{p,v} = 1.7z_0$. This value can vary depending on the experimental setup. Falcão *et al.* [23] emphasizes that the value of $\triangle z_{p,v}$ depends also on the intensity, i.e. NL contributions of different orders will present their peaks and valleys in different positions. By substituting Eq. 3.54 in Eq. 3.56, we have

$$\frac{\triangle T_{p,v}}{I} \cong 0.406kn_2\left[\frac{1-exp\left(-\alpha_0 L\right)}{\alpha_0}\right] + 0.210kn_4 I\left[\frac{1-exp\left(-2\alpha_0 L\right)}{2\alpha_0}\right] + 0.130kn_6 I^2\left[\frac{1-exp\left(-3\alpha_0 L\right)}{3\alpha_0}\right] + 0.087kn_8 I^3\left[\frac{1-exp\left(-4\alpha_0 L\right)}{4\alpha_0}\right] + \ldots, \tag{3.57}$$

$$\frac{\triangle T_{p,v}}{I} = n_{2,eff} + n_{4,eff}I + n_{6,eff}I^2 + n_{8,eff}I^3 + \ldots, \tag{3.58}$$

which reduce the number of terms to be fitted. Eq. 3.58 also reveals that $\triangle T_{p,v}/I$ will be constant in media with only cubic nonlinearity. In cubic-quintic media, $\triangle T_{p,v}/I$ will have a linear dependence with the intensity. Media exhibiting HON higher than fifth-order, will show a polynomial dependence of $\triangle T_{p,v}/I$ with the intensity.

The analysis of the NL absorption regime is similar. The only modification in the experimental setup of the Z-scan technique is that the small aperture is removed, so it is called *open-aperture* (OA) Z-scan scheme. In this configuration, the transmittance curve displays only one valley (or peak) in the region of highest intensity, that is around the focus plane ($z = 0$), due to NL absorption (or saturated absorption) effects. Here, the original expression to dissipative media, developed in [27], is used to model the normalized transmittance in far field:

$$T\left(z, q_0\right) = \frac{1}{\sqrt{\pi}q_0}\int_{-\infty}^{\infty} ln\left[1 + q_0 exp\left(-\tau^2\right)\right]d\tau, \tag{3.59}$$

with

$$q_0 = \frac{\alpha_{NL} I}{1+\left(z^2/z_0^2\right)}\left[\frac{1-exp\left(-\alpha_0 L\right)}{\alpha_0}\right], \tag{3.60}$$

$$\alpha_{NL} = \sum_N \alpha_{2N,eff} I^N \tag{3.61}$$

and $\alpha_{2N,eff}$ being the effective $(2N+1)$th-order absorption coefficient of the medium. In analogy to the refractive treatment, the intensity dependence of $\triangle T$ can be expressed by [23]:

$$\frac{\triangle T}{I} = (2)^{-\frac{3}{2}}\left[\frac{1-exp\left(-\alpha_0 L\right)}{\alpha_0}\right]\left[\alpha_2 + \alpha_4 I + \alpha_6 I^2 + \alpha_8 I^3 + \ldots\right]. \tag{3.62}$$

Eq. 3.62 shows also a polynomial dependence of $\triangle T/I$ with the intensity, where the coefficients correspond to the NL absorption coefficients of different orders.

Therefore, high-order NL susceptibilities are obtained by measuring the transmittance variation, $\triangle T$, in the experimental CA and OA Z-scan curves and plot a graphics of $\triangle T/I$ vs I. Then, Eqs. 3.58 and 3.62 are used to fit the experimental points, allowing to find the values of the NL parameters $\left(n_{2N,eff} \text{ and } \alpha_{2N,eff}\right)$. Finally, these coefficients are used in Eqs. 3.55 and 3.59 to model the CA and OA Z-scan curves, corroborating the values previously found. High-order NL susceptibilities are obtained by using the Eqs. 2.85 and 2.86.

3.6 GENERALIZED MAXWELL-GARNETT MODEL

Section 3.2 presented the importance of using the Maxwell-Garnett model to interpret the linear optical properties of MDNCs. An extension of this model was performed in [100] including the contributions of lower-order nonlinearity, as shown in section 3.5. However, in both theoretical treatments the contributions of HON were neglected.

In order to understand the high-order NL optical properties exhibited by the MDNCs, it has been developed an extension of the Maxwell-Garnett model including the contributions of $\chi^{(3)}_{eff}$, $\chi^{(5)}_{eff}$ and $\chi^{(7)}_{eff}$. This section and the next chapters correspond to original contributions of this thesis. Here, the MDNC is considered to be composed by spherical NPs with diameter a, being smaller than their relative distance b, suspended in a NL solvent (host). The nanocomposite is supposed to be homogeneous and highly diluted, $f \ll 1$, where f corresponds to volume fraction occupied by metal NPs. The light wavelength, λ , satisfies the condition: $\lambda > b > a$.

Under these conditions the optical field $\tilde{E}_0$, considered uniform on each particle, induces an optical polarization that in the quasi-static approximation regime can be written as:

$$\tilde{P} = \tilde{P}_h + \frac{1}{V}\sum_{i=1}^{N_{NP}} \tilde{p}_i, \tag{3.63}$$

where $\tilde{P}_h$ is the host polarization, N_{NP} is the number of NPs inside the volume V and $\tilde{p}_i = \varepsilon_h \sigma_i \tilde{E}_0$ is the induced dipole moment of each NP; $\sigma_i = 3v_i\beta$ is the NP polarizability, with $\Theta = (\varepsilon_{NP} - \varepsilon_h)/(\varepsilon_{NP} + 2\varepsilon_h)$ [Eq. 3.23], where ε_{NP} (ε_h) is the dielectric function of the NPs (host) and v_i is the NP volume; Θ depends on $|E_0|$ through of the dielectric functions of NP (ε_{NP}) and the host (ε_h). Hence, the optical polarization is given by:

$$\begin{aligned}\tilde{P} &= \varepsilon_h^L \left\{ \frac{\varepsilon_h}{\varepsilon_h^L} \left[\chi_h + \frac{3\Theta f}{1 - \Theta f} \right] \right\} \tilde{E}_0, \\ &= \varepsilon_h^L \left\{ \chi\left(|\tilde{E}_0|^2 \right) \right\} \tilde{E}_0, \end{aligned} \tag{3.64}$$

where $f = V^{-1}\sum_{i=1}^{N_{NP}} v_i$ is the volume fraction, χ_h is the host susceptibility, ε_{NP} and ε_h can be expressed as a sum of the linear and NL contributions as $\varepsilon_{h,NP} = \varepsilon^L_{h,NP} + \varepsilon^{NL}_{h,NP}$, where the NL terms are given by:

$$\varepsilon_{NP}^{NL} = \varepsilon_h^L \left[\frac{3}{4}\chi_{NP}^{(3)} \left\langle \left|\tilde{E}_{NP}\right|^2 \right\rangle + \frac{5}{8}\chi_{NP}^{(5)} \left(\left\langle \left|\tilde{E}_{NP}\right|^2 \right\rangle\right)^2 + \frac{35}{64}\chi_{NP}^{(7)} \left(\left\langle \left|\tilde{E}_{NP}\right|^2 \right\rangle\right)^3\right], \tag{3.65}$$

$$\varepsilon_h^{NL} = \varepsilon_h^L \left[\frac{3}{4}\chi_h^{(3)} \left\langle \left|\tilde{E}_0\right|^2 \right\rangle\right], \tag{3.66}$$

with $\chi_{NP}^{(j)}$, j = 3, 5, 7 , being the j-th susceptibility of the NPs and $\chi_h^{(3)}$ belongs to the host, $\left\langle \left|\tilde{E}_0\right|^2 \right\rangle$ correspond to the mean square modulus of the applied electric field. The contributions of $\chi_h^{(2j+1)}$, $j \geq 2$, were neglected because the solvents (host) used for the experiments exhibits only third-order nonlinearity for the range of intensities used. The numerical coefficients of Eqs. 3.65 and 3.66 correspond to the degeneracy factors for the i-th order process in the convention of [58], adopted in this thesis. Due to the small value of f the intensity dependent susceptibility is written as:

$$\chi \left\langle \left|\tilde{E}_0\right|^2 \right\rangle = \chi_h + 3\Theta f, \tag{3.67}$$

where the NL terms in f were neglected because: $(\Theta f)^j \ll 1 + \Theta f$, $j \geq 2$. The mean squared modulus of the electric field inside the NP is represented by $\left\langle \left|\tilde{E}_{NP}\right|^2 \right\rangle = |\eta'|^2 \left|\tilde{E}_0\right|^2$ with $\eta' = 3\varepsilon_h / (\varepsilon_{NP} + 2\varepsilon_h)$.

The effective NL susceptibilities of different orders are determined by performing two series expansions in terms of $\left|\tilde{E}_0\right|^2$ and $\left|\tilde{E}_{NP}\right|^2$. The first expansion consists in expressing $\chi(y)$ as a Taylor series up to third order in $y = \left|\tilde{E}_0\right|^2$ that assumes the form:

$$\chi(y) \approx \chi(0) + \left(\frac{\partial [\chi(y)]}{\partial y}\right)_{y=0} y + \frac{1}{2}\left(\frac{\partial^2 [\chi(y)]}{\partial y^2}\right)_{y=0} y^2 + \frac{1}{6}\left(\frac{\partial^3 [\chi(y)]}{\partial y^3}\right)_{y=0} y^3, \tag{3.68}$$

with the coefficients of the expansion obtained by introducing Eqs. 3.65 and 3.66 in Eq. 3.64 and calculating the derivatives of $\chi(y)$ with respect to y. Since $f \ll 1$, the coefficients in Eq. 3.68 can be written as:

$$\left(\frac{\partial [\chi(y)]}{\partial y}\right)_{y=0} = \frac{3}{4}\chi_h^{(3)} + \frac{3}{4} f \eta^2 |\eta|^2 \chi_{NP}^{(3)}, \tag{3.69}$$

$$\left(\frac{\partial^2 [\chi(y)]}{\partial y^2}\right)_{y=0} = \frac{5}{4} f \eta^2 |\eta|^4 \chi_{NP}^{(5)} - \frac{3}{8} f \eta^3 |\eta|^4 \left[\chi_{NP}^{(3)}\right]^2, \tag{3.70}$$

$$\left(\frac{\partial^3 [\chi(y)]}{\partial y^3}\right)_{y=0} = \frac{105}{32} f \eta^2 |\eta|^6 \chi_{NP}^{(7)} + \frac{9}{32} f \eta^4 |\eta|^6 \left[\chi_{NP}^{(3)}\right]^3 - \frac{15}{8} f \eta^3 |\eta|^6 \left[\chi_{NP}^{(3)} \chi_{NP}^{(5)}\right]^2, \tag{3.71}$$

where $\eta = 3\varepsilon_h^L / \left(\varepsilon_{NP}^L + 2\varepsilon_h^L\right)$ [Eq. 3.40]. Equations 3.69-3.71 were derived neglecting $\chi_h^{(5)}$ and $\chi_h^{(7)}$, and terms proportional to $\left(\chi_h^{(3)}\right)^2$ and $\left(\chi_h^{(3)} \chi_{NP}^{(3)}\right)$. These considerations are based on the assumption that $\chi_h^{(3)} \ll \chi_{NP}^{(3)}$. For instance, silver colloids used in the next chapters display values of $\chi_{NP}^{(3)}$ that are approximately five orders of magnitude larger than $\chi_h^{(3)}$, when $f = 10^{-5}$.

In order to obtain an expression of the electric field inside the NPs in terms of $\tilde{E}_0$, a second expansion was performed for $|\eta'|^2$ as function of $z = \sqrt{\left\langle |\tilde{E}_{NP}|^2 \right\rangle}$ written as:

$$\left\langle |\tilde{E}_{NP}|^2 \right\rangle \approx \left(|\eta'|^2\right)_{z=0} \left\{ 1 + \frac{1}{2} \left[\frac{\partial^2 \left(|\eta'|^2\right)}{\partial z^2} \right]_{z=0} |\tilde{E}_0|^2 + \frac{1}{4} \left[\frac{\partial^2 \left(|\eta'|^2\right)}{\partial z^2} \right]_{z=0}^2 \left(|\tilde{E}_0|^2\right)^2 \right\} |E_0|^2, \tag{3.72}$$

considering $\left(\partial |\eta'|^2 / \partial z\right)_{z=0} = 0$ and $\left\langle |\tilde{E}_{NP}|^2 \right\rangle = |\eta'|^2 |\tilde{E}_0|^2$. Introducing Eqs. 3.65 and 3.66 in the expression for $|\eta'|^2$ and calculating the derivatives with respect to z, we obtain

$$\left\langle |\tilde{E}_{NP}|^2 \right\rangle \approx |\eta|^2 \left\{ 1 - \frac{1}{2} |\eta|^2 Re\left[\eta \chi_{NP}^{(3)}\right] |\tilde{E}_0|^2 + \frac{1}{4} |\eta|^4 \left(Re\left[\eta \chi_{NP}^{(3)}\right] \right)^2 |\tilde{E}_0|^4 \right\} |\tilde{E}_0|^2. \tag{3.73}$$

The expansion of χ as a Taylor series up to third order in z^2 is given by:

$$\chi\left(z^2\right) \approx \chi(0) + \left(\frac{\partial\left[\chi\left(z^2\right)\right]}{\partial\left(z^2\right)} \right)_{z^2=0} z^2 + \frac{1}{2} \left(\frac{\partial^2\left[\chi\left(z^2\right)\right]}{\partial\left(z^2\right)^2} \right)_{z^2=0} \left(z^2\right)^2 + \frac{1}{6} \left(\frac{\partial^3\left[\chi\left(z^2\right)\right]}{\partial\left(z^2\right)^3} \right)_{z^2=0} \left(z^2\right)^3, \tag{3.74}$$

and substituting Eq. 3.73 in Eq. 3.74 we have

$$\begin{aligned}
\chi\left(|\tilde{E}_0|^2\right) \approx \chi(0) &+ |\eta|^2 \left(\frac{\partial\left[\chi\left(z^2\right)\right]}{\partial\left(z^2\right)} \right)_{z^2=0} |\tilde{E}_0|^2 \\
&+ \frac{1}{2} |\eta|^4 \left(\frac{\partial^2\left[\chi\left(z^2\right)\right]}{\partial\left(z^2\right)^2} - \frac{\partial\left[\chi\left(z^2\right)\right]}{\partial\left(z^2\right)} Re\left[\eta \chi_{NP}^{(3)}\right] \right)_{z^2=0} |\tilde{E}_0|^4 \\
&+ \frac{1}{6} |\eta|^6 \left(\frac{\partial^3\left[\chi\left(z^2\right)\right]}{\partial\left(z^2\right)^3} - 3 \frac{\partial^2\left[\chi\left(z^2\right)\right]}{\partial\left(z^2\right)^2} Re\left[\eta \chi_{NP}^{(3)}\right] \right. \\
&\qquad \left. + \frac{3}{2} \frac{\partial\left[\chi\left(z^2\right)\right]}{\partial\left(z^2\right)} \left(Re\left[\eta \chi_{NP}^{(3)}\right] \right)^2 \right)_{z^2=0} |\tilde{E}_0|^6.
\end{aligned} \tag{3.75}$$

Expressing the effective dielectric function of the MDNC as 2.80:

$$\varepsilon_{eff} = \varepsilon_h + \sum_{j-odd} \frac{j! 2^{1-j}}{\left[\frac{j-1}{2}\right]! \left[\frac{j+1}{2}\right]!} \chi_{eff}^{(j)}(\omega) |\tilde{E}_0|^{j-1}, \tag{3.76}$$

it is possible to obtain the effective susceptibility as a function of $|\tilde{E}_0|^2$ that can be written, according to [58], as

$$\chi_{eff}\left(|\tilde{E}_0|^2\right) = \chi_{eff}^{(1)} + \frac{3}{4} \chi_{eff}^{(3)} |\tilde{E}_0|^2 + \frac{5}{8} \chi_{eff}^{(5)} |\tilde{E}_0|^4 + \frac{35}{64} \chi_{eff}^{(7)} |\tilde{E}_0|^6. \tag{3.77}$$

Finally, by comparison of Eqs. 3.76 and 3.77, using the coefficients given by Eqs. 3.69-3.71, we obtain expressions for the effective third-, fifth- and seventh-order susceptibilities as:

$$\begin{aligned}
\chi_{eff}^{(3)} &= f\eta^2 |\eta|^2 \chi_{NP}^{(3)} + \chi_h^{(3)}, && (3.78)\\
\chi_{eff}^{(5)} &= f\eta^2 |\eta|^4 \chi_{NP}^{(5)} - \frac{6}{10} f\eta^3 |\eta|^4 \left[\chi_{NP}^{(3)}\right]^2 - \frac{3}{10} f\eta |\eta|^6 \left|\chi_{NP}^{(3)}\right|^2, && (3.79)\\
\chi_{eff}^{(7)} &= f\eta^2 |\eta|^6 \chi_{NP}^{(7)} + \frac{12}{35} f\eta^4 |\eta|^6 \left[\chi_{NP}^{(3)}\right]^3 + \frac{3}{35} f |\eta|^8 \left[4|\eta|^2 \chi_{NP}^{(3)} + |\eta|^2 \left(\chi_{NP}^{(3)}\right)^*\right] \left|\chi_{NP}^{(3)}\right|^2 \\
&\quad - \frac{4}{7} f\eta |\eta|^6 \left[2\eta^2 \chi_{NP}^{(3)} + |\eta|^2 \left(\chi_{NP}^{(3)}\right)^*\right] \chi_{NP}^{(5)}. && (3.80)
\end{aligned}$$

It can be seen from Eq. 3.78 that $\chi_{eff}^{(3)}$ may be cancelled adjusting f and the result is independent of the laser intensity. However, $Re\left(\chi_{eff}^{(3)}\right)$ and $Im\left(\chi_{eff}^{(3)}\right)$ are canceled for different f values. Eq. 3.79 indicates that the effective fifth-order susceptibility, $\chi_{eff}^{(5)}$, is due to the NPs nonlinearity corresponding to intrinsic contribution, $\chi_{NP}^{(5)}$, and contributions depending on the second power of $\chi_{NP}^{(3)}$, in analogy to the treatment developed by Dolgaleva [Eqs. 3.51 and 3.52]. Similarly, Eq. 3.80 shows that the NPs contribution to $\chi_{eff}^{(7)}$ are due to $\chi_{NP}^{(3)}$, $\chi_{NP}^{(5)}$, and $\chi_{NP}^{(7)}$, with different powers. Notice that the contributions of the NPs susceptibilities are enhanced due to the high powers of η and $|\eta|$.

> *Out of the cradle onto dry land here it is standing: atoms with consciousness; matter with curiosity.*
> *Stands at the sea, wonders at wondering: I a universe of atoms an atom in the universe.*
> - RICHARD FEYNMAN

4 NONLINEARITY MANAGEMENT (NM) OF MDNCs

4.1 INTRODUCTION

Metal-dielectric nanocomposites is attracting large interest due to their high NL optical susceptibility, fast response and the possibility of controlling their optical behavior manipulating its LSP. Glasses, polymers and liquids containing metallic NPs are illustrative examples of MDNCs of interest for photonics, nanoscience and nanotechnology [145, 161, 162, 163, 164, 165].

The NL response of a MDNC to optical fields is described by effective susceptibilities containing information on the host and the NPs. Therefore, the induced polarization of a centro-symmetric MDNC is described by a power series in the optical field having the effective susceptibilities, $\chi_{eff}^{(2j+1)}$, $j = 1, 2, 3, \ldots$, as coefficients of the expansion. However, most of the NL studies reported are related to lowest-order NL susceptibility $\left(\chi_{eff}^{(3)}\right)$ that is responsible for effects such as 2PA, coherent Raman scattering, among other. Up to now, the majority of studies based on the NL optical properties of MDNCs were focused on $\chi_{eff}^{(3)}$ [166, 162, 167, 163, 168, 169, 170, 171].

Nowadays, due to the development of short pulse lasers it is possible to use high optical fields without destruction of samples and the contributions of HON become detectable. Due to the mismatch between the dielectric function of the NPs and the host, there is an enhancement of the electromagnetic field that depends on the laser frequency and its detuning from the LSPR of NPs. Therefore, high values of the effective susceptibilities are observed that may favor detection of effects related to HON either associated to intrinsic NL processes or due to cascade processes [23, 24, 33, 158].

In particular, contributions of fifth-order suceptibility are significant at high intensities due to dependence on the quintic power of the incident field. The interest in effects related to quintic and cubic-quintic nonlinearities has led several authors to investigate theoretically new NL phenomena and propose experiments with MDNCs [172, 173, 174, 108, 175, 176]. Nevertheless, these new proposals require apart from a high NL response, an appropriate control on the contributions of the different HON, which is non-trivial. Concerning to this point, MDNCs are very interesting systems because their NL response can be controlled by a simple procedure which consists in vary the NPs volume fraction [171].

In this chapter we present a procedure for nonlinearity management of a MDNC aiming its exploitation for practical realization of mathematical models and experiments related to HON. As model systems we use colloids consisting of metallic NPs suspended in transparent NL liquids (acetone and CS_2). HON up to seventh-order can be measured as a function of the NP volume fraction for intensities of few GW/cm^2. Here, by varying the volume fraction, f, occupied by silver NPs and the incident laser intensity it is possible to enhance, decrease and even suppress a specific NL susceptibility due to the interference between the contributions of $\chi^{(3)}_{eff}$, $\chi^{(5)}_{eff}$ and $\chi^{(7)}_{eff}$ derived from intrinsic and cascade processes. Analysis of the results were performed by using the generalized Maxwell-Garnet model, developed in Section 3.6, that includes the HON contributions. Under these conditions, the NM procedure was applied to silver colloids in order to investigate for the first time the phenomena of SSPM, SXPM and SMI in MDNCs presenting quintic and septimal refractive nonlinearities, in the absence of contributions due to the lower order NL refractive indices. In addition, a proposal for practical applications of the NM procedure in all-optical switches based in MDNCs is introduced and validated by performing proof-of-principle experiments with metal colloids.

4.2 DESCRIPTION AND ANALYSIS OF THE NM PROCEDURE

The concept of NM emerges in optics as a theoretical proposal to study the stable propagation of intense optical beams in layered Kerr media [177, 178]. The idea of managing the NL parameters of a medium (NL refractive index and NL absorption coefficient) allowed to predict the collapse arrest of [(2+1)D] two-dimensional soliton in Kerr-type optical media [178, 179], as well as in Bose–Einstein condensate [180].

In MDNCs, NM procedure refers to a method for controlling their NL response by varying intrinsic parameters (such as: size, shape, environment and volume fraction of metal NPs) and extrinsic parameters (such as: wavelength, repetition rate, laser intensity and pulse duration). This thesis introduces a NM procedure that consists in varying the volume fraction, occupied by metallic NPs with respect to the host volume, and the incident intensity. To analyze the NM procedure, this section was divided into three stages:

(A) *Measurement of NL parameters*

The MDNCs used for these studies are colloids containing silver NPs suspended in acetone (labeled as sample A) and in CS_2 (labeled as sample B). Both NL samples were prepared by chemical reduction methods and then subjected to a laser photofragmentation process to obtain an homogeneous size distribution of silver NPs. Details on the preparation and characterization of the MDNCs are specified in Appendix B.

Nonlinear characterization of the MDNCs, which consists in measurements of effective NL refractive indices and NL absorption coefficients was performed using the Z-scan technique [27]. The basic principle of operation of the Z-scan technique can be found in Appendix A. Fig. 4.1 shows the experimental setup used to measure the contributions of HON in metal colloids. The second harmonic of a Q-switched and mode-locked Nd: YAG laser (80 ps, 532 nm, maximum pulse energy of 10 μJ) was used as light source. Single pulses at 10 Hz were selected using a pulse picker, with extinction ratio of 500:1, in order to avoid thermal contributions. Control of the total power and the linear polarization of the incident beam was accomplished by using a $\lambda/2$ plate followed by a Glan prism. A spatial filter was mounted to obtain a beam with a nearly Gaussian spatial profile corresponding to the beam quality factor $M^2 \approx 1.1$. The laser beam was focused by a 10 cm focal distance lens (beam waist: 20 μm) on a sample with thickness of 1 mm, contained in a quartz cell. Slow photodetectors placed in

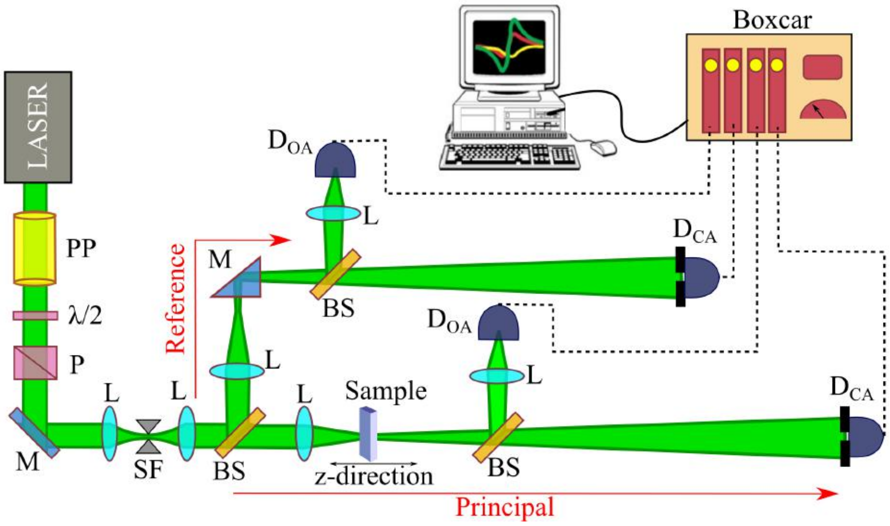

Figure 4.1 Experimental setup for the Z-scan measurements. (PP) Pulse picker, (P) polarizer, (M) mirrors, (SF) spatial filter, (L) lenses, (BS) beam splitter and detectors for the *closed-aperture* (D_{CA}) and *open-aperture* (D_{OA}) schemes.

the far-field region with adjustable apertures in front of them were used to measure the beam intensity transmitted by the sample. The aperture radius, r_a, is related to its transmittance by $S = 1 - exp\left(-2r_a^2/w_a^2\right)$, with w_a being the beam radius at the aperture plane. CA $(S < 1)$ and OA $(S = 1)$ schemes were used to determine the NL refractive indices and the NL absorptive coefficients, respectively. The detected signals were processed by boxcar integrators and computer. In order to improve the signal-to-noise ratio in the measurements, mainly caused by lasers intensity fluctuations and beam-point instability[1], a reference channel was added to the typical Z-scan setup as in [181]. CS_2 with NL refractive index equal to 3.1×10^{-14} cm^2/W [27] was the reference standard for calibration of measurements.

The methodology used to obtain the high-order NL parameters of the MDNCs was described in Section 3.5.3. Fig. 4.2 and 4.3 display the Z-scan traces for samples A and B, respectively. Figure 4.2(a) shows CA Z-scan traces corresponding to four f values. The colloid inside a 1-mm-long quartz cell was scanned along the Z axis using a translation stage. Figures 4.2(a-*i*) and 4.2(a-*ii*) show profiles that indicate positive NL refractive index for $f = 0.8 \times 10^{-5}$ and $f = 1.3 \times 10^{-5}$, respectively. The normalized peak-to-valley transmittance change, $\left|\triangle T_{p,v}\right|$, is smaller in Fig. 4.2(a-*ii*) than in Fig. 4.2(a-*i*) because the NPs contribute to the NL refractive index with the opposite sign than acetone that has $n_2 = +2.16 \times 10^{-15}$ cm^2/W [182]. Figures 4.2(a-*iii*) and 4.2(a-*iv*), corresponding to $f \geq 2 \times 10^{-5}$, indicate that the NL refractive index of the colloid became negative because the silver NPs dominate the NL response. For small laser intensities ($I \leq 2.0$ GW/cm^2) we determined $n_{2,eff}$ for different f values using the expression

---

[1] Beam-point instability refers to fluctuations in the transverse position or direction of the output beam of a laser, which can cause significant problems in the alignment of experiments, light coupling and light filtering, among others. In our case, beam-point instability is mainly caused by temperature variations within the laser cavity.

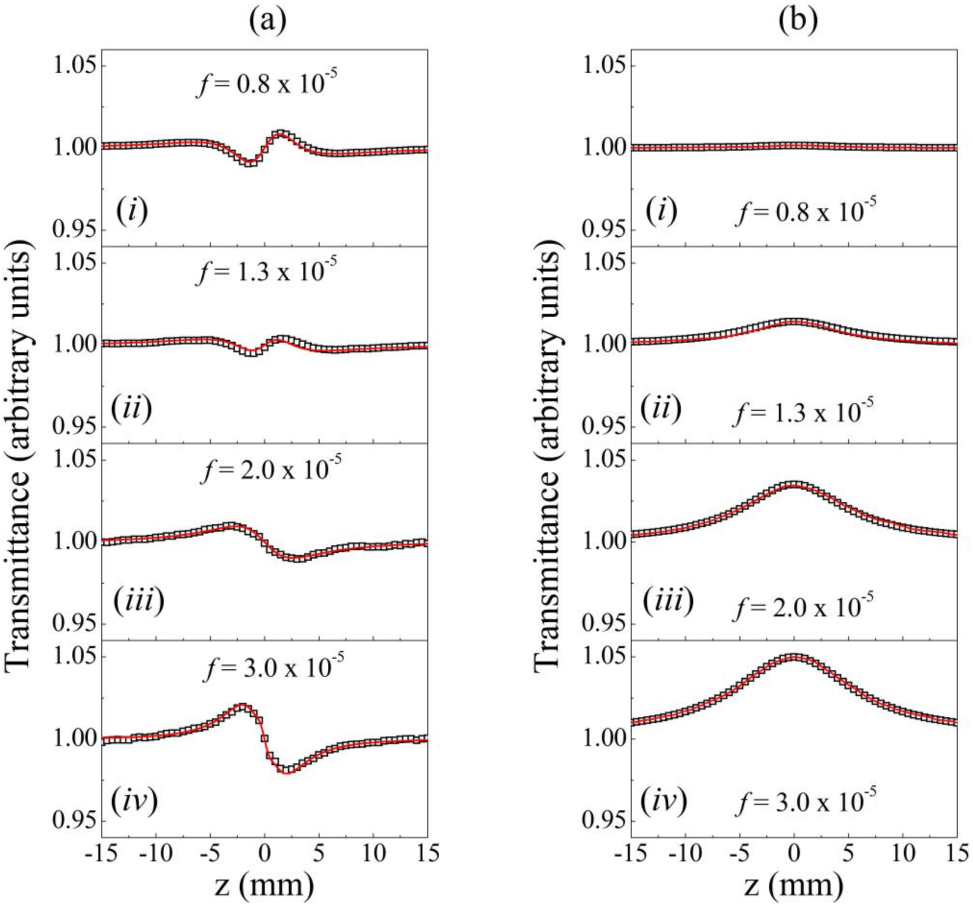

Figure 4.2 Typical (a) *closed-aperture* and (b) *open-aperture* Z-scan traces obtained for sample A with different volume fractions. Negative values of Z correspond to locations of the sample between the focusing lens and its focal plane. Laser peak intensity: 5.0 GW/cm^2.

$\triangle T_{p,v} = 0.406 k L_{eff}^{(1)} n_{2,eff} I$ [see Eq. 3.57], where $k = 2\pi n_0/\lambda$, $L_{eff}^{(1)} = [1 - exp(-\alpha_0 L)]/\alpha_0$, L is the sample length, α_0 is the linear absorption coefficient, and λ is the laser wavelength. The sign reversal of $n_{2,eff}$ as a function of f was observed for all intensities used.

Open-aperture Z-scan profiles did not show NL absorption for $f \leq 0.8 \times 10^{-5}$. However, for $1.3 \times 10^{-5} < f \leq 3.0 \times 10^{-5}$ the colloid presented saturated absorption as shown in Fig. 4.2(b) due to the small detuning between the laser frequency and the LSPR.

Closed-apertureand OA Z-scan measurements were also performed for sample B with f varying from 0.4×10^{-5} to 4.5×10^{-5} as displayed in Figs. 4.3(a) and 4.3(b), respectively. Sign-reversal of the NL refractive index as a function of f can also be seen in the interval $1.3 \times 10^{-5} < f \leq 3.3 \times 10^{-5}$.

A similar measurement procedure was performed by fixing f and changing the incident intensity, I, for the whole range of f values. Here, no sign reversal of $n_{2,eff}$ was observed, in both samples. However, Fig 4.4(a) shows additional features in the CA Z-scan profiles of sample A due to HON for $I > 6.0$ GW/cm^2 and Fig. 4.4(b) shows OA profiles for various laser intensities. The appearance of a second structure of peaks and valleys, to the highest intensities of

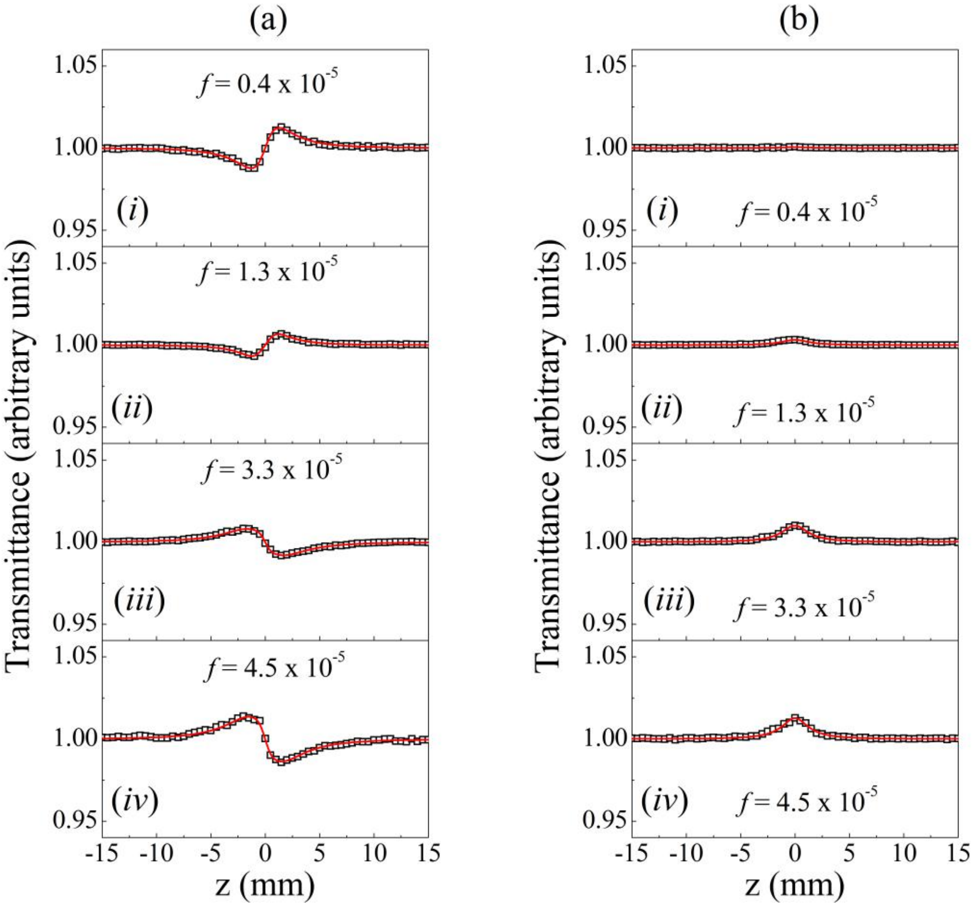

Figure 4.3 Typical (a) *closed-aperture* and (b) *open-aperture* Z-scan traces obtained for sample B with different volume fractions. Negative values of Z correspond to locations of the sample between the focusing lens and its focal plane. Laser peak intensity: 0.2 GW/cm^2.

Figure 4.4(a), is related to contributions of HON, since HON produce maximum and minimum transmittance at different positions to those who corresponds to the third-order nonlinearity, as discussed in Section 3.5.3. The solid curves were obtained by plot the Eqs. 3.55 and 3.59 using the NL parameters found by fitting the curve $\left|\Delta T_{p,v}\right|/I$ versus I, as shown in the next stage. Because the results for the sample B are very similar, these are not shown in this thesis. After each Z-scan experiment no changes were observed in the linear absorption spectrum indicating that the energy of the laser pulses did not change the samples' characteristics. All NL experiments were repeated more than one time with each sample and the results were reproduced.

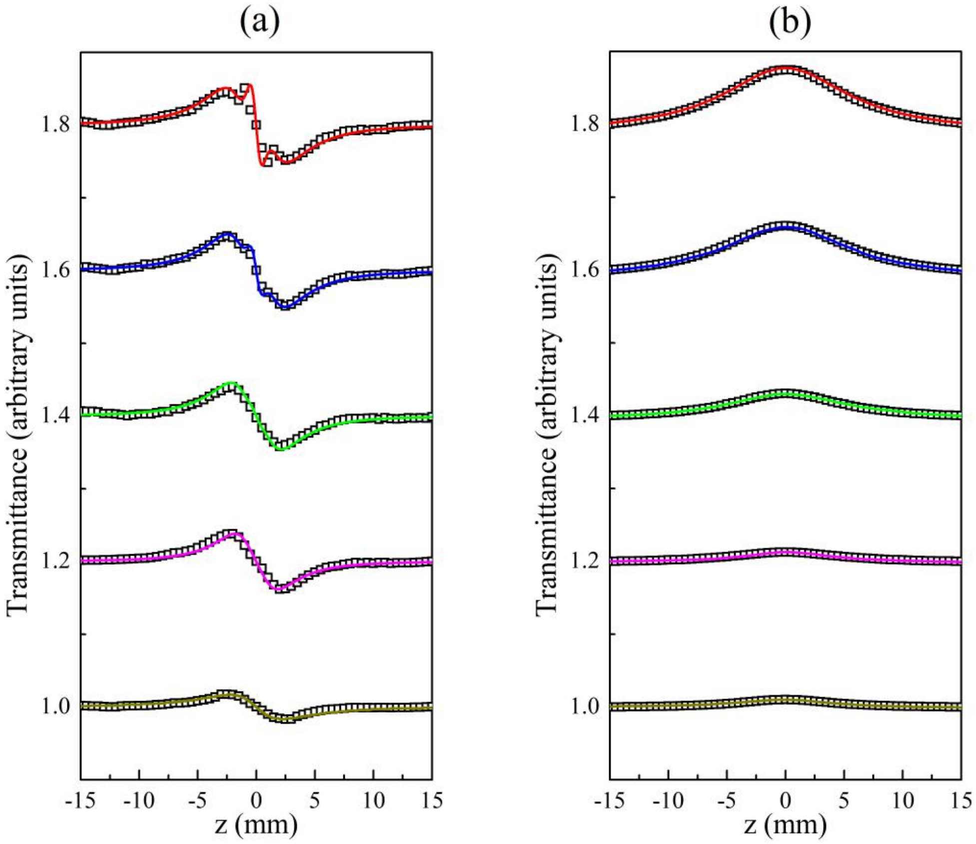

Figure 4.4 Normalized Z-scan traces for sample A obtained for different laser peak intensities: (a) Closed-aperture scheme and (b) open-aperture scheme. From bottom to top, the curves correspond to 2, 4, 6, 8, and 9 GW/cm^2. Volume fraction: $f = 5.0 \times 10^{-5}$. The curves were normalized and shifted in the vertical to prevent overlap.

(B) *Analysis of HON*

After performing several Z-scan measurements for different volume fractions and each one for different intensities, we calculate the transmittance variation, $\triangle T_{p,v}$, and we plot $\left|\Delta T_{p,v}\right|/I$ versus I following the procedure described in Section 3.5.3. Figure 4.5(a) illustrates the results for sample A. For $f < 0.8 \times 10^{-5}$ the ratio $\left|\Delta T_{p,v}\right|/I$ remains constant for intensities up to 10 GW/cm^2, indicating negligible contributions of $\chi_{eff}^{(2j+1)}$ $(j > 1)$. For $f \approx 1.3 \times 10^{-5}$, the ratio $\left|\Delta T_{p,v}\right|/I$ presents linear dependence with the laser intensity and from the slope of the straight line we can determine $n_{4,eff} \propto Re\left[\chi_{eff}^{(5)}\right]$. For $f \geq 2.0 \times 10^{-5}$ the laser intensity dependence of $\left|\Delta T_{p,v}\right|/I$ is a polynomial function that allows obtaining the refractive indices associated to NL susceptibilities up to the seventh order. The effective NL parameters were obtained by fitting Fig. 4.5(a) with Eq. 3.57. The polynomial fit was performed based on 20 experimental points corresponding to intensities between 2 and 10 GW/cm^2, for each f value, with a measurement uncertainty of 15% due to the laser intensity fluctuations. The algorithm used to obtain the best fit was a combination of the Levenberg-Marquardt and the least-squares minimum method

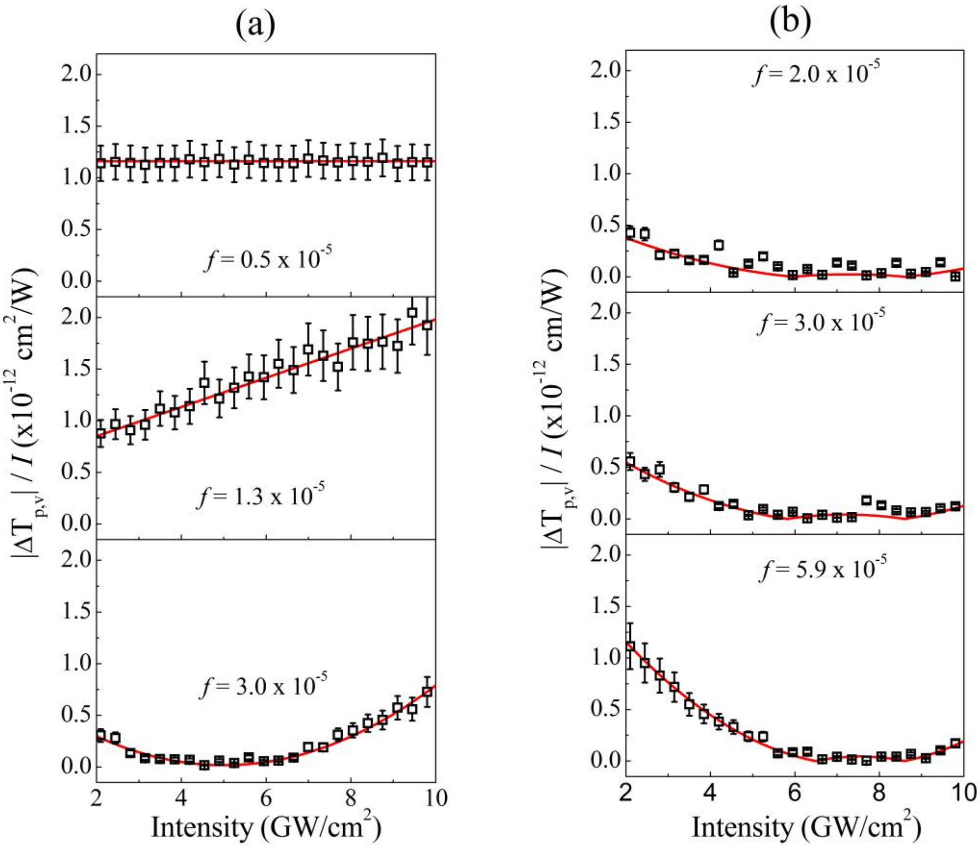

Figure 4.5 Intensity dependence of $|\Delta T_{p,v}|/I$ for sample A in the (a) NL refraction and (b) NL absorption regimes. (Sample length: 1 mm). The solid lines are fit curves obtained from Eqs. 3.57 and 3.62.

with determination coefficient, $R^2 > 0.95$. For instance, when $f = 2.5 \times 10^{-5}$ and $I = 9.0$ GW/cm^2 we determined $n_{2,eff} = -1.1 \times 10^{-15}$ cm^2/W, $n_{4,eff} = +6.9 \times 10^{-25}$ cm^4/W^2, and $n_{6,eff} = -1.1 \times 10^{-34}$ cm^6/W^3.

The ratio $\left|\Delta T_{p,v}\right|/I$ also exhibited a polynomial dependence with I in the OA experiments, as shown in Fig. 4.5(b). Here, we obtained $\alpha_{j,eff}$ $(j = 2, 4, 6)$ for different values of f by fitting Fig. 4.5(b) using Eq. 3.62. For example, for $f = 5.0 \times 10^{-5}$, we have $\alpha_{2,eff} = -4.9 \times 10^{-10}$ cm/W, $\alpha_{4,eff} = +1.4 \times 10^{-19}$ cm^3/W^2, and $\alpha_{6,eff} = -1.7 \times 10^{-29}$ cm^5/W^3.

Notice that the values of $n_{2,eff}$, $n_{4,eff}$, $n_{6,eff}$ and $\alpha_{2,eff}$, $\alpha_{4,eff}$, $\alpha_{6,eff}$ obtained from the polynomial fit were used to adjust the experimental Z-scan profiles shown in Figs. 4.2, and 4.4 with good agreement. It is important to remark that if the NL coefficients values used (including their signs) were different, the Z-scan traces would present other profiles. The same treatment is used for sample B. The error bars shown in the figures of this chapter were obtained by computing the standard deviation of the values after at least five times' averaging.

Summary of the results for sample A is shown in Figure 4.6, showing that $n_{2,eff}$, $n_{4,eff}$, $n_{6,eff}$, $\alpha_{2,eff}$, $\alpha_{4,eff}$ and $\alpha_{6,eff}$ present linear dependence with f. Notice that for $f \approx 1.6 \times 10^{-5}$ we have $n_{2,eff} = 0$ but $n_{4,eff} = +3.2 \times 10^{-25}$ cm^4/W^2. It is important to note that the

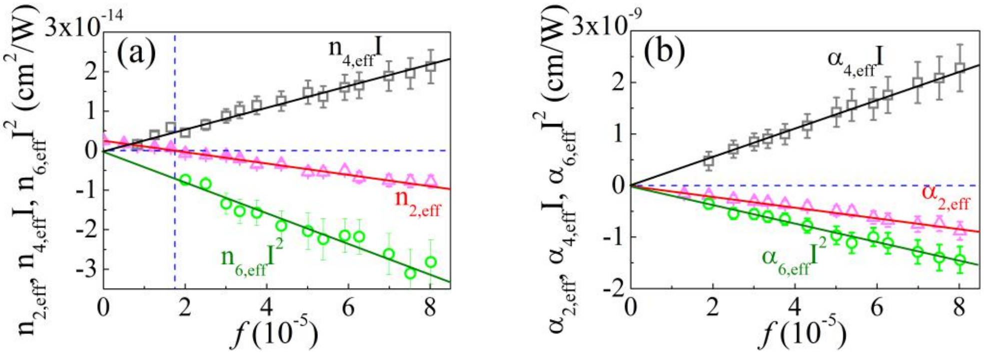

Figure 4.6 Dependence of the effective third-order coefficients ($n_{2,eff} \propto Re\chi^{(3)}_{eff}$ and $\alpha_{2,eff} \propto Im\chi^{(3)}_{eff}$), effective fifth-order coefficients ($n_{4,eff} \propto Re\chi^{(5)}_{eff}$ and $\alpha_{4,eff} \propto Im\chi^{(5)}_{eff}$) and the effective seventh-order coefficients ($n_{6,eff} \propto Re\chi^{(7)}_{eff}$ and $\alpha_{6,eff} \propto Im\chi^{(7)}_{eff}$) versus the NP volume fraction, f: (a) $n_{2,eff}$, $n_{4,eff}I$ and $n_{6,eff}I^2$; (b) $\alpha_{2,eff}$, $\alpha_{4,eff}I$ and $\alpha_{6,eff}I^2$. Laser peak intensity: $I = 9.5$ GW/cm^2.

solvent nonlinearity plays an important role to annul the effective third-order refractive index, because the sign of its refractive cubic nonlinearity is contrary to the contribution of silver NPs. However, HON of the solvent are negligible and the effective fifth- and seventh-order nonlinearities are due to the intrinsic and cascade contributions of the NPs.These results do not violate the powers series of the NL polarization and opens routes for exploitation of unique effects considering that under the conditions identified here $Re\chi^{(5)}_{eff}$ is the lowest-order NL refractive response. The solid lines are fit curves obtained by using the generalized Maxwell-Garnett model, which is discussed in the next stage.

The silver colloid with $f \approx 1.6\times10^{-5}$ reveals an exotic material, that had not been reported in the literature so far, because its NL behavior corresponds to a quintic refractive medium, in absence of the cubic refraction. This behavior can also be deduced from the CA Z-scan curves. Figure 4.7(a) shows the NL refractive response of sample A for $f = 1.6\times10^{-5}$ ($Re\chi^{(3)}_{eff} = 0$ and $Re\chi^{(5)}_{eff} \neq 0$). For laser intensities up to 4 GW/cm^2 no feature is observed in the CA Z-scan trace while for 9 GW/cm^2 a positive effective NL refractive index is observed due to the HON (mainly of positive quintic nonlinearity). On the other hand, when $f \neq 1.6\times10^{-5}$ and for laser intensity of 2 GW/cm^2 larger CA Z-scan signal, dominated by the negative third-order nonlinearity, is observed. This behavior is illustrated in Fig. 4.7(b) which shows the Z-scan trace obtained for 4 GW/cm^2 . For larger intensities clear indication of HON contribution is observed in the Z-scan traces as illustrated in Fig. 4.7(b) corresponding to $n_{2,eff} = -5.5\times10^{-15}$ cm^2/W, $n_{4,eff} = +2.1\times10^{-24}$ cm^4/W^2, and $n_{6,eff} = -2.6\times10^{-34}$ cm^6/W^3 for $f = 5.0\times10^{-5}$.

Similarly, the results for sample B are summarized in Fig. 4.8. Figure 4.8(a) illustrates the destructive interference between the $n_{2,eff} \propto Re\chi^{(3)}_{eff}$ and $n_{4,eff} \propto Re\chi^{(5)}_{eff}$ contributions versus f. For $f = 3.3\times10^{-5}$ we obtain a NL refractive MDNC with $n_{6,eff} = -1.1\times10^{-30}$ cm^6/W^3 (septimal refractive nonlinearity). Analogously, a NL refractive MDNC with $n_{4,eff} = +1.1\times10^{-22}$ cm^4/W^2 (quintic refractive nonlinearity), is shown in Fig. 4.8(b) for $f = 1.5\times10^{-5}$ due

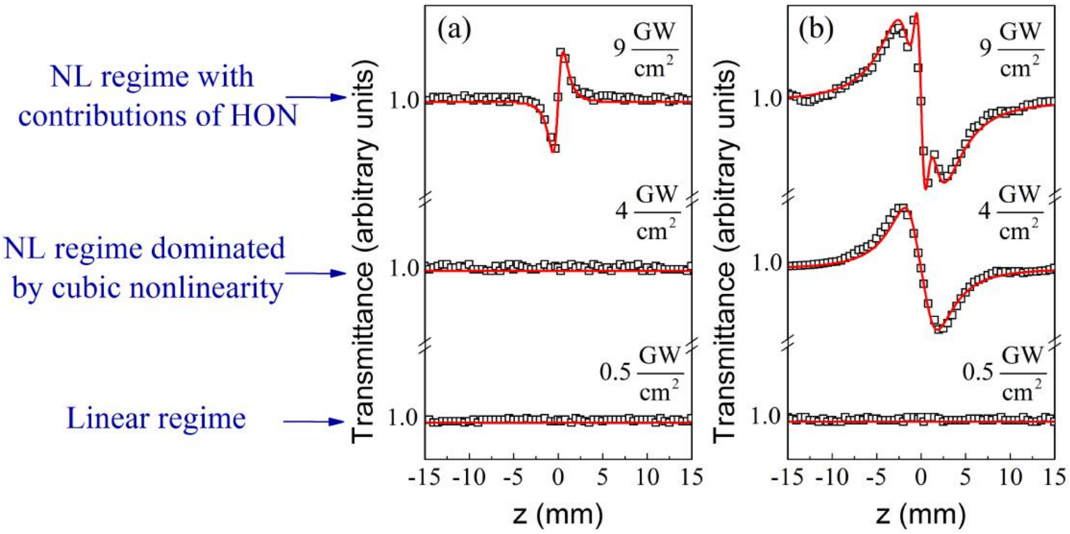

Figure 4.7 CA Z-scan profiles, for sample A, obtained for different laser peak intensities with two NPs volume fractions: (a) $f = 1.6 \times 10^{-5}$ and (b) $f = 5.0 \times 10^{-5}$. The solid lines were obtained using Eq. 3.55.

to destructive interference between the third- and seventh-order contributions. Figure 4.8(c) exhibits a NL absorptive behavior with $\alpha_{6,eff} = -7.5 \times 10^{-27}$ cm^5/W^3 , for $f = 1.2 \times 10^{-5}$ and $I = 2.5 \times 10^8$ W/cm^2.

(C) *Interpretation of HON by using the Maxwell-Garnett model*

The last step of our NM procedure involves the interpretation of the results of Figs. 4.6 and 4.8 by using the generalized Maxwell-Garnett model, described in Section 3.6.

By fitting Eqs. 3.78-3.80 in Figs. 4.6 and 4.8, we obtained the third-order susceptibility of the acetone, $\chi^{(3)}_{acetone} = 1.67 \times 10^{-21}$ m^2/V^2 and the CS_2, $\chi^{(3)}_{CS_2} = \left(2.9 \times 10^{-20} + i3.41 \times 10^{-22}\right)$ m^2/V^2 in agreement with [182] and [27, 183], respectively. In the same way, the NL susceptibilities for the NPs are given by $\chi^{(3)}_{NP} = (-5.9 - i8.5) \times 10^{-16}$ m^2/V^2, $\chi^{(5)}_{NP} = (-1.0 - i17) \times 10^{-33}$ m^4/V^4 and $\chi^{(7)}_{NP} = (-3.2 + i1.6) \times 10^{-52}$ m^6/V^6 for the sample A, while the values of $\chi^{(3)}_{NP} = (-6.4 + i2.0) \times 10^{-16}$ m^2/V^2, $\chi^{(5)}_{NP} = (-1.37 - i2.2) \times 10^{-33}$ m^4/V^4 and $\chi^{(7)}_{NP} = (-4.1 + i5.1) \times 10^{-51}$ m^6/V^6 were calculated for the sample B. Notice that the values of $\chi^{(3)}_{NP}$ are in agreement with [171] that was determined in the absence of HON. However, we recall that the silver NPs susceptibility depends on its shape, size, stabilizing agents attached to the NPs surface as well as the host solvent, as discussed in Section 3.5.1.

Probably, one of the most significant results is the manipulation of the NL response of a MDNC to obtain a refractive quintic medium with $Re\chi^{(3)}_{eff} = 0$, which was predicted only theoretically. Eqs. 3.78 and 3.79 allows to understand this phenomenon. Eq. 3.78 shows that the sign reversal of $\chi^{(3)}_{eff}$ as a function of f is mainly due to competition between the terms containing $Re\left[\chi^{(3)}_{NP}\right]$ and $Re\left[\chi^{(3)}_{h}\right]$ that have opposite signs. Thus, $\chi^{(3)}_{eff}$ may be cancelled

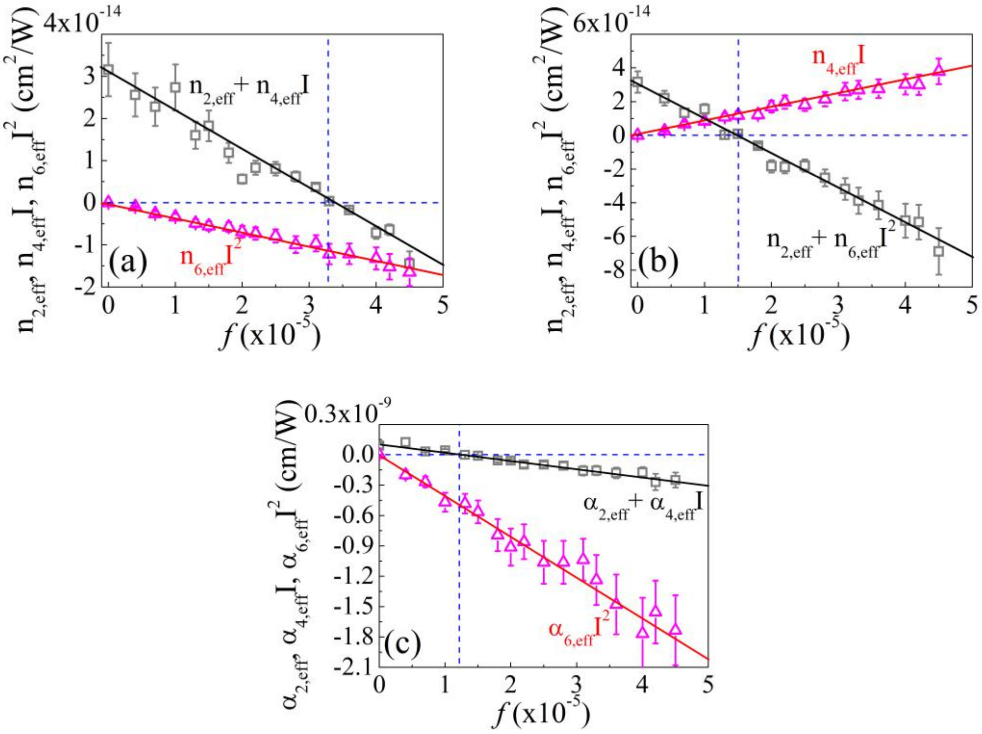

Figure 4.8 Dependence of the effective third-, fifth- and seventh-order coefficients of sample B as a function of the volume fraction, f. Notice that the sample presents: septimal refractive nonlinearity at $f = 3.3 \times 10^{-5}$ (a) and quintic refractive nonlinearity at $f = 1.5 \times 10^{-5}$ (b). Figures (a) and (b) were obtained with laser peak intensity of 10^8 W/cm^2. When $f = 1.2 \times 10^{-5}$ and the laser peak intensity is 2.5×10^8 W/cm^2, the NL absorption is due to $\alpha_{6,eff} \propto Im\chi^{(7)}_{eff}$.

adjusting f and the result is independent of the laser intensity. At first, one might think that because the NL susceptibility responds to an expansion in power series of electric field, if the lowest-order susceptibility is zero, then the higher-order susceptibilities also should be zero, in order to not violate the expansion criterion. However, it is important to note that the expansion is performed for the susceptibilities of the host and NPs, separately. This means that the expansion has physical sense when $\left|\chi^{(2j+3)}_{NP,h}\right| |E|^2 < \left|\chi^{(2j+1)}_{NP,h}\right|$ with j =1, 2, 3, so that the power series converges. This condition is fulfilled for all our cases. Nevetheless, when the expressions for the effective NL susceptibilities are analyzed [Eqs. 3.78-3.80], it is possible to note that $\chi^{(5)}_{eff}$ and $\chi^{(7)}_{eff}$ depends only on the intrinsic and cascade contributions of NPs, because the high-order contributions of the solvent are neglected, whereas $\chi^{(3)}_{eff}$ depends on $\chi^{(3)}_{NP}$ and $\chi^{(3)}_{h}$. Thus, $\chi^{(3)}_{eff} = 0$ due to balance between the contributions of $\chi^{(3)}_{NP}$ and $\chi^{(3)}_{h}$ and not because $\chi^{(3)}_{NP} = 0$. As a consequence, sample A with $f = 1.6 \times 10^{-5}$ can be considered as a quintic medium, since that the NL susceptibility used to characterize the NL response of the composite is the effective susceptibility. In addition, contributions of septimal nonlinearity are significant at higher intensities, depending strongly on the incident intensity. Using this to our advantage, it is possible to add the intensity as a new parameter to our NM procedure.

Therefore, varying both the volume fraction and the incident intensity is possible to induce constructive and destructive interferences between the susceptibilities of different NL orders in order to enhance, decrease and even suppress a specific NL susceptibility, as shown in Fig 4.8.

4.3 APPLICATION OF THE NM PROCEDURE TO EXPLOIT HON

One of the main applications of HON in MDNCs is the enhancement of its NL response, and consequently the improvement of the NL effects related to the cubic nonlinearity. However, without an adequate control of high-order susceptibilities, it is very difficult to use their contributions in favor of observing and analyzing new optical phenomena. In this way, the NM procedure described in the previous section arises as an excellent alternative to exploit the different applications based on HON. In this section, we will discuss and show the importance of the NM procedure in the study of transverse NL effects, already known for the lowest-order nonlinearity (cubic nonlinearity), but being induced by HON. In addition, it will be demostrated how the use of a proper NM procedure allows optimize the performance of all-optical devices based in MDNCs.

4.3.1 Spatial Self-Phase Modulation

The interaction of an intense coherent beam with a NL medium that presents an intensity dependent refractive index can produce changes in the beam phase, which are reflected on the transverse beam profile [51]. This effect known as spatial self-phase modulation (SSPM) can generate concentric ring intensity patterns observed in far-field [Fig. 2(a)]. The first observation of SSPM was reported in CS_2, illuminated by a He-Ne laser, due to refractive index modulation induced by thermal effects [184]. Subsequently, several studies were reported in media exhibiting thermal nonlinearities [185, 186, 187], Kerr-type media [188, 189, 190], photorefractive crystals [191], nematic-liquid-crystals [192], among others [193, 194, 195]. In particular, SSPM effect in MDNCs has been studied on the basis of the lowest-order nonlinearity. However, a previous work has reported that in high intensities SSPM is influenced by HON and the simultaneous presence of third- and fifth-order nonlinearities allow the propagation of spatial solitons in liquids [30].

Figure 4.9 illustrate the experimental setup used to investigate the SSPM effects induced by HON. Here, the light source used was the second harmonic of a Q-switched and mode-locked Nd: YAG laser (the same used in the Z-scan technique), but being focused by a 2 cm focal length lens[2], producing a beam waist of 7 μm (confocal parameter: 0.8 mm). The far-field diffraction patterns produced by the strong interaction of the Gaussian beam with a silver colloid were captured by a charge-coupled device (CCD) camera located 20 cm from the exit plane of the sample (sample length: 1 mm). Dependence of intensity distribution patterns with the nonlinearity and the curvature radius of the wavefront, R, were analyzed by locating the sample on the focal plane of the lens L $(R \to \infty)$, 0.3 mm before $(R < 0)$ and 0.3 mm after $(R > 0)$ the focal plane.

---

[2] A strong focus was used to obtain high light intensities.

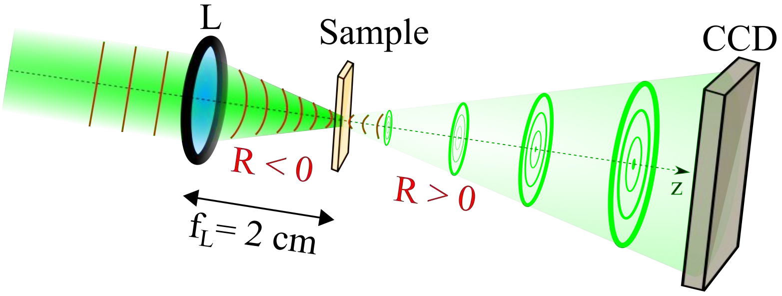

Figure 4.9 Experimental setup for study the SSPM effects. (L) lens with focal length $f_L = 2$ cm, (R) curvature radius of the wavefront.

Figures 4.10(a)-(c) show the experimental diffraction patterns observed in the beam transmitted by sample A (with $f = 1.6 \times 10^{-5}$) due to the SSPM effect. The f value used corresponds to a medium having NL response dominated by $Re\chi^{(5)}_{eff}$ with $Re\chi^{(3)}_{eff} = 0$. The diffraction patterns observed in the far-field consist of concentric rings that vary in number, thickness and positions depending on the NL phase shift $\triangle\Phi_{NL}$, given by Eq. 3.53 with $n_{2,eff} = 0$, and laser intensity. The noise observed in Fig. 4.10 is coming from mostly effects introduced by cell walls and the colloid-glass interface. This statement was corroborated by perform a measurement with an empty cell and with a cell containing only the solvent. This effect is also present in Figs. 4.11, 4.13, 4.14 and 4.15.

To describe the conical diffraction we used the Fraunhofer approximation of the Fresnel-Kirchhoff diffraction integral, described in Section 2.5.2.1, but considering the contribution of HON, given by:

$$I = I_0 \left| \int_0^{\infty} J_0\left(k\theta r\right) exp\left[-\frac{r^2}{w_p^2} - i\phi\left(r\right)\right] rdr \right|^2, \tag{4.1}$$

where $I_0 = 4\pi^2 \left|E\left(0,z_0\right) exp\left[-\alpha_0 L/2\right] / \left(i\lambda D\right)\right|^2$, $E\left(0,z_0\right)$ is the electric field at the beam axis, z_0 is the focal plane position, θ is the far-field diffraction angle, and $J_0\left(k\theta r\right)$ is the first kind zero-order Bessel function. $\phi\left(r\right) = kn_0 r^2/\left(2R\right) + \triangle\Phi_{NL} exp\left[-2r^2/w_p^2\right]$ represents to the total phase-shift, including the Gaussian phase due to the linear propagation plus the transverse NL phase-shift, r is the radial distance from the laser axis measured in a plane perpendicular to the z-axis, R is the wavefront radius of curvature, w_p is the beam radius at the entrance plane of the NL medium, and D is the distance from the exit plane of the cell and the far-field detection plane. It is important to mention that this model only considers the effects of NL phase variation induced by NL refractive indices. Effects due to NL absorption, scattering, stimulated effects, among others were disregarded for simplicity. Besides, propagation effects inside the NL medium were also neglected because the cell thickness is slightly larger than the confocal parameter. However, all these effects may produce differences between experimental and numerical results.

Figures 4.10(d)-(f) show the intensity distribution versus the radial coordinate (black line) obtained from CCD images processed as intensity matrices. The red lines correspond to the numerical results obtained from Eq. 4.1, considering the NL phase-shift due to $n_{4,eff}$ and $n_{6,eff}$

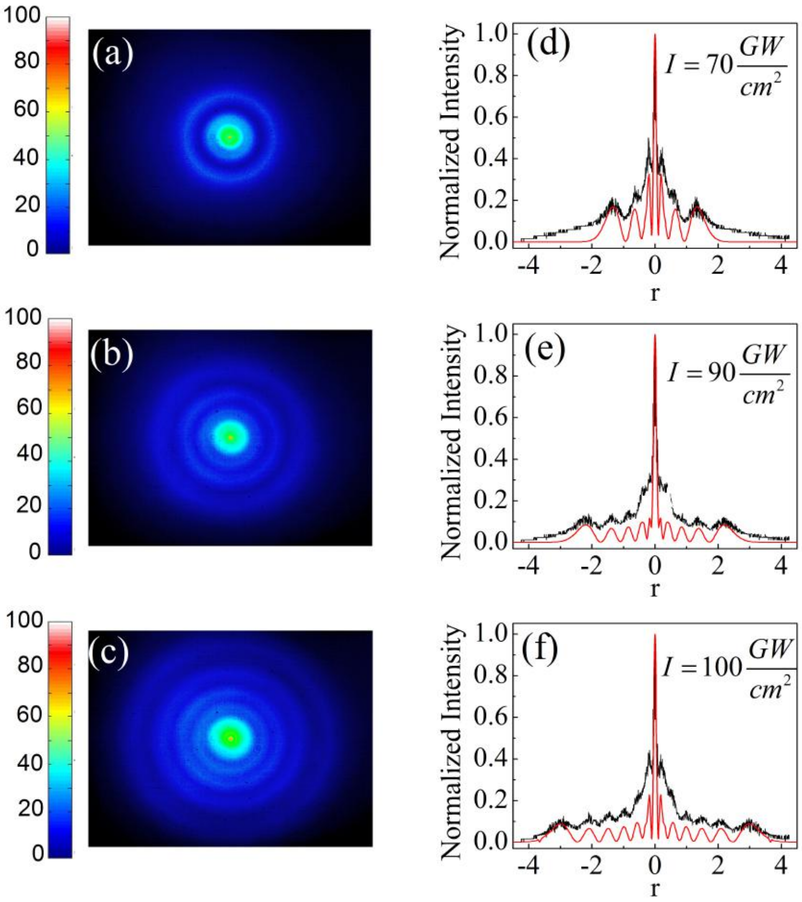

Figure 4.10 Diffraction patterns of a Gaussian beam induced by a NL medium dominated by quintic refractive nonlinearity, placed in the focal plane. Laser peak intensities: (a, d) 70 GW/ cm^2, (b, e) 90 GW/ cm^2 and (c, f) 100 GW/ cm^2. The black lines in (c-f) represent the experimental intensity distribution versus the radial coordinates obtained from (a-c). The red lines were obtained by numerical simulation of Eq. 4.1 using the NL parameters determined in the Z-scan.

obtained from the Z-scan experiments $\left(n_{2,eff} = 0\right)$. A low-intensity background is observed in the experimental profile due to linear light scattering. Notice that the number of rings, their thickness and the spacing are in good agreement with the numerical results.

Figures 4.11(a) and 4.11(b) illustrate the SSPM effect in the sample A for $f = 1.6 \times 10^{-5}$. Notice that different diffraction patterns are observed when the sample is located of 0.3 mm before $(R < 0)$ and 0.3 mm after $(R > 0)$ the focal plane, respectively. The curves in Figs. 4.11(c)-(d) show that the analysis of the experimental images (black line) are consistent with the theoretical result (red line), for $R \approx \pm 0.4$ mm. The present experimental results are in agreement with the numerical results of [62] that predicted a far-field diffraction pattern formation that depends on the sign of the product between the wavefront curvature radius and the NL phase-shift induced in the sample. It is important to notice that diffraction patterns, due to HON, in absence of the third-order nonlinearity, are reported here for the first time, presenting good agreement with theoretical predictions.

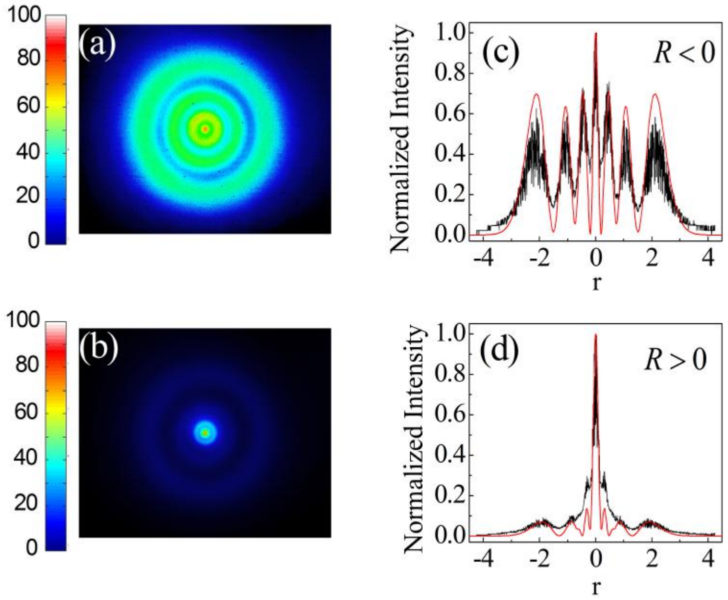

Figure 4.11 Diffraction patterns of a Gaussian beam induced by a NL medium dominated by quintic refractive nonlinearity, placed 0.3 mm (a) before and (b) after of the focal plane with laser peak intensity of 70 GW/ cm^2. Intensity distribution as a function of the radial coordinates considering (c) $R \approx -0.4$ mm ; (d) $R \approx +0.4$ mm . The red curves were obtained by numerical simulation of Eq. 4.1 using the NL parameters determined in the Z-scan experiments.

4.3.2 Spatial Modulation Instability

Spatial modulation instability is a common phenomenon in NL optics, which appears as a result of the exponential growth of small amplitude or phase perturbations, due to competition between nonlinearity and diffraction effects. In NL systems, SMI is strongly affected by various mechanisms such as: higher order dispersive terms [66], saturation of the nonlinearity [196], nonlocal nonlinearity [197, 198] and coherence properties of optical beams [199, 200]. This growth of spatial instability produces changes in the transverse beam profile, along its propagation, which may lead to a filamentation regime [95].

Of special interest is the study of SMI effect induced by HON, which was reported in theoretical works [201, 202, 203, 204]. In order to demonstrate experimentally this phenomenon, experiments of SXPM were mounted to analyze the response of the MDNCs managed to present cubic, quintic and septimal nonlinearities. The experimental setup is illustrated in Fig. 4.12. Here, the light exiting the laser, after passing through the pulse picker, $\lambda/2$ and Glan prism, was split into probe and pump beams with intensity ratio 1:10. The probe beam was weak in order to not induce NL changes in the beam profile. The pump and probe beams were aligned to counterpropagate along the sample (cell length: 5 cm) and a careful adjustment of the spatial and temporal overlap between the pulses was made. The pump (probe) beam waist was of ~ 100 μm (~ 80 μm) with Rayleigh length of ~ 8 cm (~ 5 cm). The beams' profiles, obtained at the exit face of the cell, were imagined in the CCD' plane by using a lens with focal length of 10 cm.

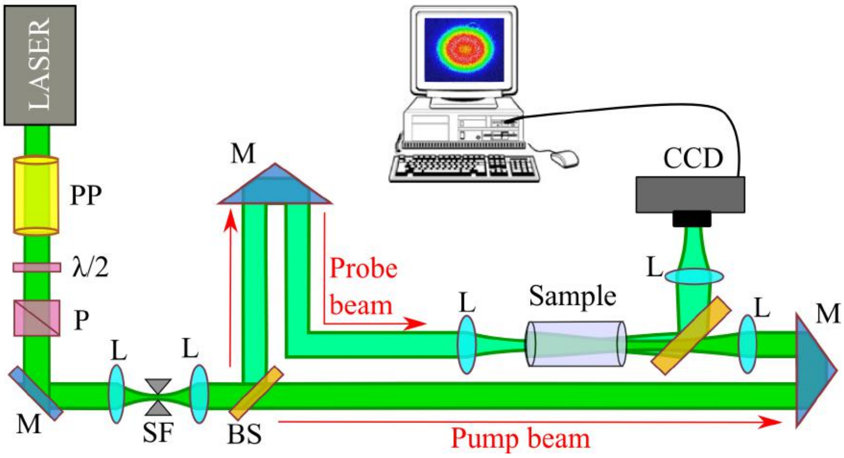

Figure 4.12 Experimental setup for the SXPM measurements in a counter-propagating pump-probe scheme. (PP) Pulse picker, (P) polarizer, (M) mirrors, (SF) spatial filter, (L) lenses and (BS) beam splitter.

Figure 4.13 shows the results of the transverse SMI induced by SXPM, for three volume fractions of silver NPs suspended in acetone (sample A). Due to the f values used, the three columns of Fig. 4.13 correspond to a refractive cubic medium $\left(f = 0.5 \times 10^{-5}\right)$, refractive quintic medium $\left(f = 1.6 \times 10^{-5}\right)$ and cubic-quintic medium $\left(f = 2.5 \times 10^{-5}\right)$, respectively. Septimal nonlinearities were neglected due to the low incident intensity ($I_{pump} = 2$ GW/cm^2). Figs. 4.13(a)-(c) display the probe transverse beam profiles, after crossing the NL sample, in presence of the pump beam. The amplitude of the signal shown in Fig. 4.13(b) is approximately threefold smaller than the signals corresponding to 4.13(a) and 4.13(c) because it is due to the quintic nonlinearity only. We analyzed the spatial profile of the probe beam as an intensity matrix; the curves in Figs. 4.13(d)-(f) represent column matrix components passing through the axis of the probe beam exhibiting the beam intensity versus the radial coordinate. Here, it is clearly appreciated two features associated to the HON that induces SXPM and SMI effects. The first one is the difference in the beam spot size, which is expected because the contributions of cubic [Fig. 4.13(a)] and quintic nonlinearities [Fig. 4.13(b) and 4.13(c)] have opposite signs. While the second feature refers to the formation of new spatial frequencies induced by SMI effect, that can be identified by the decline formed in the center of the probe beam profile [Fig. 4.13(b) and Fig. 4.13(c)]. Figs. 4.13(g)-(i) are the result of numerical simulations based on two-coupled NLSE considering the contributions of cubic and quintic nonlinearities, for each sample, as shown in Eqs. 4.2 and 4.3. The experimental results show excellent agreement with the numerical analysis. It is important to emphasize that the experimental results shown in Fig. 4.13 represent a demonstration of SMI due to the fifth-order susceptibility in a system with $n_{2,eff} = 0$ and $n_{4,eff} \neq 0$, which has not been demonstrated so far. All numerical simulations of this section were initiated with a Gaussian beam whose field is described by Eq. 2.54.

Another experiment was performed with colloids containing silver NPs suspended in CS_2 (sample B), in order to observe and analyze the SXPM and SMI effects induced by septimal nonlinearities. In this case, adjustable displacements between the centers of the incident pump

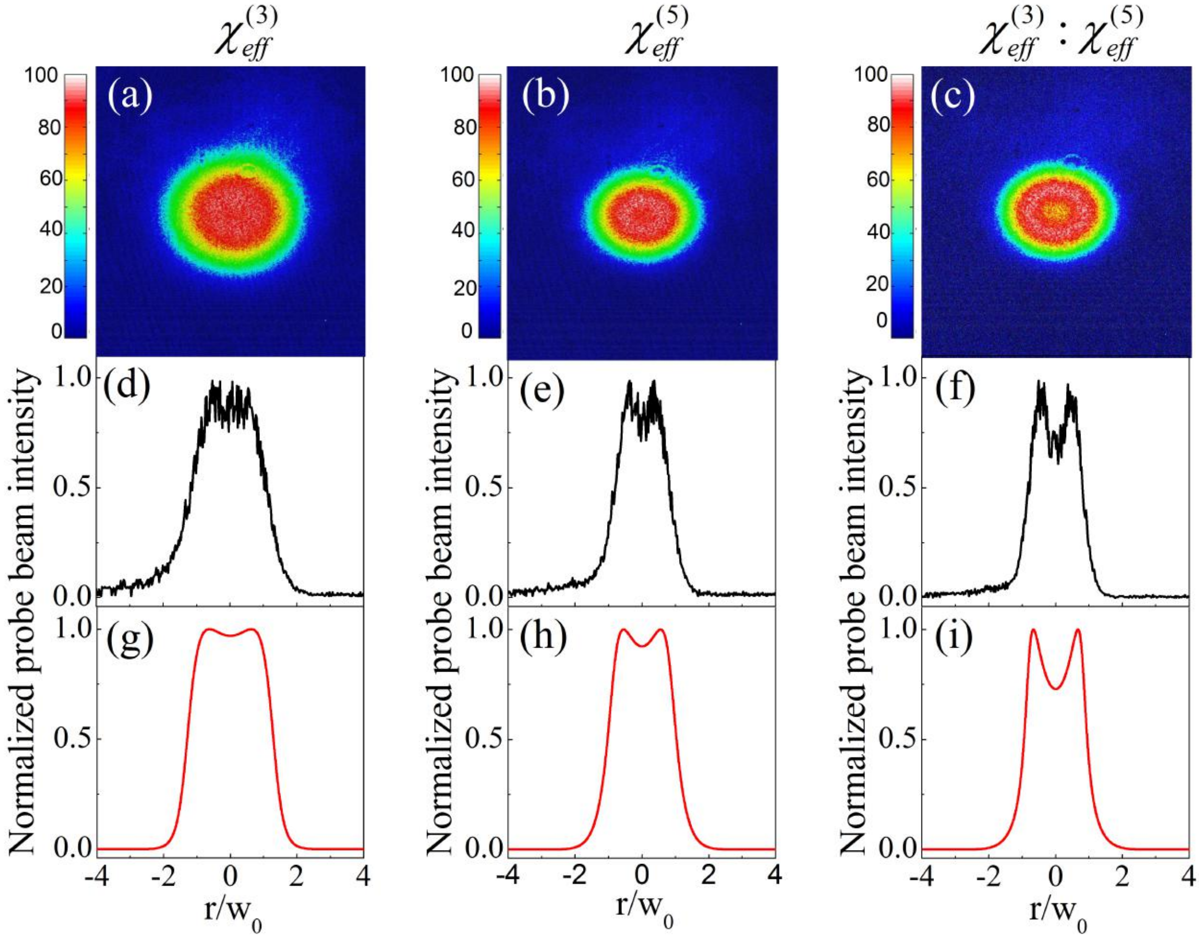

Figure 4.13 Probe beam profile in the presence of the counterpropagating pump beam: (a) $f_1 = 0.5 \times 10^{-5}$; (b) $f_2 = 1.6 \times 10^{-5}$; (c) $f_3 = 2.5 \times 10^{-5}$. Probe beam intensity versus the radial coordinate: (d) f_1; (e) f_2; (f) f_3. Numerical results using the values of $n_{2,eff}$ and $n_{4,eff}$ determined in the Z-scan experiments for sample A (silver NPs suspended in acetone) for each f as in (d)–(f). Pump beam intensity: 2.0 GW/cm^2; probe beam intensity: 0.2 GW/cm^2.

and probe beams were produced to characterize the local influence of the SXPM induced by the pump beam. To obtain a refractive septimal medium, due to destructive interference between the cubic and quintic nonlinearities, the sample B was prepared with $f = 3.3 \times 10^{-5}$ and the pump beam intensity used in the SXPM experiments was of 0.1 GW/cm^2. Here, the probe-to-pump intensities ratio was also of 1:10 to ensure that the NL phase shift is due to the pump beam only.

Figure 4.14 shows the pump beam profile after propagation through the refractive septimal medium . Figure 4.14(a) exhibits the beam profile at the far-field region for $I_{pump} = 10^6$ W/cm^2, while Fig. 4.14(b) shows the spatial broadening by a factor of ~ 2, for $I_{pump} = 10^8$ W/cm^2, due to $n_{6,eff} = -1.1 \times 10^{-30}$ cm^6/W^3. Figure 4.14(c) shows the intensity distribution of the pump beam transverse profile (black lines), obtained from Figs. 4.14(a)-(b). The red and blue lines correspond to the calculated profile for pump intensity of 10^6 W/cm^2(linear regime) and 10^8

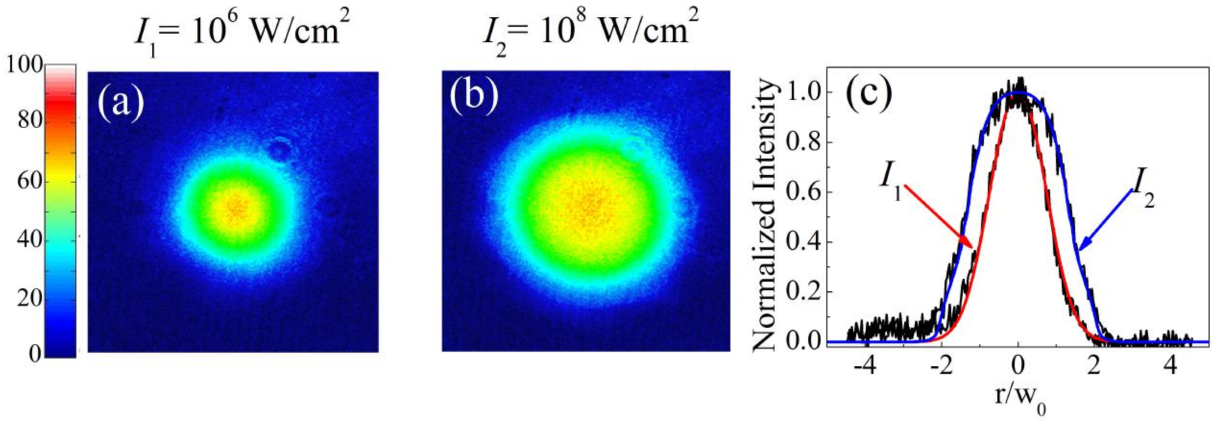

Figure 4.14 Pump beam profile after propagation through sample B (silver NPs suspended in CS_2), for $f = 3.3 \times 10^{-5}$: (a) $I_1 = 10^6$ W/cm^2 ; (b) $I_2 = 10^8$ W/cm^2. (c) Self-defocusing traces due to $\chi^{(7)}_{eff}$ obtained from (a) and (b). The red and blue lines are theoretical results for the respective intensities.

W/cm^2 (NL regime), respectively, by using the Eq. 4.2 considering $A_2 = 0$.

The XPM effects due to $\chi^{(7)}_{eff}$ were also studied by changing the relative distance (x/w_0) between the centers of the incident pump and probe beams. Figures 4.15(a)-(c) shows the experimental probe beam profiles after propagation through a refractive septimal medium (sample B with $f = 3.3 \times 10^{-5}$), in presence of pump beam, $I_{pump} = 10^8$ W/cm^2, for different values of relative distance (x/w_0). The pink and white lines represent the positions of incident probe and pump beams, respectively. Black lines in Fig. 4.15(d)-(f) correspond to the intensity profiles of the probe beam in the presence of the pump beam, obtained from Fig. 4.15(a)-(c), respectively. Dashed red lines represent the output probe beam profiles in absence of the pump beam, i.e. the probe beam being affected only by the linear diffraction. Figs. 4.15(a) and 4.15(d), corresponding to the total spatial overlap of the beams, show the generation of new spatial frequencies, in analogy with Fig. 4.13(b)-(c), but induced by septimal nonlinearities. Notice in particular a partial focusing of the probe beam induced by the pump beam, in the position of beams overlap, although the sample presents negative value of $n_{6,eff}$ [Figs. 4.15(b), (e) and 4.15(c), (f)]. This effect is analogous to the third-order induced focusing effect reported in [67] where the sample presented a cubic self-defocusing behavior at the laser frequency used.

The experimental results of SXPM-induced transverse SMI are understand by modeling the propagation, in opposite directions, of the probe and pump beams using the two-coupled NLSE considering the NL contributions up to the seventh-order, given by:

$$\begin{aligned}
-2ik\frac{\partial A_1}{\partial z} + \nabla^2_{\perp} A_1 = -\frac{\omega^2}{c^2} \Big[& 3\chi^{(3)}_{eff} \left(|A_1|^2 + 2|A_2|^2 \right) A_1 \\
& + 10\chi^{(5)}_{eff} \left(|A_1|^4 + 6|A_1|^2 |A_2|^2 + 3|A_2|^4 \right) A_1 \\
& + 35\chi^{(7)}_{eff} \left(|A_1|^6 + 18|A_1|^2 |A_2|^4 + 12|A_1|^4 |A_2|^2 + 4|A_2|^6 \right) A_1 \Big],
\end{aligned} \tag{4.2}$$

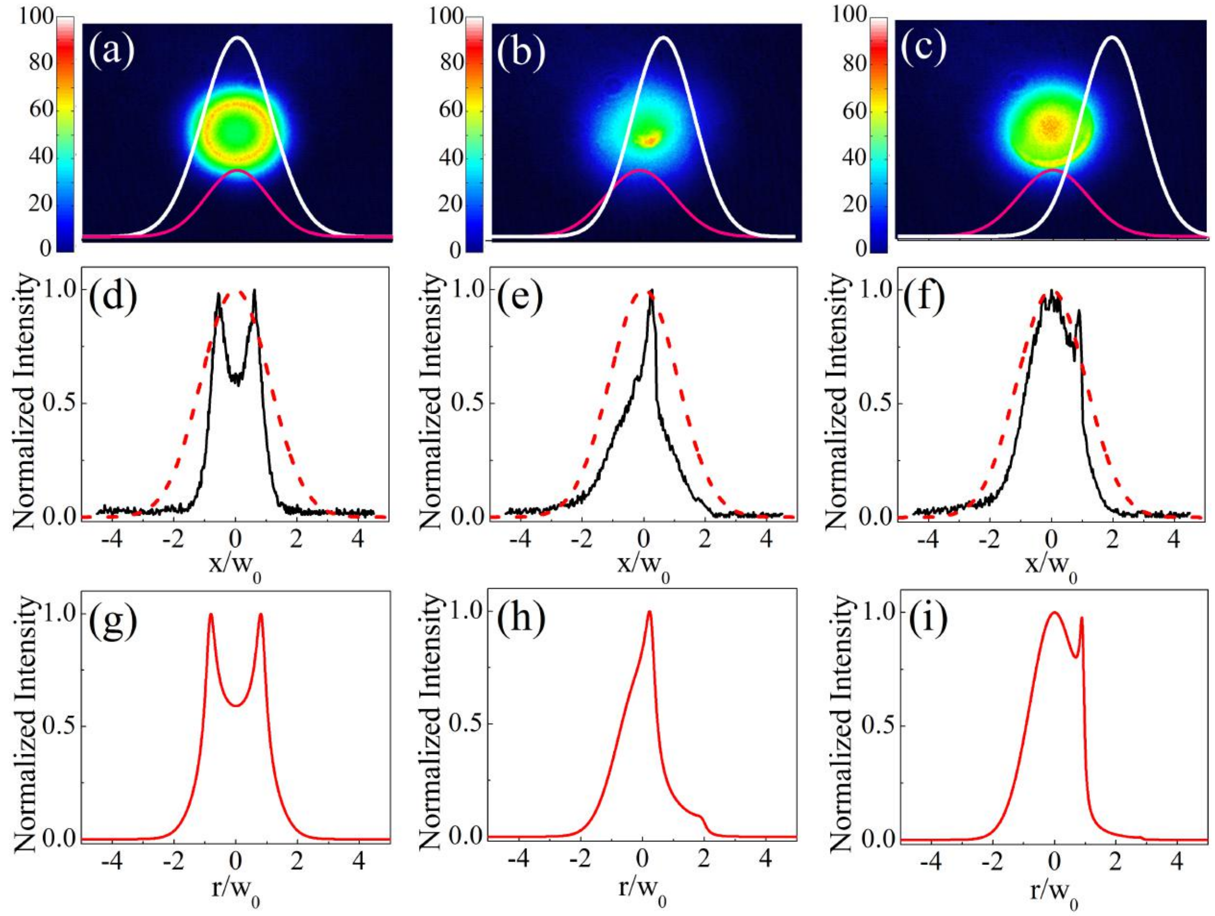

Figure 4.15 Experimental probe beam profile due to $\chi^{(7)}_{eff}$ for a distance of (a) $x = 0$; (b) $x = w_0$ and (c) $x = 2.2w_0$ between the centers of the incident pump (white line) and probe (pink line) beams; (d)-(f) Normalized intensity distribution of the probe beam transverse profile without the pump beam (red dashed line) and with the pump beam (black line); (g)-(i) Theoretical probe beam profile calculated using Eqs. 4.2 and 4.3 with the NL coefficients determined in the Z-scan experiments for the relative distances of (a)-(c). Pump beam intensity: 10^8 W/cm^2; probe beam intensity: 10^7 W/cm^2.

$$\begin{aligned} 2ik\frac{\partial A_2}{\partial z} + \nabla^2_{\perp} A_2 = -\frac{\omega^2}{c^2} \Big[& 3\chi^{(3)}_{eff}\left(2|A_1|^2 + |A_2|^2\right) A_2 \\ & + 10\chi^{(5)}_{eff}\left(3|A_1|^4 + 6|A_1|^2|A_2|^2 + |A_2|^4\right) A_2 \\ & + 35\chi^{(7)}_{eff}\left(4|A_1|^6 + 12|A_1|^2|A_2|^4 + 18|A_1|^4|A_2|^2 + |A_2|^6\right) A_2 \Big], \end{aligned} \quad (4.3)$$

where A_1 and A_2 are the optical field amplitudes of the pump and probe beams, respectively; $\nabla^2_{\perp} = \frac{\partial^2}{\partial x^2} + \frac{\partial^2}{\partial y^2}$ is the transverse Laplacian operator, ω is the laser frequency and c is the speed of light in vacuum. The values of $\chi^{(3)}_{eff}$, $\chi^{(5)}_{eff}$ and $\chi^{(7)}_{eff}$, for each volume fraction f, is obtained by using the generalized Maxwell-Garnett model considering the measures carried out using the Z-scan technique. Details on the deduction of cubic-quintic-septimal NLSE are given in Section 5.3.1. However, as in this section are described experiments based on the propagation of two counterpropagating and linearly polarized beams, then the total incident field can be expressed by:

$$\vec{E}\left(\vec{r},t\right)=\frac{1}{2}\hat{x}\sum_{j=1}^{2}A_{j}\left(\vec{r},t\right)exp\left[i\left(\left(-1\right)^{j}k_{0}z-\omega t\right)\right]+c.c. \tag{4.4}$$

Equations 4.2 and 4.3 were obtained by introducing Eq. 4.4 into the wave equation [Eq. 5.11] and follow the same procedure described in Section 5.3.

Figures 4.15(g)-(i) show the theoretical probe beam transverse profile, obtained from Eqs. 4.2 and 4.3, using the NL parameters measured in the Z-scan experiments ($n_{2,eff}=n_{4,eff}=0$ and $n_{6,eff}=-1.1\times10^{-30}$ cm^6/W^3) when $f=3.3\times10^{-5}$, $I_{probe}=10^7$ W/cm^2 and $I_{pump}=10^8$ W/cm^2. A good agreement is observed between experimental and theoretical results that support the given interpretation.

In this way, the experimental and numerical results of Figs. 4.13 and 4.15 allow to recognize the importance of the HON on the SMI effect. These interesting results were possible thanks to the application of the NM procedure, which consist of a simple, but effective, way to control the NL response of MDNCs. In addition, several applications of HON contributions become extremely attractive, since the SMI effect has important connections with numerous NL processes. A particular example is the spatial soliton, which is discussed in Chapters 6 and 7. The relation between SMI and spatial solitons is manifested in the fact that the filaments that emerge from the SMI process have the behavior of solitary waves that travel without suffering deformation [198]. Therefore, at first instance, SMI can be considered to be a precursor of the spatial solitons.

4.3.3 Metal-Dielectric Nanocomposites in All-Optical Switches

The rapid increase in global communications networks requires data processing devices ever faster. This need motivates the development of the all-optical devices (AODs), allowing the processing of signals at bit rates from hundreds of GB/s up to 1 TB/s [205]. To achieve very high data processing speeds, these ultrafast devices exploit the strong NL interaction between the light and highly NL materials. For this reason, the choice of suitable NL material is extremely important to achieve the proper performance of an AOD. Among the main physical systems of interest, MDNCs deserve special attention due to their high optical susceptibility, ultrafast response and the possibility of changing their NL susceptibility by changing the NPs volume fraction. However, the presence of large NL absorption limits their applications in devices such as all-optical switches (AOS) . This problem is common to all materials with large nonlinearity, since that large NL refractive index corresponds to large NL absorption coefficients [206], and therefore it becomes difficult to find proper materials for efficient AOS. To circumvent this problem, two figures-of-merit for AOS are considered: $T=\left|\alpha_{2,eff}\lambda\left(n_{2,eff}\right)^{-1}\right|$ and $W=\left|\triangle n\left(\alpha_{0}\lambda\right)^{-1}\right|$, where λ is the laser wavelength, α_0 is the linear absorption coefficient, $\alpha_{2,eff}\propto Im\chi_{eff}^{(3)}$ is the two-photon absorption coefficient, $n_{2,eff}\propto Re\chi_{eff}^{(3)}$ is the third-order refractive index and $\triangle n$ is the maximum variation of the refractive index that can be induced in the material [207, 208]. In order to obtain efficient AOSs, it is required that $T<1$ and $W>1$.

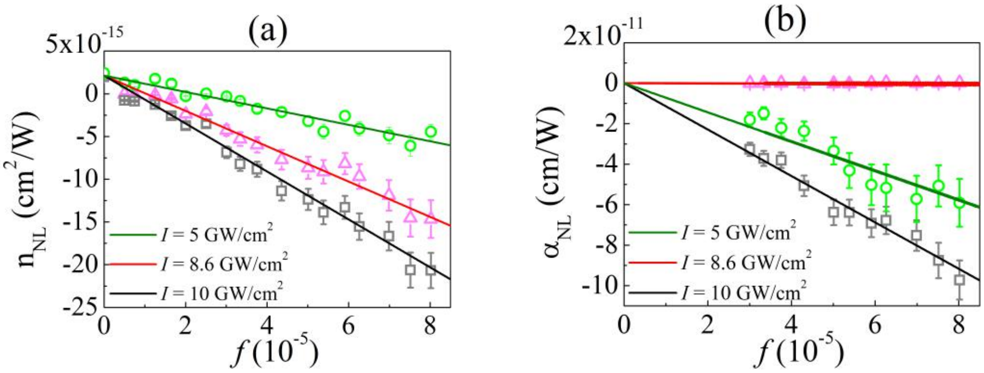

Figure 4.16 Dependence with the NPs volume fraction of the total effective (a) NL refractive index and (d) NL absorption coefficient, for different intensities, corresponding to sample A.

In this Section we applied the NM procedure of MDNCs in order to demonstrate the optimization of AOS in proof-of-principle experiments with silver colloids. However, as MDNCs present HON, it was necessary to redefine one of the figures-of-merit by: $T' = \left|\alpha_{NL}\lambda\left(n_{NL}\right)^{-1}\right|$, where $n_{NL} = n_2^{eff} + n_4^{eff} I + n_6^{eff} I^2$ and $\alpha_{NL} = \alpha_2^{eff} + \alpha_4^{eff} I + \alpha_6^{eff} I^2$. Fig. 4.16(a) and 4.16(b) show the linear dependence of the total effective NL refractive index, n_{NL}, and total effective NL absorption coefficient, α_{NL}, with f, for different intensities, corresponding to sample A. For NL refraction, it is possible to observe that the magnitude of n_{NL} increases while increasing the laser intensity. Nevertheless, for the NL absorption, α_{NL} reaches a minimum value for intensity of 8.6 GW/cm^2. The solid lines were obtained using the generalized Maxwell-Garnett model, as discussed above. These behaviors can be corroborated with the CA and OA Z-scan curves. Figures 4.17(a) and 4.17(b) show the CA and OA Z-scan profiles for sample A with the same intensities as in Figs. 4.16(a) and 4.16(b), where $f = 5.9 \times 10^{-5}$. Cancellation of NL absorption in Fig. 4.16(b) is due to destructive interference between the imaginary parts of the third-, fifth- and seventh-order susceptibilities. Therefore, the results of Figs. 4.16 and 4.17 show that using the NM procedure, which consists in controlling the NL response of a MDNC by selecting appropriate values of f and I, it is possible to obtain large n_{NL} and small

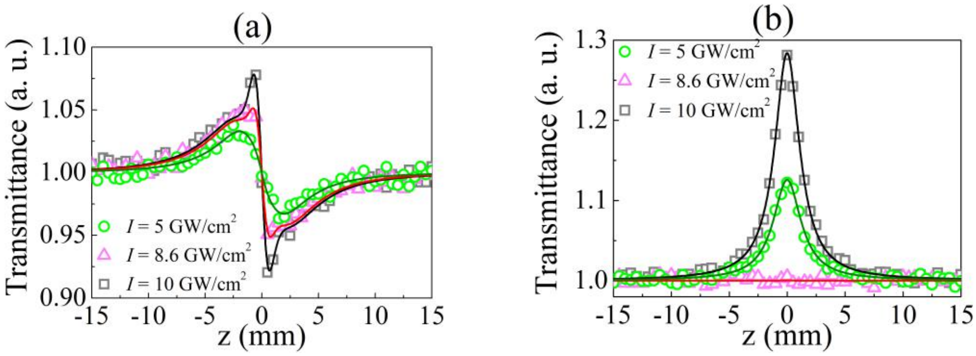

Figure 4.17 Normalized (e) *Closed-aperture* and (f) *Open-aperture* Z-scan profiles for sample A with $f = 5.9 \times 10^{-5}$, obtained for different laser peak intensities.

α_{NL} simultaneously.

From these new NL parameters, it is possible to calculate the figures-of-merit W and T'. However, for better visualization of the results we plotted $(T')^{-1}$ instead of T'. Figure 4.18(a) shows W versus f for intensities between 7.0 and 10 GW/cm^2. The dependence of $\triangle n$ and α_0 with f was considered. For example for $f = 5.9 \times 10^{-5}$ the values of $\triangle n \approx 10^{-4}$ and $\alpha_0 = 0.06$ mm^{-1} were used. Then, $W > 1$ was obtained for intensities larger than 7.0 GW/cm^2. Figure 4.18(b) shows $(T')^{-1}$ versus f. Notice, for instance, that for 10 GW/cm^2 we obtained $(T')^{-1} \approx 3$ corresponding to $f > 2.0 \times 10^{-5}$, while for 8.6 GW/cm^2 the value of $(T')^{-1}$ increases by about two orders of magnitude.

For a more detailed evaluation, Table 4.1 gives the values of the NL parameters for particular choices of f, laser intensity and the corresponding figures-of-merit for AOS. Notice that the values of n_{NL} increase by approximately a factor of 3 for an increase of f from 3.0×10^{-5} to 8.0×10^{-5}, for a constant intensity. However, a dramatic variation of α_{NL}, which produces a significant reduction of the figure of merit T', is observed for small variations in intensity and fixed value of f. The very small values of α_{NL}, for $I_0 = 8.6$ GW/cm^2, were obtained due to the cancelling contributions between the contributions of negative $\alpha_{2,eff}$ and $\alpha_{6,eff}$ with positive $\alpha_{4,eff}$. Therefore, metal-colloids with appropriate values of f and laser intensity may present optimal figures-of-merit for all-optical switching.

It is important to consider that the use of MDNCs in AOS is possible since it is found that the metal-colloids have a fast NL response. To corroborate this condition in our samples, a Kerr shutter experiment was conducted using the same light source. The experimental setup is shown in Fig. 4.19 and details on its principle of operation are discussed in Appendix A. The laser beam was split into probe and pump beams with relative intensities: $I_{probe} = 0.1 I_{pump}$. The angle between the beams was 2.3° and the angle between their electric fields was 45°. Both beams were focused inside the sample by a 10 cm focal length lens. When the two beams overlap spatially and temporally inside the sample, the pump beam induces a NL birefringence that produces rotation of the probe beam electric field. Then, a fraction of the transmitted I_{probe} by the sample passes through a polarizer crossed to the input probe beam electric field. A detector was used to record the transmitted I_{probe} versus the delay time, τ, between the pump and probe pulses. Liquid CS_2 was also the reference standard for calibration of the

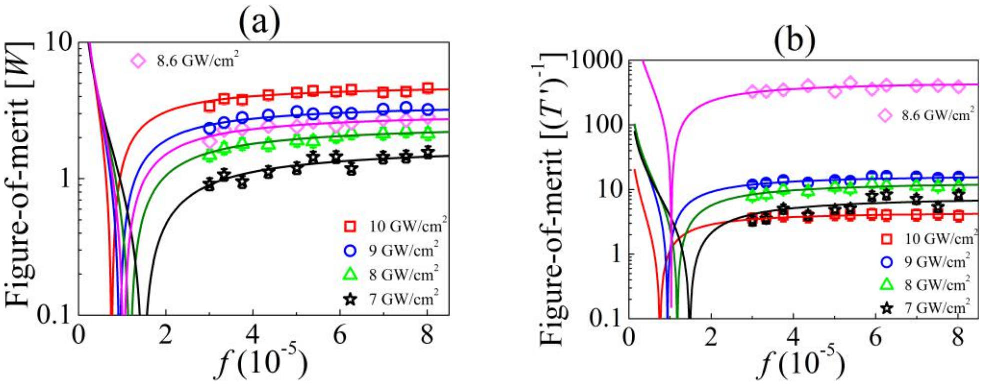

Figure 4.18 Figures-of-merit for all-optical switching.

f $(\times 10^{-5})$	I_0 (GW/cm^2)	n_{NL} $(\times 10^{-15} cm^2/\mathrm{W})$	α_{NL} $(\times 10^{-11}\mathrm{cm/W})$	W	T
3.0	7.0	-2.04	-1.16	0.91	0.30
	8.6	-4.28	-1.75×10^{-3}	1.87	3.07×10^{-3}
	10.0	-6.85	-3.27	3.39	0.28
3.8	7.0	-3.56	-1.33	0.95	0.20
	8.6	-5.98	-3.75×10^{-3}	2.32	2.87×10^{-3}
	10.0	-8.84	-3.81	3.79	0.25
5.9	7.0	-4.94	-0.91	1.45	0.13
	8.6	-8.19	-3.72×10^{-3}	2.45	2.80×10^{-3}
	10.0	-13.30	-6.92	4.34	0.24
8.0	7.0	-7.47	-1.61	1.56	0.12
	8.6	-14.68	-3.68×10^{-3}	2.83	2.85×10^{-3}
	10.0	-20.68	-9.72	4.62	0.25

Table 4.1 NPs volume fraction, f, laser intensity, I, and the corresponding total NL refractive indices, n_{NL}, total NL absorption coefficients, α_{NL}, and figures-of-merit (W and T).

measurements.

Figure 4.20(a) shows the Kerr shutter signals for sample A with $f = 5.9 \times 10^{-5}$ and pump intensities equal to 10 , 8.6 , 8.0 , and 7.0 GW/cm^2. The symmetric profiles are due to the fast NL response of the free electrons in the NPs. Similar behavior was observed for other values of f. The inset of Fig. 4.20(a) shows the CS_2 signal that exhibits asymmetry with respect to τ due to molecular reorientation. The result for CS_2 is shown to illustrate the fast temporal response of the apparatus. The signal for pure acetone is smaller than our detection limit.

Figure 4.20(b) shows a polynomial dependence of $\triangle T/I_{pump}$ versus I_{pump} (red line) due to HON. For $I_{pump} \leq 4$ GW/cm^2 the ratio $\triangle T/I_{pump}$ is constant and the signal is properly

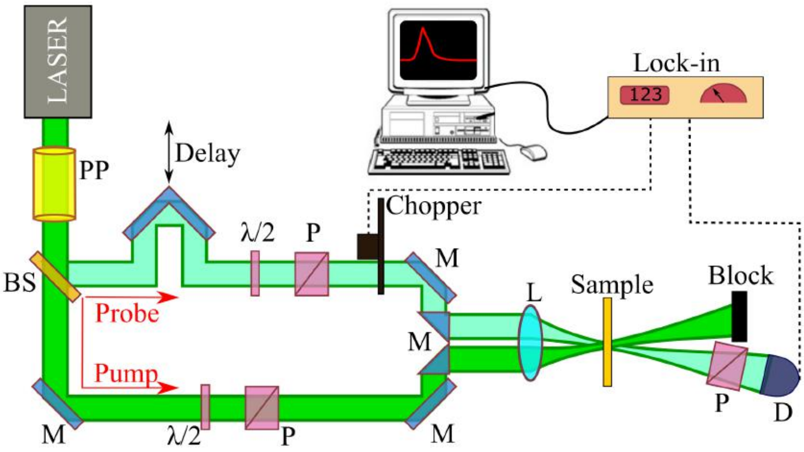

Figure 4.19 Experimental setup of the Kerr shutter technique. (PP) Pulse picker, (P) polarizer, (M) mirrors, (L) lens, (BS) beam splitter and (D) fast detector.

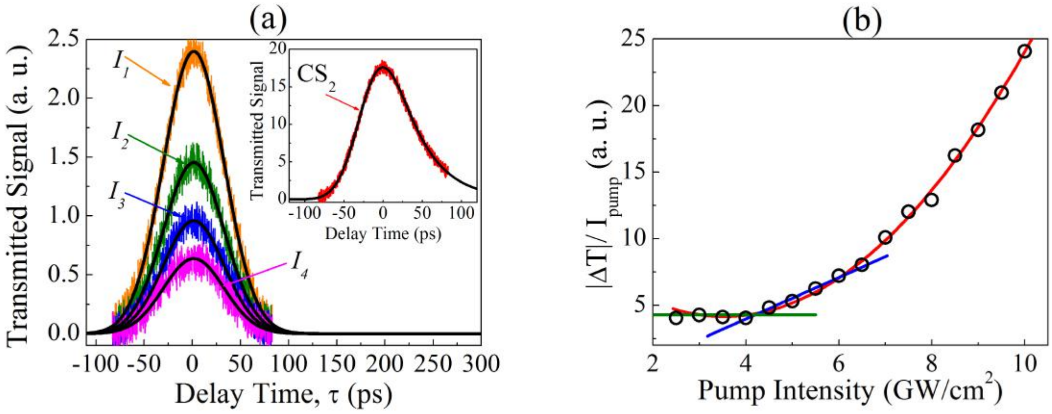

Figure 4.20 (a) Transmitted Kerr signal in 532 nm for silver colloid for pump intensities of: $I_1 = 10\,\mathrm{GW/c}m^2$, $I_2 = 8.6\,\mathrm{GW/c}m^2$, $I_3 = 8.0\,\mathrm{GW/c}m^2$ and $I_4 = 7\,\mathrm{GW/c}m^2$ and $I_{probe} = 0.1\,(I_{pump})$. The inset is the Kerr signal for CS_2. (b) Dependence of $\triangle T/I_{pump}$ as a function of the pump intensity. Volume fraction: $f = 5.9 \times 10^{-5}$. Solid lines are guides to the eyes.

described by $n_{2,eff}$. For $4\,\mathrm{GW/c}m^2 < I_{pump} \leq 7\,\mathrm{GW/c}m^2$ the ratio pump $\triangle T/I_{pump}$ presents linear dependence with I_{pump} and the slope of the straight line is related to $n_{4,eff}$. For $I_{pump} > 7\,\mathrm{GW/c}m^2$ the contribution of $n_{6,eff}$ becomes relevant, in analogy with the Z-scan results.

Therefore, it was demonstrated that MDNCs have a fast NL response, of the order of picoseconds (which was limited by the pulse duration time), and that the NM procedure applied on them can be much useful for the fabrication of efficient AOS.

The only thing that we keep under control, is the illusion that we have
control over something.
- UNKNOWN

5 LIGHT PROPAGATION IN NONLINEAR MEDIA

5.1 INTRODUCTION

The spatiotemporal evolution of light in NL media is one of the main fields of study of NL optics. In principle, the characteristics of the EMFs and behavior of light are governed by Maxwell's equations. From them a wave equation can be deduced, in a very simple and straightforward way, to describe the essential propagation characteristics of light. In particular, light propagation in NL media is modeled by the well known NL Schrödinger equation (NLSE), which allows to know the step-by-step evolution of optical fields being affected by the NL parameters of the medium (NL refraction, NL absorption, NL dispersion, among others). However, the NLSE can take different forms depending on the type of medium nonlinearity and the type of phenomenon that it is intended to be described. In this chapter, the NLSE including contributions of HON is deduced starting from Maxwell's equations. Two special cases of the NLSE are developed to model the light propagation in MDNCs and CS_2, in picosecond and femtosecond regimes, in order to be applied in the study of spatial solitons. A description of the analytical variational technique is also introduced to obtain approximate solutions of the NLSE and to analyze the stability and instability regimes of spatial solitons propagation. In addition, a model to describe the evolution of the light polarization state in a capillary is developed considering the contributions of the third- and fifth-order susceptibilities. All theoretical models introduced and discussed here are extremely important to corroborate the experimental results observed in the next chapters.

5.2 MAXWELL'S EQUATION AND THE WAVE EQUATION

Similarly to all electromagnetic phenomena, the light propagation in a NL medium is also governed by Maxwell's equations. By assuming a dielectric medium with no free charges $(\rho = 0)$ and currents $\left(\overrightarrow{J} = 0\right)$, we can write:

$$\overrightarrow{\nabla} \cdot \overrightarrow{D} = 0, \tag{5.1}$$

$$\overrightarrow{\nabla} \cdot \overrightarrow{B} = 0, \tag{5.2}$$

$$\overrightarrow{\nabla} \times \overrightarrow{E} = -\frac{\partial \overrightarrow{B}}{\partial t}, \tag{5.3}$$

$$\overrightarrow{\nabla} \times \overrightarrow{H} = -\frac{\partial \overrightarrow{D}}{\partial t}, \tag{5.4}$$

where $\overrightarrow{E}$ and $\overrightarrow{H}$ are the electric and magnetic field vectors, respectively; $\overrightarrow{D}$ is the electric displacement vector and $\overrightarrow{B}$ is the vector magnetic flux density. $\overrightarrow{\nabla} = \hat{x}\partial/\partial x + \hat{y}\partial/\partial y + \hat{z}\partial/\partial z$ is the differential nabla operator.

Vectors $\overrightarrow{D}$ and $\overrightarrow{B}$ originate from the response of the medium to electric and magnetic fields $\overrightarrow{E}$ and $\overrightarrow{H}$, respectively, and are connected with them through the following constitutive relations:

$$\overrightarrow{D} = \varepsilon_0 \overrightarrow{E} + \overrightarrow{P}, \tag{5.5}$$

$$\overrightarrow{B} = \mu_0 \overrightarrow{H} + \overrightarrow{M}, \tag{5.6}$$

where μ_0 is the magnetic vacuum permeability, $\overrightarrow{P}$ and $\overrightarrow{M}$ are the induced electric and magnetic polarizations, respectively.

For nonmagnetic dielectric media, we have $\left(\overrightarrow{M} = 0\right)$, and by considering that the nonlinearity of the medium is included over the constitutive relation given by Eq. 5.5, the polarization can be separated in linear and NL contributions, making $\overrightarrow{P} = \overrightarrow{P}^{(L)} + \overrightarrow{P}^{(NL)}$. Then, it is possible to rewrite the electric displacement vector as follows:

$$\begin{aligned} \overrightarrow{D} &= \varepsilon_0 \overrightarrow{E} + \overrightarrow{P}^{(L)} + \overrightarrow{P}^{(NL)}, \\ \overrightarrow{D} &= \overrightarrow{D}^{(L)} + \overrightarrow{P}^{(NL)}, \end{aligned} \tag{5.7}$$

where $\overrightarrow{D}^{(L)} = \varepsilon \overrightarrow{E}$ is the linear part of the electric displacement vector, with $\varepsilon = \varepsilon_0 \left(1 + \chi^{(1)}\right)$ being the linear permittivity tensor of the medium

Using Maxwell's equations, it is possible to obtain the wave equation which describes the light propagation in a NL medium. By following the standard procedure to obtain the wave equation, we take the curl of Eq. 5.3, then we change the order of the spatial and temporal derivatives on the right side of the resulting equation, and by using Eqs. 5.6 and 5.4, we get:

$$\overrightarrow{\nabla} \times \overrightarrow{\nabla} \times \overrightarrow{E} + \mu_0 \frac{\partial^2 \overrightarrow{D}}{\partial t^2} = 0. \tag{5.8}$$

Substituting the value of $\overrightarrow{D}$ by Eq. 5.7 and using the vector identity $\overrightarrow{\nabla} \times \overrightarrow{\nabla} \times \overrightarrow{E} = \overrightarrow{\nabla}\left(\overrightarrow{\nabla} \cdot \overrightarrow{E}\right) - \overrightarrow{\nabla}^2 \overrightarrow{E}$, we can rewrite the previous equation as:

$$\overrightarrow{\nabla}\left(\overrightarrow{\nabla} \cdot \overrightarrow{E}\right) - \overrightarrow{\nabla}^2 \overrightarrow{E} + \frac{1}{\varepsilon_0 c^2} \frac{\partial^2 \overrightarrow{D}^{(L)}}{\partial t^2} = -\frac{1}{\varepsilon_0 c^2} \frac{\partial^2 \overrightarrow{P}^{(NL)}}{\partial t^2}, \tag{5.9}$$

where $c = (\mu_0 \varepsilon_0)^{-1/2}$ is the light speed in the vacuum. Eq. 5.9 is the most general form of the wave equation used in NL optics. Nevertheless, by neglecting the first term on the left side, which is common in most cases of interest in NL optics, for example when $\overrightarrow{E}$ is described as a transverse plane wave, this term vanishes. Thus, we can write the wave equation as follows:

$$-\overrightarrow{\nabla}^2 \overrightarrow{E} + \frac{1}{\varepsilon_0 c^2} \frac{\partial^2 \overrightarrow{D}^{(L)}}{\partial t^2} = -\frac{1}{\varepsilon_0 c^2} \frac{\partial^2 \overrightarrow{P}^{(NL)}}{\partial t^2}. \tag{5.10}$$

For the simplest case, of a NL isotropic medium without loss and without dispersion $\left(\overrightarrow{D}^{(L)} = \varepsilon_0 \varepsilon^{(L)} \overrightarrow{E}\right)$, the wave equation takes the following form:

$$-\overrightarrow{\nabla}^2 \overrightarrow{E} + \frac{\varepsilon^{(L)}}{c^2} \frac{\partial^2 \overrightarrow{E}}{\partial t^2} = -\frac{1}{\varepsilon_0 c^2} \frac{\partial^2 \overrightarrow{P}^{(NL)}}{\partial t^2}, \tag{5.11}$$

where $\varepsilon^{(L)}$is the dimensionless relative permittivity which is different for each material. Here, it can be seen that Eq. 5.11 has the form of an inhomogeneous wave equation, where the NL polarization acts as a source of new frequency components of the EMF.

5.3 NONLINEAR SCHRÖDINGER EQUATION FOR HON

NLSE, commonly used to model the light propagation in NL media, can be found by expressing the wave equation in the frequency domain $\left(\frac{\partial}{\partial t} \rightarrow i\omega\right)$ given by:

$$\left[\overrightarrow{\nabla}^2 + \frac{\omega^2}{c^2}\left(1 + \chi^{(1)}\right)\right] \overrightarrow{E}(\omega) = -\mu_0 \omega^2 \overrightarrow{P}^{(NL)}(\omega), \tag{5.12}$$

where it is assumed that the polarization response of the medium is instantaneous, i.e., $\overrightarrow{P}$ is determined only by the present conditions, there is no delayed response or memory effect in the system. Also, it should be recognized that the electric field has a time structure that has a slow and a fast varying component. The fast time scale corresponds to the optical cycle, which is order of $\lambda/c \sim 3$ fs. The slow time scale corresponds to the width of the pulse, being proportional to $\left|\overrightarrow{E}\right|^2$, which is typically 100 fs or much longer. Rarely do we have to deal with pulses less than 10 fs, where this separation of the time scales is not so clean anymore. Thus, the polarization, $\overrightarrow{P}$, and electric field, $\overrightarrow{E}$, propagating along the $z-$axis, with frequency ω_0 and associated to a wavevector $\vec{k}_0 = k_0 \hat{k}$, are given in the frequency domain by:

$$\overrightarrow{E}(\overrightarrow{r}, \omega) = \overrightarrow{A}(\overrightarrow{r}, \omega - \omega_0)\, exp[ik_0 z] + c.c., \tag{5.13}$$

$$\overrightarrow{P}(\overrightarrow{r}, \omega) = \overrightarrow{P}(\overrightarrow{r}, \omega - \omega_0)\, exp[ik_0 z] + c.c.. \tag{5.14}$$

From linear optics, it is known that in lossless media: $n_0^2(\omega) = 1 + \chi^{(1)}(\omega)$ and $k(\omega) = [\omega/c]\, n_0(\omega)$. Therefore:

$$\chi^{(1)}(\omega) = \frac{c^2 k^2(\omega)}{\omega^2} - 1. \tag{5.15}$$

Thus, using Eq. 5.15 is possible to write Eq. 5.12 of the form:

$$\left[\overrightarrow{\nabla}^2 + k^2(\omega)\right] \overrightarrow{E}(\omega) = -\mu_0 \omega^2 \overrightarrow{P}^{(NL)}(\omega), \tag{5.16}$$

which is known as the NL Helmholtz equation.

From here we assume that the field is polarized in a fixed direction in the plane perpendicular to the direction of propagation. In addition, by substituting Eqs. 5.13 and 5.14 in Eq. 5.16, we have:

$$\left[\frac{\partial^2}{\partial x^2}+\frac{\partial^2}{\partial y^2}+\frac{\partial^2}{\partial z^2}+2ik_0\frac{\partial}{\partial z}-k_0^2\right]A\left(\overrightarrow{r},\omega-\omega_0\right)$$
$$+k^2\left(\omega\right)A\left(\overrightarrow{r},\omega-\omega_0\right)=-\mu_0\omega^2P^{(NL)}\left(\overrightarrow{r},\omega-\omega_0\right). \qquad (5.17)$$

The first parenthesis groups all the spatial terms, the next term incorporates dispersion and the term on the right describes the NL corrections to this otherwise linear equation.

Moreover, we make the usually very well justified approximation that $k\left(\omega\right)$ is a reasonably slowly varying function of ω, such that it can be expanded in powers of ω as:

$$k\left(\omega\right)=k_0+k_1\left(\omega-\omega_0\right)+\frac{1}{2!}k_2\left(\omega-\omega_0\right)^2+\frac{1}{3!}k_3\left(\omega-\omega_0\right)^3+\cdots, \qquad (5.18)$$

where $k_0=n_0\omega_0/c$ is related to the phase velocity of light in the medium, $k_1=\left(dk/d\omega\right)_{\omega=\omega_0}$ is the inverse of the group velocity $\left(k_1=v_g^{-1}\right)$. $k_2=\left(d^2k/d\omega^2\right)_{\omega=\omega_0}$ is the second order dispersion and k_n gives the $n-$th order dispersion.

To return to the time domain, Eq. 5.17 is multiplied by $exp\left[-i(\omega-\omega_0)t\right]$ and integrated on ω. This results in:

$$\left[\frac{\partial^2}{\partial x^2}+\frac{\partial^2}{\partial y^2}+\frac{\partial^2}{\partial z^2}+2ik_0\frac{\partial}{\partial z}-k_0^2\right]A\left(\overrightarrow{r},t\right)$$
$$+\left[k_0+ik_1\frac{\partial}{\partial t}-\frac{1}{2}k_2\frac{\partial^2}{\partial t^2}+\ldots\right]^2A\left(\overrightarrow{r},t\right)=-\mu_0\left[\omega_0+i\frac{\partial}{\partial t}\right]^2P^{(NL)}\left(\overrightarrow{r},t\right). \qquad (5.19)$$

As a next step, we will make a reference frame transformation to that of the pulse, which propagates nominally at the group velocity (v_g): $(z,t)\rightarrow(z,\tau=t-z/v_g)$. Thus, the function that represents the optical pulse is described by $A'\left(\overrightarrow{r},\tau\right)$, where:

$$\frac{\partial}{\partial z}=\frac{\partial}{\partial z}+\frac{\partial}{\partial\tau}\frac{\partial\tau}{\partial z}=\frac{\partial}{\partial z}+\left(-\frac{1}{v_g}\right)\frac{\partial}{\partial\tau}=\frac{\partial}{\partial z}-k_1\frac{\partial}{\partial\tau}, \qquad (5.20)$$

$$\frac{\partial}{\partial t}=\frac{\partial}{\partial z}\frac{\partial z}{\partial\tau}+\frac{\partial}{\partial\tau}\frac{\partial\tau}{\partial t}=\frac{\partial}{\partial\tau}, \qquad (5.21)$$

$$\frac{\partial^2}{\partial z^2}=\left(\frac{\partial}{\partial z}-k_1\frac{\partial}{\partial\tau}\right)\left(\frac{\partial}{\partial z}-k_1\frac{\partial}{\partial\tau}\right)=\frac{\partial^2}{\partial z^2}-2k_1\frac{\partial}{\partial z}\frac{\partial}{\partial\tau}+k_1^2\frac{\partial^2}{\partial\tau^2}. \qquad (5.22)$$

Therefore, Eq. 5.19 can be rewrite in the new coordinates by:

$$\left[\frac{\partial^2}{\partial x^2}+\frac{\partial^2}{\partial y^2}+\frac{\partial^2}{\partial z^2}\right]A'\left(\overrightarrow{r},\tau\right)+2ik_0\left[1+i\frac{k_1}{k_0}\frac{\partial}{\partial\tau}\right]\frac{\partial}{\partial z}A'\left(\overrightarrow{r},\tau\right)$$
$$+\left[2k_0\left(1+i\frac{k_1}{k_0}\frac{\partial}{\partial\tau}\right)D+D^2\right]A'\left(\overrightarrow{r},\tau\right)=-\mu_0\omega_0^2\left(1+i\frac{1}{\omega_0}\frac{\partial}{\partial\tau}\right)^2P'^{(NL)}\left(\overrightarrow{r},\tau\right), \qquad (5.23)$$

with

$$D = \frac{1}{2!}k_2\left(i\frac{\partial}{\partial\tau}\right)^2 + \frac{1}{3!}k_3\left(i\frac{\partial}{\partial\tau}\right)^3 + \cdots. \tag{5.24}$$

Here, we will make several important approximations:

- The slowly varying envelope approximation (SVEA) in time domain $\left(\frac{k_1}{k_0} = \frac{c}{n_0\omega_0 v_g} = \frac{1}{\omega}\frac{v_p}{v_g} \sim \frac{1}{\omega}\right) \Rightarrow \left(\frac{k_1}{k_0}\frac{\partial}{\partial\tau} \sim \frac{T_{optical}}{T_{pulse}} \ll 1\right)$

$$\begin{aligned}\left[\frac{\partial^2}{\partial x^2} + \frac{\partial^2}{\partial y^2} + \frac{\partial^2}{\partial z^2}\right] A'(\vec{r},\tau) + 2ik_0\frac{\partial}{\partial z}A'(\vec{r},\tau) \\ + \left[2k_0 D + D^2\right] A'(\vec{r},\tau) = -\mu_0\omega_0^2 P'^{(NL)}(\vec{r},\tau).\end{aligned} \tag{5.25}$$

- The SVEA in spatial domain $\left(\frac{\partial^2 A'}{\partial z^2} \ll k_0\frac{\partial A'}{\partial z}\right)$

$$\begin{aligned}\left[\frac{\partial^2}{\partial x^2} + \frac{\partial^2}{\partial y^2}\right] A'(\vec{r},\tau) + 2ik_0\frac{\partial}{\partial z}A'(\vec{r},\tau) \\ + \left[2k_0 D + D^2\right] A'(\vec{r},\tau) = -\mu_0\omega_0^2 P'^{(NL)}(\vec{r},\tau).\end{aligned} \tag{5.26}$$

- Ignoring the contribution of D^2, which is already too weak to be of interest to us.

$$\left[\frac{\partial^2}{\partial x^2} + \frac{\partial^2}{\partial y^2}\right] A'(\vec{r},\tau) + 2ik_0\frac{\partial}{\partial z}A'(\vec{r},\tau) + [2k_0 D] A'(\vec{r},\tau) = -\mu_0\omega_0^2 P'^{(NL)}(\vec{r},\tau). \tag{5.27}$$

Finally, the NLSE in its most general form is given by:

$$2ik_0\frac{\partial A'}{\partial z} + \nabla_\perp A' - k_0 k_2\frac{\partial^2 A'}{\partial\tau^2} = -\mu_0\omega_0^2 P'^{(NL)}, \tag{5.28}$$

where $D = \frac{1}{2!}k_2\left(i\frac{\partial}{\partial\tau}\right)^2$ in first approximation and $\nabla_\perp$ is the transverse Laplacian operator.

Is worth mentioning that Eq. 5.28 was developed neglecting losses. However, for dissipative NL media, the NLSE is given by:

$$2ik_0\frac{\partial A'}{\partial z} + \nabla_\perp A' - k_0 k_2\frac{\partial^2 A'}{\partial\tau^2} + ik_0\alpha_0 A' = -\mu_0\omega_0^2 P'^{(NL)}, \tag{5.29}$$

where α_0 represents the linear absorption coefficient and the contribution of NL absorption is included in the imaginary part of the NL polarization.

5.3.1 NLSE for Metal-Dielectric Nanocomposites

As seen in the previous chapter, the MDNCs that were used for the experiments of this thesis present relevant nonlinearities up to the seventh-order. Therefore, the NL polarization, $P'^{(NL)}$, in Eq. 5.29 is given by [Eq. 2.79]:

$$\begin{aligned} P'^{(NL)} &= P'^{(3)} + P'^{(5)} + P'^{(7)} \\ &= \frac{3}{4}\varepsilon_0\chi^{(3)}_{eff}\left|A'\right|^2 A' + \frac{5}{8}\varepsilon_0\chi^{(5)}_{eff}\left|A'\right|^4 A' + \frac{35}{64}\varepsilon_0\chi^{(7)}_{eff}\left|A'\right|^6 A'. \end{aligned} \tag{5.30}$$

By substituting Eq. 5.30 in the NLSE (Eq. 5.29), we have:

$$i\frac{\partial A'}{\partial z} + \frac{1}{2k_0}\nabla_\perp A' - \frac{1}{2}k_2\frac{\partial^2 A'}{\partial \tau^2} + \frac{i}{2}\alpha_0 A' = -\frac{k_0}{2n_0^2}\left[\frac{3}{4}\chi^{(3)}_{eff}\left|A'\right|^2 + \frac{5}{8}\chi^{(5)}_{eff}\left|A'\right|^4 + \frac{35}{64}\chi^{(7)}_{eff}\left|A'\right|^6\right]A'. \tag{5.31}$$

Eq. 5.31 is known as cubic-quintic-septimal NLSE (CQS-NLSE).

5.3.2 NLSE for Liquid Carbon Disulfide

For the special case of liquid CS_2, different types of NL behavior have been reported by varying the incident laser parameters such as: wavelength, pulse duration time, repetition rate and intensity [209]. In this thesis, studies in CS_2 were performed by using two intense short-pulse lasers at: (a) 532 nm with pulses of 80 ps and (b) 800 nm with pulses of 100 fs. At high intensities, it was observed that the NL refractive behavior of CS_2 simulates a saturable-type medium in picosecond regime [26], while in femtosecond regime, CS_2 acts as a cubic-quintic refractive medium [25]. Further, in both regimes, CS_2 presents dissipative terms which vary depending on the wavelength used, as discussed with more details in Appendix C. These different NL behaviors have a strong influence on the propagation of the fields inside the material.

In 532 nm and picosecond regime, Besse *et al.* reported an unusual behavior of the NL refractive index, as observed in Fig. 1.5(a). Based on experimental results, they developed an empirical expression that allowed to adjust the effective third-order refractive index, $n_{2,eff}$,as a function of intensity, given by [26]:

$$n_{2,eff}(I) = \frac{aI}{1+b^2I^2}, \tag{5.32}$$

where $a = 3.39 \times 10^{-32}$ m^4/W^2 and $b = 5.76 \times 10^{-15}$ m^2/W. As concerns the NL absorption, it was also concluded in [26] that the 2PA is negligible, while the 3PA must be taken into account, with respective coefficient $\alpha_4 = 9.3 \times 10^{-26}$ m^3/W^2. Considering these parameters, we can define the equations of evolution of the phase, $\triangle\Phi$, and intensity, I, as:

$$\frac{\partial \triangle\Phi}{\partial z} = k_0 \left[n_{2,eff}(I) \right] I = k_0 \frac{aI}{1+b^2I^2} I, \tag{5.33}$$

$$\frac{\partial I}{\partial z} = -\alpha_4 I^3. \tag{5.34}$$

On the other hand, NL polarization in Eq. 5.29 can be expressed as $P'^{(NL)} = \varepsilon_0 \chi_{eff}^{(NL)} A'$, where $\chi_{eff}^{(NL)}$ represents a total effective NL susceptibility. Separating the amplitude and phase of $A' = |A'| e^{i\triangle\Phi}$, Eq. 5.29 becomes:

$$i\frac{\partial [|A'|]}{\partial z} - |A'| \frac{\partial [\triangle\Phi]}{\partial z} + \frac{1}{2k_0} \left[\frac{\partial^2 |A'|}{\partial x^2} + 2i\frac{\partial |A'|}{\partial x}\frac{\partial \triangle\Phi}{\partial x} + i|A'| \frac{\partial^2 \triangle\Phi}{\partial x^2} - |A'| \left(\frac{\partial \triangle\Phi}{\partial x} \right)^2 \right]$$
$$+ \frac{1}{2k_0} \left[\frac{\partial^2 |A'|}{\partial y^2} + 2i\frac{\partial |A'|}{\partial y}\frac{\partial \triangle\Phi}{\partial y} + i|A'| \frac{\partial^2 \triangle\Phi}{\partial y^2} - |A'| \left(\frac{\partial \triangle\Phi}{\partial y} \right)^2 \right] = -\frac{k_0}{2n_0^2} \chi_{eff}^{(NL)} \left[|A'| \right], \tag{5.35}$$

where it was considered that $\alpha_0 = 0$, because CS_2 is a transparent liquid in 532 nm.

Separating the real of the imaginary part and using the plane wave approximation, we have:

$$\frac{\partial [\triangle\Phi]}{\partial z} = \frac{k_0}{2n_0^2} Re \left[\chi_{eff}^{(NL)} \right], \tag{5.36}$$

$$\frac{\partial [|A'|]}{\partial z} = -\frac{k_0}{2n_0^2} Im \left[\chi_{eff}^{(NL)} \right] |A'|. \tag{5.37}$$

Multiplying both sides of Eq. 5.37 by $2|A'|$ and using the relationship between the electric field amplitude and intensity, $I = \frac{1}{2} c\varepsilon_0 n_0 |A'|$, Eq. 5.37 is rewritten as:

$$\frac{\partial I}{\partial z} = -\frac{k_0}{2n_0^2} 2Im \left[\chi_{eff}^{(NL)} \right] I. \tag{5.38}$$

Then, comparing Eqs. 5.36 and 5.38 with the Eqs. 5.33 and 5.34, we obtain:

$$Re \left[\chi_{eff}^{(NL)} \right] = \frac{2n_0^2}{k_0} \left[k_0 \frac{aI}{1+b^2I^2} I \right], \tag{5.39}$$

$$Im \left[\chi_{eff}^{(NL)} \right] = \frac{2n_0^2}{k_0} \left[\frac{\alpha_4}{2} I^2 \right]. \tag{5.40}$$

Finally, substituting Eqs. 5.39 and 5.40 in the expression for the NL polarization $\left(P'^{(NL)} = \varepsilon_0 \chi_{eff}^{(NL)} A' \right)$, it is possible to write the NLSE [Eq. 5.29] of the form:

$$i\frac{\partial A'}{\partial z} + \frac{1}{2k_0} \nabla_\perp A' - \frac{1}{2} k_2 \frac{\partial^2 A'}{\partial \tau^2} = -\left[\frac{k_0 a I^2}{1+b^2I^2} + i\frac{\alpha_4 I^2}{2} \right] A'. \tag{5.41}$$

Eq. 5.41 governs the evolution of a light pulse (532 nm and picosecond regime) in CS_2. The first term in brackets represents the saturable-type NL refraction while the second term corresponds to the 3PA.

On the other hand, the NL behavior of CS_2 in 800 nm and femtosecond regime is attributed to the cubic, n_2, and quintic, n_4, refractive indices, as well as to the losses processes which are summarized in a NL coefficient, α_{NL}, given by Eq. C.4. Thus, following the same procedure used for the picosecond regime, but substituting Eqs. 5.33 and 5.34 by:

$$\frac{\partial \triangle\Phi}{\partial z} = k_0\left[n_2 + n_4 I\right] I, \tag{5.42}$$

$$\frac{\partial I}{\partial z} = -\left[\alpha_{NL}(I)\right] I = -B\left(\frac{exp\left[\frac{I-C}{D}\right] - exp\left[-\frac{C}{D}\right]}{exp\left[\frac{I-C}{D}\right]+1}\right) I, \tag{5.43}$$

where B, C and D are constants defined in Appendix C ($B = 5.39$ cm^{-1}, $C = 186.7$ GW/cm^2 and $D = 27.16$ GW/cm^2). We can describe the propagation of a light pulse in 800 nm and 100 fs in CS_2 by:

$$i\frac{\partial A'}{\partial z} + \frac{1}{2k_0}\nabla_\perp A' - \frac{1}{2}k_2\frac{\partial^2 A'}{\partial \tau^2} = -\left[k_0\left(n_2 + n_4 I\right) I + \frac{i}{2}B\left(\frac{exp\left[\frac{I-C}{D}\right] - exp\left[-\frac{C}{D}\right]}{exp\left[\frac{I-C}{D}\right]+1}\right)\right] A'. \tag{5.44}$$

In two transverse dimensions (2+1)D, the laser beam propagation in CS_2 can be modeled by solving numerically Eqs. 5.41 and 5.44 for picosecond and femtosecond regimes, respectively.

5.4 ANALYTICAL VARIATIONAL TECHNIQUE

Variational calculus is a powerful analytical technique that allows to find an approximate solution of NLSE, in cases in which there is no exact analytical solution [210]. In order to apply the mathematical formalism of variational calculus we initiate by identifying the conditions under which a type of integral assumes a stationary value, which can be a maximum, minimum or saddle point [1]. The simplest integral can be written as:

$$J = \int_{\mathbf{x_1}}^{\mathbf{x_2}} L\left(x, y, y'\right) dx, \tag{5.45}$$

where L is a known function that depends on the variables x, y and the derivatives $y' = dy/dx$. It will be seen later that L is related with the Lagrangian function and Eq. 5.45 is sometimes called the action integral. The integration limits are given by $\mathbf{x_1} = (x_1, y_1)$ and $\mathbf{x_2} = (x_2, y_2)$, and J depends on the integration path between these two points.

We assume that the integral of $y = y(x)$, between the points $\mathbf{x_1}$ and $\mathbf{x_2}$, results in a stationary value J_m. In addition, we define a curve $Y = y(x) + \varsigma h(x)$, neighboring to $y = y(x)$, which also

---

[1] A saddle point is a point in the domain of a function where the slopes of orthogonal function components defining the surface become zero, but are not a local extremum on both axes.

passes through points $\mathbf{x_1}$ and $\mathbf{x_2}$, whose integral is $J_m + \delta J_m$. Here, ς is a parameter that defines if the function $y = y(x)$ is subject to weak or strong variations; $h(x)$ is a function only of x, which is zero at $\mathbf{x_1}$ and $\mathbf{x_2}$, and has a continuous second derivative in the interval from $\mathbf{x_1}$ to $\mathbf{x_2}$. These assumptions are mathematically expressed by:

$$J_m = \int_{\mathbf{x_1}}^{\mathbf{x_2}} L\left(x, y, y'\right) dx, \tag{5.46}$$

$$J_m + \delta J_m = \int_{\mathbf{x_1}}^{\mathbf{x_2}} L\left(x, y + \varsigma h, y' + \varsigma h'\right) dx. \tag{5.47}$$

Both equations can be related using the mean-value theorem for functions of several variables, given by:

$$\begin{aligned} L\left(x, y + \varsigma h, y' + \varsigma h'\right) &= L\left(x, y, y'\right) + \varsigma \left[h \frac{\partial L}{\partial y} + h' \frac{\partial L}{\partial y'}\right] \\ &+ \frac{\varsigma^2}{2} \left[h^2 \frac{\partial^2 L}{\partial y^2} + 2hh' \frac{\partial^2 L}{\partial y \partial y'} + h'^2 \frac{\partial^2 L}{\partial y'^2}\right] + \mathcal{O}\left(\varsigma^3\right). \end{aligned} \tag{5.48}$$

Integrating Eq. 5.48 in x, between the points $\mathbf{x_1}$ and $\mathbf{x_2}$, and using Eqs. 5.46 and 5.47, we obtain

$$\delta J_m = \varsigma \int_{\mathbf{x_1}}^{\mathbf{x_2}} \left[h \frac{\partial L}{\partial y} + h' \frac{\partial L}{\partial y'}\right] dx + \frac{\varsigma^2}{2} \int_{\mathbf{x_1}}^{\mathbf{x_2}} \left[h^2 \frac{\partial^2 L}{\partial y^2} + 2hh' \frac{\partial^2 L}{\partial y \partial y'} + h'^2 \frac{\partial^2 L}{\partial y'^2}\right] dx + \mathcal{O}\left(\varsigma^3\right), \tag{5.49}$$

where the integral terms with ς and ς^2 are known as the first and second variations, and they are denoted by J_1 and J_2, respectively. It is possible to note that in a stationary point, the first derivatives of L are zero, i.e. the first-order variation vanishes. Nevertheless, J_2 is the term that establishes the type of stationary value (if it is a minimum, maximum or saddle point).

We focus our attention in the first-order variation. At a stationary point, δJ_1 can be expressed in a more simple form by integrating by parts the term concerning to h', as follow:

$$\begin{aligned} \delta J_1 &= \left(\frac{\partial J_1}{\partial \varsigma}\right)_{\varsigma = 0} d\varsigma, \\ &= \int_{\mathbf{x_1}}^{\mathbf{x_2}} \left[\frac{\partial L}{\partial y} - \frac{d}{dx} \frac{\partial L}{\partial y'}\right] \delta y dx, \end{aligned} \tag{5.50}$$

where $\delta y = (\partial Y/\partial \varsigma)_{\varsigma=0} d\varsigma$, with $Y = y(x) + \varsigma h(x)$. Also, $\delta J_1 = 0$ for being evaluated at a stationary point. Thus, by using the fundamental lemma of variational calculus[2], Eq. 5.50 can only be satisfied if:

$$\frac{\partial L}{\partial y} - \frac{d}{dx}\frac{\partial L}{\partial y'} = 0. \tag{5.51}$$

Eq. 5.51 is known as the Euler-Lagrange equation and L is referred to Lagrangian function. This equation can be generalized for N dependent variables and M independent variables, of the form:

$$\frac{\partial L}{\partial y_p} - \sum_{q=1}^{M} \frac{d}{dx_q}\left(\frac{\partial L}{\partial y_{pq}}\right) = 0, \tag{5.52}$$

with $p = 1, 2, \ldots, N$, $y_{pq} = \left(\partial y_p/\partial x_q\right)$ and the Eq. 5.45 is rewritten as:

$$J = \int \ldots \int L\left(x_1, x_2, \ldots, x_M, y_1, y_2, \ldots, y_N, y_{11}, \ldots, y_{pq}, \ldots, y_{NM}\right) dx_1 dx_2 \cdots dx_M. \tag{5.53}$$

The derivation of the Euler-Lagrange equations were performed of the more general nature, without reference to a specific physical system. However, in Section 6.1, the variational method is applied to the CQS-NLSE, in order to obtain the stability and instability regions of fundamental solitons, identified by using the Vakhitov-Kolokolov criterion [211].

5.5 NONLINEAR BIREFRINGENCE IN CAPILLARIES WITH METAL COLLOIDS CORE

The study of NL polarization instability, discussed in Chapter 8, was conducted for propagating a linearly polarized laser pulse on a hollow capillary filled with a silver colloid. For the intensity regime used in the experiments, silver colloids behave like a cubic-quintic media. Thus, in this section, it is developed a theoretical model that describes the evolution of the right- and left-circular polarization in media exhibiting cubic-quintic nonlinearities. This theoretical proposal is based on the typical model used for the propagation of light in fibers, as discussed in [212].

We begin expressing the complex electric field associated with an arbitrarily polarized optical wave by:

$$\vec{E}\left(\vec{r}, t\right) = \frac{1}{2}\left(\hat{x}E_x + \hat{y}E_y\right) exp\left[-i\omega_0 t\right] + c.c., \tag{5.54}$$

where E_x and E_y are the complex amplitudes of the polarization components of the field in the $x-$ and $y-$axis, with the carrier frequency ω_0.

---

[2] The fundamental lemma of variational calculus states that: if $f(x)$ is continuous in the interval (x_1, x_2) and the integral $\int_{x_1}^{x_2} f(x)g(x)dx$ vanishes for every $g(x)$ continuously differentiable in (x_1, x_2) and that vanishes at x_1 and x_2, then $f(x) = 0$ in the closed interval $[x_1, x_2]$.

The NL light propagation inside the colloid hosted by the capillary can be modeled by using the Helmholtz equation given by

$$\nabla^2 \overrightarrow{E}\left(\overrightarrow{r},\omega\right) + \left(k_0'\right)^2 \overrightarrow{\varepsilon}\left(\omega\right) \cdot \overrightarrow{E}\left(\overrightarrow{r},\omega\right) = 0, \tag{5.55}$$

where $\overrightarrow{E}\left(\overrightarrow{r},\omega\right)$ and $\overrightarrow{\varepsilon}\left(\omega\right)$ represent the frequency-dependent field and the dielectric tensor, respectively. ∇^2 is the Laplacian operator, $k_0' = \omega_0/c$, ω_0 is the laser frequency and c is the speed of light in vacuum[3]. By using the relationship between the total polarization and total dielectric function, given by Eqs. 2.79 and 2.80, we have to Eq. 5.55 is equal to the expression derived in 5.16.

As follows from Eqs. 5.54 and 5.55 the field components obeys the Helmholtz equation:

$$\nabla^2 E_\mu\left(\overrightarrow{r},\omega\right) + \left(k_0'\right)^2 \varepsilon_{\mu\sigma}\left(\omega\right) \cdot E_\sigma\left(\overrightarrow{r},\omega\right) = 0, \tag{5.56}$$

with μ and σ equal to x or y. In the principal-axis system, the dielectric tensor is represented as a diagonal matrix $\left(\varepsilon_{\mu\sigma} \to \varepsilon_{\mu\sigma}\delta_{\mu,\sigma}\right)$, with $\varepsilon_{xx} = \varepsilon_x$ and $\varepsilon_{yy} = \varepsilon_y$ being the only nonzero components. This complex dielectric function $\left(\varepsilon_\mu\right)$ is associated to the refractive index, n_μ, and the absorption coefficient, α_μ, of the material through the expression $\varepsilon_\mu = \left[n_\mu + i\alpha_\mu/(2k_0')\right]^2$. For media exhibiting NL response, the dielectric function can be expressed as a sum of the linear and NL contributions as $\varepsilon_\mu\left(\omega\right) = \varepsilon_\mu^L\left(\omega\right) + \varepsilon_\mu^{NL}\left(\omega\right)$, where the NL term is related to the NL optical polarization by:

$$P_\mu^{NL}\left(\omega\right) = \varepsilon_0 \varepsilon_\mu^{NL}\left(\omega\right) E_\mu\left(\omega\right). \tag{5.57}$$

For media exhibiting cubic-quintic nonlinearities, the NL polarization is adequately described by the sum of the third- and fifth-order contributions, $P_\mu^{NL} = P_\mu^{(3)} + P_\mu^{(5)}$, with:

$$\begin{aligned} P_\mu^{(3)}\left(\omega\right) = \frac{3}{4}\varepsilon_0 \Big\{ & 2\chi_{xxyy}^{(3)}\left(\omega\right) E_\mu\left(\omega\right) \left[\overrightarrow{E}\left(\omega\right) \cdot \overrightarrow{E}^*\left(\omega\right)\right] \\ & + \chi_{xyyx}^{(3)}\left(\omega\right) E_\mu^*\left(\omega\right) \left[\overrightarrow{E}\left(\omega\right) \cdot \overrightarrow{E}\left(\omega\right)\right] \Big\}, \end{aligned} \tag{5.58}$$

$$\begin{aligned} P_\mu^{(5)}\left(\omega\right) = \frac{5}{8}\varepsilon_0 \Bigg\{ & \frac{10}{3}\chi_{xxyyxx}^{(5)}\left(\omega\right) \left|E_\mu\left(\omega\right)\right|^2 \left[\overrightarrow{E}\left(\omega\right) \cdot \overrightarrow{E}\left(\omega\right)\right] E_\mu^*\left(\omega\right) \\ & + \frac{5}{3}\chi_{xxyyyy}^{(5)}\left(\omega\right) \sum_{\sigma=x,y} \left|E_\sigma\left(\omega\right)\right|^4 E_\mu\left(\omega\right) \Bigg\}. \end{aligned} \tag{5.59}$$

A detailed explanation to obtain Eqs. 5.58 and 5.59 is given in Appendix D. By comparing Eq. 5.57 with Eqs. 5.58 and 5.59 we obtain an expression for the dielectric function in the

---

[3] the symbol ($'$) was used to differentiate $k_0' = \omega_0/c$ from $k_0 = n_0\omega_0/c$, used in the analysis of the NLSE

form:

$$\begin{aligned}\varepsilon_{\mu}^{NL}(\omega) = {} & \frac{3}{4}\left[\left(2\chi^{(3)}_{xxyy}(\omega)+\chi^{(3)}_{xyyx}(\omega)\right)\left|E_{\mu}(\omega)\right|^{2}+2\chi^{(3)}_{xxyy}(\omega)\sum_{\sigma=x,y}\left|E_{\sigma}(\omega)\right|^{2}\left(1-\delta_{\mu,\sigma}\right)\right] \\ & +\frac{5}{8}\left[\frac{10}{3}\chi^{(5)}_{xxyyxx}(\omega)\left|E_{\mu}(\omega)\right|^{4}+\frac{5}{3}\chi^{(5)}_{xxyyyy}(\omega)\left(\left|E_{\mu}(\omega)\right|^{4}+\sum_{\sigma=x,y}\left|E_{\sigma}(\omega)\right|^{4}\left(1-\delta_{\mu,\sigma}\right)\right)\right] \\ & +\left[\frac{3}{4}\chi^{(3)}_{xyyx}(\omega)+\frac{5}{8}\frac{10}{3}\chi^{(5)}_{xxyyxx}(\omega)\left|E_{\mu}(\omega)\right|^{2}\right]\sum_{\sigma=x,y}\left|E_{\sigma}(\omega)\right|^{2}\left(1-\delta_{\mu,\sigma}\right)\frac{E^{*}_{\mu}(\omega)}{E_{\mu}(\omega)}.\end{aligned} \tag{5.60}$$

The Helmholtz equation [Eq. 5.56] can be solved by the separation of variables method for each component of the electric field:

$$E_{\mu}\left(\overrightarrow{r},\omega\right)=F\left(x,y\right)A_{\mu}\left(z,\omega-\omega_{0}\right)exp\left(i\beta_{0,\mu}z\right), \tag{5.61}$$

where $F(x,y)$ is the transverse mode pattern supported by the capillary, $A_{\mu}(z,\omega-\omega_{0})$ is the slowly varying amplitude and $\beta_{0,\mu}$ is the propagation constant for $\mu = x$, y. Substituting Eq. 5.61 in Eq. 5.56, and separating the terms dependent upon the propagation distance (z) and the transverse coordinates (x, y), we obtain:

$$2i\beta_{0,\mu}\frac{\partial A_{\mu}}{\partial z}+\left(\beta_{\mu}^{2}-\beta_{0,\mu}^{2}\right)A_{\mu}=0, \tag{5.62}$$

$$\frac{\partial^{2}F}{\partial x^{2}}+\frac{\partial^{2}F}{\partial y^{2}}+\left[\varepsilon_{\mu}(\omega)\left(k_{0}'\right)^{2}-\beta_{\mu}^{2}\right]F=0, \tag{5.63}$$

where the slowly varying envelope approximation $\left[\left(\partial^{2}A_{\mu}/\partial z^{2}\right)\ll\beta_{0,\mu}\left(\partial A_{\mu}/\partial z\right)\right]$ was made to obtain Eq. 5.62. The dielectric function in Eq. 5.63 can be approximated by:

$$\varepsilon_{\mu}=\left(n_{0,\mu}+\triangle N_{\mu}\right)^{2}\approx\left(n_{0,\mu}\right)^{2}+2\left(n_{0,\mu}\right)\left(\triangle N_{\mu}\right), \tag{5.64}$$

where $\triangle N_{\mu}=i\alpha_{0,\mu}/2k_{0}'+\left[\triangle n_{\mu}+i\triangle\alpha_{\mu}/(2k_{0}')\right]$, $n_{0,\mu}$ $\left(\alpha_{0,\mu}\right)$ is the linear refractive index (linear absorption coefficient) and $\triangle n_{\mu}$ $\left(\triangle\alpha_{\mu}\right)$ represents the NL contributions of the refractive index (absorption coefficient). The linear and NL dielectric functions are given by $\varepsilon_{\mu}^{L}=\left[n_{0,\mu}+i\alpha_{0,\mu}/(2k_{0}')\right]$ and $\varepsilon_{\mu}^{NL}=2\left(n_{0,\mu}\right)\left[\triangle n_{\mu}+i\triangle\alpha_{\mu}/(2k_{0}')\right]$, and substituting in Eqs. 5.60 and 5.61, we have:

$$\begin{aligned}\left(\triangle n_{\mu}+i\frac{\triangle\alpha_{\mu}}{2k_{0}'}\right)= {} & \frac{3}{8n_{0,\mu}}\left|F\right|^{2}\left[\left(2\chi^{(3)}_{xxyy}+\chi^{(3)}_{xyyx}\right)\left|A_{\mu}\right|^{2}+2\chi^{(3)}_{xxyy}\sum_{\sigma=x,y}\left|A_{\sigma}\right|^{2}\left(1-\delta_{\mu,\sigma}\right)\right] \\ & +\frac{5}{16n_{0,\mu}}\left|F\right|^{4}\left[\frac{10}{3}\chi^{(5)}_{xxyyxx}\left|A_{\mu}\right|^{4}+\frac{5}{3}\chi^{(5)}_{xxyyyy}\left(\left|A_{\mu}\right|^{4}+\sum_{\sigma=x,y}\left|A_{\sigma}\right|^{4}\left(1-\delta_{\mu,\sigma}\right)\right)\right] \\ & +\frac{1}{2n_{0,\mu}}\left|F\right|^{2}\left[\frac{3}{4}\chi^{(3)}_{xyyx}+\frac{5}{8}\frac{10}{3}\chi^{(5)}_{xxyyxx}\left|F\right|^{2}\left|A_{\mu}\right|^{2}\right]\sum_{\sigma=x,y}\left[A_{\sigma}\right]^{2}\left(1-\delta_{\mu,\sigma}\right) \\ & \times\frac{A_{\mu}^{*}}{A_{\mu}}exp\left[2i\left(\beta_{0,\sigma}-\beta_{0,\mu}\right)z\right].\end{aligned} \tag{5.65}$$

β_μ can be determined by solving Eq. 5.63 using the first-order approximation $\left(\beta_\mu \to \beta_\mu + \triangle\beta_\mu\right)$, where F and the eigenvalue $\beta_\mu^2 \to \beta_\mu^2 + 2\beta_\mu \triangle\beta_\mu$ are represented by:

$$F = F^{(0)} + \xi F^{(1)} + \ldots, \tag{5.66}$$

$$\beta_\mu^2 = \left(\beta_\mu\right)^2 + \xi 2\beta_\mu \left(\triangle\beta_\mu\right) + \ldots, \tag{5.67}$$

where ξ is a perturbation parameter which can vary over a continuous range from 0 (no perturbation) to 1 (full perturbation). Inserting Eqs. 5.66 and 5.67 into the eigenvalue equation 5.63, and using the Eq. 5.64, we obtain:

$$\xi^{(0)}: \qquad \left[\left(\frac{\partial^2}{\partial x^2} + \frac{\partial^2}{\partial y^2} + (n_{0,\mu}k_0')^2\right) - \beta_\mu^2\right] F^{(0)} = 0, \tag{5.68}$$

$$\begin{aligned} \xi^{(1)}: \quad & \left[\left(\frac{\partial^2}{\partial x^2} + \frac{\partial^2}{\partial y^2} + (n_{0,\mu}k_0')^2\right) - \beta_\mu^2\right] F^{(1)} \\ & + \left[2\left(n_{0,\mu}\right)\left(\triangle N_\mu\right)(k_0')^2 - 2\beta_\mu\left(\triangle\beta_\mu\right)\right] F^{(0)} = 0. \end{aligned} \tag{5.69}$$

In order to find an expression for $F^{(0)}$, Eq. 5.68 is written in cylindrical coordinates (ρ, ϕ, z) and by using the separation of variables $F^{(0)}(\rho,\phi) = F^{(0)}(\rho)\, exp\left[im\phi\right]$, it is possible to recognize Eq. 5.68 as the modified Bessel differential equation: $\frac{\partial^2 F^{(0)}}{\partial \rho^2} + \frac{1}{\rho}\frac{\partial F^{(0)}}{\partial \rho} + \left[(n_{0,\mu}k_0')^2 - \beta_\mu^2 - \frac{m^2}{\rho^2}\right] F^{(0)} = 0$. Then, a solution for the region filled with a NL medium, corresponding to the capillary core $\left(n_{core} = n_{0,\mu}\right)$ is:

$$F_{core}^{(0)}(\rho) = C_1 J_m\left(\rho\sqrt{(n_{0,\mu}k_0')^2 - \beta_\mu^2}\right), \tag{5.70}$$

where J_m is the first kind $m-$order Bessel function. For the region formed by the capillary' wall $\left(n_{0,\mu} = n_{cladding}\right)$, $F^{(0)}$ should decay exponentially for ρ. A function that describes such behavior is the modified Bessel function of second kind, K_m, given by

$$F_{cladding}^{(0)}(\rho) = C_2 K_m\left(\rho\sqrt{\beta_\mu^2 - (n_{cladding}k_0')^2}\right), \tag{5.71}$$

where C_1 and C_2 are determined by considering the boundary conditions.

From Eq. 5.69, corresponding to the first-order of perturbation, we get

$$\triangle\beta_\mu = k_0 \frac{\int\int \left(\triangle N_\mu\right)\left|F^{(0)}\right|^2 dxdy}{\int\int \left|F^{(0)}\right|^2 dxdy}, \tag{5.72}$$

where $F^{(0)}$ is given by Eqs. 5.70 and 5.71, and $\triangle N_\mu$ was defined in Eq. 5.64.

On the other hand, by considering $\beta_\mu \to \beta_\mu + \triangle\beta_\mu$ into Eq. 5.62 we obtain the expression

$$\frac{\partial A_\mu}{\partial z} = i\left(\beta_\mu + \triangle\beta_\mu - \beta_{0,\mu}\right) A_\mu, \tag{5.73}$$

where the approximation $\beta_\mu^2 - \beta_{0,\mu}^2 \to 2\beta_{0,\mu}\left(\beta_\mu - \beta_{0,\mu}\right)$ was used. Nevertheless, as an exact functional form of β_μ is generally unknown, an expansion in Taylor series about the frequency ω_0 is made to obtain the more specialized expression

$$\beta_\mu(\omega) = \beta_{0,\mu} + \beta_\mu^{(1)}(\omega-\omega_0) + \frac{1}{2}\beta_\mu^{(2)}(\omega-\omega_0)^2 + \mathscr{O}\left[(\omega-\omega_0)^3\right], \tag{5.74}$$

where $\beta_\mu^{(N)} = \left(d^N\beta_\mu/d\omega^N\right)$, $N = 1, 2$, represent the dispersion terms and the last term represents higher-order contributions that will be neglected. Then, substituting Eq. 5.74 in Eq. 5.73 and using Eqs. 5.65 and 5.72, we obtain two coupled differential equations that describe the evolution of the two polarization components along a capillary filled with a cubic-quintic isotropic media. Both equations can be summarized as:

$$\begin{aligned}
&\frac{\partial A_\mu}{\partial z} + \beta_\mu^{(1)}\frac{\partial A_\mu}{\partial t} + i\frac{\beta^{(2)}}{2}\frac{\partial^2 A_\mu}{\partial t^2} + \frac{\alpha_0}{2}A_\mu \\
&\quad = i\frac{k_0'}{2n_{0,\mu}}\frac{3}{4}F^{(1)}\left\{\left[\left(2\chi^{(3)}_{xxyy} + \chi^{(3)}_{xyyx}\right)\left|A_\mu\right|^2 + 2\chi^{(3)}_{xxyy}\sum_{\sigma=x,y}\left(1-\delta_{\mu,\sigma}\right)\left|A_\sigma\right|^2\right]A_\mu\right. \\
&\qquad\qquad \left. + \chi^{(3)}_{xyyx}\left[\sum_{\sigma=x,y}\left(1-\delta_{\mu,\sigma}\right)\left(A_\sigma\right)^2\right]A_\mu^* exp\left[2i\left(\beta_{0,\sigma}-\beta_{0,\mu}\right)z\right]\right\} \\
&\quad + i\frac{k_0'}{2n_{0,\mu}}\frac{5}{8}F^{(2)}\left\{\left[\frac{10}{3}\chi^{(5)}_{xxyyxx}\left|A_\mu\right|^4 + \frac{5}{3}\chi^{(5)}_{xxyyyy}\left[\left|A_\mu\right|^4 + \sum_{\sigma=x,y}\left(1-\delta_{\mu,\sigma}\right)\left|A_\sigma\right|^4\right]\right]A_\mu\right. \\
&\qquad\qquad \left. + \frac{10}{3}\chi^{(5)}_{xxyyxx}\left[\sum_{\sigma=x,y}\left(1-\delta_{\mu,\sigma}\right)\left|A_\mu\right|^2\left(A_\sigma\right)^2\right]A_\mu^* exp\left[2i\left(\beta_{0,\sigma}-\beta_{0,\mu}\right)z\right]\right\},
\end{aligned} \tag{5.75}$$

with $\mu = x, y$, $F^{(1)} = \left(\int\int|F^{(0)}|^4 dxdy\right)/\left(\int\int|F^{(0)}|^2 dxdy\right)^2$ and $F^{(2)} = \left(\int\int|F^{(0)}|^6 dxdy\right)/\left(\int\int|F^{(0)}|^2 dxdy\right)^3$. The modal birefringence of the capillary is expressed by $\triangle\beta_0 = \beta_{0,x} - \beta_{0,y} = 2\pi/\lambda\left|n_x - n_y\right|$, which leads to different group velocities for the two polarization components $\left(\beta_x^{(1)} \neq \beta_y^{(1)}\right)$. However, $\beta^{(2)}$ and α_0 are assumed to be the same for both polarization components.

For convenience, we rewrite Eq. 5.75 using the circularly polarized components $A_\pm = 2^{-1/2}\left(\bar{A}_x \pm i\bar{A}_y\right)$, where $\bar{A}_x = A_x exp\left[i\triangle\beta z/2\right]$ and $\bar{A}_y = A_y exp\left[-i\triangle\beta z/2\right]$, and by performing some manipulations we obtain:

$$\begin{aligned}
&\frac{\partial A_\pm}{\partial z} + \frac{1}{2}\left[\beta_+^{(1)}\frac{\partial A_\pm}{\partial t} + \beta_-^{(1)}\frac{\partial A_\mp}{\partial t}\right] + \frac{i}{2}\beta^{(2)}\frac{\partial^2 A_\pm}{\partial t^2} + \frac{\alpha_0}{2}A_\pm \\
&\quad = \frac{i}{2}\left(\triangle\beta_0\right)A_\mp + i\frac{3\omega_0}{4n_0c}F^{(1)}\left[\chi^{(3)}_{xxyy}\left(|A_+|^2 + |A_-|^2\right) + \chi^{(3)}_{xyyx}|A_\mp|^2\right]A_\pm \\
&\quad + i\frac{5\omega_0}{32n_0c}F^{(2)}\left\{\frac{10}{3}\chi^{(5)}_{xxyyxx}\left[|A_+ + A_-|^2\left(A_+ + A_-\right)^* \mp |A_+ - A_-|^2\left(A_+ - A_-\right)^*\right]A_\mp\right. \\
&\qquad\qquad \left. + \frac{5}{6}\chi^{(5)}_{xxyyyy}\left[|A_+ + A_-|^4 + |A_+ - A_-|^4\right]\right\}A_\pm,
\end{aligned} \tag{5.76}$$

with $\beta_{\pm}^{(1)} = \beta_x^{(1)} \pm \beta_y^{(1)}$. Eq. 5.76 describes the evolution of the right- and left-circular polarizations A_+ and A_- along a hollow capillary filled with an isotropic cubic-quintic media.

The theoretical models developed in this chapter correspond to an expansion of the already known models for lowest-order nonlinearity $\left(\chi^{(3)}\right)$, but considering the different behavior of the HON, corresponding to our materials.

... what is theory? An uninitiated see just a mass of incomprehensible
formulas ... However, they are not its essence.
- LUDWIG BOLTZMANN

6 FUNDAMENTAL SPATIAL SOLITONS IN MDNCS

This chapter is devoted to study the formation and propagation of fundamental spatial solitons in one- $[(1+1)\,\mathrm{D}]$ and two-transverse dimensions $[(2+1)\,\mathrm{D}]$, when HON are relevant. Here, fundamental spatial solitons are understood as first-order bright solitons propagating in the spatial domain. The notation "$(N+1)$D" refers to N transverse dimensions plus the propagation direction (which corresponds to the z-axis in all our cases). In $(1+1)$D, fundamental spatial solitons are known to be stable, when it propagates in cubic SF media. However, in media exhibiting HON, stability and instability regions are formed depending on the order of the nonlinearity, its sign and magnitude, as well as the incident power. These regions are identified and analyzed in Section 6.1 by using the variational method, discussed in Section 5.4, and a linear stability analysis. In Section 6.2, it is reported the observation of the stable propagation of $(2+1)$D fundamental spatial solitons, which are unstable in cubic media, due to the simultaneous contributions of quintic and septimal nonlinearities. Both works were inspired by the HON observed in MDNCs and in the NM procedure developed to control them. The theoretical and experimental results were corroborated with numerical simulations based on the CQS-NLSE obtained in Section 5.3.

6.1 ONE-DIMENSIONAL SPATIAL SOLITONS IN CUBIC-QUINTIC-SEPTIMAL MEDIA

6.1.1 Introduction

Optical spatial solitons are self-trapped light beams whose shape and transverse dimension remain invariant in the course of propagation, due to the balance between diffraction and nonlinearity [75, 83, 213]. Different physical mechanisms may contribute to the generation of spatial solitons in NL media [48, 214]. In this thesis, we focus on the NL processes induced by the Kerr effect. In particular, it is well established that focusing Kerr-type media support the stable propagation of bright solitons in (1+1)D [36, 78]. Usually, the soliton's dynamics is described by the C-NLSE, which gives rise to the commonly known stable solution with the hyperbolic-secant envelope shape. However, unstable soliton propagation is observed in (1+1)D when the system exhibits HON [215]. For example, in focusing quintic NL media the diffraction effect is not sufficient to balance the self-focusing, and consequently the beam is subject to critical collapse [216]. Nevertheless, the inclusion of higher-order dissipative terms can suppress the collapse. In (2 + 1)D, the stationary soliton solutions of the C-NLSE (*Townes' solitons*) are extremely unstable against propagation [217]. Therefore they are not observed in the usual Kerr media [76, 218], however stable propagation can be observed when refractive and/or dissipative HON are considered.

Large HON were reported in various physical settings [219, 220, 23, 158, 221, 222] playing an important role for the understanding of filamentation [223, 224], harmonic conical diffraction [31, 225], and other transverse NL phenomena. In particular, as mentioned above, HON may help to stabilize the propagation of spatial solitons. The theoretical analysis shows that the formation of (1+1)D spatial solitons depends on the sign and magnitude of the third- and fifth-order NL terms [226, 227]. In (2 + 1)D, stable soliton solution of the cubic-quintic NLSE (CQ-NLSE) was predicted by considering the competition between focusing third-order and defocusing fifth-order nonlinearities [228]. The experimental observation of stable (2 + 1)D fundamental solitons in cubic-quintic media, including a dissipative effect due to the three-photon absorption, was recently reported [30].

Several works dealt with the stable propagation of solitons in media with other modifications of cubic-quintic nonlinearities [229, 174, 175, 230]. A special case, which was studied, thus far, only theoretically, is *critical collapse* in focusing quintic media in the absence of the third-order nonlinearity. The corresponding model is provided by the quintic NLSE (Q-NLSE), which displays a degenerate family of 1D Townes' solitons [172, 231, 232]. The addition of an external potential allows one to arrest the beam collapse in one [172, 231] and two [233] transverse dimensions. In focusing cubic-quintic media, the cubic nonlinearity lifts the degeneracy that is characteristic of the Townes' solitons, making the solitons' propagation stable against small perturbations [234].

In addition to the cubic and quintic terms, septimal nonlinearity may also play an important role for the evolution of optical fields. For instance, a case of interest is the study of the spatial-soliton propagation in septimal media. A highly unstable behavior, due to the high degree of the seventh-order nonlinearity, is expected, and hence HON can give rise to a *supercritical collapse* of the beam. Thus, the study of the cubic-quintic-septimal NL model is relevant to complement the previous studies, and it can suggest additional possibilities for experiments. This is where MDNCs play an important role to investigate fundamental spatial solitons. In fact, the NM procedure applied to MDNCs allows controlling the interplay between different NL terms, which leads to enhancement or suppression of specific HON, as discussed in Chapter 4. Therefore, the availability of the management technique, which allows to obtain a quintic or septimal medium, justifies the theoretical effort to study the respective mathematical models that identify the stability region of fundamental spatial soliton propagation as well as the instability regions where the critical and supercritical collapse occurs.

In this section, the conditions for the stable propagation of (1+1)D spatial solitons in media exhibiting nonlinearities up to the seventh order are analyzed by using the CQS-NLSE. In addition, a variational approximation (VA) , based on the *raised-sech ansatz* [173], and the Vakhitov-Kolokolov (VK) stability criterion [211] are used to identify stability and instability regions of the spatial soliton propagation. The analytical predictions obtained from the theoretical model were corroborated with numerical simulations that demonstrates the evolution of stable and unstable fundamental spatial solitons in cubic-quintic-septimal media.

6.1.2 Variational Approximation to Cubic-Quintic-Septimal Nonlinear Schrödinger Equation

The evolution of optical fields in a medium exhibiting nonlinearities up to the seventh-order is modeled by the CQS-NLSE, given by Eq. 5.31. For simplicity, we neglect the dispersion effects ($k_2 = 0$) and the contributions of both linear ($\alpha_0 = 0$) and NL absorption. Thus, in (1+1)D, the CQS-NLSE of a non-dispersive and non-dissipative medium takes the form:

$$i\frac{\partial A'}{\partial z} + \frac{1}{2k_0}\frac{\partial^2 A'}{\partial x^2} = -\frac{k_0}{2n_0^2}\left[\frac{3}{4}\chi_{eff}^{(3)}\left|A'\right|^2 + \frac{5}{8}\chi_{eff}^{(5)}\left|A'\right|^4 + \frac{35}{64}\chi_{eff}^{(7)}\left|A'\right|^6\right]A', \tag{6.1}$$

where the $(2N+1)$th-order susceptibility, $\chi_{eff}^{(2N+1)}$ with $N = 1, 2, 3$, are real parameters. However, the most practical way to analyze the Eq. 6.1 is by using the normalized CQS-NLSE given by:

$$i\frac{\partial \psi}{\partial Z} + \frac{1}{2}\frac{\partial^2 \psi}{\partial X^2} + g_3\psi\left|\psi\right|^2 + g_5\psi\left|\psi\right|^4 + \psi\left|\psi\right|^6 = 0, \tag{6.2}$$

which is obtained by making a change of variables: $X = x/w_0$, $Z = z/L_D$, where $L_D = k_0 w_0^2$ and w_0 is the beam waist of the input beam. The field amplitude was normalized by the septimal susceptibility of the form: $\psi = \frac{A'}{\sqrt{I_r}}$ with $I_r = \left[\frac{2n_0^2}{k_0^2 w_0^2}\frac{64}{35}\frac{1}{\chi_{eff}^{(7)}}\right]^{1/3}$. The dimensionless coefficients $g_3 = \left[\frac{27}{35}\frac{k_0^4 w_0^4}{4n_0^4}\right]^{1/3}\frac{\chi_{eff}^{(3)}}{\left[\chi_{eff}^{(7)}\right]^{1/3}}$ and $g_5 = \left[\frac{40}{49}\frac{k_0^2 w_0^2}{2n_0^2}\right]^{1/3}\frac{\chi_{eff}^{(5)}}{\left[\chi_{eff}^{(7)}\right]^{2/3}}$ represent the strengths of the third and quintic NL terms, while $g_7 = +1$ corresponds to a normalized focusing septimal nonlinearity. The stability of the spatial solitons was studied by varying g_3 and g_5 both between -1.5 and $+1.5$. We stress that the models in which the magnitudes of g_3, g_5, and g_7 are comparable, or, in some cases, g_7 is dominant, do not violate the convergence principle of the power-series expansion. Clear examples of that was observed experimentally in the NL behavior of the MDNCs studied in Chapter 4.

We begin by considering that the stationary solution of Eq. 6.2 with a real propagation constant K have the form of $\psi(X,Z) = \varphi(X)\,exp[iKZ]$, where the real function $\varphi = \varphi(X)$ satisfies the stationary equation

$$0 = -K\varphi + \frac{1}{2}\frac{d^2\varphi}{dX^2} + g_3\varphi^3 + g_5\varphi^5 + \varphi^7. \tag{6.3}$$

An effective potential energy U can be defined by casting Eq. 6.3 into the form of $d^2\varphi/dX^2 = -dU/d\varphi$. Therefore, the corresponding Lagrangian density $\mathscr{L} = (\varphi')^2/2 - U$ is given by:

$$\mathscr{L} = \frac{1}{2}\left(\varphi'\right)^2 + K\varphi^2 - \frac{1}{2}g_3\varphi^4 - \frac{1}{3}g_5\varphi^6 - \frac{1}{4}\varphi^8. \tag{6.4}$$

In analogy to the case of the Q-NLSE, Eq. 6.2 is nonintegrable; hence the VA, discussed in Section 5.4, is necessary to predict conditions for stable soliton propagation. Thus, taking into regard the commonly known fact that, for the ordinary cubic nonlinearity, the exact solution for the (1+1)D C-NLSE is $\varphi(X) \propto sech\left(\sqrt{2K}X\right)$, we here adopt the raised-sech *ansatz* [173]

$$\varphi(X) = \Lambda\left[sech\left(\sqrt{2K}X\right)\right]^{\eta}, \tag{6.5}$$

where Λ and η are variational parameters. This ansatz allows one to control the beam's radius by changing the parameter η. It is important to emphasize that while the *Ansatz* is closer to the exact solution of Eq. 6.2, the predictions of the variational model will be much more accurate.

In addition, the total power $P = \int_{-\infty}^{\infty}[\varphi(X)]^2 dX$ of *ansatz* 6.5 is

$$P = \frac{\Lambda^2}{\sqrt{2K}}\left[\frac{\sqrt{\pi}\mathit{\Gamma}(\eta)}{\mathit{\Gamma}\left(\frac{1}{2}+\eta\right)}\right], \tag{6.6}$$

where $\mathit{\Gamma}$ is the Gamma-function. Then, by substituting the raised-sech *ansatz* into Eq. 6.4 and integrating over the 1D space, the following expression for the effective Lagrangian, L, is obtained:

$$\begin{aligned} L = {} & \frac{\Lambda^2 K\eta^2}{2\sqrt{2k}}\left[\frac{1}{\eta} - \frac{\sqrt{\pi}\mathit{\Gamma}(1+\eta)}{\mathit{\Gamma}\left(\frac{3}{2}+\eta\right)} + \frac{2^{2\eta}\mathit{\Gamma}(\eta)\mathit{\Gamma}(2+\eta)}{\mathit{\Gamma}(2+2\eta)} + \frac{2^{1+2\eta}\mathscr{F}_{21}(2+2\eta, 2+\eta, 3+\eta; -1)}{2+\eta}\right] \\ & + \frac{\Lambda^2 K}{2\sqrt{2K}}\left[\frac{\sqrt{\pi}\mathit{\Gamma}(\eta)}{\mathit{\Gamma}\left(\frac{1}{2}+\eta\right)}\right] - \frac{g_3\Lambda^4}{2\sqrt{2K}}\left[\frac{\sqrt{\pi}\mathit{\Gamma}(2\eta)}{\mathit{\Gamma}\left(\frac{1}{2}+2\eta\right)}\right] \\ & - \frac{g_5\Lambda^6}{3\sqrt{2K}}\left[\frac{\sqrt{\pi}\mathit{\Gamma}(3\eta)}{\mathit{\Gamma}\left(\frac{1}{2}+3\eta\right)}\right] - \frac{\Lambda^8}{4\sqrt{2K}}\left[\frac{\sqrt{\pi}\mathit{\Gamma}(4\eta)}{\mathit{\Gamma}\left(\frac{1}{2}+4\eta\right)}\right], \end{aligned} \tag{6.7}$$

where $\mathscr{F}_{21}$ is the hypergeometric function. Eq. 6.7 can be simplified by using the properties of the gamma function:

$$\Gamma(1+t) = t\Gamma(t), \tag{6.8}$$

$$\Gamma(mt) = \frac{\prod_{s=0}^{m-1}\mathit{\Gamma}\left(t+\frac{s}{m}\right)}{(2\pi)^{\frac{m-1}{2}}(m)^{\frac{1}{2}-mt}}. \tag{6.9}$$

By using the recurrence relations for hypergeometric functions:

$$(c-a)\mathscr{F}_{21}(a-1,b,c;z) = -(2a-c-az+bz)\mathscr{F}_{21}(a,b,c;z) - a(z-1)\mathscr{F}_{21}(a+1,b,c;z), \tag{6.10}$$

$$\mathscr{F}_{21}(a,b,a-b+1;-1) = 2^{-a}\sqrt{\pi}\frac{\Gamma(1+a-b)}{\Gamma\left(1+\frac{1}{2}a-b\right)\Gamma\left(\frac{1}{2}+\frac{1}{2}a\right)}, \tag{6.11}$$

$$\mathscr{F}_{21}(a,b,a-b+2;-1) = \frac{2^{-a}\sqrt{\pi}}{(b-1)}\Gamma(a-b+2)\left\{\frac{1}{\Gamma\left(\frac{a}{2}\right)\Gamma\left(\frac{3}{2}+\frac{a}{2}-b\right)} - \frac{1}{\Gamma\left(\frac{1}{2}+\frac{a}{2}\right)\Gamma\left(1+\frac{a}{2}-b\right)}\right\}, \tag{6.12}$$

we obtain that:

$$\mathscr{F}_{21}\left(2+2\eta,2+\eta,3+\eta;-1\right)=2^{-1-2\eta}\sqrt{\pi}\left(1+\eta\right)\left(2+\eta\right)\left[\frac{1}{2}\frac{\Gamma(\eta)}{\left(\frac{1}{2}+\eta\right)\Gamma\left(\frac{1}{2}+\eta\right)}-\frac{1}{\eta\left(1+\eta\right)\sqrt{\pi}}\right]. \tag{6.13}$$

Therefore, the simplified expression for the effective Lagrangian is:

$$L=KP\left[1+\frac{\eta^2}{2\eta+1}\right]-\sum_{m=1}^{3}\frac{\left(m^2-m+6\right)}{6}g_{2m+1}\left(\frac{K}{2\pi}\right)^{\frac{m}{2}}A_{m+1}P^{m+1}, \tag{6.14}$$

with $g_7=+1$ and

$$A_m=\left[\frac{\Gamma\left(m\eta\right)}{\Gamma\left(\frac{1}{2}+m\eta\right)}\right]\left[\frac{\Gamma\left(\frac{1}{2}+\eta\right)}{\Gamma\left(\eta\right)}\right]^m. \tag{6.15}$$

The respective Euler-Lagrange equations for the variational parameters [see Section 5.4], $\partial L/\partial P=0$ and $\partial L/\partial\alpha=0$, lead to the following system of equations:

$$0=K\left[1+\frac{\eta^2}{2\eta+1}\right]-\sum_{m=1}^{3}\frac{\left(m^2-m+6\right)\left(m+1\right)}{6}g_{2m+1}\left(\frac{K}{2\pi}\right)^{\frac{m}{2}}A_{m+1}P^{m}, \tag{6.16}$$

$$0=2\eta KP\left[\frac{\eta+1}{\left(2\eta+1\right)^2}\right]-\sum_{m=1}^{3}\frac{\left(m^2-m+6\right)}{6}g_{2m+1}\left(\frac{K}{2\pi}\right)^{\frac{m}{2}}B_{m+1}P^{m+1}, \tag{6.17}$$

with

$$\begin{aligned}B_m=\frac{\left[\Gamma\left(\frac{1}{2}+\eta\right)\right]^{m-1}}{\left[\Gamma\left(\eta\right)\right]^m\Gamma\left(\frac{1}{2}+m\eta\right)}&\left\{m\Gamma\left(m\eta\right)\left[\Gamma'\left(\frac{1}{2}+\eta\right)-\frac{\Gamma\left(\frac{1}{2}+\eta\right)\Gamma'\left(\eta\right)}{\Gamma\left(\eta\right)}\right]\right.\\&\left.+\Gamma\left(\frac{1}{2}+\eta\right)\left[\Gamma'\left(m\eta\right)-\frac{\Gamma\left(m\eta\right)\Gamma'\left(\frac{1}{2}+m\eta\right)}{\Gamma\left(\frac{1}{2}+m\eta\right)}\right]\right\},\end{aligned} \tag{6.18}$$

where Γ' is the derivative of the Gamma-function.

So far, an analytical procedure of the VA applied to the solution of the CQS-NLSE was developed. However, in order to identify the soliton's stability regions, we performed a study of the linear stability analysis. Here, we open a parenthesis to discuss the basis of a stability analysis criterion developed by Vakhitov and Kolokolov [211]. To facilitate the interpretation, we express the CQS-NLSE (Eq. 6.2) in a more general form, given by:

$$i\frac{\partial\psi}{\partial Z}+\frac{1}{2}\frac{\partial^2\psi}{\partial X^2}+F\left(I\right)\psi=0, \tag{6.19}$$

where $I\left(X,Z\right)=\left|\psi\left(X,Z\right)\right|^2$ is the beam intensity and the function $F\left(I\right)$ characterize the NL properties of the medium. As mentioned above, the shape-preserving solution of Eq. 6.19 has the form: $\psi(X,Z) = \varphi(X)\, exp\,[iKz]$. For a linear stability analysis, we add a small perturbation to the stationary solution:

$$\psi(X,Z) = \{\varphi(X) + [v(X) - w(X)]\, exp\,(i\bar{K}Z) + [v^*(X) - w^*(X)]\, exp\,(-i\bar{K}^*Z)\}\, exp\,[iKz]\,, \tag{6.20}$$

where $v(X)$ and $w(X)$ represents small perturbations. By introducing Eq. 6.20 in Eq. 6.19 and linearizing as a function of $v = v(X)$ and $w = w(X)$, we have two coupled eigenvalue equations:

$$L_0 w = \bar{K}v, \tag{6.21}$$

$$L_1 v = \bar{K}w, \tag{6.22}$$

with $L_0 = \left[-{}^{d^2}\!/_{dX^2} + K - F(I)\right]$, $L_1 = \left[-{}^{d^2}\!/_{dX^2} + K - F(I) - 2I^{\partial F(I)}\!/_{\partial I}\right]$ and $L_0\varphi = 0$. However, since the operator L_0 is positive for any function orthogonal to $\varphi(X)$, then its inverse operator L_0^{-1} exist in a space function orthogonal to $\varphi(X)$. Thus, Eqs. 6.21 and 6.22 can be associated in a single eigenvalue equation

$$L_1 v = \bar{K}^2 L_0^{-1} v, \tag{6.23}$$

where $v(X)$ and $\varphi(X)$ are orthonormal functions:

$$\int\limits_{-\infty}^{\infty} v^*(X)\,\varphi(X)\,dX = 0, \tag{6.24}$$

$$\int\limits_{-\infty}^{\infty} |v(X)|^2\,dX = 1. \tag{6.25}$$

From Eq. 6.23, it is possible to obtain an expression for $\bar{K}$, multiplying both sides by $v^*(X)$ and integrating with respect to X, of the form:

$$\bar{K}^2 = \frac{\int_{-\infty}^{\infty} v^* L_1 v dX}{\int_{-\infty}^{\infty} v^* L_0^{-1} v dX}. \tag{6.26}$$

In this case, the instability appears when $\bar{K}^2 < 0$, because $\bar{K}$ should be imaginary. Thus, as the denominator is always positive, then the condition for instability is related only to the numerator:

$$min\left(\int\limits_{-\infty}^{\infty} v^*(X)\, L_1 v(X)\, dX\right) < 0. \tag{6.27}$$

A method to analyze the local minimum of the function $\int_{-\infty}^{\infty} v^*(X)\, L_1 v(X)\, dX$, which is subject to equality constraints given by Eq. 6.24 and 6.25, is by using the Lagrange multipliers. Here, the functional can be expressed by:

$$\bar{\mathscr{L}} = \int_{-\infty}^{\infty} v^{*}(X) L_1 v(X)\, dX - \kappa \int_{-\infty}^{\infty} v^{*}(X) v(X)\, dX - \mu \int_{-\infty}^{\infty} v^{*}(X)\, \varphi(X)\, dX, \tag{6.28}$$

where κ and μ are the Lagrange multipliers. Without loss of generality, we can assume that $\mu \geq 0$ (otherwise the sign of the function $v(X)$ can be inverted). Then, the extrema of the functional $\bar{\mathscr{L}}$ can be found by the condition $\delta\bar{\mathscr{L}}/\delta v^{*} = 0$[1], resulting in:

$$L_1 v(X) = \kappa v(X) + \mu\varphi(X). \tag{6.29}$$

Therefore, $\int_{-\infty}^{\infty} v^{*}(X) L_1 v(X)\, dX = \kappa \int_{-\infty}^{\infty} v^{*}(X) v(X)\, dX = \kappa$ and the instability occurs when $\kappa < 0$.

On the other hand, we can expand the functions $v(X)$ and $\varphi(X)$ in a complete orthonormalized system of eigenfunctions of the operator L_1 $(L_1\phi_n = \ell_n\phi_n)$ a

$$v(X) = \sum_{n} D_n\phi_n(X), \tag{6.30}$$

$$\varphi(X) = \sum_{m} C_m\phi_m(X), \tag{6.31}$$

with $C_m = \int_{-\infty}^{\infty} \phi_m^{*}(X)\varphi(X)\, dX$ and $D_n = \int_{-\infty}^{\infty} \phi_n^{*}(X) v(X)\, dX$. By substituting Eqs. 6.30 and 6.31 in Eq. 6.29 we have:

$$D_n = \frac{\mu C_n}{(\ell_n - \kappa)}, \tag{6.32}$$

and the orthogonality condition (Eq. 6.24), it is possible to obtain the following relation:

$$\mu \sum_{n} \frac{|C_n|^2}{(\ell_n - \kappa)} = \mu f_1(\kappa) = 0. \tag{6.33}$$

Therefore, if Eq. 6.33 has a solution when $\kappa < 0$, the instability occurs, as mentioned earlier.

- For $\mu = 0$, Eq. 6.33 has a trivial solution and it can be observed of Eq. 6.29 that $v(X)$ is a eigenfunction of L_1 and is orthogonal to $\varphi(X)$.
- For $\mu \neq 0$ (and positive as defined above), we have, in first approximation, that:

$$\sum_{n} \left(\frac{|C_n|^2}{\ell_n} + \frac{|C_n|^2}{\ell_n^2}\kappa \right) = f_1(0) + \left(\sum_{n} \frac{|C_n|^2}{\ell_n^2} \right) \kappa = 0. \tag{6.34}$$

---

[1] δ denotes the variational derivative

Since $f_1(\kappa)$ increases monotonically from $-\infty$ to ∞ and $\sum_n \frac{|C_n|^2}{\ell_n^2} \geq 0$, then to determine the sign of κ it is sufficient to determine $f_1(0)$, that is: for $f_1(0) < 0$, then $\kappa > 0$ and the solution is stable. Nevertheless, for $f_1(0) > 0$ the instability occurs, because $\kappa < 0$. In addition, we can express $f_1(0)$, by using Eq. 6.29, of the form:

$$f_1(0) = \sum_n \frac{|C_n|^2}{\ell_n} = \int_{-\infty}^{\infty} \varphi^*(X) L_1^{-1} \varphi(X)\, dX. \tag{6.35}$$

Moreover, by differentiate the relation $L_0\varphi = 0$ with respect to K, we have:

$$L_1 \frac{\partial \varphi}{\partial K} = -\varphi. \tag{6.36}$$

Therefore, applying the inverse operator, L_1^{-1}, in Eq. 6.36 and then introducing the result in Eq. 6.35, we have:

$$f_1(0) = -\int_{-\infty}^{\infty} \varphi^*(X) \frac{\partial \varphi}{\partial K} dX = -\frac{1}{2}\frac{\partial}{\partial K}\left[\int_{-\infty}^{\infty} |\varphi(X)|^2 dX\right] = -\frac{1}{2}\frac{\partial P}{\partial K}. \tag{6.37}$$

This is, a soliton solution is stable whenever $f_1(0) < 0$ and as a consequence $\partial P/\partial K > 0$. This condition is known as the VK criterion [211] and we use it to identify the stability and instability regions for (1+1)D spatial solitons in cubic-quintic-septimal media.

Returning to our discussion on the analysis of the CQS-NLSE, we can model the behavior of the power, P, as a function of K through two procedures: the first one consists in solving the equation system given by Eqs. 6.16 and 6.17 obtained from the VA. However, due to their complexity, we resort to numerical solutions. These results will be compared with the second procedure, which consists in the direct numerical solution of Eq. 6.3 by using a finite difference method. Fig. 6.1 shows results obtained by numerical solution of the full stationary version of the CQS-NLSE, Eq. 6.3 (circles and triangles), and produced by the VA (dashed lines), i.e., by the numerical solution of Eqs. 6.16 and 6.17. The red line and circles illustrate the dependence of the propagation constant K on the soliton's power P for the septimal-only medium ($g_3 = 0$, $g_5 = 0$) while the blue line and the triangles display the same for a quintic-septimal medium ($g_3 = 0$, $g_5 \neq 0$). The soliton's stability regions were identified on the basis of the VK stability criterion $\partial P/\partial K > 0$. For the two cases shown in Fig. 6.1 we observe $\partial P/\partial K < 0$, indicating that the spatial soliton is unstable in the septimal-only and quintic-septimal media. We recall that the quintic-only medium also gives rise to the instability [217]. In the present case, the addition of the positive seventh-order term leads to additional strong self-focusing, which may result in a supercritical collapse, as shown below.

By contrast, when the focusing cubic nonlinearity is also present ($g_3 > 0$), regions of stability are observed for different values of g_5, as shown in Fig. 6.2, where the third- and seventh-order nonlinearities are fixed to be $g_3 = +1$ and $g_7 = +1$, respectively. In that figure, solid (dashed) lines correspond to regions of stable (unstable) soliton propagation, identified by $\partial P/\partial K > 0$ ($\partial P/\partial K < 0$). Also, it is possible to observe that the maximum power P_{max} for the stable soliton propagation in media with $g_5 = -1$ (red line and circles) is larger than in the

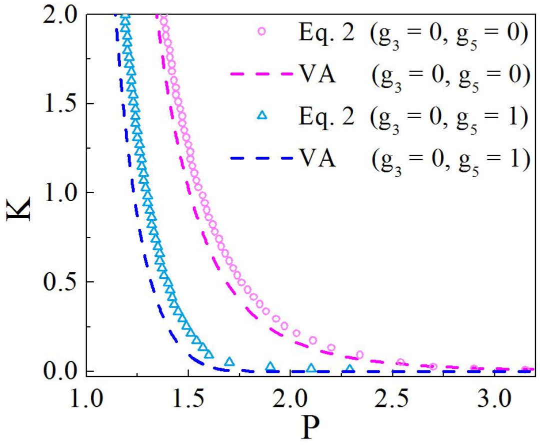

Figure 6.1 The soliton propagation constant K versus the total power P for media with suppressed third-order nonlinearity ($g_3 = 0$). Discrete points correspond to the solution of Eq. 6.3 with $g_5 = 0$ (circles) and $g_5 = 1$ (triangles). Dashed lines were obtained using the variational approximation.

medium with $g_5 = 0$ (blue line and triangles), and larger too than in the medium with $g_5 = +1$ (black line and squares). This is because the negative (defocusing) fifth-order nonlinearity balances the self-focusing effect, enlarging the stability region, while the positive (focusing) fifth-order term accelerates the onset of the critical self-focusing.

To extend these conclusions, numerical solutions of Eqs. 6.3, 6.16 and 6.17 were obtained for various values of g_5 between -1.5 and $+1.5$, with fixed $g_3, g_7 = +1$. For each value of g_5, the maximum power P_{max} which allows the stable soliton propagation was found. Fig. 6.3 shows that, with the growth of the quintic nonlinearity (going from negative to positive, i.e., from defocusing to focusing), the stability region for the soliton propagation is reduced.

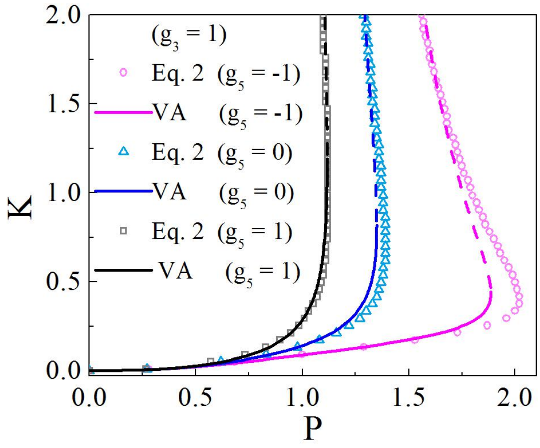

Figure 6.2 Dependence of the soliton propagation constant K on the total power P obtained from solution of Eq. 6.3 and from the VA for media with $g_3 = 1$ and $g_5 = -1$ (red line and circles), $g_5 = 0$ (blue line and triangles), and $g_5 = +1$ (black line and squares). Solid (dashed) lines represent stable (unstable) solitons, as per the VK criterion.

Therefore, large negative values of g_5 help to stabilize the soliton, while large positive values of g_5 promote the onset of the collapse, even at low powers.

From the analysis of Figs. 6.1-6.3, we conclude that the VA using the raised-sech *ansatz* adequately describes the spatial soliton propagation in media exhibiting nonlinearities up to the seventh order.

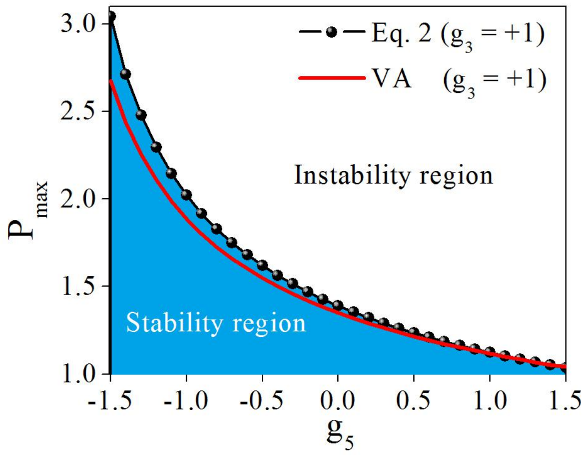

Figure 6.3 The maximum power P_{max} admitting the stable soliton propagation, as per the VK criterion, in media with the focusing cubic and septimal nonlinearity $(g_3, g_7 = +1)$ and different values of the quintic coefficient g_5.

6.1.3 Numerical Simulations of the One-Dimensional CQS-NLSE

The beam propagation in a cubic-quintic-septimal medium was simulated by solving numerically the full CQS-NLSE, Eq. (1), using the split-step compact finite-difference method [235]. Stability and instability regions, predicted by the VA with the help of the VK criterion, were verified by using the raised-sech ansatz, given by Eq. 6.5, as the input for the direct simulations. The details on the numerical method used to simulate the evolution of optical fields in NL media are discussed in Appendix E.

Figure 6.4 exhibits the beam's collapse in the medium without third-order nonlinearity $(g_3 = 0)$, after a very small propagation distance (less than 1.5 times the length diffraction, L_D). Fig. 6.4(a) corresponds to the beam propagation in the septimal-only medium $(g_3 = g_5 = 0)$, for the soliton propagation constant $K = 1$, with the respective values $P = 1.51$ and $\eta = 1.97$ obtained from Eqs. 6.16 and 6.17. Strong self-focusing is observed at $Z \approx 1.3$, resulting in the formation of jets induced by the seventh-order nonlinearity (the supercritical collapse). A still faster collapse is observed by adding the focusing quintic term $(g_3 = 0,\ g_5 = +1)$, which additionally contributes to the development of the collapse, as shown in Fig. 6.4(b). The values of $K = 1$, $P = 1.23$, and $\eta = 1.90$, predicted by the VA, were used to construct the input beam for the simulations of the quintic-septimal medium. In both cases, unstable propagation of spatial solitons is observed due to the dominant role of the septimal nonlinearity, in agreement with Fig. 6.1. Here and in Fig. 6.5, the region after the onset of the collapse is not displayed, as

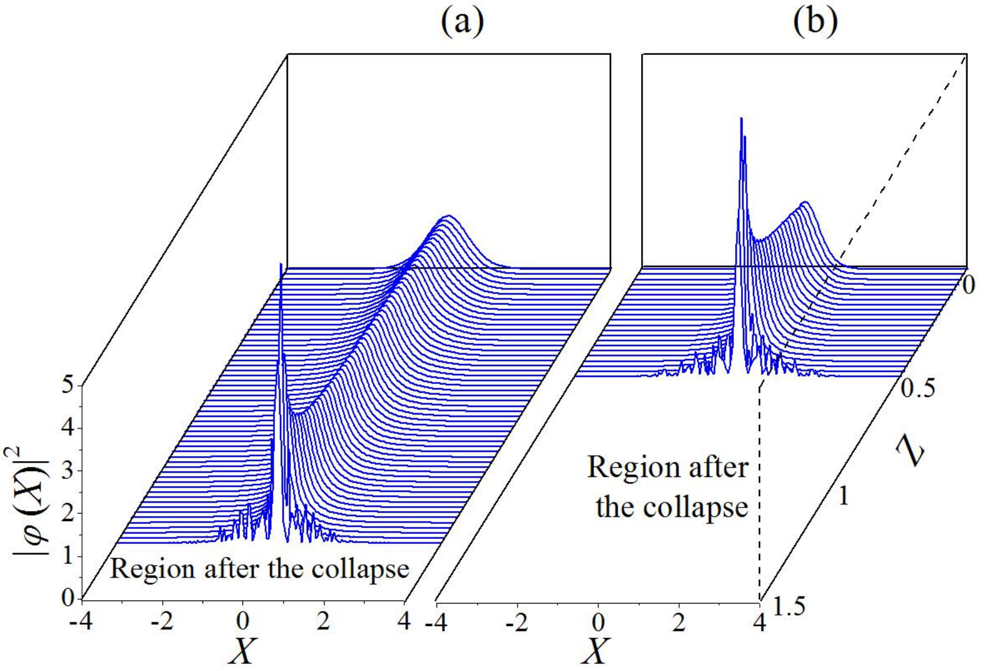

Figure 6.4 The supercritical collapse of the beam produced by numerical solutions of the CQS-NLSE in media with the third-order nonlinearity suppressed $(g_3 = 0)$ and (a) $g_5 = 0$; (b) $g_5 = +1$.

simulations of the present model are not sufficient for tracing the postcollapse evolution.

Figure 6.5 shows the predicted beam propagation in the cubic-quintic-septimal medium, for different values of K. Figures 6.5(a)-6.5(d) exhibit a stable family of solitons obtained by solving the CQS-NLSE with $g_3 = +1$ and $g_5 = +1$. For values of K and P below the limit values for the stable propagation $(K_{max}, P_{max}) = (1.19, 1.11)$, it is possible to observe the formation of periodically oscillating breathers, probably due to a small inaccuracy of the input with respect to the exact wave form. On the other hand, Figs. 6.5(e) and 6.5(f) show the collapse for $(K = 1.5, P = 1.11)$ and $(K = 2.0, P = 1.10)$, respectively. Thus, the stability boundaries, predicted by the VA in combination with the VK criterion, enable the identification of the stability boundaries, which separate the formation of the fundamental soliton and the collapse, with good accuracy.

Additional simulations of Eq. 6.2 were performed to confirm the predictions of the VA. In particular, similar results were obtained for the media with $(g_3 = +1, g_5 = -1)$ and $(g_3 = +1, g_5 = 0)$, in agreement with Fig. 6.2.

From the experimental point of view, suitable conditions for observing stability regions, as well as the critical and supercritical collapse, may be provided by the NM procedure reported in MDNCs. In principle, manipulating the volume fraction of silver colloids studied in Chapter 4, we can obtain a focusing quintic medium which would allow to observe the critical collapse. However, to observe the supercritical collapse is necessary a positive septimal nonlinearity, contrary to what was observed in the Ag colloids of Chapter 4. Nevertheless, experiments in the infrared will help to expand the relevant parameters space, as one may flip the signs of the NL refractive indices of different orders by varying the detuning with respect to the SPR in the

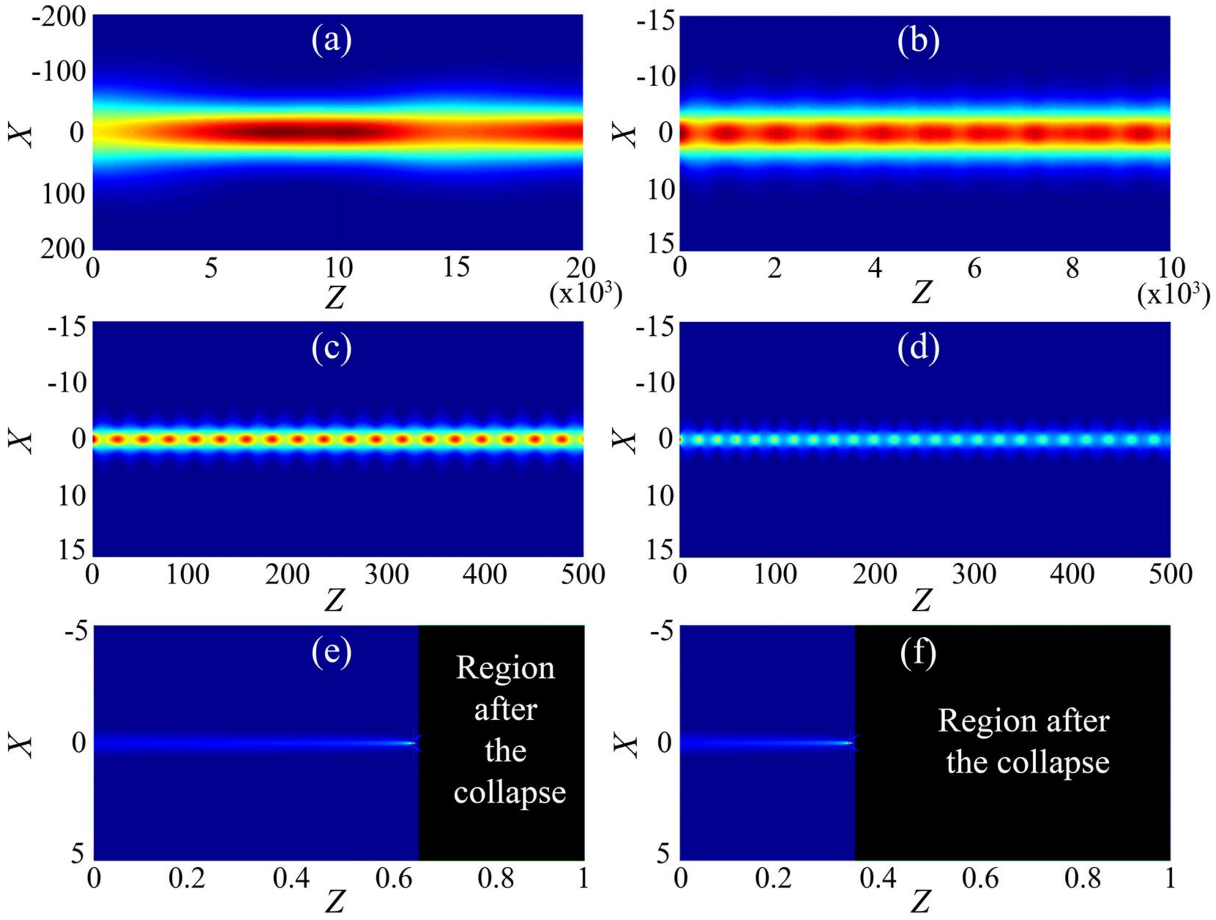

Figure 6.5 The evolution of stable and unstable fundamental solitons in the focusing cubic-quintic-septimal media $(g_3 = g_5 = g_7 = +1)$ with values of (K, P, η) taken as (a) $\left(10^{-4}, 0.05, 1.47\right)$, (b) (0.05, 0.63, 1.48), (c) (0.3, 1.0, 1.60), (d) (1, 1.11, 1.69), (e) (1.5, 1.11, 1.70), and (f) (2, 1.10, 1.77).

NPs. Thus, taking into regard nonlinearity parameters reported in Chapter 4 and the perspective of further experiments with different laser wavelengths and pulse durations, it should be quite realistic to reach conditions for the observation of the effects predicted in the present work, using planar waveguides filled with silver colloids.

6.2 TWO-DIMENSIONAL SPATIAL SOLITONS IN QUINTIC-SEPTIMAL MDNCS

6.2.1 Introduction

The study of NL phenomena induced by laser pulses propagating in transparent media is a complex subject of great interest. For moderate laser intensities the NL propagation of light is understood in terms of the optical Kerr effect which describes light-induced changes in the materials' refractive index that may lead to beam self-focusing, spectral broadening, and several other NL phenomena [21]. For large light intensities the optical response is affected by saturation of the Kerr effect and HON may induce optical phenomena such as multiphoton absorption and change of the refractive index due to plasma formation [223, 236]. Although for some applications HON may cause problems, in several cases their contributions are very important and desired. For instance, HON may enable formation of stable solitons in homogeneous isotropic media [173, 237] and influence many aspects of filamentation in gases and condensed matter [93, 97]. HON-assisted phenomena such as liquid light condensates [28], harmonic conical diffraction [225], and filamentation [26, 224, 238] are largely studied with basis on the NL interaction of light with various physical systems. Also of great interest is the exploitation of HON for quantum information [239], quantum memories [240], and for coherent quantum control [241]. From the theoretical point of view analogies between superfluids [242], plasmas [243], and Bose-Einstein condensates [244] can be evaluated from the behavior of highly NL optical systems. In studies related to the phenomena mentioned above, several authors devoted special attention to the concept of nonlinearity management which also inspired large activity in theoretical physics and mathematics research [214, 178, 179, 245, 246]. In the present Section the management of HON is performed to investigate the formation of optical spatial solitons.

As mentioned earlier, spatial solitons are self-trapped optical beams that propagate with invariant shape due to a balance between linear diffraction and NL interaction with the medium where they propagate [48]. Various kinds of spatial solitons supported by different types of nonlinearities were studied since the report of self-trapping of optical beams in [75], aiming to be implemented for applications such as optical interconnects [247], image transmission [248], and waveguides for optical communication devices [249, 250]. In particular, the observation of (1+1)D spatial solitons was reported in [36, 78] and their behavior is described by the cubic NL Schrödinger equation. However, the stable propagation of (2+1)D spatial solitons is not supported in homogeneous isotropic media with instantaneous cubic nonlinearity (Kerr media), due to catastrophic self-focusing [76, 218, 251]. Nevertheless, HONs are manifested in media with large NL susceptibility allowing arrest of the catastrophic beam collapse. Indeed, the propagation of stable (2+1)D spatial solitons was reported in a glass presenting large 3PA cross section [45, 46]. More recently, there was a report of the propagation of stable (2+1)D spatial solitons in liquid CS_2 due to the simultaneous contributions of third- and fifth-order susceptibilities, $\chi^{(3)}$ and $\chi^{(5)}$, respectively [30]. The theoretical description based on the CQ-NLSE including 3PA showed good agreement with the experimental results. The opposite signs of $Re\left(\chi^{(3)}\right) > 0$ and $Re\left(\chi^{(5)}\right) < 0$, as well as the contribution of $Im\left(\chi^{(5)}\right) > 0$, were the ingredients that allowed the observation of robust bright spatial soliton propagation for a long distance.

Unfortunately, homogeneous systems do not allow easy control of HON in order to suppress or enhance particular NL contributions. On the other hand, NM of nanocomposites enables the control of effects associated with NL susceptibilities of different order, as discussed in Chapter 4. Thus, HONs of colloids containing silver NPs are very interesting for demonstration of unique optical effects, among these, applications in optical spatial solitons. In principle, NL parameters previously determined in MDNCs have been considered in theoretical papers that proposed the observation of many NL effects in systems with quintic and cubic-quintic nonlinearity [172, 174, 252, 175]. However, as seen in the previous section, septimal nonlinearities can also generate important contributions to the evolution and stable propagation of spatial solitons.

In this Section, we exploit the NM procedure presented in Chapter 4 and report the propagation of (2+1)D spatial solitons in a quintic-septimal nanocomposite. Robust spatial solitons propagating by $\sim$ 10 Rayleigh lengths were observed due to simultaneous contributions of the focusing fifth- and defocusing seventh-order susceptibilities. Here, the behavior of the propagating optical pulses was described by numerical solution of the CQS-NLSE with appropriate relative contributions of $\chi_{eff}^{(2N+1)}$, $N = 1, 2, 3$, for different f values, as discussed in Section 5.3.1.

6.2.2 Experimental Details

The experimental setup for investigation of bright spatial solitons is illustrated in Fig. 6.6. The second harmonic of a Q-switched and mode-locked Nd:YAG laser (80 ps, 10 Hz, 532 nm) with maximum pulse energy of 10 μJ was used. The control of the incident beam power on the sample was made with a $\lambda/2$ plate followed by a Glan prism. A spatial filter was used to obtain a beam with a nearly Gaussian spatial profile, which was focused by a 1-cm focal length lens on the input face of the quartz cell (length: 10 mm) containing silver NPs suspended in acetone (sample A of Appendix B).

Characterization of input beam was performed by placing a CCD camera on a motorized displacement stage and by capturing several images around the focus of the lens L1, as schematized in Fig. 6.7(a). Transverse images were analyzed by a numerical program in Matlab

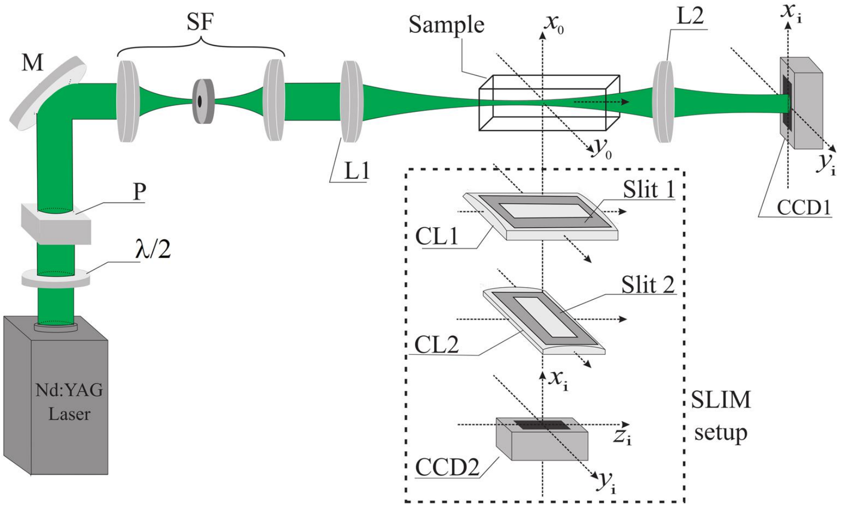

Figure 6.6 Experimental setup. Polarizer (P); mirror (M); spatial filter (SF); spherical lens with $f = 10$ mm (L1). The CCD1 camera was used to obtain the transmitted beam spatial profile. Cylindrical lenses with $f = 40$ mm (CL1) and $f = 80$ mm (CL2), and CCD2 were used in the SLIM setup. Sample length: 10 mm.

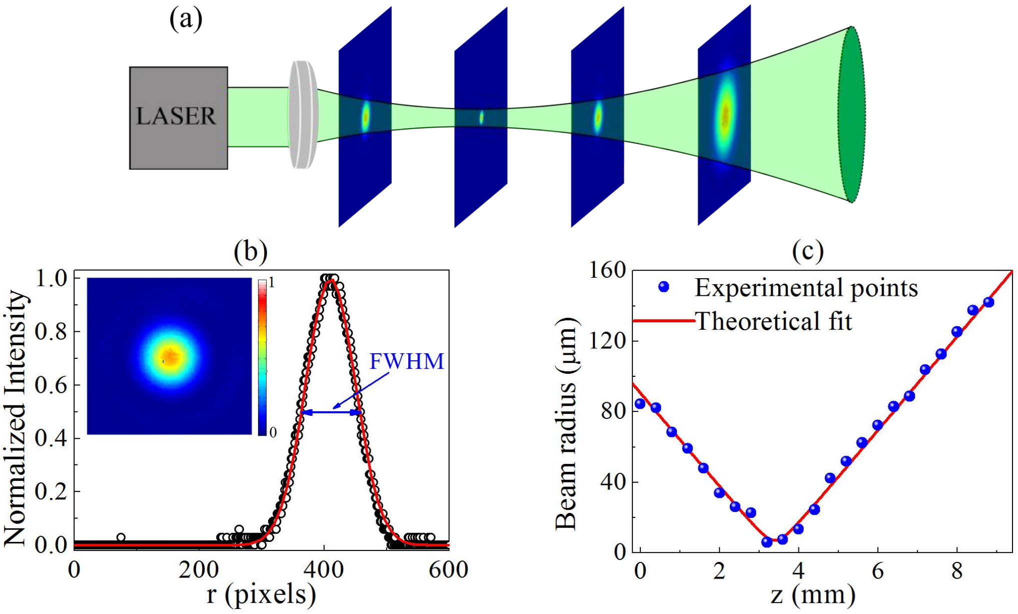

Figure 6.7 (a) Experimental scheme for characterization of the input Gaussian beam. (b) Transverse beam profile of the input Gaussian beam and its respective intensity distribution (black circles). The red line corresponds to a Gaussian fit. (c) Beam radius of Gaussian beam $[w(z)]$ as a function of the propagation distance, z. The red line was obtained by fitting Eq. 6.38.

which allows to find the full-width of the beam at half of the maximum intensity (FWHM), see for example Fig. 6.7(b). Fig. 6.7(c) shows the radius of the input beam at different positions along the propagation axis. The experimental points were adjusted by the expression of the beam radius as a function of the propagation distance, given by:

$$w(z) = w0\sqrt{1+\left(\frac{z-z_0}{z_R}\right)^2}, \tag{6.38}$$

where w_0 is the beam waist in the focus of the lens L1, located at position $z = z_0$, $z_R = \frac{n_0 \pi w_0^2}{\lambda M^2}$ is the Rayleigh length, n_0 is the linear refractive index ($n_0 = 1$ for the air), λ is the light wavelength and M^2 is the beam quality (or propagation) factor. A beam waist of 7.2 µm with Rayleigh length of 0.27 mm and beam quality factor $M^2 = 1.13$ were measured for our experimental setup.

The spatial profile of the propagating beam along the sample was characterized following two complementary procedures. The first procedure was used in [30, 253] and consists in imaging the transverse beam profile in the output face of the cell by placing a lens L2 and a CCD camera (1360×1024 pixels) in the far-field region, aligned with the beam-propagation axis. Lens L2 was used to obtain the beam's image with magnification of 5. The second procedure was based on the scattered light imaging method (SLIM) [254]. This method allows the observation and characterization of the beam propagation inside the sample by monitoring the light scattered in the direction perpendicular to the beam axis. To perform measurements an imaging optical system, consisting of two cylindrical lenses oriented with orthogonal axes and a CCD camera, were used as shown in Fig. 6.6. Lenses with 40-mm and 80-mm focal lengths focusing on the y-axis (transverse direction) and z-axis (the beam-propagation direction) were used to obtain an image magnification of 7 and 1/2, respectively.

For calibration of the SLIM, it was used a liquid scattering medium (soluble oil). Fig 6.8(a) shows the scattered light image for a laser intensity of 5 GW/cm^2. NL behavior of soluble oil was not observed even for the maximum laser intensity, and the evolution of the beam radius along propagation can be adequately described by Eq. 6.38. Notice that the beam can be visualized in the entire cell. The image is processed as a matrix where each element is an image pixel. Each column represents a specific z position and the elements of the row are the measured intensity along the y-direction. Fig 6.8(b) shows the beam radius as a function of the z position obtained by numerical fit of the laser beam profile using a Gaussian function along the columns. From this figure and using Eq. 6.38, we can find the values of beam waist and its position along the z-axis, as well as the beam quality factor and the Rayleigh length, which allows the comparison with the results of Fig. 6.7. Values of $w_0 = 7.1$ µm, $z_R = 0.26$ mm and $M^2 = 1.14$ were found using the SLIM.

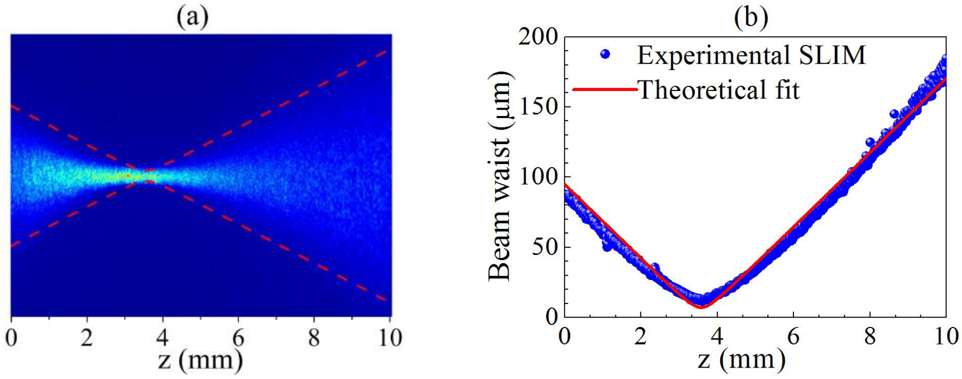

Figure 6.8 (a) Scattered light image obtained by SLIM of a Gaussian beam propagating in soluble oil (linear scattering medium). (b) Beam radius of Gaussian beam $[w(z)]$ as a function of the propagation distance, z. The red line was obtained by fitting Eq. 6.38.

After characterization of the input beam, the cell containing the silver colloid was placed with its input face located at the focus position of the lens L1, which was identified by the characterization techniques mentioned above. This position guarantees that the Gaussian beam is entering into the sample with a plane wavefront.

As an additional comment, our research group developed a methodology to implement the SLIM for measurement of NL parameters of scattering media, precisely where Z-scan technique presents great limitations. This work will not be discussed in this thesis, but further details can be seen in [255].

6.2.3 Results and Discussions

The experiments were performed with various laser intensities to investigate the formation of the bright spatial solitons.

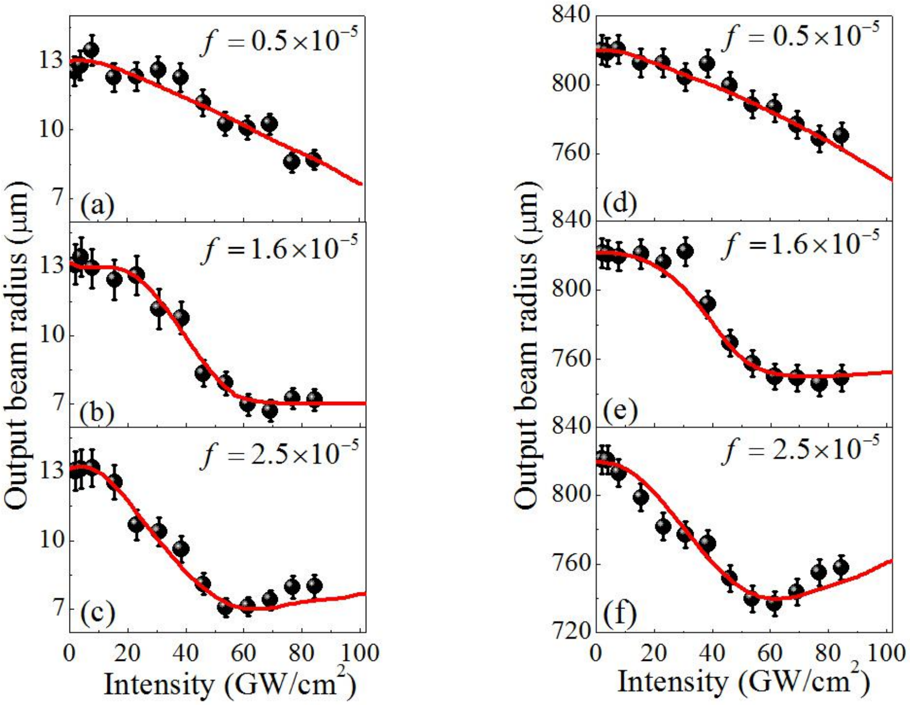

Figure 6.9 Dependence of the transmitted laser beam radius as a function of the input intensity for (a) $f_1 = 0.5 \times 10^{-5}$, (b) $f_2 = 1.6 \times 10^{-5}$, and (c) $f_3 = 2.5 \times 10^{-5}$ using a 2-mm-long cell. A CCD camera acquired the beam profile at the output face of the cell; for (d) f_1, (e) f_2, and (f) f_3 using a 1-cm-long cell. The CCD camera was placed 7 cm away from the output face. The red solid lines represent theoretical results obtained from the CQS-NLSE taking into account the beam diffraction in the propagation from the cell to the camera.

Figures 6.9(a)-(c) summarize the beam radius measurements obtained according to the first procedure as a function of the incident intensity. The data were collected after the beam passed through a 2-mm-long sample. A telescope with magnification of 5 was placed in front of the CCD camera in order to obtain an image of the exit plane of the sample over a large detection area. The black dots represent the experimental data while the red lines were obtained by solving the CQS-NLSE, as described below. For $I \leq 10$ GW/cm^2 the beam radius does not change much for the three volume fractions and its value is equal to that of a beam propagating in a linear host medium with linear refractive index equal to 1.36; the small changes are only due to the linear diffraction. For $I > 10$ GW/cm^2 a gradual decrease in the beam radius size is observed due to the samples' nonlinearity, reaching a minimum radius for $I \approx 60$ GW/cm^2, as shown in Figs. 6.9(b) and 6.9(c). The minimum radius reached, $w \approx 7$ μm, is equal to the input beam waist. The behavior shown in Fig. 6.9(b), where a beam waist remains constant for $I \geq 60$ GW/cm^2, indicates the formation of stable spatial solitons.

Figures 6.9(d)-(f) show similar results using a 1-cm-long sample. The CCD camera was placed 7 cm away from the exit face of the cell to exploit a large detection area. A similar behavior of the beam radius as a function of the incident intensity was observed for the three volume fractions, with minimum beam radius of $w \approx 750$ μm, recorded by the camera positioned in the far-field region, for $I \approx 60$ GW/cm^2. Numerical results were obtained by solving the NL propagation equation using the parameters determined by Z-scan measurements for each f value, considering a light propagation distance of 2 mm inside the cell corresponding to Figs. 6.9(a)-(c); the results shown in Figs. 6.9(d)-(f) were obtained by considering the light propagation inside the 10-mm cell and 7 cm in the free space where the beam suffers only linear diffraction.

The results shown in Figs. 6.9(a) and 6.9(d) for $I < 20$ GW/cm^2 are essentially due to $\chi_{eff}^{(3)}$ while Figs. 6.9(b) and 6.9(e) correspond to a colloid with NL behavior dominated by $Re\left[\chi_{eff}^{(5)}\right] > 0$ and $Re\left[\chi_{eff}^{(7)}\right] < 0$, with $Re\left[\chi_{eff}^{(3)}\right] = 0$. Figures 6.9(c) and 6.9(f) show results contributed by $\chi_{eff}^{(3)}$, $\chi_{eff}^{(5)}$, and $\chi_{eff}^{(7)}$, as characterized in Chapter 4. For intensities larger than 20 GW/cm^2 the contribution of $\chi_{eff}^{(7)}$ becomes relevant in all cases illustrated by Fig. 6.9. The corresponding values of the effective NL parameters, determined using the Z-scan technique, were $n_{2,eff} = +1.7 \times 10^{-15}$ cm^2/W, $n_{4,eff} = +1.3 \times 10^{-25}$ cm^4/W^2, and $n_{6,eff} = -2.0 \times 10^{-35}$ cm^6/W^3 for $f = 0.5 \times 10^{-5}$; $n_{2,eff} = 0$, $n_{4,eff} = +3.2 \times 10^{-25}$ cm^4/W^2, and $n_{6,eff} = -7.0 \times 10^{-35}$ cm^6/W^3 for $f = 1.6 \times 10^{-5}$; and $n_{2,eff} = -1.3 \times 10^{-15}$ cm^2/W, $n_{4,eff} = +7.0 \times 10^{-25}$ cm^4/W^2, and $n_{6,eff} = -1.1 \times 10^{-34}$ cm^6/W^3 for $f = 2.5 \times 10^{-5}$.

Figure 6.10(a) shows transverse beam images for $f = 1.6 \times 10^{-5}$ with intensities varying from 7 GW/cm^2 to 85 GW/cm^2, obtained using the SLIM. For $I > 20$ GW/cm^2, it is possible to observe a region where the beam radius remains constant, which corresponds to the stable propagation of bright solitons. A (2+1)D spatial soliton with maximum

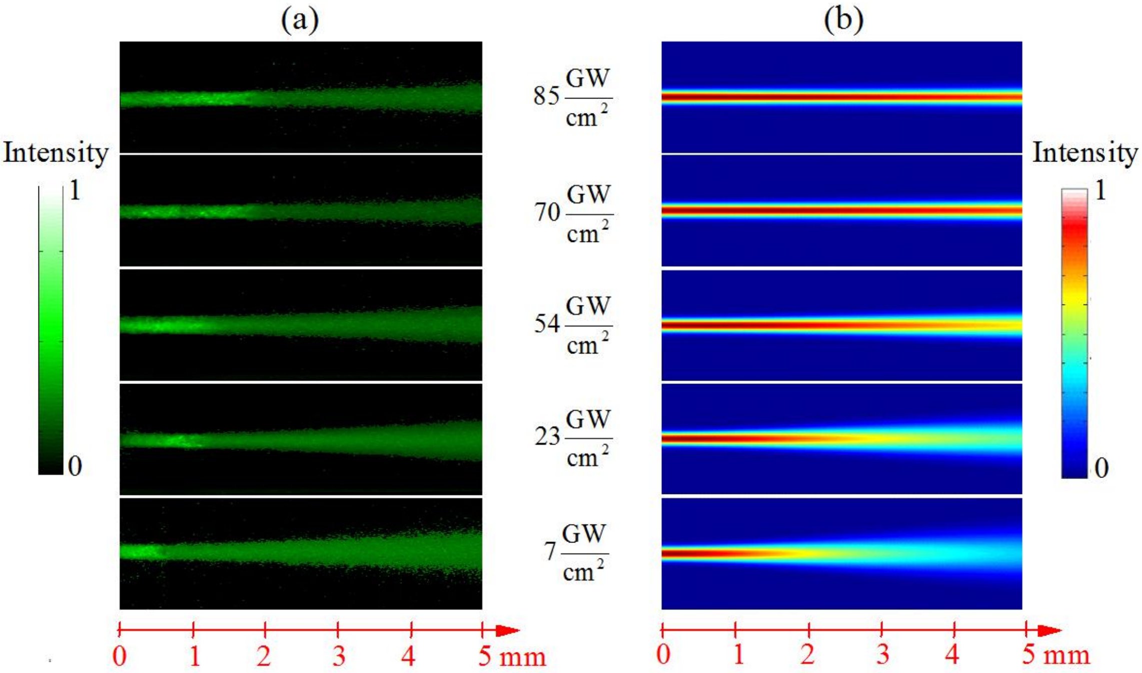

Figure 6.10 Transverse beam images: (a) experimental data obtained using the SLIM and (b) numerical results obtained from Eq. 6.39, for $f = 1.6 \times 10^{-5}$.

propagation distance of ~ 2.3 mm was reached for $I \geq 70$ GW/cm^2.

In order to describe the laser beam propagation we solved numerically the CQS-NLSE, discussed in Section 5.3.1, given by

$$i\frac{\partial A_0}{\partial z}+\frac{1}{2k_0}\nabla_\perp A_0=-\frac{k_0}{2n_0^2}\left[3\chi_{eff}^{(3)}|A_0|^2+10\chi_{eff}^{(5)}|A_0|^4+35\chi_{eff}^{(7)}|A_0|^6\right]A_0, \tag{6.39}$$

where A_0 is the optical field amplitude ($A_0 = A'/2$ in Eq. 5.31). Dispersion effects and linear losses were ignored due to the linear absorption coefficient α_0, at 532 nm for the three volume fractions discussed above, are approximately two orders of magnitude smaller than the contributions of $\alpha_{2N,eff}I^N$ with $N = 1, 2, 3$, for the intensities studied. The values of $\chi_{eff}^{(3)} = -i6.3 \times 10^{-22}$ m^2/V^2, $\chi_{eff}^{(5)} = \left(+3.7\times10^{-38}+i3.3\times10^{-37}\right)$ m^4/V^4 and $\chi_{eff}^{(7)} = \left(-4.2\times10^{-54}-i3.5\times10^{-54}\right)$ m^6/V^6, for $f = 1.6\times10^{-5}$, were obtained from the NL characterization of sample A measured in Chapter 4.

Figure 6.10(b) shows the numerical results obtained by solving Eq. 6.39, using the split-step compact finite difference method [235] for the five laser intensities corresponding to Fig. 6.10(a). Further details on the numerical simulations can be obtained in Appendix E. The agreement between the numerical and the experimental results corroborates the observation of (2+1)D stable soliton propagation with maximum propagation distance for $I \geq 70$ GW/cm^2.

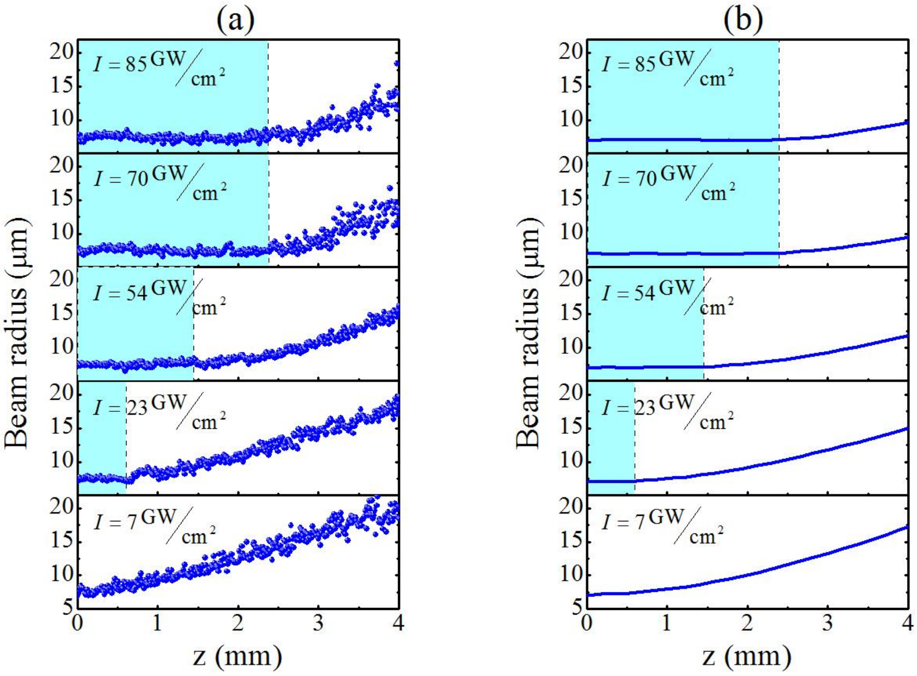

Figure 6.11 (a) Experimental and (b) theoretical beam radius as a function of propagation distance obtained from Fig. 6.10. The shaded areas indicate the region of stable soliton propagation $\left(f = 1.6\times10^{-5}\right)$.

Figure 6.11 shows the variation of the laser beam radius along the pathway inside the sample with $f = 1.6 \times 10^{-5}$, determined from the images of Fig. 6.10, using the SLIM. The experimental results in Fig. 6.11(a) clearly show that as the laser intensity increases, the propagation distance at which the beam waist remains constant also increases. The maximum propagation distance of ~ 2.3 mm corresponding to ~ 10 Rayleigh lengths was observed at the highest input intensities. The good agreement between the experimental and theoretical results can be observed comparing the shaded rectangles drawn in Figs. 6.11(a) and 6.11(b).

Results of similar measurements and analysis for $f = 2.5 \times 10^{-5}$ are shown in Fig. 6.12. Here, soliton propagation was not observed for intensities between 3 and 85 GW/cm^2 due to the negative third-order refractive index that dominates the NL response. Notice that Fig. 6.12(a) for $I \geq 54$ GW/cm^2 shows a change in the laser beam radius followed by formation of a new focus around of $z = 2$ mm; Fig. 6.12(b), obtained solving Eq. 6.39, displays similar behavior.

For $f = 0.5 \times 10^{-5}$ the scattered light intensity was very weak and transverse beam images based on the SLIM were not acquired because of the low sensitivity of the CCD camera.

Therefore, through the NM procedure in MDNCs, it was possible to manage a quintic-septimal (focusing-defocusing) medium which supports the stable propagation of (2+1)D bright solitons for approximately 10 Rayleigh lengths. In other cases, where the nonlinearity is dominated by a defocusing cubic nonlinearity or both cubic and quintic nonlinearities are focusing, the brigth spatial solitons were observed to be unstable.

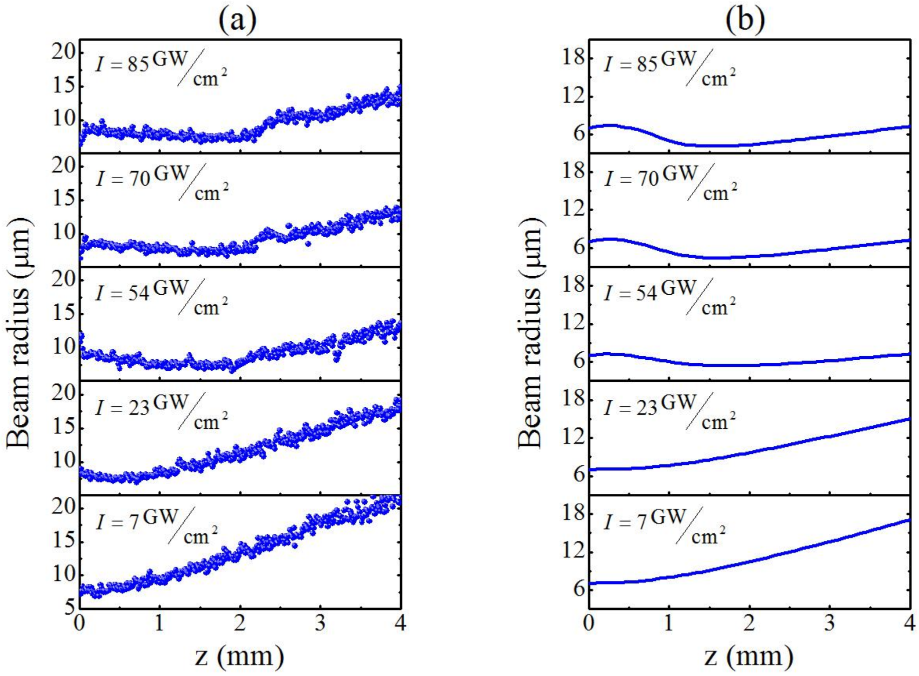

Figure 6.12 (a) Experimental and (b) theoretical beam radius as a function of propagation distance for $f = 2.5 \times 10^{-5}$.

What is now proved was once only imagined.
- WILLIAM BLAKE

7 OPTICAL VORTEX SOLITONS

7.1 INTRODUCTION

Optical vortices (OVs) are singularities in phase fronts of light beams [90]. The spiral phase of OV beams rotates about the optical axis that causes the wavefront of the light to twist like a corkscrew as it propagates. Thus, one of the most essential characteristic of these helical beams is that it carry a phase factor, $exp\left(im\theta\right)$, where θ is the azimuthal coordinate and m is the topological charge, which indicates the number of complete 2π twists of the phase on the transverse plane perpendicular to the beam axis. The topological charge can be integer or fractional [256], with positive or negative signal depending on the handedness of the twist. Another important feature of the OV beams is the special behavior of the phase near the vortex pivot which gives rise to a circular flow of energy in a given direction, being related to the ability of OVs to carry orbital angular momentum (OAM) l [257]. In fact, an interesting phenomenon occurs in the center of the vortex, because the velocity of this rotation become infinite and thus the light intensity vanishes at the vortex pivot [90]. In most cases, studies in OVs tend to be driven to beams with azimuthal symmetry, called cylindrical OVs. This special type of vortices, which is studied in this thesis, are characterized by exhibiting the same values of topological charge, m, and the average classical OAM per photon, l [258]. However, this equality is violated to shaped-OV beams, which are asymmetric beams that can be obtained, for example, by distributing the topological charge in different asymmetric geometries [259].

OVs can be generated by using different schemes, such as computer-synthesized holograms [259, 260], spiral phase plates [261, 262], double cylindrical lens phase converter [263], interference of three and more plane waves [264] and NL optical processes [265, 266]. In all our experiments, OV beams were produced by a spiral phase plate or also called vortex phase plate (VPP), which was manufactured by RPC Photonics. VPP is a disc-shaped optical component with refractive index n_0 and optical thickness $\triangle t$ that increases with azimuthal angle, θ, according to the function: $\triangle t = \theta\left(n_0 - 1\right)m\lambda/\left(2\pi\right)$, where m and λ are the topological charge and the laser wavelength, respectively. The function of this optical component is to introduce a phase $exp\left(im\theta\right)$ during the transmission of an incident plane wave, in order to produce a OV beam with its associated OAM. Fig. 7.1 shows a representative diagram of how to generate a doughnut-shaped OV beam with $m = \pm 1$ after pass a Gaussian beam through a VVP, just as it was done in our experiments.

The study and understanding of the formation and propagation of OV beams allowed significant contributions in many areas that include optical tweezers [268, 269], astrophysics [270], microscopy [271], plasmonics [272, 273] and optical communication systems [274, 275]. In the context of NL optics, OVs are analyzed on the basis of self-trapped beams or solitons. Optical vortex solitons (OVSs) are stable (2+1)D structures which appears in defocusing Kerr media, contrary to the bright solitons discussed in the previous chapter [91]. It comes about when the defocusing effect is balanced by diffraction of the vortex core. Thus, an OVS will propagate

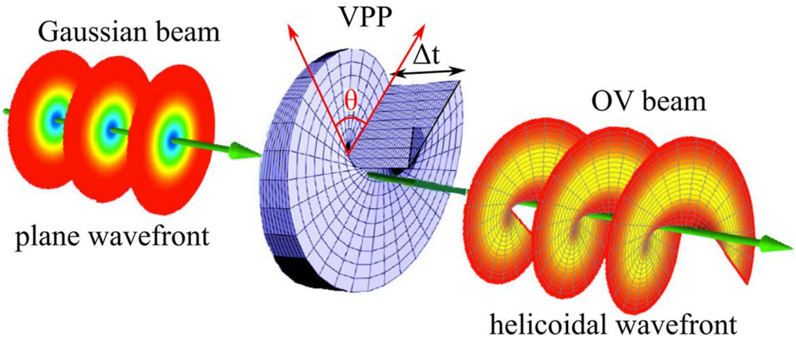

Figure 7.1 OV beam generation by passing a Gaussian beam through a VPP [267].

without any change of size, assuming an infinite plane wave background [90]. However, it is well known that OVSs are highly sensitive to azimuthal instability. In particular, OVSs in self-focusing Kerr media are subject to spontaneous azimuthal symmetry breaking into one or more beams due to the modulational instability [49]. Although there are several theoretical proposals to stabilize the OVSs in SF media (see [90] and references therein), only one was experimentally proved by using an external potential such as optically induced photonic lattices [276, 277].

In this chapter, we study the OVS propagation in SF and SDF Kerr media, as well as we describe two applications based on the manipulation of light-by-light using OVSs. In section 7.2, we show, for the first time, the observation of the stable propagation of OVSs in a saturable self-focusing medium. This stability region, which is not identified by theoretical models studied so far, was obtained by exploiting a simultaneous contribution of the saturation of the refractive nonlinearity and 3PA, corresponding to the NL behavior of CS_2 in the picosecond regime (see Appendix C). However, at larger intensities, the OV beams lose their stability, spontaneously breaking into bright fragments due to spatial modulation instability, as predicted by previous theory [49]. In section 7.3, we exploit the instability regime of saturable SF media (CS_2) in order to control the emerging beams, produced by the spontaneous splitting of the OVSs, by adding a weak Gaussian beam propagating collinearly with the OVS. Rotation of the emerging beams and energy transfer between them were obtained using a control Gaussian beam with smaller intensity than the vortex beam, revealing an alternative approach for the design of all-optical modulators. Numerical simulations based on the NLSE, including the 3PA and nonpolynomial saturation of the refractive nonlinearity, discussed in Section 5.3.2 for CS_2 in picosecond regime, demonstrate close agreement with experimental results obtained in Sections 7.2 and 7.3. On the other hand, Section 7.4 is focuses on the stability regime to produce an optically induced OVS waveguide in a cubic-quintic SDF medium (silver colloid). The waveguide effect induced by the bright region of the vortex beam, is mainly due to the defocusing nonlinearity that allows the guiding and confinement of a probe beam propagating inside of the OVS dark region. In this case, the experimental results were corroborated by numerical simulations based on the CQ-NLSE, discussed in Section 5.3.1, showing excellent agreement.

7.2 OVS IN SATURABLE SELF-FOCUSING MEDIA

7.2.1 Introduction

The spatiotemporal evolution of light beams in NL media is a subject of broad interest in fundamental and applied research [278, 279, 280]. In transparent condensed (solid or liquid) materials, the beam propagation is generically dominated by the nonresonant Kerr nonlinearity, which induces changes in the materials' refractive index that may lead to the beam's self-focusing (or defocusing), spectral broadening, and other NL phenomena (see Section 7.5.2 of [21]). The beam propagation in centrosymmetric materials with the nonlinearity described by the third-order susceptibility, $\chi^{(3)}$, is usually modeled by the C-NLSE [21]. Of particular interest are beams representing spatial solitons, with diverse applications to photonics, optical computing, telecommunications, etc. It is commonly known that SF media allow the stable propagation of (1+1)D spatial brigth solitons, due to the balance between the linear diffraction and self-focusing [36, 78, 75]. However, (2+1)D optical solitons in media with the instantaneous cubic nonlinearity are unstable, due to the catastrophic self-focusing (critical collapse) at high powers [76, 218, 251]. Nevertheless, saturation of the nonlinearity may prevent the collapse, securing stable soliton propagation. In particular, the analysis has shown that the NLSE produces stable solutions for materials exhibiting an interplay of the focusing third-order and defocusing fifth-order susceptibilities, with $Re\left[\chi^{(3)}\right] > 0$ and $Re\left[\chi^{(5)}\right] < 0$, in one, two, and three dimensions [228, 281]. Recently, the stable propagation of (2+1)D spatial solitons in carbon disulfide, CS_2, supported by this mechanism, has been demonstrated experimentally [30]. On the other hand, by using resonant nonlinearity in the rarefied gas of three-level atoms—which includes competing cubic and quintic nonlinearities, along with the four-wave mixing (FWM)—it was possible to demonstrate the stabilization, on a long propagation distance ($\sim$ 20 diffraction lengths), of various soliton species including fundamental, dipole, and vortex ones. The FWM in a nonresonant medium (glass) was exploited too to arrest the collapse of (2+1)D quasisolitons [282, 283]. Furthermore, applying a NM procedure in MDNCs, it was possible to observe stable (2+1)D spatial solitons in a composite with suppressed $\chi^{(3)}$ but conspicuous focusing $\chi^{(5)}$ and defocusing $\chi^{(7)}$ susceptibilities, as discussed in Section 6.2.

In defocusing media, spatial solitons appear as optical vortices and dark solitons [284, 48]. Contrary to bright (fundamental) spatial solitons, delocalized (dark) optical vortex solitons (DOVSs), supported by a finite background, are stable structures in defocusing NL Kerr media [91]. Experimental observations of DOVSs in defocusing media were reported by several groups [237]. However, bright (self-trapped) optical vortex solitons in self-focusing media are subject to spontaneous azimuthal symmetry breaking due to the corresponding modulational instability [49, 285, 286, 287, 288, 289]. Many works have aimed to identify suitable conditions for the stabilization of self-trapped OVSs [290, 291, 292, 293, 50, 294, 295, 296]. In particular, bright OVSs in media combining cubic focusing and quintic defocusing nonlinearities have regions of stability and azimuthal instability, depending on the beams' power [50, 295, 297]. While this subject has been elaborated upon theoretically, no experimental report showing the stable propagation of a self-trapped vortex beam in a SF uniform medium with local nonlinearity has been presented, thus far.

In this section, we report the observation of effectively stable propagation of (2+1)D self-trapped vortex beams, with topological charge $m = 1$, in a condensed optical medium, viz., liquid CS_2, which features strong self-focusing [209]. The stable propagation of self-trapped OVSs, which keep their shape and size unaltered over approximately five Rayleigh lengths, is obtained by exploiting a combination of the saturation of the refractive nonlinearity and 3PA. The behavior of the self-trapped vortex beam is reproduced by using a modified NLSE which very well models the filamentation of light in CS_2, generated by a picosecond laser input at 532 nm [26]. In the instability regime, splitting of the vortex beam into two separating fragments is observed at large intensities, in agreement with the numerical simulations.

7.2.2 Experimental Details

The setup used to study the vortex-beam propagation is displayed in Fig. 7.2. The second-harmonic beam at 532 nm, obtained from a Nd:YAG laser (80 ps, 10 Hz, 1064 nm), with the maximum pulse energy of 10 µJ, was used. An optical vortex beam with topological charge $m = 1$ was produced by passing the Gaussian beam through a VPP. The control of the incident beam's power was provided by a $\lambda/2$ plate followed by a Glan prism, which assures that the beam is linearly polarized. A telescope was used to adjust the beam waist, in order to illuminate a large area of the VPP, and a spatial filter was used to eliminate higher-order diffracted light. The OV beam was focused by a 5-cm focal distance lens (L1) on the input face of a glass cell filled by CS_2.

Following the same procedure used for the characterization of a Gaussian beam (see Section 6.2.2), we recorded several images of the transverse OV beam profiles around the focus of the lens L1. Fig. 7.3(a) displays an example of the transverse image of our incident OV beam being focused by the lens L1. Subsequently, a two dimensional (2D) fit was performed for each

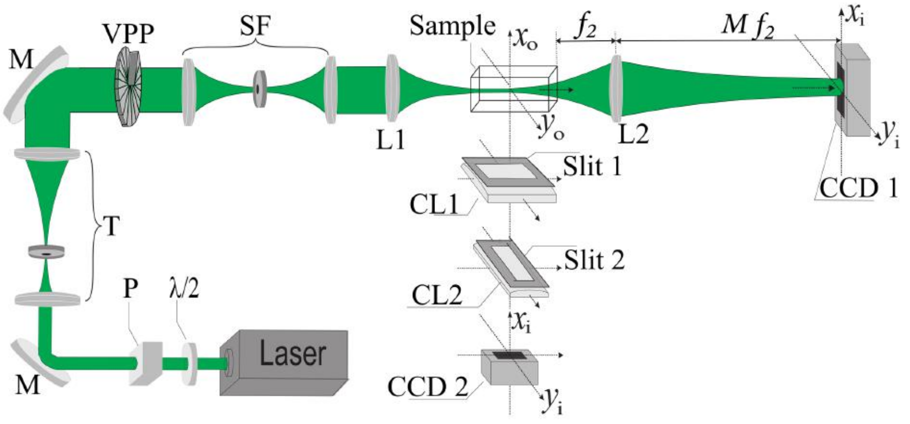

Figure 7.2 Experimental setup for investigation of OVSs in CS_2: polarizer (P); mirror (M); telescope (T); vortex phase plate (VPP); spatial filter (SF); spherical lenses with $f_1 = 5$ mm (L1) and $f_2 = 5$ mm (L2). The CCD 1 camera produced the transmitted-beam spatial profile. Cylindrical lenses with $f = 40$ mm (CL1) and $f = 80$ mm (CL2), and CCD 2 were used in the SLIM setup. The cell's length is 10 mm.

image by using the expression: $I(r) = I_0 \left\{ exp\left[0.347 \left({}^{r}/_{w_{BG}}\right)^2\right] tanh\left({}^{r}/_{w_v}\right)\right\}^2$, where w_{BG} and w_v are the radius of the Gaussian background (bright region of the OV beam) and the vortex core[1], respectively; $r = \sqrt{(x-x_0)^2 + (y-y_0)^2}$ with (x_0, y_0) being the position of the vortex core $[I(x_0, y_0) = 0]$. Fig. 7.3(b) shows the numerical reconstruction of the transverse OV beam profile corresponding to Fig. 7.3(a), obtained from 2D fit. Fig. 7.3(c) shows the radius of the Gaussian background (black squares) and the vortex core (red circles) at different positions along the propagation axis. The solid lines were obtained by fitting Eq. 6.38 in both cases. Values of $w_{BG} = 11$ μm and $w_v = 3$ μm, at the focus of lens L1, were measured to the OV beam used in this experiment. In addition, to confirm the presence of the topological charge carried by the beam, the triangle aperture method was used [298]. The respective diffraction pattern is shown in Fig. 7.3(d), where the two bright points on each side of a triangular lattice indicate that the topological charge is $m = 1$.

In order to characterize the formation and propagation of OVSs, we use two procedures of measurement corresponding to the capture of the transverse and longitudinal profiles of a OV beam along propagation direction, as shown in Fig 7.2. In the first procedure, transverse vortex-beam profiles were recorded using a CCD camera aligned with the beam propagation direction (the z-axis). Cells of thickness 1, 2, 3, 4, and 5 mm filled by CS_2 were used to image the propagation of the vortex beam over different distances, in analogy to the procedure described

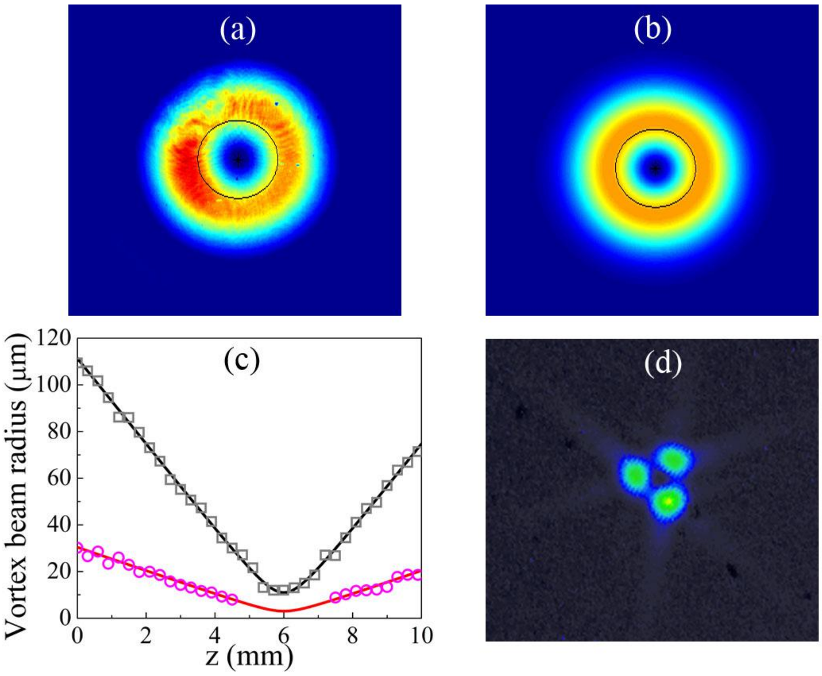

Figure 7.3 (a) Experimental and (b) Numerical transverse profiles of the incident OV beam. (c) Radius of the Gaussian background (black squares) and the vortex core (red circles) as a function of the propagation distance, z. The solid lines were obtained by fitting Eq. 6.38. (d) The diffraction pattern of the beam with topological charge $m = 1$, produced by the triangle aperture method [298].

---

[1] In this thesis, vortex core is defined as the dark region of the vortex beam.

in [299]. Lens L2 was used to obtain the beam's image at the output face with magnification of 4. The imaging system, consisting of lens L2 and the CCD 1, can scan along z to image the input and output face of the five cells, maintaining the same magnification. Small marks on the input and output faces of the cells help to identify the correct position of the imaging system, by observing a sharp image of the mark in the CCD. To observe the evolution of the vortex beam in the transverse plane, measurements were first performed with 1-mm-long cell. The imaging system was translated along the z-axis to image the entry (at $z = 0$) and output of the cell (at $z = 1$ mm). Then, the 1-mm-long cell was replaced by a 2-mm-long cell maintaining the same position of the input face, with respect to lens L1, and translating the imaging system over $z = 2$ mm. The initial position of the cell was corroborated using side-view measurements (with precision of ~ 1 μm), as described below. The same procedure was performed for the other cells with different thicknesses. In addition, side-view beam images were obtained using the SLIM [255], by measuring the weak scattered light in the direction perpendicular to the beam's pathway. A cell 10 mm long was used for these measurements. The setup collecting the scattered light consisted of two cylindrical lenses with 40-mm (y-axis) and 80-mm (z-axis) focal lengths, used to obtain images with magnification of 7 and 1/2, respectively. The experiments were performed with intensities adjusted from $I = 0.5$ GW/cm^2 to $I = 25$ GW/cm^2, to identify regions of stable and unstable propagation of the vortex beam. The margin of error in the experimental measurements is given by the camera pixel size (4.6 μm) divided by the magnification. To ensure that the images correspond to the same laser pulses, both CCD cameras were triggered by Nd:YAG laser pulses, at the repetition rate of 10 Hz. Additionally, to keep control over intensity fluctuations of the laser, a postfiltering selection was carried out to keep records solely of images corresponding to the intensities varying at most by $\pm 2\%$.

7.2.3 Results and Discussions

Figure 7.4 presents the beam profiles at the entrance and exit faces of each cell used, for two values of the laser intensity. Figure 7.4(a), corresponding to relatively low intensity, $I = 1$ GW/cm^2, shows that the transverse profile of the initial doughnut-type beam diverges along the propagation pathway without changing its ringlike shape, NL effects being negligible in this case. On the other hand, it is observed in Fig. 7.4(b) that, for $I = 9$ GW/cm^2, the beams' shape and radius remain constant for the propagation over 3 mm, which corresponds to approximately five Rayleigh lengths; this result clearly indicates the formation of a stable self-trapped vortex beam. At $z > 3$ mm, the beam diverges because the intensity is depleted by the NL absorption. As shown below, numerical simulations corroborate that a long distance of the stable propagation of self-trapped vortex beams can be attained. Figures 7.4(c) and 7.4(d) show the intensity distribution along the radial coordinate corresponding to Figs. 7.4(a) and 7.4(b), respectively. The solid and dashed lines are guides to the eyes, which represent the evolution of the beam size.

Figure 7.5 displays side-view images recorded for intensities from 1 to 18 GW/cm^2. Figures 7.5(a) and 7.5(b), in conjunction with Fig. 7.4(a), demonstrate that, for $I \leq 5$ GW/cm^2, the vortex beam does not change its ring shape, while diverging due to the linear diffraction. For

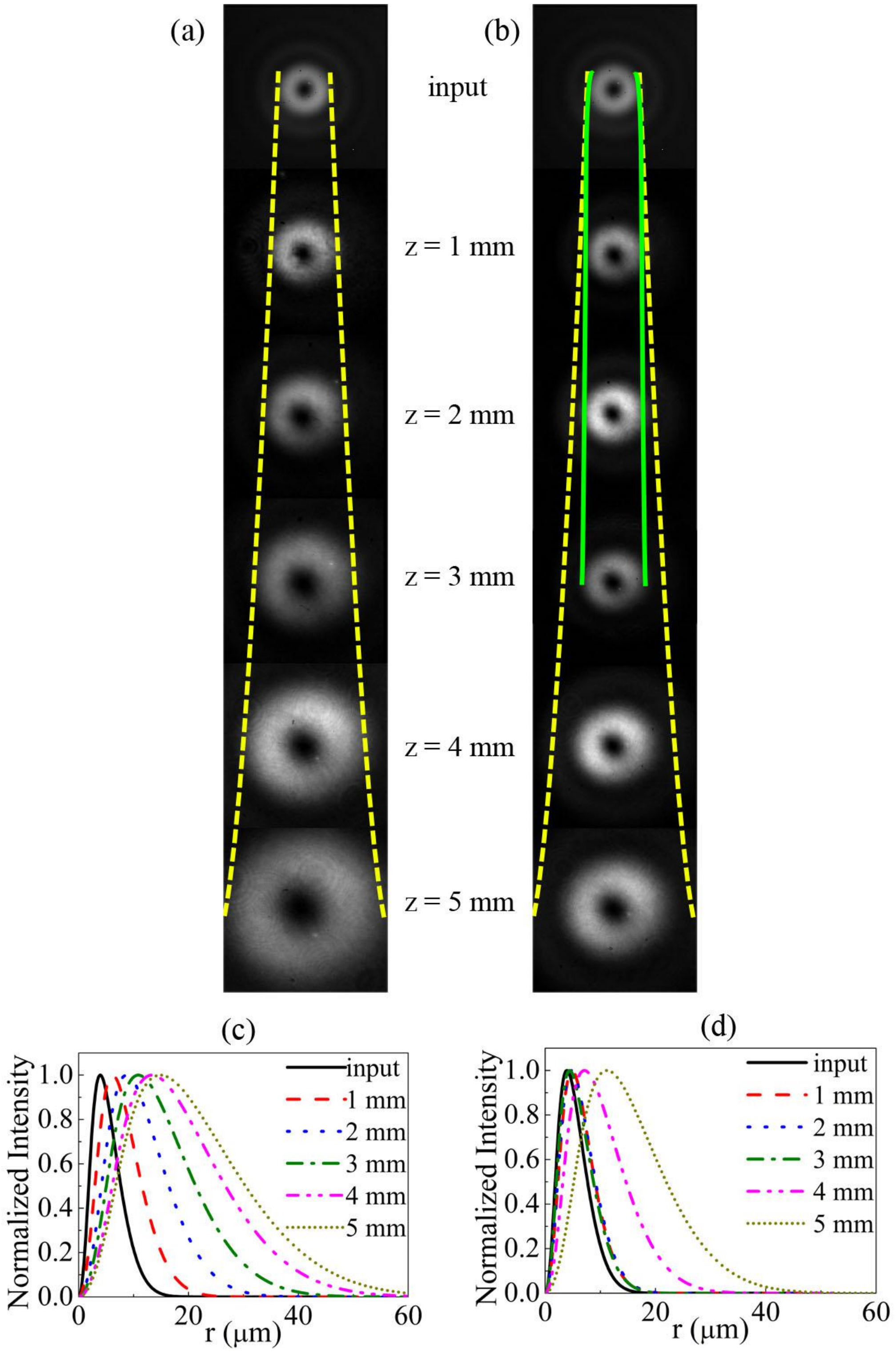

Figure 7.4 Transverse vortex-beam profiles at input and output faces for cells with thicknesses 1, 2, 3, 4, and 5 mm: (a) $I = 1$ GW/cm^2 and (b) $I = 9$ GW/cm^2. The lines are guides to the eye. (c,d) Normalized intensity distributions of the beam at each position from (a,b).

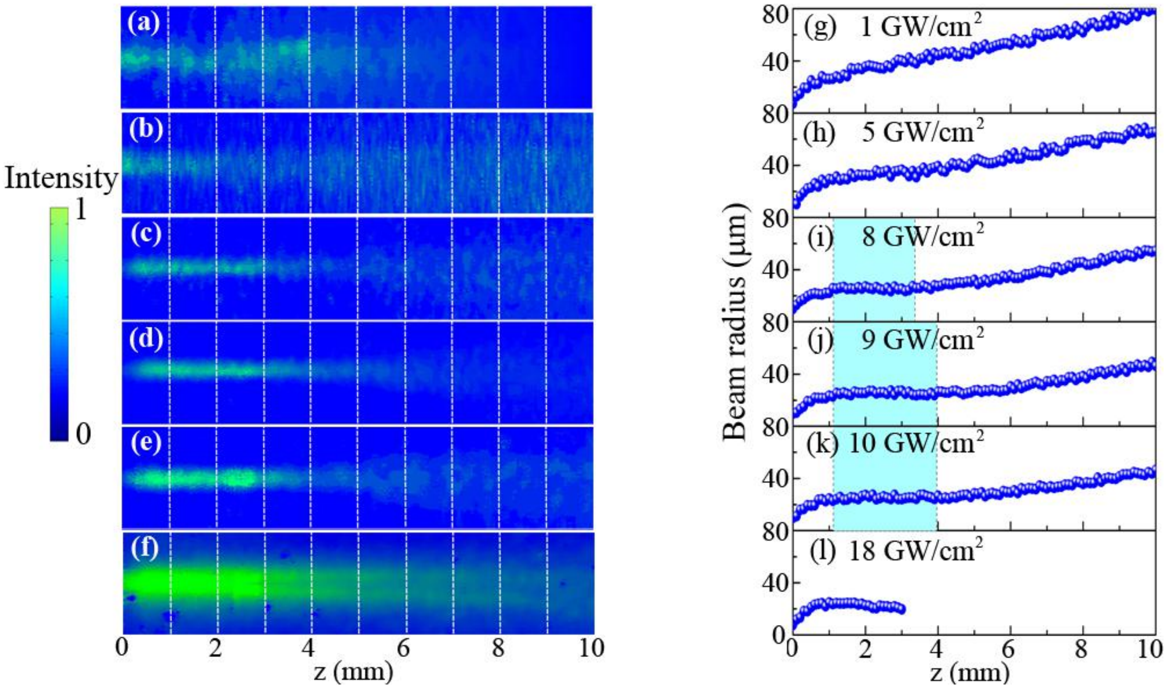

Figure 7.5 Experimental side-view images of the vortex-beam propagation for intensities (a) 1 GW/cm^2, (b) 5 GW/cm^2, (c) 8 GW/cm^2, (d) 9 GW/cm^2, (e) 10 GW/cm^2, and (f) 18 GW/cm^2. (g-l) The beam's radius as a function of the propagation distance, corresponding to (a-f), respectively. The shaded areas indicate the region of the stable vortex-beam propagation.

5 GW/$cm^2 < I <$ 8 GW/cm^2, the beam's divergence weakens with the increase of the intensity, due to the self-focusing effect. Figures 7.5(c)-(e), obtained for 8 GW/$cm^2 \leq I \leq$ 10 GW/cm^2, exhibit the stable propagation of the vortex beam up to the distance of $\sim$ 3 mm. Thus, Figs. 7.4(b) and 7.5(c)-(e) provide the direct evidence for the propagation of a stable ring-shaped vortex. However, at $I >$ 10 GW/cm^2, strong concentration of the power was observed in the course of the first 3 mm of the propagation, and the transverse images exhibit distortion of the beam profiles. These asymmetries gradually increase, up to splitting of the vortex beam observed at $I \geq$ 18 GW/cm^2, as shown in Fig. 7.5(f). The low resolution of the image after the splitting is due to the weakness of the scattered light. Figures 7.5(g)-(l) present the variation of the beam's radius in the course of the propagation, corresponding to Figs. 7.5(a)-(f), respectively. Shaded rectangles display the regions where the self-trapped vortex beam is stable. Fig. 7.5(l) shows the beam radius analysis only until before vortex splitting. The formation of the two emergent beams, after the vortex split, can be clearly seen in the transverse images shown in Fig. 7.8.

To describe the propagation of the vortex beams, we used a modified NLSE given by Eq. 5.41, which includes the saturable-refractive index and the 3PA concerning the NL behavior of CS_2 in the picosecond regime, as described in Appendix C. However, for numerical simulations it is more convenient to work with the normalized expression of the Eq. 5.41, which takes the form:

$$\frac{\partial U}{\partial Z}=\frac{i}{2}\left(\frac{\partial^2 U}{\partial X^2}+\frac{\partial^2 U}{\partial Y^2}\right)+i\frac{\eta\,|U|^4\,U}{1+|U|^4}-\mu\,|U|^4\,U, \tag{7.1}$$

where were used the dimensionless variables: $X=x/w_{BG}$, $Y=y/w_{BG}$, $Z=z/L_D$, $U=A'/A'_r$, with $L_D=k_0 w_{BG}^2$ and $A'_r=\left(1/2bn_0c\varepsilon_0\right)^{-1/2}$, where c the speed of light in vacuum and ε_0 the vacuum permittivity. Further, $\eta=L_D k_0 a/b^2$, $\mu=\alpha_4 L_D/\left(2b^2\right)$ and the intensity is related to the normalized field by $I=|U|^2/b$.

Simulations of Eq. 7.1 were initiated with the input wave form $U\left(R,\theta,Z=0\right)\propto exp\left(-R^2+im\theta\right)tanh\left[w_{BG}R/\left(2w_v\right)\right]$, where $R=\sqrt{X^2+Y^2}$ and θ are the adimensional polar coordinates and m is the topological charge. Numerical results for the vortex-beam propagation in the 10-mm-long cell filled by CS_2 were produced for $L=2.3$ mm, $\eta=28$, and $\mu=3.3$.

Figure 7.6 shows the evolution of the transverse beam's profiles for intensities between 1 and 15 GW/cm^2, obtained by simulations of Eq. 7.1, which were performed by using the split-step compact finite-difference method [235]. Figure 7.6(a) displays the divergence of the doughnut-type beam for $I=1$ GW/cm^2, which is similar to what happens in the linear regime, according to Figs. 7.4(a) and 7.5(a). For $I=9$ GW/cm^2, the propagation of the self-trapped vortex beam can be observed over a distance of ~ 3 mm, as shown in Fig. 7.6(b), which agrees with Figs. 7.4(b) and 7.5(d). Figure 7.6(c) shows a deformation of the beam's profile for $I=12$ GW/cm^2, which gradually grows, leading to the complete split of the vortex beam at $I=15$ GW/cm^2, as shown in Fig. 7.6(d).

Figure 7.7 shows a longitudinal cross section of the vortex beam propagation, produced by simulations of Eq. 7.1. At $I=1$ GW/cm^2 [Fig. 7.7(a)], the vortex beam keeps the ring shape but diverges due to the diffraction. On the other hand, in Fig. 7.7(b), corresponding to $I=8.5$ GW/cm^2, the beam slightly diverges at first, but, after passing ~ 1.2 mm, it keeps constant shape and width in the course of the propagation over ~ 3 mm, and diverges afterwards. Figure 7.7(c) shows the variation of the vortex-beam radius at several positions in the cell for different intensities, the shaded rectangles displaying the region of the stable propagation of the (2+1)D self-trapped vortex beams, for $I=8$ and 9 GW/cm^2. For 15 GW/cm^2, the curve ends at $z=3$ mm, as the vortex splits in two fragments beyond this point.

To highlight the effect of the 3PA ($\alpha_4>0$), Fig. 7.7(d) shows the evolution of the vortex-beam radius produced by simulations of Eq. 7.1 with $\alpha_4=0$. In this case, at $I<7$ GW/cm^2 the beam diverges, as in Fig. 7.7(c). At $I=7.5$ GW/cm^2, it initially diverges, passing 1.2 mm, but features stable propagation of the self-trapped vortex beam over the subsequent 2.5 mm. For $I=8$ GW/cm^2, the vortex is unstable, splitting into two fragments.

Figure 7.8(a), corresponding to instability regime, shows, at $I=18$ GW/cm^2, two bright fragments of radius 17 μm at the output face, with distance 68 μm between them, the intensity of each beam being 10% of the initial value. The intensity loss is caused by the 3PA, while the difference between the fragments results from a small asymmetry in the input beam. Figure 7.8(b) shows the respective numerical result, obtained from Eq. 7.1 for $I=15$ GW/cm^2. The spiral emerging around the fragments in the simulations (it is more salient at $I=16$ GW/cm^2) was not observed in the experiment, as the camera was not sensitive enough for that.

The experiment was repeated for the input beam with vorticity $m=-1$, obtained by reversing the input face of the VPP. Figures 7.8(c) and 7.8(d) display the respective experimental and

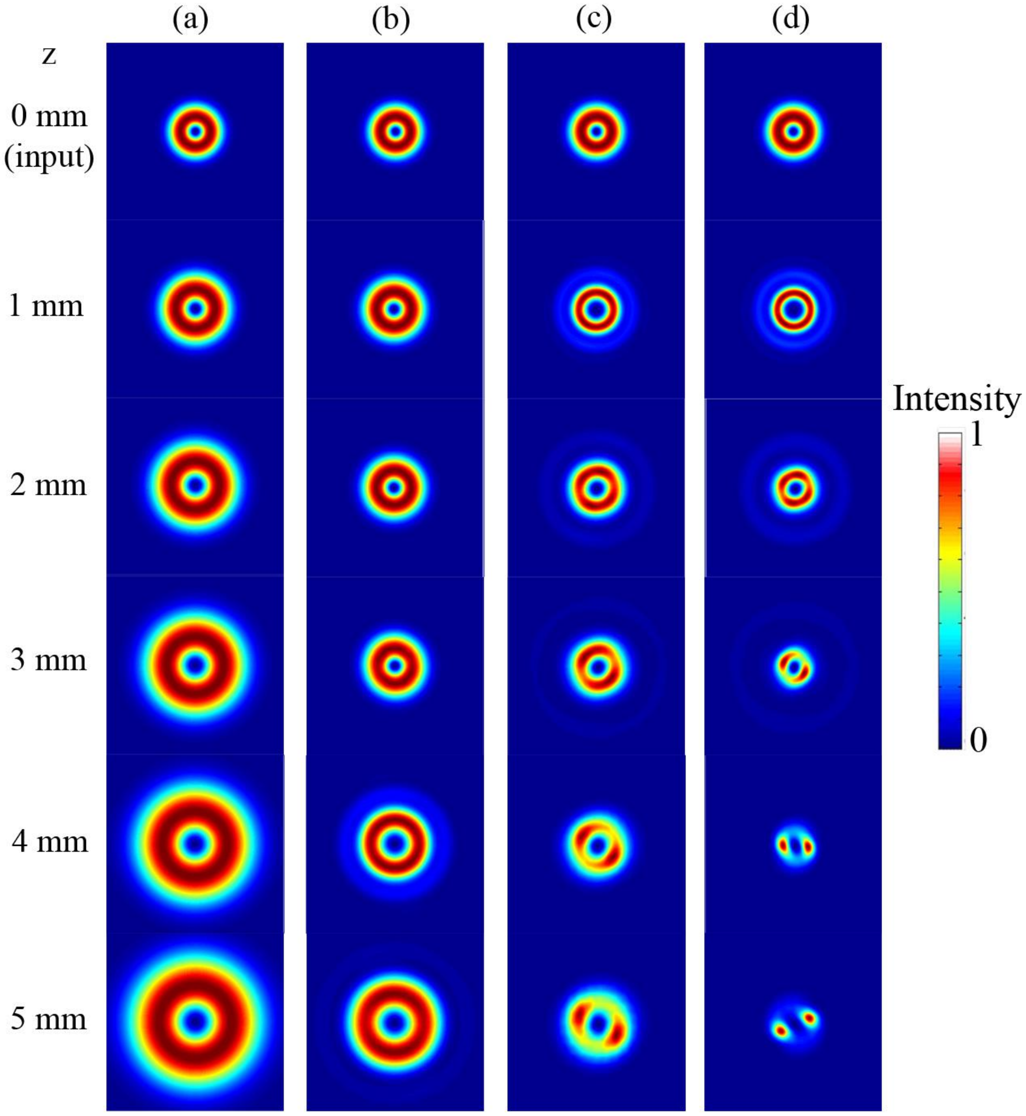

Figure 7.6 Numerically generated images showing the evolution of transverse vortex-beam profiles (with $m = 1$) along the propagation direction, for intensities of 1 GW/cm^2 (a), 9 GW/cm^2 (b), 12 GW/cm^2 (c), and 15 GW/cm^2 (d).

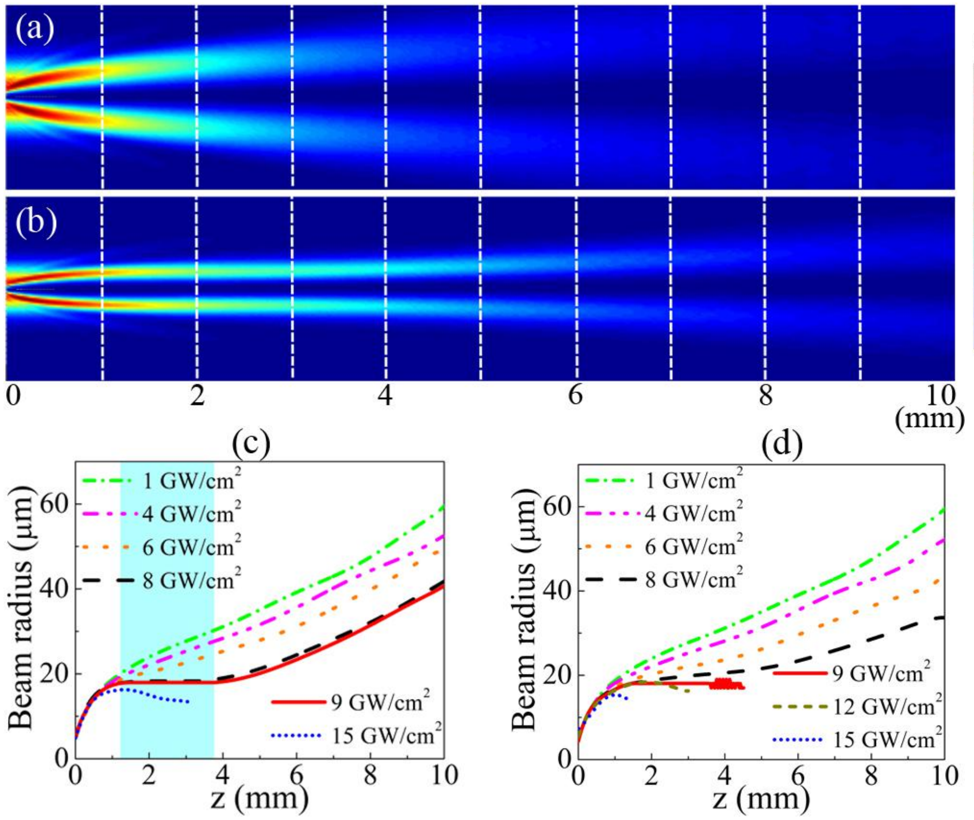

Figure 7.7 Numerical results for the vortex-beam propagation at (a) $I = 1$ GW/cm^2 and (b) $I = 8.5$ GW/cm^2, obtained by simulations of Eq. 7.1. (c,d) The beam's radius as a function of the propagation distance, produced by the simulations considering the 3PA coefficient (c) $\alpha_4 = 9.3\times10^{-26}$ m^3/W^2 and (d) $\alpha_4 = 0$, with various intensities. The shaded area in (c) indicates the intensity range of stable propagation of self-trapped vortex beams. The beam radius for $I \geq 9$ GW/cm^2 in (d) were calculated only until before vortex splitting.

numerical results, with two fragments similar to those in Figs. 7.8(a) and 7.8(b), but rotated by 90°. The experimental and related numerical images obtained for $m = -1$ demonstrate that the results are highly reproducible. Similar results have been obtained for other input intensities.

In the simulations, the fragments emerging after the splitting of the vortex beam move along tangents to the vortex ring, due to conservation of the OAM. However, unlike previous theoretical results which predict the formation of fundamental solitons after the splitting [49, 285, 286], in the present case the fragments are not solitons, because of the losses induced by the 3PA. The model presented here can be applied to the propagation of vortex beams with multiple topological charges too, but they tend to be unstable against splitting, unlike the vortex with $m = 1$.

Simulations were also performed with $I/\left(1+b^2I^2\right)$ in Eq. 7.1 replaced by $I/(1+b'I)$, which is the most common form of the saturable nonlinearity described in Appendix C and adopted in [49]. Varying the input intensity from 1 to 25 GW/cm^2, no stability region for self-trapped vortex beams was found in that case. Thus, the crucially important ingredients

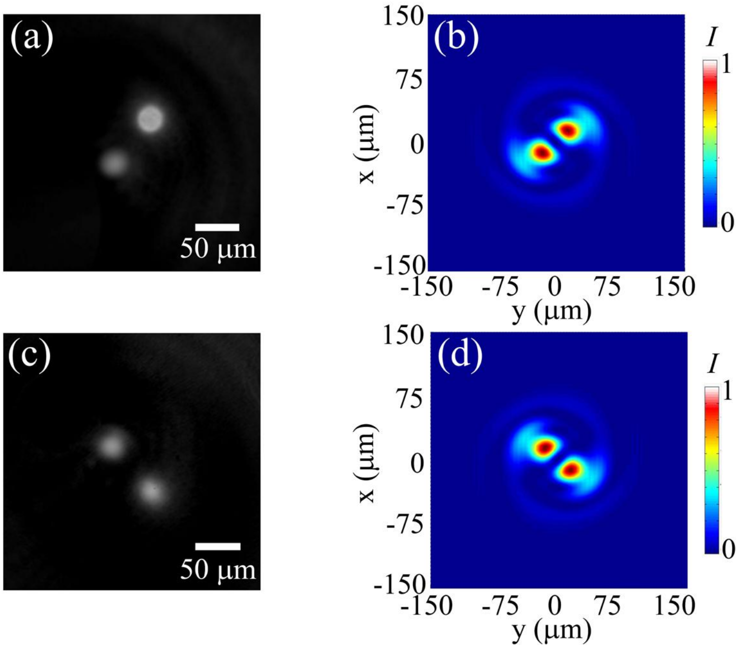

Figure 7.8 (a,c) Experimental images obtained in the output face of the cell, after the splitting of the vortex beam with topological charge $m = +1$ (a) and $m = -1$ (c), for laser intensity $I = 18$ GW/cm^2. (b,d) Simulations of Eq. 7.1 for (b) $m = +1$ and (d) $m = -1$, at $I = 15$ GW/cm^2.

necessary for the stable propagation of the self-trapped vortex beams are the appropriate intensity dependence of the NL refractive index, as derived in [26], and the 3PA. Actually, the 3PA term in Eq. 7.1 helps to expand the stability region for the self-trapped vortex beam. In particular, with this term kept in Eq. 7.1, the splitting of the vortex into two fragments is observed at $I > 13$ GW/cm^2, while the stable propagation occurs at 8 GW/$cm^2 \leq I < 10$ GW/cm^2. However, if the 3PA term is dropped, the splitting occurs at $I \geq 8$ GW/cm^2, with a tiny stability region spotted at 7.4 GW/$cm^2 \leq I \leq 7.6$ GW/cm^2.

Therefore, experimental and numerical results presented in this Section demonstrate the first evidence of stable propagation of OVSs, with topological charge $m = 1$, in a saturable SF medium. Strictly speaking, the stability of the self-trapped vortex beams reported here is a transient effect, as the 3PA eventually causes degeneration into the linear regime,while the saturablerefractive nonlinearity alone cannot stabilize self-trapped vortex beams in the absence of the NL loss [49].

7.3 TAMING THE UNSTABLE BEHAVIOR OF OVSS IN SELF-FOCUSING SATURABLE MEDIA

7.3.1 Introduction

The control of light by light is one fascinating process in NL optics with important applications in high speed optical processing and telecommunications [205, 223]. Usually the all-optical control of a laser beam is obtained using an intense laser which couples with the weaker beam through cross-phase modulation (XPM) inducing polarization rotation and/or light bending [21]. Nowadays all-optical devices and prototypes can be operated with basis on the XPM allowing signal processing with high bit rates [300, 301, 302, 303]. In this context, temporal and spatial solitons have attracted great attention because the invariance of their shape is an important feature in long-distance data transmission where solitons may play the role of information bits [83, 304, 305, 306, 307].

However, the exploitation of solitons for optical processing is affected by several instabilities. In particular, it is known that the propagation of OVSs in SF media are subject to spontaneous azimuthal symmetry breaking due to the SMI, as discussed in the previous Section. As a consequence the OVS is split into bright fragments, which have characteristics of fundamental solitons when the propagating medium is lossless. In most cases, the number of fragments is equal to twice the OVSs topological charge, but this number may also be dependent on the incident power, as reported for a cubic SF medium [288]. However, although many studies analyzing the splitting of OVSs were reported [308, 309, 310], no experimental study showing a way to manage the emerging beams, via all-optical control, is known.

In this Section, we report two schemes for controlling the relative azimuthal position and energy transfer (ET) between the emerging beams after the splitting of an OVS propagating in CS_2. The superposition of copropagating Gaussian and vortex beams allowed the control of the fragments producing an angular rotation in the transverse plane that may reach $\sim 90°$ by adjusting the Gaussian beam intensity. Additionally, ET between the fragments, with efficiency up to 92%, is observed by varying the size and the relative positions of the vortex and Gaussian beams' axis. The experimental results were reproduced by numerical simulation considering the saturation of the NL refractive index and the 3PA coefficient that characterizes the NL behavior of CS_2 (see Appendix C). It is important to notice that the procedure presented here is general enough to be successfully applied for other saturable SF media.

7.3.2 Experimental Details

The experimental setup used is sketched in Fig. 7.9(a). The second-harmonic beam at 532 nm, obtained from a Nd:YAG laser (80 ps, 10 Hz, 1064 nm), with the maximum pulse energy of 10 μJ, was split into two beams using a 50:50 beam splitter (BS1). The variation of the total beam power was made using a $\lambda/2$ plate followed by a Glan prism which assures the linear polarization of the beam. Two telescopes, formed by lenses L1-L2 and L1-L3, were used to adjust the transverse beams' dimensions. The beam transmitted by the BS1 passes through a phase plate (VPP) which produces a vortex beam with $m = 1$ [the signal beam (SB) with intensity I_S]. A spatial filter, located after the VPP, was used to eliminate high-order diffracted light. The reflected beam by BS1 with Gaussian profile was the control beam (CB) with intensity I_C. This beam was collimated by lens L3, which allows adjustment of its diameter[2]. Neutral density filters were used to vary I_C maintaining constant the beams' polarization. The SB and CB were combined using a beam splitter (BS2) and focused by a 5-cm-focal-distance lens (L4)

---

[2] To adjust the Gaussian beam diameter were used lenses with different focal distances, which are represented in Fig. 7.9 by the lens L3.

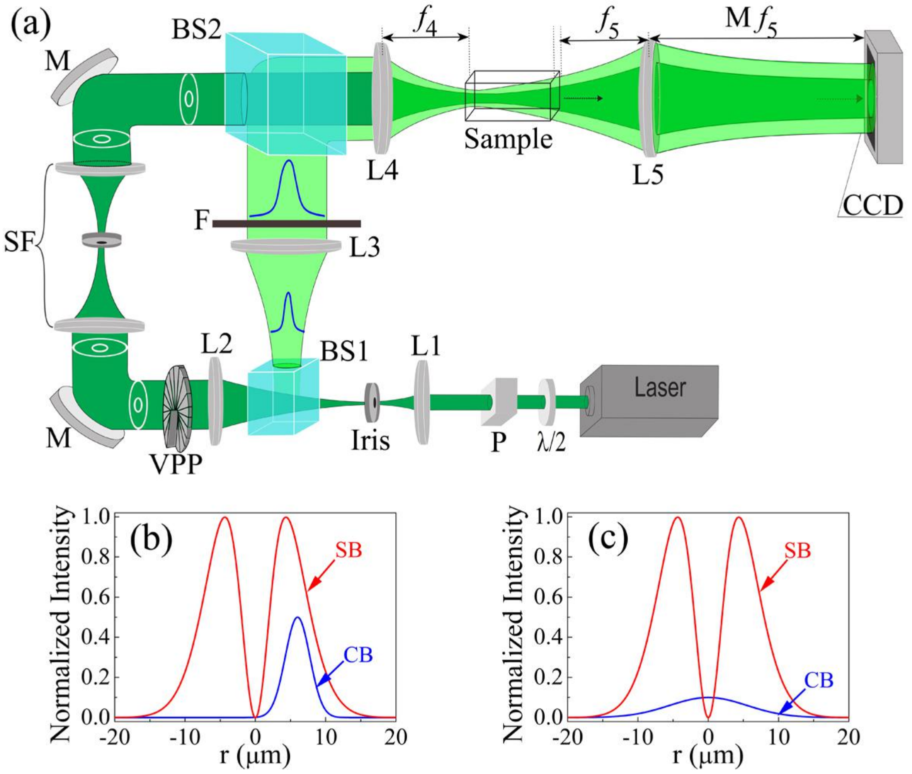

Figure 7.9 (a) Schematics of the experimental setup: polarizer (P); telescopes (L1-L2 and L1-L3); vortex phase plate (VPP); mirror (M); spatial filter (SF); beam splitters (BS1 and BS2); neutral density filter (F); spherical lenses with $f_4 = 50$ mm (L4) and $f_5 = 50$ mm (L5). The CCD camera records the transverse beam spatial profile with magnification M. Transverse beam profiles at the cell's entry face used for the experimental schemes: A (b) and B (c), where SB and CB is the signal and control beam, respectively.

on the input face of a 10-mm-long quartz cell filled by CS_2. The transverse beams' profiles were imaged on a CCD camera aligned with the beam-propagation direction. The lens L5 was used to obtain the beam's image at the output face of the cell with magnification $M = 4$. Single-pulse images were captured by triggering the CCD, using a digital delay and pulse generator (DDPG), which was triggered by the Nd:YAG laser pulses, at 10 Hz, avoiding contributions of slow NL response due to thermal effects. The SB at the input face (positioned in the focal plane of the lens L4) consists of a Gaussian background, with beam waist of 11 μm, and the vortex core with radius of 3 μm, values obtained by using the OV beam characterization described in Section 7.2.2. Under these conditions and for $8\ \mathrm{GW}/cm^2 \leq I_S \leq 10\ \mathrm{GW}/cm^2$ a self-trapped vortex beam is formed and propagates along $\sim$ 3 mm as reported in previous Section. For $I_S > 10\ \mathrm{GW/cm^2}$, the SMI produces distortions in the transverse beam profile, which gradually increase up to splitting of the OVS. At 3 mm from the entrance face of the cell, the OVS is split into two bright fragments for $I_S \geq 18\ \mathrm{GW/cm^2}$.

In order to control the azimuthal positions and relative intensities of the OVS fragments, two experimental schemes (A and B) were implemented varying the radius, position, and intensity of the CB with respect to the SB. Scheme A consisted of the collinear propagation of the two beams with the CB located on the side of the vortex around the core, as shown in Fig. 7.9(b). The CB radius is 3.5 μm. In scheme B, the SB and CB have the same transverse dimensions (the CB and vortex beam radii are of 11 μm) and their axes are coincident, as indicated in Fig. 7.9(c). The maximum ratio I_C/I_S used was of 0.5 and 0.1 in scheme A and scheme B, respectively. In both cases, the signal and control beams were overlapped spatially and temporally inside the sample.

7.3.3 Results and Discussions

Figure 7.10 shows images of the OVS fragments at the exit face of the cell corresponding to scheme A. Figure 7.10(a) shows the two emerging beams when $I_S = 18$ GW/cm^2, in the absence of the CB. The two fragments, resulting from the splitting of a single vortex beam with approximately uniform field background, have equal shape, size, and intensity. Figures 7.10(b)-(h) show the rotation of the fragments, in the transverse plane, for 0.5 GW/$cm^2 \leq I_C \leq$ 10 GW/cm^2. The initial angle, $\varphi_0 = \pi/22$, between the vertical direction and the line along the fragments, in the absence of the CB, depends on the phase-plate position and the samples' nonlinearity [308, 310, 311]. By rotating the phase plate in a plane transverse to the beams' axis we observed changes of φ_0, but in the experiments described here the VPP is kept fixed. The maximum rotation angle induced by the CB, $\varphi \approx \varphi_0 + \pi/2$, was obtained for $I_C = 10$ GW/cm^2 and $I_S = 18$ GW/cm^2. The results suggest the possibility for operation of an optical switch, where the emerging beams obtained from the split of an OVS are controlled by a CB with smaller intensity than the SB intensity. It is known that CS_2 has two response times: an ultrafast one (< 50 fs) and a fast one of ~ 2 ps [35]. However, in our case, the NL response of CS_2 is limited by the pulse duration of the incident beam (80 ps), as observed in Fig. 4.20(a). Thereby, the modulation is as fast as the duration of the pulse.

The rotation of the fragments was investigated by placing the CB in different azimuthal positions around the vortex core and the largest rotation angle was obtained when the CB was located approximately at the bottom of the vortex on the line corresponding to $\varphi_0 = \pi/22$.

Figure 7.11 presents the spatial profiles of the fragments at the exit face of the cell following scheme B, for $I_S = 18$ GW/cm^2. In the absence of the CB, the two fragments have identical characteristics, as shown in Fig. 7.10(a). Figure 7.11(a) shows ET of $\sim 10\%$ between the two fragments when $I_C = 0.3$ GW/cm^2. The ET was controlled by varying I_C reaching a maximum efficiency of 92% for $I_C = 2$ GW/cm^2 as shown in Fig. 7.11(d). In Figs. 7.11(a)-(d), the color scale, which represents the intensity in the transverse plane, was normalized with respect to its maximum value in each case, but the total power was conserved in all cases. The white dashed lines (pink cross) correspond to the initial (final) position of the vortex core, in the absence (presence) of CB.

In order to understand the results of Figs. 7.10 and 7.11 we recall that the vortex beam propagation is very sensitive to the presence of external perturbations. For the I_S used, in the absence of CB, the splitting of the vortex is due to the SMI effect, as discussed in previous Section. In the present experiments, the SMI is enhanced by the presence of the CB that induces changes in samples' refractive index in the region where the CB and SB overlap. In

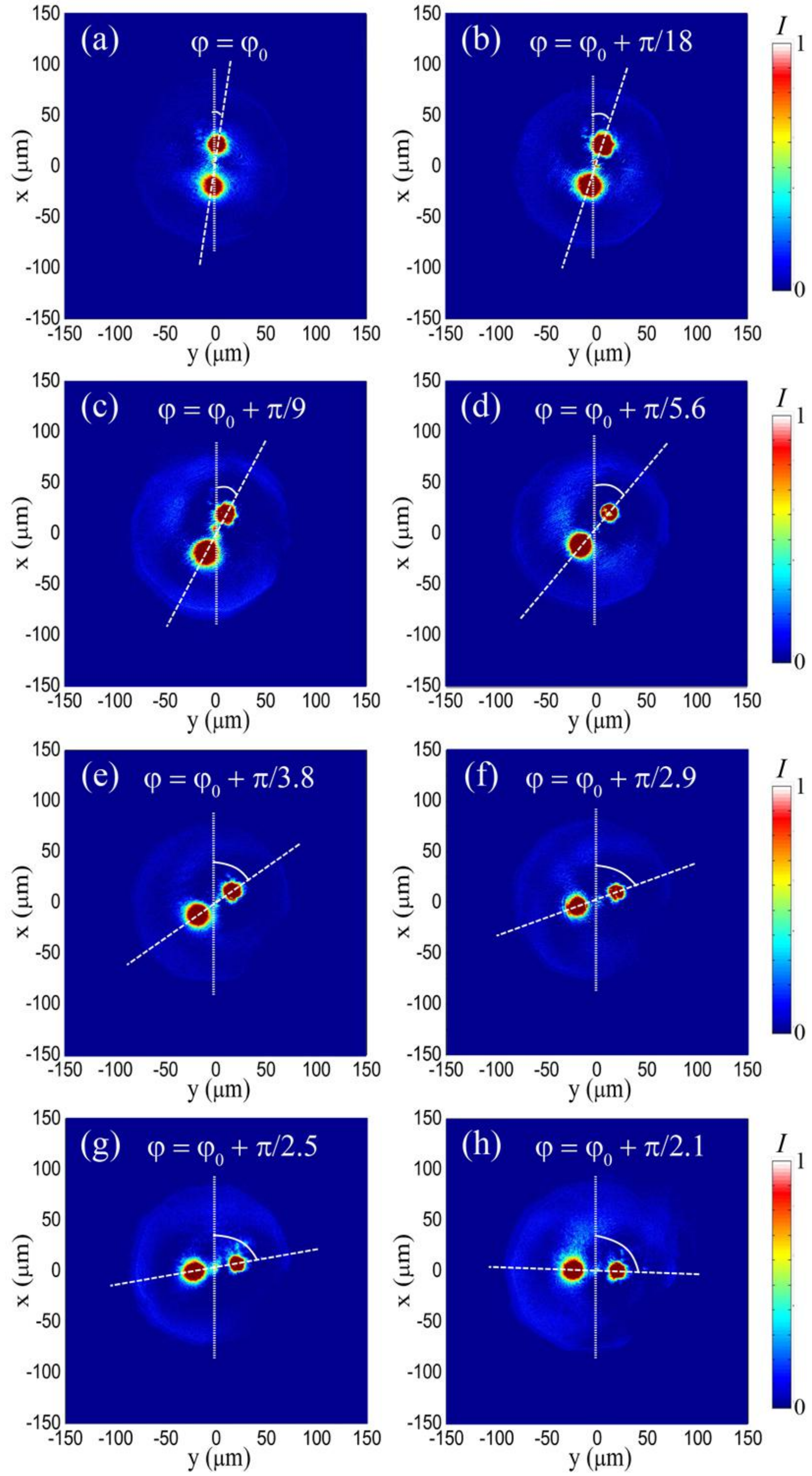

Figure 7.10 Experimental images of the emerging beam's profiles at the output face of the cell obtained using scheme A. Vortex beam intensity: 18 GW/cm^2. Gaussian beam intensity (in GW/cm^2): (a) 0, (b) 0.5, (c) 1, (d) 3, (e) 5, (f) 7, (g) 9, and (h) 10. Cell length: 10 mm and $\varphi_0 = \pi/22$.

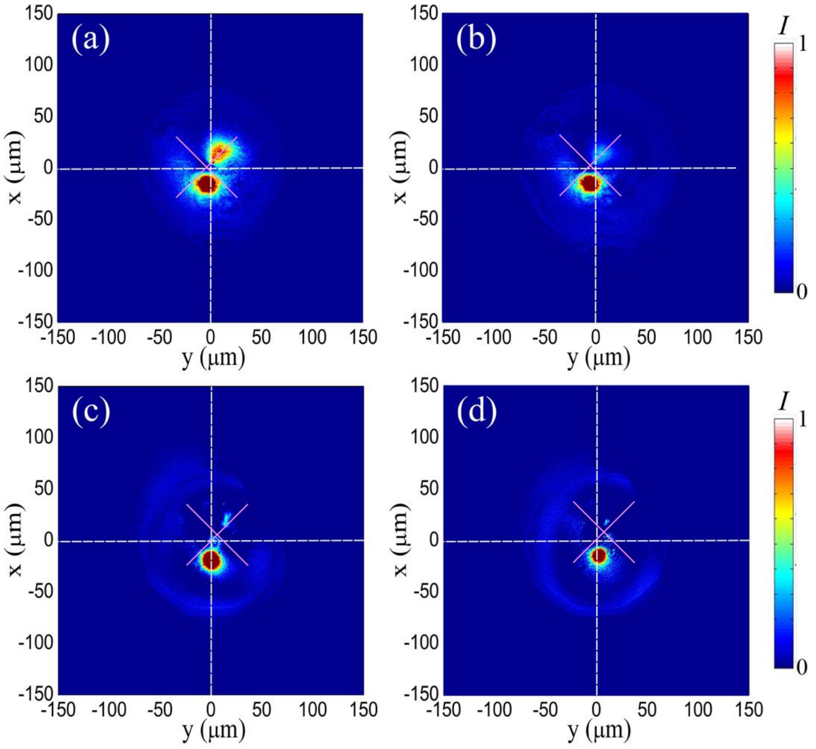

Figure 7.11 Experimental images of the resultant transverse beam profiles at the output face of the cell obtained when the axis of the vortex and Gaussian beams are coincident (scheme B). Vortex beam intensity: 18 GW/cm^2. Gaussian beam intensity: (a) 0.3, (b) 0.8, (c) 1.4, and (d) 2 GW/cm^2. Cell length: 10 mm.

scheme A the CB is an off-axis perturbation for the SB. Then, the refractive index induced in the region illuminated by the CB is larger because the CS_2 is a SF medium. Thus, the bright fragments formed after the splitting of the OVS suffer changes in their rotation, which alter its final relative position, when they pass through the region where the refractive index is larger. Then, the largest rotation angle is obtained when the CB is placed closer to the position of one of the fragments, just after the split of the OVS[3]. On the other hand, in scheme B, the CB field affects the whole area of the SB. The superposition of the Gaussian and vortex beams provides a coherent field which induces a displacement of the vortex core in the radial direction that increases with the propagation distance, incident intensity, and nonlinearity of the medium [312]. Nonuniformity in the intensity profile and asymmetries in the spatial shape of the CB contribute for enhancement of the vortex core displacement [313]. Therefore, the SB splitting is affected by the azimuthal asymmetry caused by the displacement of the vortex core. Then, the two emerging beams have different size and shape, and one of them, which has higher energy, is located in the opposite direction to the displacement direction of the vortex core. The intensity ratio between the emerging beams is controlled by I_C which also controls the displacement of

---

[3] This statement is proposed based on the results observed in the numerical simulations of Eq. 7.1, after several simulation of the SB evolution with the CB located at different positions along the vortex ring. Experimentally, different positions of the CB were tested until a larger rotation angle was reached ($\sim \pi/2$).

the vortex core. Nevertheless, the total power in the output face of the sample is conserved.

In order to compare the experimental results with a theoretical model, the propagation of both beams was described by the normalized Eq. 7.1, which consider the contributions of the saturated refractive nonlinearity and the 3PA previously demonstrated for CS_2 at 532 nm, in the picosecond regime [26]. Numerical simulations of Eq. 7.1 were performed by using the split-step compact finite-difference method [235] with the input beam profile in adimensional polar coordinates $\left(R=\sqrt{X^2+Y^2} \text{ and } \theta\right)$ given by: $U\left(R,\theta,Z=0\right)=U_S exp\left(-R^2+i\theta\right) tanh\left[w_{BG}R/(2w_v)\right] exp\left(i\triangle\phi\right)+U_C exp\left[-\left(w_{BG}/w_G\right)^2\left(R-d\right)^2\right]$, where U_S and U_C correspond to incident vortex (signal) and Gaussian (control) field amplitudes. d is the initial transverse distance between SB and CB and $\triangle\phi$ is the phase difference between the beams. w_{BG}, w_v, and w_G are the waists of the Gaussian background, vortex core, and CB, respectively. Values of $L=2.3$ mm, $\eta=28$, $\mu=3.3$, and $\triangle\phi=0$ were used to model the beams' propagation in the 10-mm-long cell filled by CS_2.

Figure 7.12 shows numerical images of the emerging beams when scheme A is used, according to Fig. 7.9(b). Figure 7.12(a) shows the spontaneous azimuthal symmetry breaking of the SB when $I_S=15$ GW/cm^2 and $I_C=0$, in agreement with Fig. 7.10(a). Figures 7.12(b)-(h) illustrate the control over the fragments' rotation obtained from Eq. 7.1 with $I_S=15$ GW/cm^2 and 0.5 GW/$cm^2 \leq I_C \leq 9.3$ GW/cm^2. The dashed lines indicate the angular positions of the fragments corresponding to Fig. 7.10.

Figure 7.13 shows the numerical results corresponding to scheme B, indicated in Fig. 7.9(c). The ETs between the emerging beams with 15%, 44%, 68%, and 92% efficiency were obtained for $I_S=15$ GW/cm^2 and I_C values of 0.15, 0.75, 1.2, and 2.2 GW/cm^2, respectively. Figures 7.13(a)-(d) reproduce the experimental results shown in Figs. 7.11(a)-(d). Displacement of the vortex core, by varying the value of I_C, is observed in Fig. 7.13 corroborating our interpretation given above. The SB intensity used for the numerical calculations (15 GW/cm^2), slightly different from the experimental SB intensity (18 GW/cm^2), was used to obtain very good agreement between the experimental and numerical results, for both schemes. The dashed lines correspond to the position of the vortex core when $I_C=0$. The different I_C values used in the simulation and in the experiment are acceptable since fluctuations of $\sim$ 20% of the laser peak intensity are observed.

In order to get a qualitative understanding of the results we recall that in a nondissipative medium the emergent beams are fundamental solitons [49] that fly along the tangent of the initial ring-type beam profile due to OAM conservation. The movement of these emerging solitons is adequately described by using Newtonian conservation laws for energy, momentum, and angular momentum. In dissipative media, as in the case of CS_2, the fragments are not fundamental solitons because of the energy losses due to the 3PA, which allows linear diffraction to be again dominant. However, the conservation of angular momentum must be respected so that the emerging beams will travel tangentially to initial vortex ring, acquiring an angular velocity which will decrease when the beams move away from each other. Therefore, the final position and distance between the two spots, after a certain distance, strongly depend on the characteristics of the input vortex beam and the nonlinearity of the medium. On the other hand, the control of rotation and the ET between the emerging fragments depend on the initial intensity,

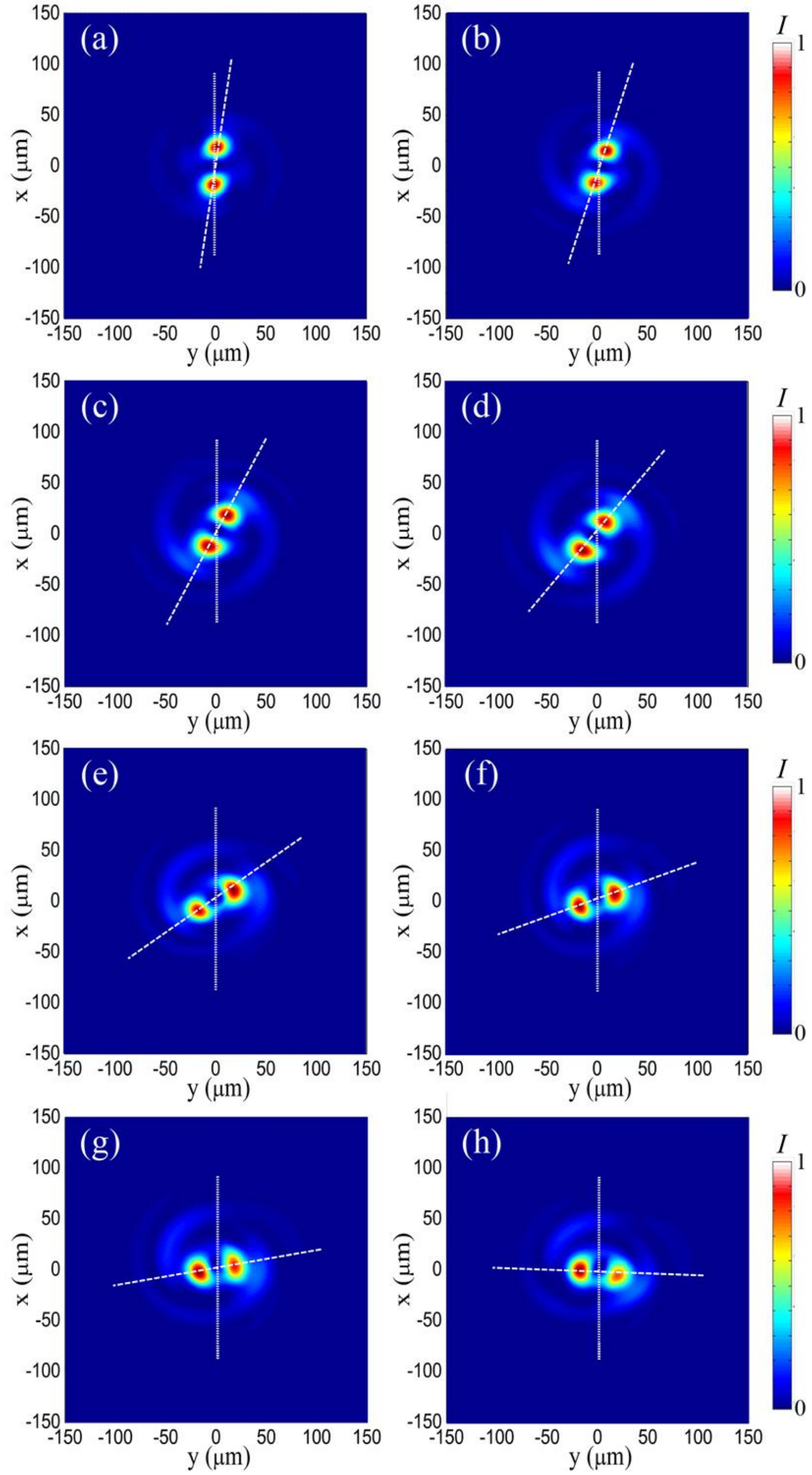

Figure 7.12 Images of the emerging beam's profiles obtained from Eq. 7.1, following the input scheme of Fig. 7.9(b). $I_S = 15$ GW/cm^2 and I_C values of (a) 0 (only SB), (b) 0.5, (c) 1, (d) 2.8, (e) 4.4, (f) 6.3, (g) 8.1, and (h) 9.3 GW/cm^2.

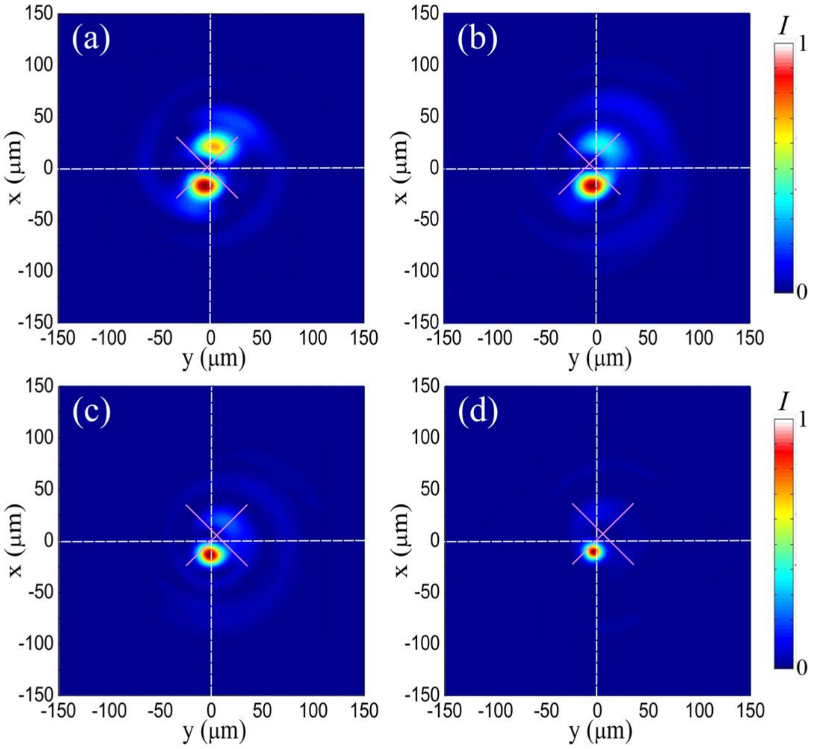

Figure 7.13 Numerical output images of the fragments obtained from Eq. 7.1, following the scheme of Fig. 7.9(c). $I_S = 15$ GW/cm^2 and I_C values of (a) 0.15, (b) 0.75, (c) 1.2, and (d) 2.2 GW/cm^2.

position, and radius of the control beam.

The results shown here reveal an effective method to control the relative positions and energy of the emerging beams after the splitting of an OVS in saturable SF media. These results allow us to introduce an alternative and efficient approach for the design of all-optical modulators, where the output beams are strongly related because they are generated from a single initial beam.

7.4 GUIDING AND CONFINEMENT OF LIGHT INDUCED BY OVSS IN SELF-DEFOCUSING MEDIA

7.4.1 Introduction

Confinement and guiding of light essentially relies on the phenomenon of total internal reflection (TIR) in a high refractive index medium surrounded by a low refractive index region. Exploitation of the TIR phenomenon in the fabrication of optical waveguides/fibers revolutionized telecommunications, enabling fast information transfer over long distances (see Chapter 9 of [60]). The all-optical analog of conventional waveguides/fibers can be obtained exploiting effects induced by intense light beams propagating through NL materials. For instance, the proper choice of a NL material allows the excitation of optical spatial solitons that propagate with constant transverse dimensions as self-induced waveguides, thanks to the balance between the linear diffraction and its nonlinearity [75]. Of special interest are the self-trapped beam originated from the Kerr effect, such as: bright and dark spatial solitons, which appear in SF and SDF media, respectively [48]. Initially, experiments involving both types of Kerr solitons were conducted in NL planar waveguides, being limited to one-transverse dimension [36, 314]. Subsequent works showed the formation of discrete bright and dark spatial solitons when an intense light beam is coupled into waveguide arrays [250, 315]. Under these conditions, the spatial solitons do not have full autonomy, because one of the transverse dimensions is limited by the walls of a rectangular waveguide. However, the geometric constraint is not necessary for (2+1)D spatial solitons, where the self-trapped beam propagates freely maintaining its shape and size constant.

A particular class of (2+1)D spatial solitons is the OVS that present stable propagation in defocusing NL media [91]. OVS is a type of dark soliton which carry finite OAM, as described in previous Sections. For this reason, one of the main proposals for OVSs applications is the transfer of the OAM from light to matter [316] but, due to the ring-like intensity profile that describes a bright cylindrical surface during its propagation, OVSs can be used for light guiding [317]. Indeed, the intense field region of a vortex beam can modify the refractive index of a SDF medium, producing the waveguide effect. Demonstrations of optically induced waveguides were reported using dark solitons (beams without OAM) in thermal defocusing NL media [318], atomic vapor [319], and photorefractive materials [320]. More recently, an OVS-induced waveguide was reported in a $LiNbO_3$ crystal due to the action of the photorefractive-photovoltaic effect [321]. Unfortunately, thermal or photorefractive nonlinearities are slow and not suitable for fast dynamic circuitry based on spatial solitons.

In this Section, we report the formation of an optically induced waveguide by an OVS propagating in a SDF medium that is based on the excitation of electronic local nonlinearity. Colloids containing silver nanoparticles in acetone (sample A of Appendix B), managed to exhibit a cubic-quintic (defocusing-focusing) nonlinearity, were used to support the stable propagation of the OVS for up to 10 mm. An intense vortex beam was used to modify the refractive index in the bright-field region compared to the vortex core, in order to induce the waveguide effect. Confinement and guiding of a probe Gaussian beam (PGB) through the 10 mm long induced waveguide were obtained. Numerical simulations based on the CQ-NLSE corroborate the effectiveness of our experimental approach.

7.4.2 Experimental Details

The setup used is illustrated in Fig. 7.14. The excitation (pump) beam is the second harmonic of a Nd:YAG laser (80 ps, 10 Hz, 532 nm, maximum pulse energy of 10 μJ). Control of the total power and the linear polarization of the incident beam was accomplished by using a $\lambda/2$ plate followed by a Glan prism (P). An optical vortex beam with topological charge $m = 1$ was produced by passing the pump beam, previously magnified by a telescope (T), through a phase plate (VPP). A spatial filter (SF) located after the VPP was used to eliminate higher order diffracted light. The vortex beam was focused by a 5 cm focal distance lens (L1) on the input face of a glass cell containing the sample. The waist of the background Gaussian beam

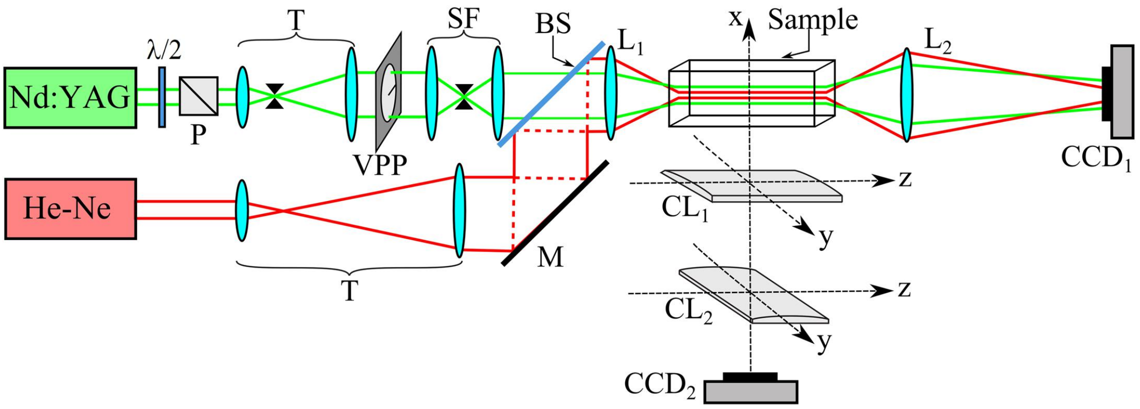

Figure 7.14 Experimental setup: P, polarizer; T, telescope; VPP, vortex phase plate; M, mirror; SF, spatial filter; BS, beam splitter; spherical lenses with $f_1 = 5$ mm (L1) and $f_2 = 5$ mm (L2). Camera CCD_1 produced the transmitted-beam spatial profile. Cylindrical lenses with $f = 40$ mm (CL1) and $f = 80$ mm (CL2), and CCD_2 were used in the SLIM setup. The cell's length is 10 mm.

of the vortex beam was 18 μm and the vortex core radius at the focus was 4.8 μm. A He-Ne laser (632.8 nm, 10 mW) was used as the PGB to be guided by the OVS. A telescope with magnification of 10 was used to increase the beam size, so that when focused by lens L1, the waist of the PGB is approximately equal to the vortex core radius.

Characterization of the transverse and longitudinal pump beam and PGB profiles were performed by using two CCD cameras, following the two complementary processes described in Figs. 6.6 and 7.2. Magnification of 6, produced by the lens L_2, was used for the transverse images, whereas for side-view images, lenses CL_1 and CL_2 produce magnifications of 7 and $1/2$ in y- and z-planes, respectively. Glass filters were used in both detection systems to separate the green (vortex beam) and red (PGB) signals.

The silver colloids were prepared as described in Appendix B with a volume fraction of $f = 3 \times 10^{-5}$. According to the NL characterization performed in Chapter 4, for the intensities used here, this value of f corresponds to an effective third-order susceptibility $\chi^{(3)}_{eff} = -(8.3 + i2.7) \times 10^{-21}$ m^2/V^2 and an effective fifth-order susceptibility $\chi^{(5)}_{eff} = (2.8 + i0.2) \times 10^{-35}$ m^4/V^4. In order to recreate the vortex beam propagation by a distance of 10 mm inside the sample, the Ag-colloid was contained in cells with thicknesses of 3, 5, and 10 mm.

7.4.3 Results and Discussions

In order to produce our OVS-induced waveguide, we must first find the proper conditions for stable propagation of a OVS. Thus, Figs. 7.15(a)-(h) show the transverse beam images after propagation through the cells filled with silver colloid. Figures 7.15(a) and 7.15(e) illustrate the beam's intensity profile at the entrance face of the cell (focal plane of lens L1)[4]. Figures 7.15(a)-(d) show the divergence of the initial doughnut-type beam when the incident intensity

---

[4] Note the difference in scale between Figs. 7.15(a)-(d) and 7.15(e)-(h)

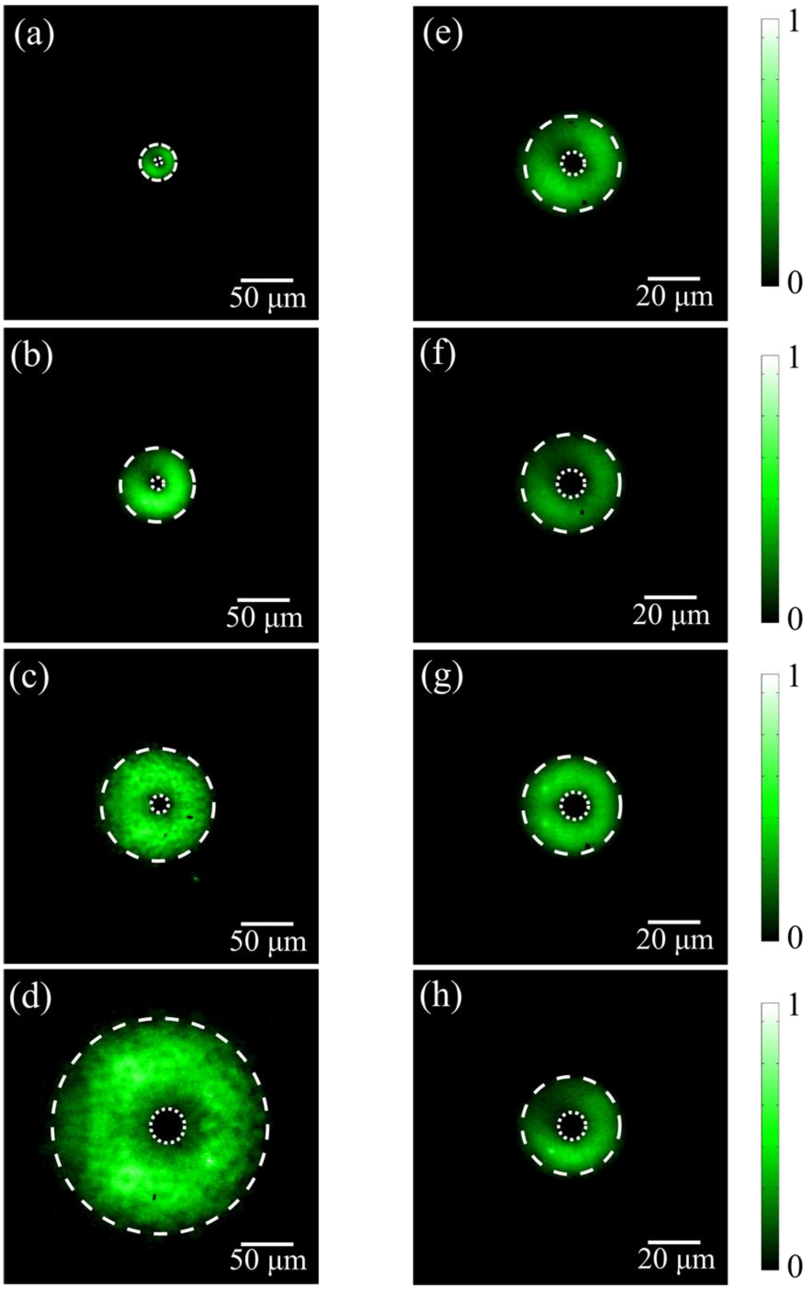

Figure 7.15 Transverse vortex-beam profiles (a), (e) at the entrance face of the cell and (b), (f) after 3 mm; (c), (g) 5 mm and (d), (h) 10 mm of propagation in silver colloids. Beam intensity: (a)-(d) $I_v = 0.1$ GW/cm^2; (e)-(h) $I_v = 3$ GW/cm^2.

is $I_v = 0.1$ GW/cm^2. The NL effects for $I_v < 0.5$ GW/cm^2 are very weak, and the images illustrate the linear regime where the beam propagation is affected mainly by linear diffraction. For $I_v = 3$ GW/cm^2, the sample exhibits NL behavior. Figures 7.15(e)-(h) show that the beams' shape and the external radius of the vortex beam remain constant for propagation over 10 mm, corresponding to $\sim$ 6 Rayleigh lengths. The vortex core diverges slightly in the first millimeter and then remains constant with a radius of 5.6 μm, which will define the inner waveguide radius. Experiments using cells longer than 10 mm were performed showing that the vortex beam loses the OVS characteristic after $\sim$ 13 mm, due to NL absorption. The pointed and dashed lines correspond to the inner and outer diameters of the vortex beam, obtained by numerical simulation of the CQ-NLSE, as described below.

Figures 7.16(a) and 7.16(b) show the images of the vortex beam collected by the side-view measurement system (corresponding to the SLIM). Figure 7.16(a), corresponding to $I_v = 0.1$ GW/cm^2, shows the vortex beam propagation being affected by linear diffraction, in accordance with Figs. 7.15(a)-(d). Nevertheless, for $I_v = 3$ GW/cm^2, the external radius of the vortex beam remains constant over a 10 mm propagation distance, as shown in Fig. 7.16(b). It is worth mentioning that, to define a stable propagation region of an OVS, it is necessary to ensure that the shape and size of the beam remain invariant during propagation. In the present case, the shape-invariance region of the vortex beam is analyzed along the propagation, as seen in Figs. 7.15(e)-(h), while the invariance of the beam radius is monitored using the side-view technique [Fig. 7.16(b)]. Therefore Figs. 7.15(e)-(h) and Fig. 7.16(b) demonstrate the stable propagation of the OVS.

To corroborate the formation and stable propagation of the OVS, numerical simulations were performed based on the CQ-NLSE, given by Eq. 5.31 with $\chi^{(7)}_{eff} = 0$ and optical field amplitude $A_v = A'/2$, that is: $i\frac{\partial A_v}{\partial z} + \frac{1}{2k_0}\nabla_\perp A_v = -\frac{k_0}{2n_0^2}\left[3\chi^{(3)}_{eff}|A_v|^2 + 10\chi^{(5)}_{eff}|A_v|^4\right]A_v$. Figures 7.16(c) and 7.16(d) show a longitudinal section of the vortex beam propagation obtained from the numerical solution of the propagation equation, using the method described in Appendix E. The simulations were performed using as an initial condition the function $A_v(r,\theta,z=0) \propto exp\left(-r^2/w_{BG}^2 + im\theta\right) tanh\left[r/(2w_v)\right]$, where r and θ are the polar coordinates, m is the topological charge, and w_{BG} and w_v are the waists of the Gaussian background and vortex core, respectively. Figure 7.16(c) exhibits the divergence doughnut-type beam due to the linear diffraction, for $I_v = 0.1$ GW/cm^2, while Fig. 7.16(d) shows the stable propagation of the OVS, at $I_v = 3$ GW/cm^2, in accordance with Figs. 7.16(a) and 7.16(b), respectively. Therefore, the experimental [Figs. 7.15(e)-(h) and Fig. 7.16(b)] and the theoretical [Fig. 7.16(d)] results demonstrate the stable propagation of robust (2+1)D OVSs. Numerical simulations were also performed considering $\chi^{(5)}_{eff} = 0$. The results show that the outer diameter of the vortex beam for the same experimental conditions is not constant along the propagation, contrary to the results observed in Figs 7.16(b) and 7.16(d). These results show that, although the self-defocusing third-order nonlinearity is dominant, the contribution of the self-focusing fifth-order nonlinearity is crucial to obtain a stable optically induced waveguide for a long distance.

Figure 7.17 shows the transverse profiles of the PGB propagating in the Ag colloid. Figures 7.17(a)-(d) exhibit the normalized intensity distributions of the PGB as a function of the radial coordinate at the entrance face of the cell and after propagation by 3, 5, and 10 mm, in the

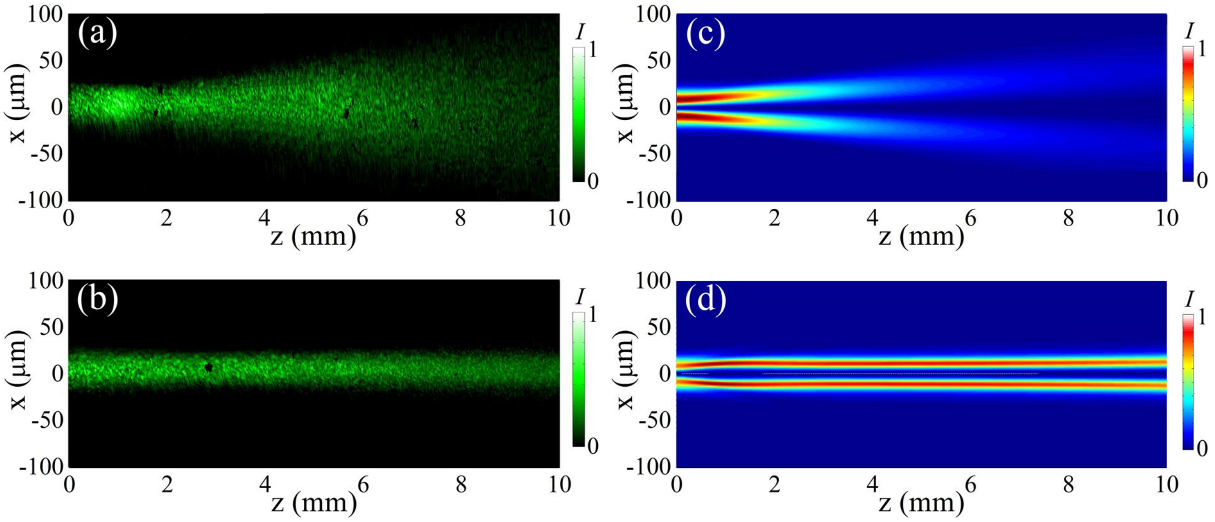

Figure 7.16 (a), (b) Experimental side-view images of the vortex-beam propagation for (a) $I_v = 0.1$ GW/cm^2 and (b) $I_v = 3$ GW/cm^2. (c), (d) Theoretical longitudinal images obtained from CQ-NLSE for the intensities used in (a) and (b), respectively.

absence of the OVS. The circles represent the radial intensity distribution obtained from the images shown in the insets of Figs. 7.17(a)-(d). These pictures show the divergence of the PGB due to the linear diffraction along the length of propagation (the beam radius increases from 7 to 178 µm after propagation of 10 mm). Figures 7.17(e)-(h) show the PGB evolution when propagating inside the OVS core with $I_v = 3$ GW/cm^2, for propagation distances of $z = 0$, 3, 5, and 10 mm. The triangles of Figs. 7.17(i)-(l) were obtained from the images [Figs. 7.17(e)-(h)] processed as intensity matrices.

To ensure that the guiding process is due to the fast electronic response, both CCD cameras were triggered using a digital delay/pulse generator (DDPG), which was triggered by the Nd:YAG laser pulses, at 10 Hz, as shown in Fig 7.18. The first pulse created by the DDPG have a duration of $\tau_1 = 20$ µs, which is the minimum exposure time required by the CCDs. A first measurement (background) was performed by introducing a time delay $\triangle\tau = 20$ µs (including the CCD timing jitter 2 µs) between the pulse used for triggering the CCDs and the pulse delivered by the Nd:YAG laser, such that the camera stop captured before the arrival of the green pulse. Then the recorded signal shows the behavior of the cw laser when it propagates through the Ag colloid in the absence of an OVS. A second measurement was performed with the same time delay, $\triangle\tau$, but with a duration of $\tau_2 = (20\,\mu\text{s} + \tau_3)$, where $\tau_3 = 135$ ps corresponding to the time interval when the OVS is present. Figures 7.17(e)-(h) and Fig. 7.19(a) were obtained by subtracting the images of the second and first measurements. Thus, the experimental images are related to NL effects of electronic origin, because corresponds to an integration time of 135 ps. It is important to note that the camera stops capturing images after 135 ps, therefore, effects related to the slow NL response of the sample are discarded.

The waveguide effect induced by the OVS allows confinement and guiding of the central region of the PGB over 10 mm propagation ($\sim$ 25 Rayleigh lengths of the PGB), compensating for the beam divergence. Nevertheless, a fraction of the beam escapes from the core of the OVS

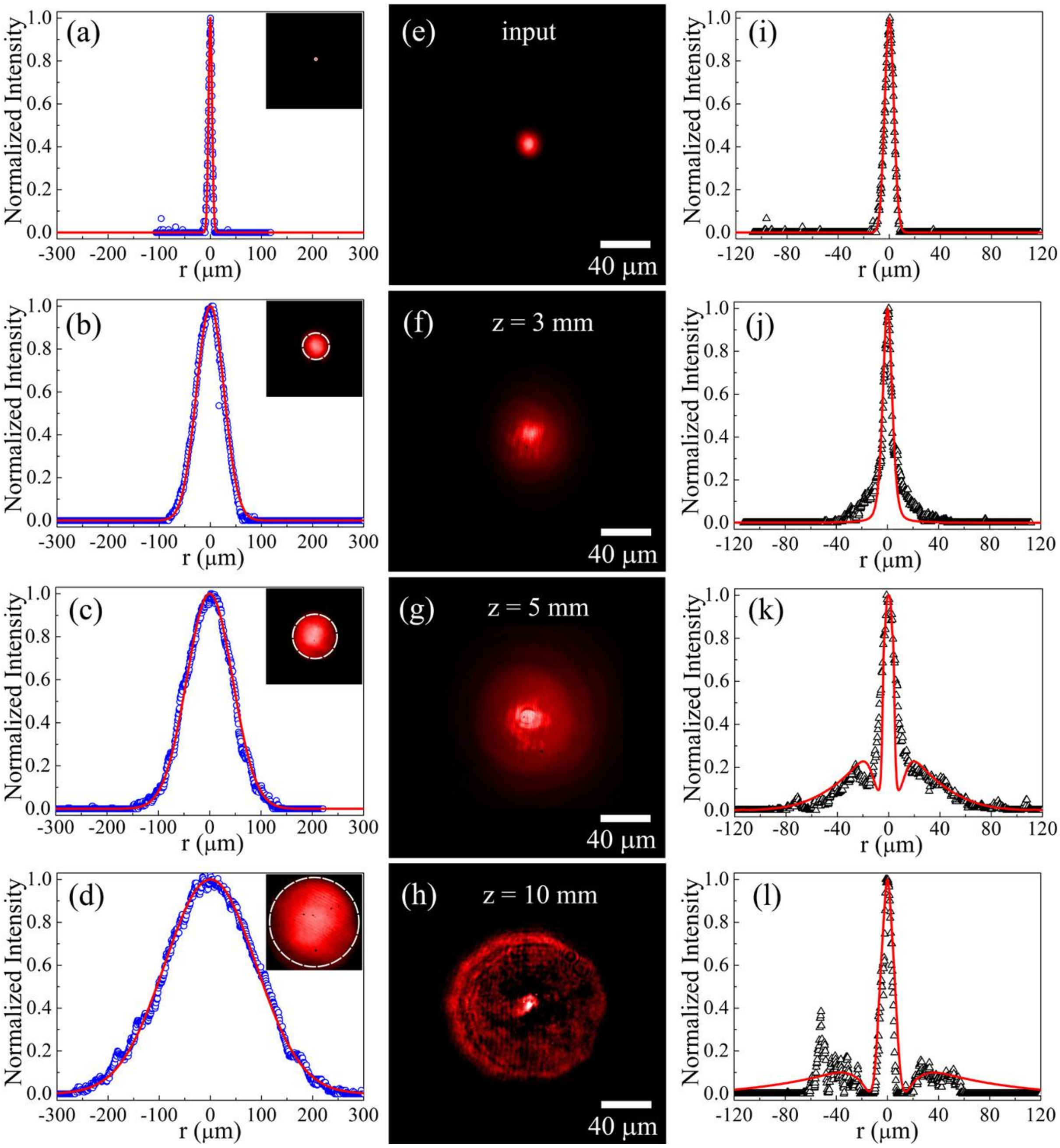

Figure 7.17 Normalized intensity distribution of Gaussian beam in absence of the OVS, for (a) $z = 1$ mm, (b) 3 mm, (c) 5 mm, and (d) 10 mm. The insets correspond to the transverse beam profile in each position. (e) Transverse Gaussian-beam profile at the entrance face of the cell and after being guided by the vortex by a distance of (f) 3 mm, (g) 5 mm, and (h) 10 mm. (i)-(l) Experimental normalized intensity distribution for $I_v = 3\ \mathrm{GW/cm^2}$ (blue triangles) obtained from (e)-(h). The red lines were obtained from Eq. 7.2.

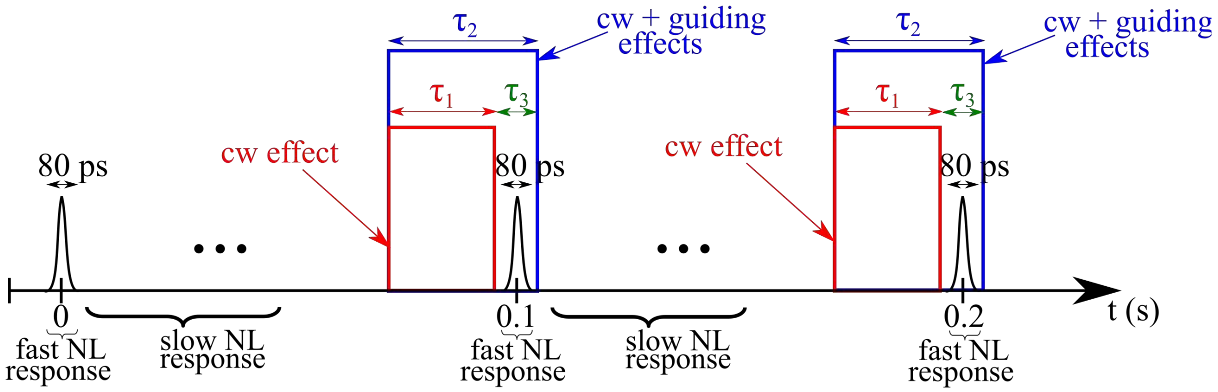

Figure 7.18 Camera trigger process to capture the transversal and side-view images. $\tau_1 = 20\ \mu$s, $\tau_2 = (20\ \mu\text{s} + \tau_3)$ and $\tau_3 = 135$ ps.

for larger propagation distances, which can be identified by the ring formed in Fig. 7.17(h). The solid lines of Figs. 7.17(i)-(l) show the theoretical intensity distributions obtained solving the two coupled CQ-NLSEs given by:

$$\begin{aligned}2ik_j\frac{\partial A_j}{\partial z}+\nabla_\perp A_j=-\frac{\omega_j^2}{c^2}\Big\{&3\chi^{(3)}_{eff}\left[|A_j|^2+2\left(|A_G|^2\delta_{j,v}+|A_v|^2\delta_{j,G}\right)\right]\\&+10\chi^{(5)}_{eff}\left[|A_j|^4+6|A_v|^2|A_G|^2+3\left(|A_G|^4\delta_{j,v}+|A_v|^4\delta_{j,G}\right)\right]\Big\}A_j,\end{aligned}\tag{7.2}$$

where $j = v, G$ corresponds to the vortex and PGB, respectively. The NL contribution of the Gaussian beam is negligible due to its small intensity $\left(|A_G|^2 \ll |A_v|^2\right)$, and, therefore, for $j = v$, Eq. 7.2 has the same form as the CQ-NLSE obeyed by the OVS alone. However, for $j = G$, the propagation of the PGB is strongly affected by the NL contributions of the vortex beam. In Figs. 7.17(i)-(l), the red lines show the theoretical PGB transverse profile obtained from Eq. 7.2 by using the NL parameters measured in Z-scan experiments for $I_v = 3\ \text{GW/cm}^2$ and $I_G = 10\ \text{kW/cm}^2$. Dispersion effects between the red and green beams were not considered, because NL contributions induced by the PGB are negligible.

Figure 7.19 illustrates the longitudinal cross section of the PGB along its propagation in the presence of the OVS. Figure 7.19(a) was obtained using the SLIM apparatus. From the picture, it is possible to observe that the central region of the PGB is guided along the 10 mm long cell; the region of the PGB confinement corresponds to the vortex core. The spreading of the Gaussian beam beyond the vortex core is observed for longer propagation distances, in accordance with Fig. 7.17. The numerical simulation of the PGB propagation being guided by the OVS, obtained from Eq. 7.2, is displayed by Fig. 7.19(b). Note that, after propagation by 1 mm, a fraction of the beam intensity passes through the "walls" induced by the OVS and continues diverging along its propagation, generating the light ring observed in Fig. 7.17(h). Guiding efficiency of 22% was obtained in all measurements after propagation by 10 mm.

The intensity losses of the PGB during propagation are due to linear scattering and diffraction. The linear absorption of the Ag colloid at 632.8 nm and its NL contributions are negligible.

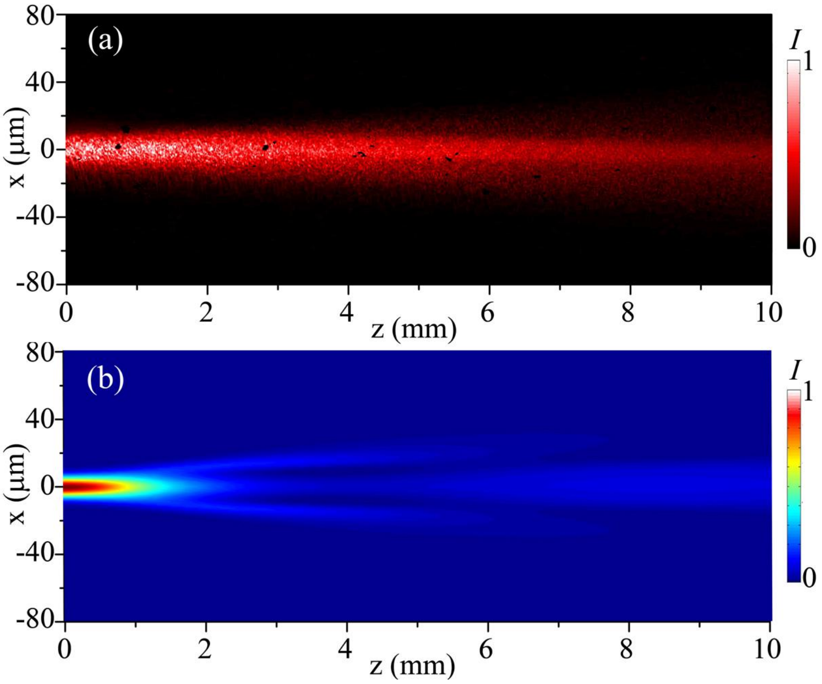

Figure 7.19 (a) Experimental and (b) numerical Gaussian beam propagation being guided by an OVS. $I_v = 3\ \mathrm{GW/cm^2}$ and $I_G = 10\ \mathrm{kW/cm^2}$.

Escape of radiation and ring formation in Figs. 7.17(h) and 7.19(a) are related to an imperfect coupling of the PGB into the vortex core, and to the small refractive index difference induced between the core and the bright region of the OVS.

Therefore, the results presented here reveal, for the first time, the importance of HON (quintic nonlinearities) in the formation and stable propagation of OVSs (vortex core and Gaussian background), essential to produce the effect of guiding and light confinement. In addition, the fast NL response of the materials used, open new routes for applications of optical phenomena induced by HON in the construction of all-optical devices and procedures of light-by-light control.

Experimental confirmation of a prediction is merely a measurement. An experiment disproving a prediction is a discovery.
- ENRICO FERMI

8 NONLINEAR POLARIZATION INSTABILITY IN CUBIC-QUINTIC MDNC

In this Chapter, I report a study of the NL birefringence induced in a MDNC due to the contributions of third- and fifth-order nonlinearities. Control of the NL polarization of a light beam was performed by using the NM procedure discussed in Chapter 5, which consists in manipulate the NL response of MDNC by changing the NPs volume fraction, f, and the light intensity. Large NL phase-shift ($\sim 20\pi$) was observed using a 9 cm long capillary filled with silver NPs suspended in CS_2. Proof-of-principle experiments were performed by using the sample B of Appendix B with $1.0 \times 10^{-5} \leq f \leq 4.5 \times 10^{-5}$ and maximum light intensities of tens of MW/cm^2. Here, we demonstrated that the modulation instability is highly sensitive to the quintic nonlinearity contribution. In addition, a model to describe the evolution of the light polarization state was developed considering the contributions of the third- and fifth-order susceptibilities. Numerical simulations were performed showing good agreement with the experimental results.

8.1 INTRODUCTION

As considered in the previous chapters, the NL optical polarization induced by a laser beam propagating through a system with inversion symmetry can be described mathematically by an expansion in powers series of the electric field where the even-order terms are null, unless the symmetry is disturbed. The nonzero expansion coefficients, $\chi^{(2N+1)}$, with $N = 1, 2, \ldots$, called of $(2N+1)$th-order susceptibility, provide a measure of how strong is the light-matter interaction [51]. The majority of articles in the literature are related to the cubic nonlinearity, due to $\chi^{(3)}$, which is the parameter that describes phenomena such as third-order self-focusing, coherent anti-Stokes Raman scattering and two-photon absorption, among other phenomena [21]. However, in several cases, the odd HON are essential for the complete characterization of the NL response [158, 220, 23, 33, 322]. For instance, novel effects such as liquid light condensates [28], high-harmonic generation [31], filamentation [243, 224, 238], stable propagation of two dimensional spatial solitons in homogeneous media [30] and optical rogue waves generation [29] are associated to HON. In addition, an important consequence of HON is the NL birefringence effect which is manifested by the polarization rotation of an elliptically polarized light beam along its propagation [212]. This effect can be much influenced by HON when the highly NL materials currently available are excited with moderate laser intensities or even when gasses are excited with intense laser pulses [219]; for instance, some years ago an experimental study showed how HON can enhance the polarization rotation of a weak probe beam induced by a strong beam [219]. The authors were able to identify HON contributions for the NL birefringence in air and determined the NL refractive indices associated to third, fifth, seventh, ninety and eleventh order susceptibilities of the main air components (nitrogen, oxygen and argon). Subsequently, a simple formalism was presented for precise characterization of the non-resonant NL birefringence [323].

Nowadays, it is well known that further advances in the telecommunications area require in-depth studies of light propagation in highly NL optical fibers [324]. Indeed, NL birefringence has been widely studied with important applications in all-optical devices [325, 326, 327]. However, the main limitation of optical fibers in all-optical circuits is related to the long propagation distances required to obtain induced polarization rotation. To minimize this problem, highly NL-core waveguides were developed allowing increasing of the polarization rotation of the coupled light field in small propagation distances [328]. A particular example was reported in the past using an optical capillary where the core was filled with nitrobenzene that is highly NL [329]. Therefore large NL phase shift of $\triangle\Phi_{NL} \approx 12\pi$ in the infrared was obtained for propagation distances of ≈ 10 cm.

On the other hand, MDNCs consisting of a dielectric host containing metal NPs emerged as excellent systems with high NL susceptibility and ultrafast response that can be used as platforms to study many associated HON phenomena. In particular, silver colloids have been extensively studied under different conditions exhibiting important HON contributions. The exploitation of these HON allowed enhancement of the NL response and even suppress NL absorption effects by using a NM procedure, as discussed in Chapter 4. In this sense, metal-colloids are strong candidates to investigate the contribution of the NL birefringence in short propagation distance, with potential applications in the construction of all-optical devices.

In this Section, we demonstrate large NL phase-shifts when picosecond laser pulses propagate in a 9 cm long capillary filled with silver NPs suspended in liquid CS_2. Control of the NL response was obtained by varying the NPs volume fraction from $f = 1.0 \times 10^{-5}$ to $f = 4.5 \times 10^{-5}$, obtaining $\triangle\Phi_{NL} \approx 20\pi$ for peak intensities of tens of MW/cm^2. In this regime of intensity, silver colloids behave like a cubic-quintic media, where depending on the values of f the NL response is dominated by the third- or fifth-order nonlinearity. The experimental results were modeled by two coupled differential NL equations that describe the evolution of the right- and left-circular polarization in samples exhibiting cubic-quintic nonlinearities, following the model developed in Section 5.5. The gain spectra of the modulation instability were obtained, showing that the instabilities increase significantly due to the presence of the quintic nonlinearity.

8.2 EXPERIMENTAL DETAILS

The setup used to study the intensity-dependent birefringence of the silver colloids is illustrated by Fig. 8.1(a). The second harmonic of a Q-switched and mode-locked Nd: YAG laser (532 nm, 80 ps, 10 Hz) was used to excite the samples with maximum pulse energy of 10 μJ. A system composed of a Glan prism (P) located between two $\lambda/2$ plates was used to control the incident power and rotate the polarization axis of a linearly polarized laser pulse by an azimuth angle θ. A 40x microscope objective (L1) was used to couple the laser light into a fused-silica capillary ($n_0 = 1.46$) with inner (outer) diameter of 2 μm (285 μm). The capillary (length: 9 cm) had at the entrance and exit faces two reservoirs with the input and output sides of the capillary touching the reservoirs windows. The silver colloid (sample B of Appendix B) was

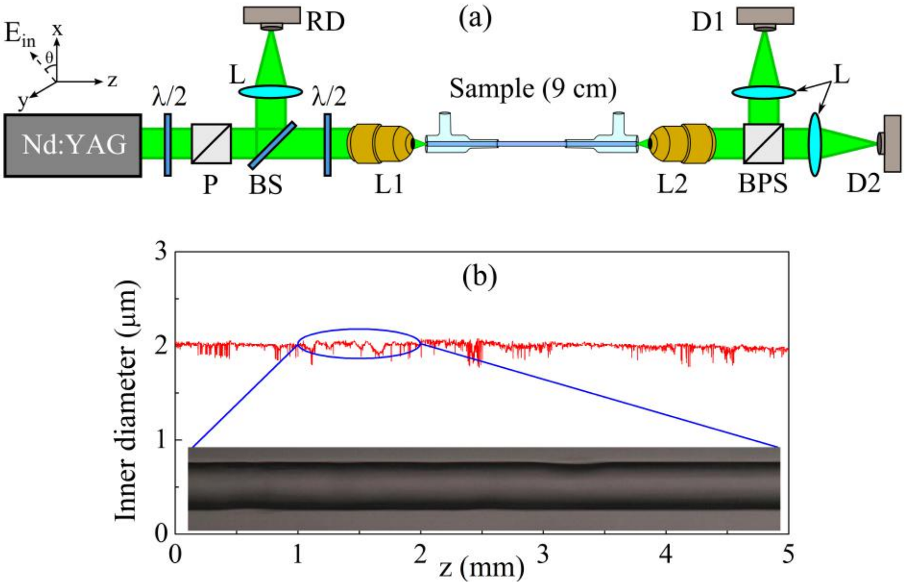

Figure 8.1 (a) The experimental setup: polarizer (P), beam splitter (BS), spherical lenses with $f = 5$ cm (L), 40x microscope objective (L1), 20x microscope objective (L1), polarizing beam splitter cube (PBS) and reference detector (RD). The transmitted light on the vertical and horizontal axis were captured in the fast detectors D1 and D2, respectively. (b) Inner diameter of capillary, in a portion of 5 mm, showing small asymmetries. The inset is an optical microscope image of a small section of the hollow capillary core (length: 1 mm).

filled in one of the reservoirs, and using a strong air pressure the colloid was conveyed through the capillary to the other reservoir, in order to guarantee that the capillary is completely filled with a homogeneous sample (no air bubbles were observed in the end of the filling process). A 20x microscope objective (L2) was used to collimate the laser light after the propagation along the capillary. The laser beam was split by a polarizing beam splitter cube (PBS) to separate the vertical (V) and horizontal (H) polarization components, that were monitored by fast detectors D1 and D2, respectively. A reference detector (RD) was used to correct for the laser intensity fluctuations. Fig 8.1(b) displays the inner diameter of the capillary, in a fragment of 5 mm, showing small asymmetries that induce linear birefringence in the sample. The inset of Fig. 8.1(b) shows an image of the capillary' core (length: 1 mm), obtained using a high resolution optical microscope.

Two experiments were performed to study the NL birefringence of the samples. In one experiment made to analyze the optical transmission as a function of the optical field polarization, the laser beam intensity was fixed and the incident polarization direction was rotated by the second $\lambda/2$ plate using a motorized rotation stage, with step of ~ 3.6 degrees. The second experiment, performed to investigate the transmittance intensity dependence was performed by rotating the first $\lambda/2$ plate using another motorized rotation stage with intensity step of ~ 350 kW/cm^2, maintaining fixed the polarization angle of the incident electric field.

8.3 RESULTS AND DISCUSSIONS

The evolution of the right- and left-circular polarization in media exhibiting cubic-quintic nonlinearities was discussed in Section 5.5 and can be generally described by Eq. 5.76. However, this expression corresponding to two coupled differential NL equations can take a specific form depending on the origin of the medium nonlinearity. In particular, silver colloids exhibit fast electronic NL response but their NL optical properties depend on the nature, shape and volume fraction of the silver NPs, the laser frequency, which it is related with the resonant and nonresonant excitation processes, and the mismatch between the dielectric functions of the NPs and their host [148, 147, 142]. In fact, for the conditions used in our experiment, the complex NL susceptibilities, that correspond to nonresonant processes of electronic origin, obey the relationship: $\chi^{(3)}_{xxyy} = \chi^{(3)}_{xyyx} = {}^{1}\!/_{3}\chi^{(3)}_{xxxx}$ and $\chi^{(5)}_{xxyyxx} = \chi^{(5)}_{xxyyyy} = {}^{1}\!/_{5}\chi^{(5)}_{xxxxxx}$ [323].

In addition, for the case of a capillary filled with a silver colloid, the induced birefringence is due to the refractive index shift $(\triangle n)$ induced by the NPs nonlinearity. For peak intensity of tens of MW/cm^2 (used in this work), we have $\triangle n < 10^{-5}$, corresponding to a weak birefringence. Therefore, we may assume $\beta_x^{(1)} \approx \beta_y^{(1)} = \beta^{(1)}$ and making a transformation of Eq. 5.76 to the pulse reference frame $(z,t) \rightarrow (z, \tau = t - {}^{z}\!/_{v_g})$, with $v_g = \left[\beta^{(1)}\right]^{-1}$, we obtain:

$$
\begin{aligned}
&\frac{\partial A_\pm}{\partial z} + \frac{i}{2}\beta^{(2)}\frac{\partial^2 A_\pm}{\partial \tau^2} + \frac{\alpha_0}{2}A_\pm \\
&\quad = \frac{i}{2}\left(\triangle\beta_0\right)A_\mp + i\frac{\omega_0}{4n_0c}F^{(1)}\chi^{(3)}_{xxxx}\left[\left(|A_+|^2+|A_-|^2\right)+|A_\mp|^2\right]A_\pm \\
&\quad + i\frac{5\omega_0}{192n_0c}F^{(2)}\chi^{(5)}_{xxxxxx}\left\{4\left[|A_+ + A_-|^2\left(A_+ + A_-\right)^* \mp |A_+ - A_-|^2\left(A_+ - A_-\right)^*\right]A_\mp\right. \\
&\qquad\qquad \left. + \left[|A_+ + A_-|^4 + |A_+ - A_-|^4\right]\right\}A_\pm,
\end{aligned}
\tag{8.1}
$$

where the dispersion coefficients for silver-colloids can be obtained by using the Maxwell-Garnett model. Here, the effective dielectric function for a macroscopically isotropic medium is given by $\varepsilon_{eff}(\lambda) = \varepsilon_h(\lambda)\left[1 + {}^{3\Theta(\lambda)f}\!/_{1-\Theta(\lambda)f}\right]$, with $\Theta = {}^{\left[\varepsilon_{NP}(\lambda)-\varepsilon_h(\lambda)\right]}\!/_{\left[\varepsilon_{NP}(\lambda)+2\varepsilon_h(\lambda)\right]}$ [see Eqs. 3.22 and 3.23], where ε_{NP} and ε_h are the linear dielectric functions of the silver NPs and the host, and f is the volume fraction occupied by the silver NPs. For the experiments reported in this Section, liquid CS_2 was used as the solvent (host) and its dielectric function can be written by $\varepsilon_h(\lambda) = \left[n_{CS_2}(\lambda)\right]^2$, where the refractive index of CS_2 is given by Eq. 3.26.

On the other hand, the dielectric function of the silver NPs found by using the Drude's free-electron model [Eqs. 3.14 and 3.15] is given by:

$$
\varepsilon_{NP}(\lambda) = \left(1 - \frac{\lambda^2}{\lambda_p^2}\right) + i\left(\frac{1}{2\pi c\tau_r}\frac{\lambda^3}{\lambda_p^2}\right),
\tag{8.2}
$$

where $\lambda_p^{-2} = Nq^2/\left(4\pi^2\varepsilon_0 m_0 c^2\right)$, N and q are the density and charge of the conduction electrons, m_0 is their effective mass, and τ_r is the relaxation time of the electrons in the metal. For silver, the values of $\lambda_p = 0.138$ μm and $\tau_r = 31$ fs were reported in [114]. Hence, the dielectric function can be written as $\varepsilon_{NP}(\lambda) = \left(1 - 52.51\lambda^2\right) + i\left(0.899\lambda^3\right)$ and consequently, by substituting Eqs. 3.26 and 8.2 in the effective dielectric function, $\varepsilon_{eff}(\lambda)$, and defining the effective refractive index by $n_{eff}(\lambda, f) = 2^{-1/2}\sqrt{Re\left[\varepsilon_{eff}(\lambda, f)\right] + \left|\varepsilon_{eff}(\lambda, f)\right|}$, we obtain the dispersion coefficients

$$\beta^{(1)}(\lambda, f) = \frac{1}{c}\left[n_{eff}(\lambda, f) - \lambda\frac{\partial\left[n_{eff}(\lambda, f)\right]}{\partial\lambda}\right], \tag{8.3}$$

$$\beta^{(2)}(\lambda, f) = \frac{\lambda^3}{2\pi c^2}\frac{\partial^2\left[n_{eff}(\lambda, f)\right]}{\partial\lambda^2}. \tag{8.4}$$

For instance, for $\lambda = 532$ nm and $f = 10^{-5}$ we determined $\beta^{(1)} = 6.06$ ns/m and $\beta^{(2)} = 0.717$ ps^2/m.

The evolution of the x- and y-components of the electric field being affected by the NL birefringence of a 9 cm long capillary filled with silver NPs suspended in CS_2 were analyzed by solving numerically the two coupled equations [Eq. 8.1], using the compact finite-difference method based on the Crank–Nicolson scheme [235], described in Appendix E. In order to compare the contributions of the NL susceptibilities of different order on the polarization instability effect, we use pure CS_2 (host) and silver-colloid with four different volume fractions (sample B of Appendix B), whose corresponding values of α_0, $\beta^{(2)}$, $\chi^{(3)}_{xxxx}$ and $\chi^{(5)}_{xxxxxx}$ are displayed in Table 8.1. Sample B1 (S-B1), corresponding to pure CS_2 $(f = 0)$, exhibits only third-order nonlinearity, for the intensities used in this Section. The other four samples (S-B2, S-B3, S-B4 and S-B5), containing silver NPs with $1.0 \times 10^{-5} \leq f \leq 4.5 \times 10^{-5}$, display contributions of third- and fifth-order susceptibilities which depend on the f value, as discussed in Chapter 4. Notice that, S-B2 represents a cubic-quintic (self-focusing) medium, where the NL refraction is dominated by the positive $Re\left[\chi^{(3)}_{xxxx}\right]$. By contrast, S-B4 and S-B5 correspond to cubic-quintic (defocusing-focusing) media, because their NL responses are dominated by the negative value

Sample	Volume fraction (f)	α_0 (m^{-1})	$\beta^{(2)}$ (ps^{2}m^{-1})	$\chi^{(3)}_{xxxx}$ $(\times 10^{-20}$ m^{2}V$^{-2})$	$\chi^{(5)}_{xxxxxx}$ $(\times 10^{-35}$ m^{4}V$^{-4})$
S-B1	0	0	0.717	$2.92 + i0.04$	$(2.9 + i0.9) \times 10^{-2}$ *
S-B2	1.0×10^{-5}	9.02	0.717	$1.79 - i0.20$	$2.05 + i0.20$
S-B3	1.8×10^{-5}	16.23	0.718	$-i0.41$	$2.98 + i0.31$
S-B4	3.0×10^{-5}	27.05	0.719	$-2.07 - i0.65$	$6.36 + i0.64$
S-B5	4.5×10^{-5}	40.57	0.720	$-4.89 - i1.02$	$9.04 + i0.87$

Table 8.1 Linear absorption coefficient (α_0), second-order dispersion coefficient $\left(\beta^{(2)}\right)$, third-order susceptibility $\left(\chi^{(3)}_{xxxx}\right)$, and fifth-order susceptibility $\left(\chi^{(5)}_{xxxxxx}\right)$ for pure CS_2 (S-B1) and silver colloids with different NPs volume fraction. The values of α_0 and $\beta^{(2)}$ were obtained following the Drude model, while the $\chi^{(3)}_{xxxx}$ and $\chi^{(5)}_{xxxxxx}$ values were reported in Chapter 4.
* $\chi^{(5)}$ for pure CS_2 was determined by using 12-ps laser pulses, with intensities of GW/cm^2 [330].

of $Re\left[\chi^{(3)}_{xxxx}\right]$. The change from self-focusing to self-defocusing media is due to the competition between the host (CS_2) and silver NPs nonlinearities, which have opposite signs. However, S-B3 exemplifies a refractive quintic medium $\left(Re\left[\chi^{(3)}_{xxxx}\right]=0\right)$ due to the destructive interference of the third-order susceptibilities of the host and the NPs, obtained by using the NM procedure of Chapter 4.

Figure 8.2 shows the numerical pulse shape evolution, for the five samples, with input intensity of 60 MW/cm^2. For all cases, the input beam has a Gaussian profile with pulse duration of 80 ps. A temporal window of 400 ps, with steps of 0.1 ps, was used for the numerical simulations. For S-B1 (black line) the pulse propagates keeping its Gaussian shape, but suffering a small broadening from 80 ps to ~89 ps. Due to the small concentration of NPs the contribution of the fifth-order nonlinearity is negligible is this case. On the other hand, the pulse propagation inside S-B2 (red line) is influenced by temporal-modulation instability (TMI). In this case $n_{2,eff}\propto Re\left[\chi^{(3)}_{xxxx}\right]$ of S-B2 is less than of S-B1 [see Table 8.1] and then we concluded that the main contribution for TMI is due to $n_{4,eff}\propto Re\left[\chi^{(5)}_{xxxxxx}\right]$. To corroborate our interpretation, we studied the pulse propagation in a quintic refractive medium (blue line), corresponding to S-B3. The TMI effect increased due to the larger $n_{4,eff}$ than in the samples S-B1 and S-B2. Moreover, more intense TMI effect is observed in S-B4 (green line) and S-B5 (pink line), corresponding to more concentrated silver-colloids. Intensity losses along the propagation, in all samples, are due to linear and NL absorptions.

In order to analyze the dependence of TMI on the third- and fifth-order nonlinearities, we studied the laser pulse stability, along its propagation, by performing a perturbation analysis of the pulse amplitude. For simplicity, we assume that the polarization state is oriented along the fast axis $(A_x=0)$. Therefore, considering a Gaussian laser pulse profile, the field amplitude is represented by:

$$A_{\pm}(z,\tau)=\pm iB(z,\tau)\,exp\left(-\frac{\alpha_0 z}{2}-i\frac{\triangle\beta_0}{2}z\right)exp\left(-\frac{\tau^2}{\tau_0^2}\right), \tag{8.5}$$

where $B(z,\tau)=B_0 exp\left[\Lambda(\tau)z+i\varphi(\tau)z\right]$ is the unperturbed pulse amplitude. B_0 is the incident power at $z=0$, τ_0 is the initial pulse duration, $\Lambda(\tau)$ and $\varphi(\tau)$ are given by:

$$\Lambda(\tau)=-\frac{B_0\omega_0}{c}\left[\frac{3}{4}F^{(1)}Im\left(\chi^{(3)}_{xxxx}\right)+\frac{5}{4}B_0^2F^{(2)}Im\left(\chi^{(5)}_{xxxxxx}\right)exp\left(-2\frac{\tau^2}{\tau_0^2}\right)\right]exp\left(-2\frac{\tau^2}{\tau_0^2}\right), \tag{8.6}$$

$$\begin{aligned}\varphi(\tau)=&-\frac{1}{2}\beta^{(2)}\left[-\frac{2}{\tau_0^2}\left(1-\frac{2\tau^2}{\tau_0^2}\right)\right]\\&+\frac{B_0^2\omega_0}{c}\left[\frac{3}{4}F^{(1)}Re\left(\chi^{(3)}_{xxxx}\right)+\frac{5}{4}B_0^2F^{(2)}Re\left(\chi^{(5)}_{xxxxxx}\right)exp\left(-2\frac{\tau^2}{\tau_0^2}\right)\right]exp\left(-2\frac{\tau^2}{\tau_0^2}\right).\end{aligned} \tag{8.7}$$

The modulated amplitude of the laser pulse may be written as the superposition of perturbed and unperturbed amplitudes, as:

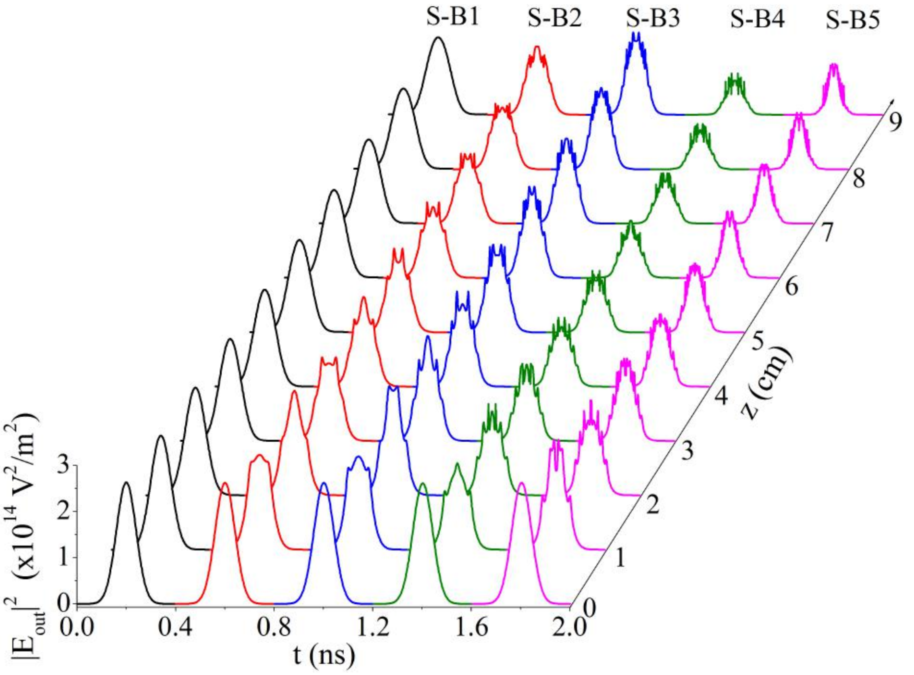

Figure 8.2 Numerical pulse shape evolution for the sample B1 (S-B1), sample B2 (S-B2), sample B3 (S-B3), sample B4 (S-B4) and sample B5 (S-B5), with input intensity of 60 MW/cm^2. Pulse duration: 80 ps. Propagation length: 9 cm.

$$a_{\pm}(z,\tau) = \pm i\left\{B_0 exp\left[\Lambda(\tau)z\right] + B_{1,\pm}(z,\tau)\right\} exp\left[i\varphi(\tau)z\right] exp\left(-\frac{\alpha_0 z}{2} - i\frac{\triangle\beta_0}{2}z\right) exp\left(-\frac{\tau^2}{\tau_0^2}\right), \tag{8.8}$$

where $B_{1,\pm}(z,\tau)$ is the complex perturbed beam amplitude. Then, by introducing Eq. 8.8 in Eq. 8.1 and linearizing as a function of $B_{1,\pm}(z,\tau)$, we obtain

$$\begin{aligned}
& i\left\{\frac{\partial B_{1,\pm}}{\partial z} + i\varphi B_{1,\pm} \mp \frac{i}{2}(\triangle\beta_0)(B_{1,+} - B_{1,-})\right\} - \frac{1}{2}\beta^{(2)}\left\{\frac{\partial^2 B_{1,\pm}}{\partial\tau^2}\right. \\
& \left. +2\left[iz\frac{\partial\varphi}{\partial\tau} - \frac{2\tau}{\tau_0^2}\right]\frac{\partial B_{1,\pm}}{\partial\tau} + izB_{1,\pm}\left[\frac{\partial^2\varphi}{\partial\tau^2} - \frac{4\tau}{\tau_0^2}\frac{\partial\varphi}{\partial\tau} + iz\left(\frac{\partial\varphi}{\partial\tau}\right)^2\right] + \frac{2}{\tau_0^2}\left[\frac{2\tau^2}{\tau_0^2} - 1\right]B_{1,\pm}\right\} \\
& \qquad = -\frac{\omega_0}{4c}|B_0|^2 F^{(1)}\chi^{(3)}_{xxxx}\left[5B_{1,\pm} + 2(B_{1,+} + B_{1,-})\right] exp\left(2\Lambda z - \alpha_0 z - \frac{2\tau^2}{\tau_0^2}\right) \\
& \qquad\quad - \frac{5\omega_0}{12c}F^{(2)}\chi^{(5)}_{xxxxxx}\left\{|B_0|^4\left[3B_{1,\pm} + 2(B_{1,+} + B_{1,-} + B_{1,\mp})\right]\right. \\
& \qquad\qquad \left. +3|B_0|^2 B_0^2\left[B_{1,+} + B_{1,-}\right]^*\right\} exp\left(4\Lambda z - 2\alpha_0 z - \frac{4\tau^2}{\tau_0^2}\right).
\end{aligned} \tag{8.9}$$

Solutions of Eq. 8.9 were found by neglecting further variations in the pulse shape and considering the perturbed wave amplitude to be a sinusoidal varying function of z and τ, that is, $B_{1,\pm} = u_{\pm} exp\left[i\left(Kz - \Omega\tau\right)\right] + iv_{\pm} exp\left[-i\left(Kz - \Omega\tau\right)\right]$, with K and Ω being the wave number and frequency of the perturbed wave amplitude, respectively. Nontrivial solutions are obtained only when the perturbation satisfies the following dispersion relation:

$$K^2 + \left[2\beta^{(2)}\Omega\left(z\frac{\partial\varphi}{\partial\tau}\right)\right]K - M = 0, \tag{8.10}$$

where

$$\begin{aligned} M ={}& Re\left(N^2\right) - 2\beta^{(2)}\Omega\left[z\frac{\partial\varphi}{\partial\tau}Re\left(N\right) - \frac{2\tau}{\tau_0^2}Im\left(N\right)\right] \\ &+ \left[\frac{5}{2}\frac{\omega_0}{c}B_0^2\left|B_0\right|^2 F^{(2)} exp\left(4\Lambda z - 2\alpha_0 z - \frac{4\tau^2}{\tau_0^2}\right)\right]^2 Re\left[\left(\chi^{(5)}_{xxxxxx}\right)^2\right], \\ N ={}& \varphi + \frac{1}{2}\beta^{(2)}\left\{-\Omega\left[\Omega + 2i\left(iz\frac{\partial\varphi}{\partial\tau} - \frac{2\tau}{\tau_0^2}\right)\right] + iz\left[\frac{\partial^2\varphi}{\partial\tau^2} - \frac{4\tau}{\tau_0^2}\frac{\partial\varphi}{\partial\tau} + iz\left(\frac{\partial\varphi}{\partial\tau}\right)^2\right] + \frac{2}{\tau_0^2}\left[\frac{2\tau^2}{\tau_0^2} - 1\right]\right\} \\ &- 3\frac{\omega_0}{c}\left|B_0\right|^2 exp\left(2\Lambda z - \alpha_0 z - \frac{2\tau^2}{\tau_0^2}\right)\left[\frac{3}{4}F^{(1)}\chi^{(3)}_{xxxx} + \frac{5}{4}\left|B_0\right|^2 F^{(2)}\chi^{(5)}_{xxxxxx} exp\left(2\Lambda z - \alpha_0 z - \frac{2\tau^2}{\tau_0^2}\right)\right]. \end{aligned} \tag{8.11}$$

Figure 8.3 shows the local gain spectra of TMI versus the frequency shift along the fast axis, obtained from the imaginary part of K $\left[g\left(\Omega, z\right) = 2Im\left(K\right)\right]$. The local gain depends only on the field amplitude in the z position, since the amplitude varies with propagation due to dissipative terms. Local TMI gain curves were calculated for a peak intensity of 42 MW/cm^2 that corresponds to the pulse intensity at $\tau = 0.1\tau_0$, after a propagation distance of 1.5 mm. In the normal-dispersion regime $\left(\beta^{(2)} > 0\right)$, the S-B1 sample, which is a self-focusing cubic medium, presents a very small modulation instability gain compared to the other samples. However, under the same conditions, samples exhibiting NL contributions of fifth-order (from S-B2 to S-B5) display a growth of the local modulation instability gain with nonlinearity increasing. The local gain curve obtained for S-B3 (refractive quintic media) clearly shows that the growth rate of TMI strongly depends on the quintic nonlinearity contribution, since that the refractive cubic nonlinearity is null, as identified in Table 8.1. Distortions in the sidebands are attributed to the presence of linear loss [203]. To obtain an analytical expression for the total gain generated after a propagation distance L, it is necessary to integrate the local gain with respect to z in the interval from 0 to L [331]. Notice however that by performing the numerical simulation based on the NL propagation equations this is automatically considered.

Figure 8.4 shows the normalized transmittance as a function of the incident polarization azimuth angle, θ, for the five samples. From top to bottom, the incident peak intensities correspond to 6, 24, 42 and 60 MW/cm^2, in each column. For $I \leq 6$ MW/cm^2 [first row of Fig. 8.4], all samples behave as linear isotropic media. As a consequence, the normalized experimental transmittance exhibits a $cos^2\left(\theta\right)$ dependence (black circles) for the vertical (V)-polarization (captured in D1) and a $sin^2\left(\theta\right)$ dependence (red squares) for the horizontal (H)-polarization

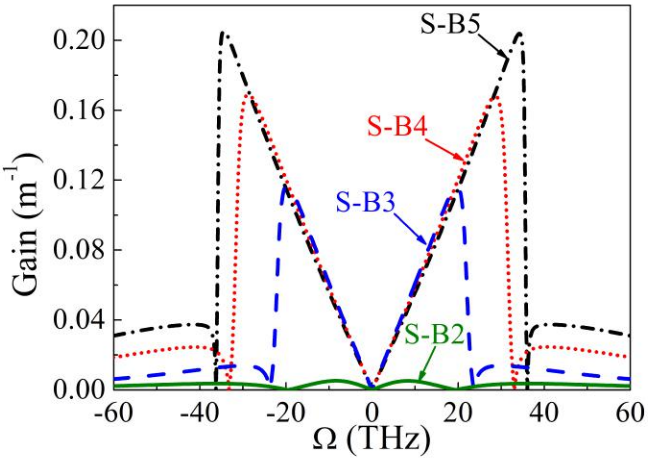

Figure 8.3 Local gain spectra of modulation instability versus the frequency shift along the fast axis, for the five samples.

(captured in D2). Black and red lines represent the normalized transmittance on the V- and H-polarization, obtained by numerical solution of Eq. 8.1 and using the coefficients of Table 8.1. At $I = 24$ MW/cm^2 [second row of Fig. 8.4], the transmittance response as a function of θ shows significant NL contributions, dominated by third-order nonlinearity. For the cubic self-focusing samples (S-B1 and S-B2), the transmittance response displays a more slowly variation, which increases with $\chi^{(3)}$, compared to the linear response shown in the first row of Fig. 8.4. The quintic self-focusing medium (S-B3 with $Re\left[\chi^{(3)}\right] = 0$) shows small response variation at 24 MW/cm^2 because the contribution of $\chi^{(5)}$ is negligible. In contrast, the cubic self-defocusing samples (S-B4 and S-B5) show a larger response as a function of the incident polarization azimuth angle. With the increase of the incident intensity, the refractive index variation between the slow and fast axis of the capillary increases or decreases depending of the sign of total NL susceptibilities (sum of the third- and fifth-order NL contributions) and the direction of the incident field polarization in the transverse plane. In this way, rotation of the incident polarization direction, in high intensities, generate multiple regions where the variation of the NL birefringence increases or decreases the polarization instability effects. As a consequence, regions of small and larger response are simultaneously observed for high intensities by varying the incident polarization azimuth angle, as shown in the third and fourth row of Fig. 8.1 that corresponds to intensities of 42 MW/cm^2 and 60 MW/cm^2, respectively. Note that in the last two rows of Fig. 8.1, the fifth-order contribution is very important to increase the modulation instability effect, in agreement with Fig. 8.3. Numerical simulations of Eq. 8.1, represented by the solid lines, were made using as initial condition a 80 ps Gaussian pulse. However, the relative orientation of the capillary fast- and slow-axis in relation to the laboratory frame (x, y) was treated as a free parameter. Values of $\triangle\beta_0$ between 0.07 and 0.12, which correspond to $\left|n_x - n_y\right| \approx 10^{-6}$, were used. These values are reasonable since the refractive index variation produced by the nonlinearities, $\triangle n = n_{2,eff} I + n_{4,eff} I^2$, are of the same order of magnitude.

Figure 8.5 shows the transmittance behavior, in the V-polarization (black circles) and H-

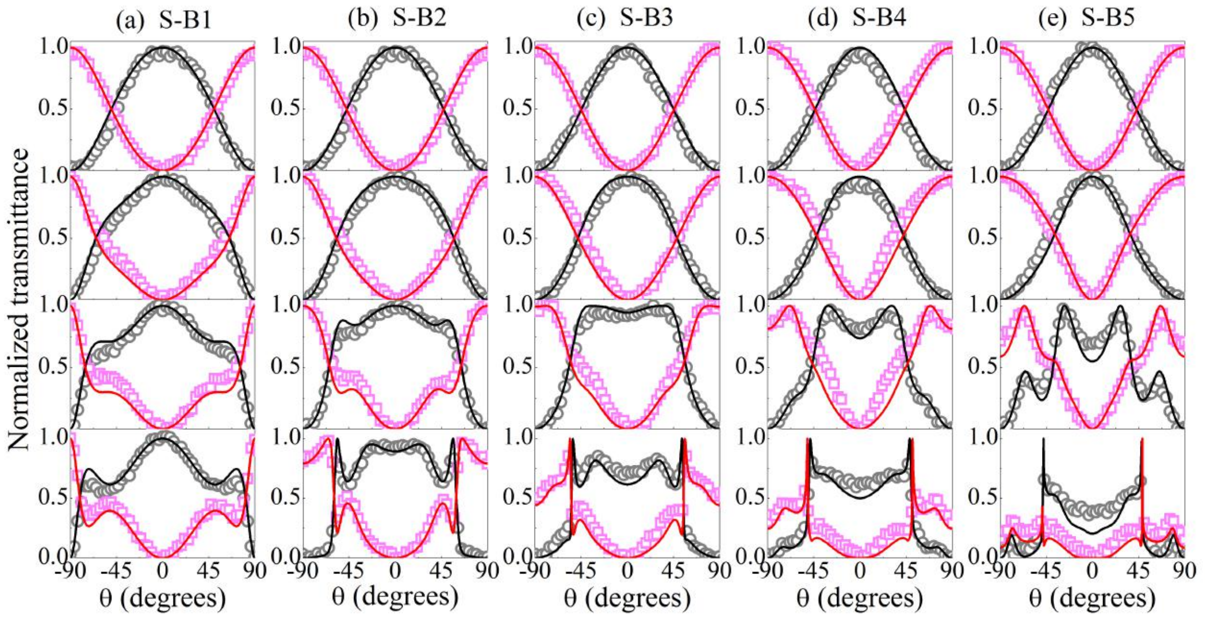

Figure 8.4 Normalized transmittance as a function of the incident polarization azimuth angle for (a) sample B1, (b) sample B2, (c) sample B3, (d) sample B4 and (e) sample B5. From top to bottom, the incident peak intensities are 6, 24, 42 and 60 MW/cm^2, in each column. Black circles and red squares correspond to vertical and horizontal polarization transmittance, respectively. Solid lines were obtained from numerical solutions of Eq. 8.1 and the parameters of Table 8.1.

polarization (red squares), for incident peak intensities between 0.1 MW/cm^2 and 70 MW/cm^2. An incident azimuth angle of 43° in relation to V-polarization was used for all samples. For non-birefringent materials or materials exhibiting only linear birefringence, the transmittance remains constant for different intensities. However, Fig. 8.5(a), corresponding to S-B1 (pure CS_2), shows modulation of the transmittance response with increasing intensity, induced by cubic nonlinearity. Each oscillation observed in the transmittance response corresponds to 2π phase-shift. It is possible to observe that with the addition of silver NPs [Fig. 8.5(b)-(e)], the modulation increases due to their large effective NL susceptibility. It is worth noting that the fifth-order nonlinearities are essential for the modulation growth, as shown in Fig. 8.5(c), which corresponds to a refractive quintic medium with $Re\left[\chi^{(3)}\right] = 0$. A maximum NL phase shift of $\sim 20\pi$ was observed for intensities up to 70 MW/cm^2, using S-B5 sample, as shown in Fig. 8.5(e). Black and red solid lines represent the numerical simulations of Eq. 8.1, showing a good agreement with the experimental results. The blue dashed lines in Figs. 8.5(b)-(e) display the transmittance behavior neglecting the $Re\left[\chi^{(5)}\right]$ contribution, showing that the modulation is highly modified due to the fifth-order contribution.

Small discrepancies between the experimental and theoretical results are due to the capillary, used for all experiments, that supports few propagation modes (V-number is ~ 9), while in the theory it was assumed, for simplicity, that the propagation occurs in a single-mode capillary. Therefore, coupling effects between the different modes were neglected in the numerical

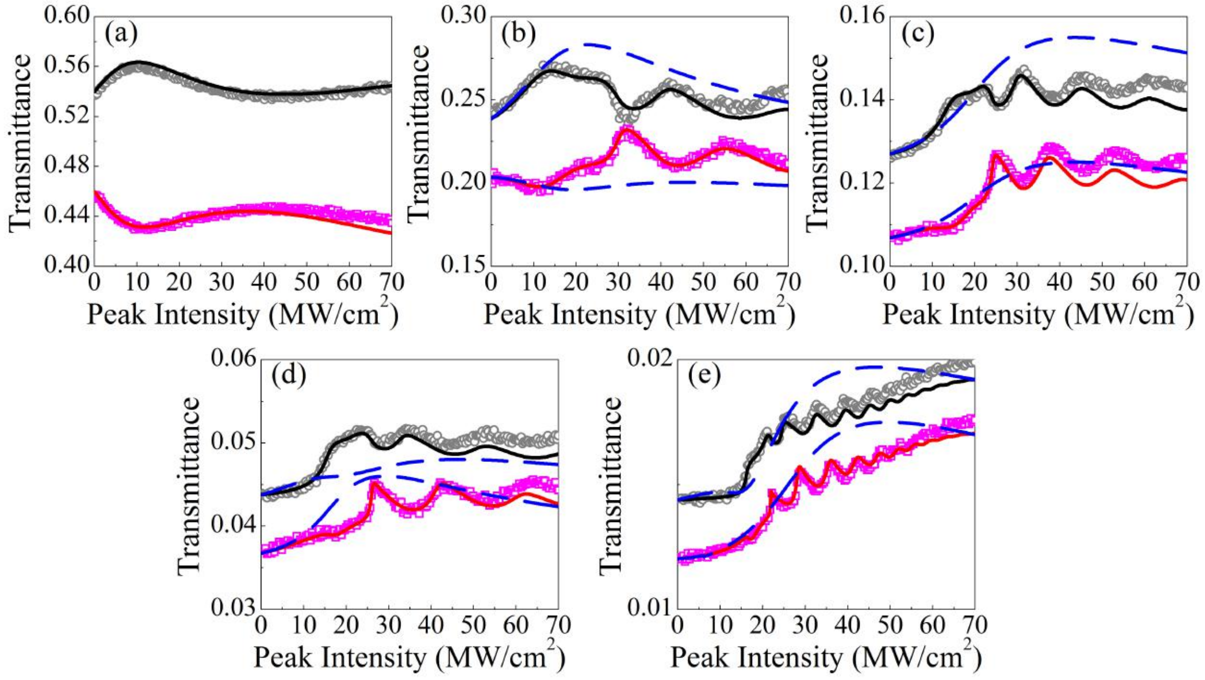

Figure 8.5 Vertical (black circles) and horizontal (red squares) polarization transmittance as a function of the incident peak intensities variation, for (a) sample B1, (b) sample B2, (c) sample B3, (d) sample B4 and (e) sample B5. Black and red solid lines were obtained from numerical solutions of Eq. 8.1 and the parameters of Table 8.1. Blue dashed lines represent the numerical solutions of Eq. 8.1 neglecting the contribution of $Re\left[\chi^{(5)}\right]$.

simulations. Free parameters used in the simulation, such as the angle of incidence of the beam and the refractive index shift $(\triangle n)$, can also introduce discrepancies between the experimental and numerical results.

Nowadays, it is well known that the NL birefringence effect is very attractive for application in all-optical switches. For the samples used in this work, a large NL phase shift $(\sim 20\pi)$ was observed in moderately diluted silver-colloids $\left(f = 4.5 \times 10^{-5}\right)$. However, more concentrated samples will present larger NL phase-shift due to the increased third- and fifth-order nonlinearities. In addition, we recall that using the NM procedure discussed in Chapter 4, it is possible to improve the figures-of-merit of all-optical switches based on MDNCs, as seen in Section 4.3.3. Therefore, once again we showed that the MDNCs are strong candidates for applications in the construction of high-speed optical devices due to its fast NL response, high NL susceptibility and the procedure for controlling its NL behavior by varying the volume fraction and incident intensity.

We cannot solve our problems with the same thinking we used when we created them.
- ALBERT EINSTEIN

9 CONCLUSIONS AND FUTURE WORKS

In this thesis was studied the NL response of metal-dielectric nanocomposites (MDNCs) and liquid carbon disulfide (CS_2), with the aim of analyzing the importance of their contributions in the generation of new NL optical phenomena induced by high-order nonlinearities (HON). In MDNCs, it was identified and characterized susceptibilities up to seventh-order, for intensities of tens of GW/cm^2. A nonlinearity management (NM) procedure, which enables to control the magnitude and phase of the different high-order susceptibilities, was developed to MDNCs by adjusting the light intensity and the volume fraction occupied by the metal nanoparticles (NPs). Thus, refractive quintic and septimal media, with suppressed cubic nonlinearity, were experimentally obtained for the first time. This control of the NL response was used to study optical phenomena commonly known for cubic nonlinearity such as spatial self- and cross-phase modulation (SSPM and SXPM), spatial modulation instability (SMI) and NL birefringence, but now being induced by HON. A generalization of the Maxwell-Garnet model, that includes the direct contributions of the NPs and the host medium as well as contributions due to lowest-order susceptibilities of the NPs, was developed to understand the behavior of the HON and corroborate the experimental results. In addition, the fast NL response of MDNCs allowed to develop potential applications of NM procedure for fabrication of all-optical devices based on NL birefringence. Further, figures-of-merit for all-optical switching were enhanced by about two orders of magnitude by using the NM procedure.

Special attention was devoted to the topic of two-dimensional (2+1)D spatial solitons, which are not stable in materials that exhibit only cubic nonlinearity. Here, the NM procedure was used to observe the stable propagation of (2+1)D bright solitons, for approximately 10 Rayleigh lengths, in a MDNC managed to present fifth-seventh (focusing-defocusing) susceptibilities with suppressed third-order refractive nonlinearity. In addition, a cubic-quintic medium, whose NL response is dominated by defocusing third-order susceptibility, was prepared to support the stable propagation of optical-vortex solitons (OVSs) with finite Gaussian background and topological charge $m = 1$. The OVS produced a NL change in the refractive index according to the vortex beam shape, allowing the formation of an optically induced waveguide capable of confine and guide a weak Gaussian beam by ~ 25 Rayleigh lengths. The behavior of the bright spatial solitons and OVS was corroborated by numerical solutions of the CQS-NLSE and CQ-NLSE, using the NL susceptibilities measured by the Z-scan technique, showing very good agreement.

In addition, it was demostrated for the first time the stable propagation of OVS in a saturable self-focusing medium with local nonlinearity. It was observed that the OVS with topological charge $m = 1$ are azimuthally stable at moderate values of the input intensity, due to the saturation of the refractive nonlinearity and the instability-suppressing effect of the 3PA (three-photon absorption), which characterizes the NL response of CS_2. However, it was also observed that at higher intensities, the vortex beams are unstable, spontaneously splitting into a pair of fragments. For the latter case, we developed a procedure to control the behavior of the emerging beams, due to the spontaneous splitting of the OVS, by adding a weak Gaussian beam propagating collinearly with the OVS. Rotation of the emerging beams and energy transfer between them were obtained using a control Gaussian beam with smaller intensity than the vortex beam, revealing a new approach for the design of all-optical modulators. Stability and instability regions of OVSs were accurately modeled by numerical simulations based on the modified NLSE, which consider the saturable NL refractive index and the 3PA coefficient, gathered from measures for the CS_2 in the picosecond regime.

As perspective of future works, we are planning to study new optical phenomena induced by HON, as well as study further properties of optical solitons in Kerr-like media (bright, dark and OVSs). In the first case, a recent work shows a new vision for NL optics, which expands their field of study beyond the limits of the perturbative regime [332]. Thus, the adaptation of our NM procedure to such experiments would allow us to work with NL metamaterials, whose NL behavior will be ideal for investigation of new NL optical phenomena. For the second proposal, there is currently a variety of theoretical models directed to the study of optical solitons from the point of view of fundamental and applied physics, many of them lacking of experimental demonstrations. Thus, experiments that allow the stable propagation of OVSs in self-focusing media over long distances, as well as the formation and propagation of cluster solitons are within of our plans. In addition, we intend to consider the temporal domain in our studies of optical solitons, which are of great interest for applications in telecommunications.

The most exciting phrase to hear in science, the one that heralds new
discoveries, is not "Eureka!" but "That's funny..."
- ISAAC ASIMOV

References

[1] O'BRIEN, J. L.; FURUSAWA, A.; VUCKOVIC, J. Photonic quantum technologies. *Nature Photon.*, v. 3, p. 687–695, 2009.

[2] MALHEIROS-SILVEIRA, G. N.; GABRIELLI, L. H.; CHANG-HASNAIN, C. J.; HERNANDEZ-FIGUEROA, H. E. Breakthroughs in photonics 2013: Advances in nanoantennas. *IEEE Photon J.*, v. 6, p. 0700706, 2014.

[3] BUTTER, M.; LEIS, M.; SANDTKE, M.; MCLEAN, M.; LINCOLN, J.; WILSON, A. The leverage effect of photonics technologies: the european perspective. Technical report, Study prepared for the European Commission, DG Information Society and Media under reference SMART 2009/0066, 2011.

[4] YAMADA, K.; TSUCHIZAWA, T.; NISHI, H.; KOU, R.; HIRAKI, T.; TAKEDA, K.; FUKUDA, H.; ISHIKAWA, Y.; WADA, K.; YAMAMOTO, T. High-performance silicon photonics technology for telecommunications applications. *Sci. Tech. Adv. Mater.*, v. 15, p. 024603, 2014.

[5] DOYLEND, J. K.; KNIGHTS, A. P. The evolution of silicon photonics as an enabling technology for optical interconnection. *Laser Photon. Rev.*, v. 6, p. 504–525, 2012.

[6] RUSSELL, P. Photonic crystal fibers. *Science*, Washington, v. 299, p. 358–362, 2003.

[7] KNIGHT, J. C. Photonic crystal fibres. *Nature*, London, v. 424, p. 847–851, 2003.

[8] FOSTER, M. A.; SALEM, R.; GERAGHTY, D. F.; TURNER-FOSTER, A. C.; LIPSON, M.; GAETA, A. L. Silicon-chip-based ultrafast optical oscilloscope. *Nature*, London, v. 456, p. 81–84, 2008.

[9] SUN, Z.; MARTINEZ, A.; WANG, F. Optical modulators with 2D layered materials. *Nature Photon.*, v. 10, p. 227–238, 2016.

[10] BRUCK, R.; VYNCK, K.; LALANNE, P.; MILLS, B.; THOMSON, D. J.; MASHANOVICH, G. Z.; REED, G. T.; MUSKENS, O. L. All-optical spatial light modulator for reconfigurable silicon photonic circuits. *Optica*, v. 3, p. 396–402, 2016.

[11] KOMLJENOVIC, T.; DAVENPORT, M.; HULME, J.; LIU, A. Y.; SANTIS, C. T.; SPOTT, A.; SRINIVASAN, S.; STANTON, E. J.; ZHANG, C.; BOWERS, J. E. Heterogeneous silicon photonic integrated circuits. *J. Lightwave Technol.*, v. 34, p. 20–35, 2016.

[12] DOERR, C. R. Integrated photonic platforms for telecommunications: InP and Si. *IEICE Trans. Electron.*, v. E96-C, p. 950–957, 2013.

[13] FRANKEN, P. A.; HILL, A. E.; PETERS, C. W.; WEINREICH, G. Generation of optical harmonics. *Phys. Rev. Lett.*, v. 7, p. 118, 1961.

[14] SONG, H.-J.; OH, K.-H.; SHIMIZU, N.; KUKUTSU, N.; KADO, Y. Generation of frequency-modulated sub-terahertz signal using microwave photonic technique. *Opt. Express*, v. 18, p. 15936, 2010.

[15] BESSONOV, A. D.; SEREBRYANNIKOV, E. E.; ZHELTIKOV, A. M. Temporal self-action and compression of intense ultrashort laser pulses in hollow photonic-crystal waveguides. *JETP*, v. 101, p. 1–10, 2005.

[16] GANZ, T.; TEISSET, C.; APOLONSKIY, A.; KOBELKE, J.; SCHUSTER, K.; BARTELT, H.; ZHELTIKOV, A. M.; KRAUSZ, F. Spatial self-action of light in a large-mode-area photonic-crystal fiber. *CLEO/Europe and EQEC 2009 Conference Digest*, Doi: 10.1109/CLEOE-EQEC.2009.5192797.

[17] RUBINO, E.; LOTTI, A.; BELGIORNO, F.; CACCIATORI, S. L.; COUAIRON, A.; LEONHARDT, U.; FACCIO, D. Soliton-induced relativistic-scattering and amplification. *Sci. Reports*, v. 2, p. 932, 2012.

[18] NEILSON, D. T. Photonics for switching and routing. *IEEE J. Sel. Top. Quantum Electron.*, v. 12, p. 669–678, 2006.

[19] RAFFAELLIA, C.; VLACHOSB, K.; ANDRIOLLIC, N.; APOSTOLOPOULOSM, D.; BUROND, J.; VAN CAENEGEMJ, R.; DANILEWICZE, G.; FINOCHIETTON, J. M.; GARCIA-HAROG, J.; KLONIDISH, D.; OMAHONYL, M.; MAIERI, G.; PATTAVINAI, A.; PAVON-MARINOG, P.; RUEPPD, S.; SAVIA, M.; SCAFFARDIC, M.; TOMKOSH, I.; TZANAKAKIH, A.; WOSINSKAK, L. Photonics in switching: Architectures, systems and enabling technologies. *Comput. Net.*, v. 52, p. 1873–1890, 2008.

[20] DONG, S.; YAO, X.; ZHANG, W.; CHEN, S.; ZHANG, W.; YOU, L.; WANG, Z.; HUANG, Y. Single-photon stimulated four wave mixing at telecom band. *arXiv:1607.04380*, 2016.

[21] BOYD, R. W. *Nonlinear optics*. Academic Press, 2008.

[22] GREENBERG, J. A.; GAUTHIER, D. J. High-order optical nonlinearity at low light levels. *Europhys. Lett.*, v. 98, p. 24001, 2012.

[23] FALCÃO-FILHO, E. L.; DE ARAÚJO, C. B.; RODRIGUES, J. J. High-order nonlinearities of aqueous colloids containing silver nanoparticles. *J. Opt. Soc. Am. B*, v. 24, p. 2948–2956, 2007.

[24] FALCÃO-FILHO, E. L.; BARBOSA-SILVA, R.; SOBRAL-FILHO, R. G.; BRITO-SILVA, A. M.; GALEMBECK, A.; DE ARAÚJO, C. B. High-order nonlinearity of silica-gold nanoshells in chloroform at 1560 nm. *Opt. Express*, v. 18, p. 21636–21644, 2010.

[25] KONG, D. G.; CHANG, Q.; YE, H.; GAO, Y. C.; WANG, Y. X.; ZHANG, X. R.; YANG, K.; WU, W. Z.; SONG, Y. L. The fifth-order nonlinearity of CS_2. *J. Phys. B: At. Mol. Opt. Phys.*, v. 42, p. 065401, 2009.

[26] BESSE, V.; LEBLOND, H.; BOUDEBS, G. Filamentation of light in carbon disulfide. *Phys. Rev. A*, v. 89, p. 043840, 2014.

[27] SHEIK-BAHAE, M.; SAID, A. A.; WEI, T.-H.; HAGAN, D. J.; STRYLAND, E. W. V. Sensitive measurement of optical nonlinearities using a single beam. *IEEE J. Quantum Electron.*, v. 26, p. 760–769, 1990.

[28] MICHINEL, H.; PAZ-ALONSO, M. J.; PÉREZ-GARCÍA, V. M. Turning light into a liquid via atomic coherence. *Phys. Rev. Lett.*, v. 96, p. 023903, 2006.

[29] ESSAMA, B. G. O.; ATANGANA, J.; FREDERICK, B. M.; MOKHTARI, B.; EDDE-QAQI, N. C.; KOFANE, T. C. Rogue wave train generation in a metamaterial induced by cubic-quintic nonlinearities and second-order dispersion. *Phys. Rev. E*, v. 90, p. 032911, 2014.

[30] FALCÃO-FILHO, E. L.; DE ARAÚJO, C. B.; BOUDEBS, G.; LEBLOND, H.; SKARKA, V. Robust two-dimensional spatial solitons in liquid carbon disulfide. *Phys. Rev. Lett.*, v. 110, p. 013901, 2013.

[31] WEERAWARNE, D. L.; GAO, X.; GAETA, A. L.; SHIM, B. Higher-order nonlinearities revisited and their effect on harmonic generation. *Phys. Rev. Lett.*, v. 114, p. 093901, 2015.

[32] KOTHARI, N. C. Effective-medium theory of a nonlinear composite medium using the T-matrix approach: exact results for spherical grains. *Phys. Rev. A*, v. 41, p. 4486–4492, 1990.

[33] JAYABALAN, J. Origin and time dependence of higher-order nonlinearities in metal nanocomposites. *J. Opt. Soc. Am. B*, v. 28, p. 2448–2455, 2011.

[34] GANEEV, R. A.; RYASNYANSKYC, A. I.; ISHIZAWAD, N.; BABAA, M.; SUZUKIA, M.; TURUA, M.; SAKAKIBARAA, S.; KURODAA, H. Two- and three-photon absorption in CS_2. *Opt. Commun.*, v. 231, p. 431–436, 2004.

[35] COURIS, S.; RENARD, M.; FAUCHER, O.; LAVOREL, B.; CHAUX, R.; KOUDOUMAS, E.; MICHAUT, X. An experimental investigation of the nonlinear refractive index (n_2) of carbon disulfide and toluene by spectral shearing interferometry and z-scan techniques. *Chem. Phys. Lett.*, v. 369, p. 318–324, 2003.

[36] BARTHÉLÉMY, A.; MANEUF, S.; FROEHLY, C. Propagation soliton et auto-confinement de faisceaux laser par non linearité optique de kerr. *Opt. Commun.*, v. 55, p. 201–206, 1985.

[37] BERGÉ, L. Wave collapse in physics: principles and applications to light and plasma waves. *Phys. Rep.*, v. 303, p. 259–370, 1998.

[38] KRÓLIKOWSKI, W.; BANG, O.; NIKOLOV, N. I.; NESHEV, D.; WYLLER, J.; RASMUSSEN, J. J.; EDMUNDSON, D. Modulational instability, solitons and beam propagation in spatially nonlocal nonlinear media. *J. Opt. B: Quantum Semiclass. Opt.*, v. 6, p. S288–S294, 2004.

[39] AKHMEDIEV, N.; SOTO-CRESPO, J. M. Generation of a train of three-dimensional optical solitons in a self-focusing medium. *Phys. Rev. A*, v. 47, p. 1358, 1993.

[40] JR., G. C. D.; SHULTZ, J. L.; SALAMO, G. J.; SEGEV, M.; YARIV, A.; CROSIGNANI, B.; PORTO, P. D.; SHARP, E. J.; NEURGAONKAR, R. R. Observation of self-trapping of an optical beam due to the photorefractive effect. *Phys. Rev. Lett.*, v. 71, p. 533, 1993.

[41] LAMHOT, Y.; BARAK, A.; PELEG, O.; SEGEV, M. Self-trapping of optical beams through thermophoresis. *Phys. Rev. Lett.*, v. 105, p. 163906, 2010.

[42] EL-GANAINY, R.; CHRISTODOULIDES, D. N.; ROTSCHILD, C.; SEGEV, M. Soliton dynamics and self-induced transparency in nonlinear nanosuspensions. *Opt. Express*, v. 15, p. 10207–10218, 2007.

[43] PASSOT, T.; SULEM, C.; SULEM, P. L. Linear versus nonlinear dissipation for critical NLS equation. *Physica (Amsterdam)*, v. 203D, p. 167, 2005.

[44] SKARKA, V.; ALEKSIC, N. B. Stability criterion for dissipative soliton solutions of the one-, two-, and three-dimensional complex cubic-quintic Ginzburg-Landau equations. *Phys. Rev. Lett.*, v. 96, p. 013903, 2006.

[45] PASQUAZI, A.; STIVALA, S.; ASSANTO, G.; GONZALO, J.; SOLIS, J.; AFONSO, C. N. Near-infrared spatial solitons in heavy metal oxide glasses. *Opt. Lett.*, v. 32, p. 2103–2105, 2007.

[46] D'ASARO, E.; HEIDARI-BATENI, S.; PASQUAZI, A.; ASSANTO, G.; GONZALO, J.; SOLIS, J.; AFONSO, C. N. Interaction of self-trapped beams in high index glass. *Opt. Express*, v. 17, p. 17150–17155, 2009.

[47] FAN, H. H.; HE, Y. J.; DONG, J. W.; CHEN, B. C.; WANG, H. Z.; TIAN, Y. P.; REID, M. F. Mechanism of effective three-photon induced lasing. *Appl. Phys. Lett.*, v. 96, p. 021109, 2010.

[48] CHEN, Z.; SEGEV, M.; CHRISTODOULIDES, D. N. Optical spatial solitons: historical overview and recent advances. *Rep. Prog. Phys.*, v. 75, p. 086401, 2012.

[49] FIRTH, W. J.; SKRYABIN, D. V. Optical solitons carrying orbital angular momentum. *Phys. Rev. Lett.*, v. 79, p. 2450, 1997.

[50] QUIROGA-TEIXEIRO, M.; MICHINEL, H. Stable azimuthal stationary state in quintic nonlinear optical media. *J. Opt. Soc. Am. B*, v. 14, p. 2004–2009, 1997.

[51] BLOEMBERGEN, N. *Nonlinear optics*. 4th. ed. World Scientific Publishing Company, 1996.

[52] RAMAN, C. V.; KRISHNAN, K. S. A new type of secondary radiation. *Nature*, London, v. 121, p. 501–502, 1928.

[53] ARMSTRONG, J. A.; BLOEMBERGEN, N.; DUCUING, J.; PERSHAN, P. S. Interactions between light waves in a nonlinear dielectric. *Phys. Rev.*, v. 127, p. 1918, 1962.

[54] BLOEMBERGEN, N.; PERSHAN, P. S. Light waves at the boundary of nonlinear media. *Phys. Rev.*, v. 128, p. 606, 1962.

[55] BRABEC, T.; KRAUSZ, F. Intense few-cycle laser fields: Frontiers of nonlinear optics. *Rev. Mod. Phys.*, v. 72, p. 545, 2000.

[56] BALTUSKA, A.; UDEM, T.; UIBERACKER, M.; HENTSCHEL, M.; GOULIELMAKIS, E.; GOHLE, C.; HOLZWARTH, R.; YAKOVLEV, V. S.; SCRINZI, A.; HANSCH, T. W.; KRAUSZ, F. Attosecond control of electronic processes by intense light fields. *Nature*, London, v. 421, p. 611–615, 2003.

[57] JACKSON, J. D. *Classical electrodynamics*. 3rd. ed. Wiley, 1998.

[58] BUTCHER, P. N.; COTTER, D. *The elements of nonlinear optics*. Cambridge University Press, 1991, Chapter 2, p. 24-28.

[59] BOYD, R. W. Topical review: Order-of-magnitude estimates of the nonlinear optical susceptibility. *J. Mod. Phys.*, v. 46, p. 367–378, 1999.

[60] AGRAWAL, G. *Applications of nonlinear fiber optics*. Academic Press, 2008.

[61] HERCHER, M. An analysis of saturable absorbers. *Appl. Opt.*, v. 6, p. 947–954, 1967.

[62] DENG, L.; HE, K.; ZHOU, T.; LI, C. Formation and evolution of far-field diffraction patterns of divergent and convergent gaussian beams passing through self-focusing and self-defocusing media. *J. Opt. A, Pure Appl. Opt.*, v. 7, p. 409–415, 2005.

[63] BORN, M.; WOLF, E. *Principles of optics*. Cambridge University Press, 1999, Chapter 8.

[64] KOTHARI, N. C.; ABBI, S. C. Instability growth and filamentation of very intense laser beams in self-focusing media. *Prog. Theor. Phys.*, v. 83, p. 414–442, 1990.

[65] TAI, K.; HASEGAWA, A.; TOMITA, A. Observation of modulational instability in optical fibers. *Phys. Rev. Lett.*, v. 56, p. 135, 1986.

[66] WEN, S.; FAN, D. Spatiotemporal instabilities in nonlinear kerr media in the presence of arbitrary higher-order dispersions. *J. Opt. Soc. Am. B*, v. 19, p. 1653–1659, 2002.

[67] HICKMANN, J. M.; GOMES, A. S. L.; DE ARAÚJO, C. B. Observation of spatial cross-phase modulation effects in a self-defocusing nonlinear medium. *Phys. Rev. Lett.*, v. 68, p. 3547–3550, 1992.

[68] JISHA, C. P.; KURIAKOSE, V. C.; PORSEZIAN, K.; KALITHASAN, B. Modulational instability of optical beams in photorefractive media due to two-wave or parametric four-wave mixing effects. *J. Opt. A, Pure Appl. Opt.*, v. 10, p. 115101, 2008.

[69] MAMAEV, A. V.; LODAHL, P.; SAFFMAN, M. Observation of spatial modulation instability in intracavity second-harmonic generation. *Opt. Lett.*, v. 28, p. 31–33, 2003.

[70] LI, J. H.; CHIANG, K. S.; CHOW, K. W. Modulation instabilities in two-core optical fibers. *J. Opt. Soc. Am. B*, v. 28, p. 1693–1701, 2011.

[71] MALENDEVICH, R.; JANKOVIC, L.; STEGEMAN, G.; AITCHISON, J. S. Spatial modulation instability in a Kerr slab waveguide. *Opt. Lett.*, v. 26, p. 1879–1881, 2001.

[72] AGRAWAL, G. P. Transverse modulation instability of copropagating optical beams in nonlinear Kerr media. *J. Opt. Soc. Am. B*, v. 7, p. 1072–1078, 1990.

[73] RUSSELL, J. S. 14th meeting of the british association reports. *York*, 1844.

[74] ASKARYAN, G. A. Effects of the gradient of a strong electromagnetic beam on electrons and atoms. *Sov. Phys. JETP*, v. 15, p. 1088, 1962.

[75] CHIAO, R. Y.; GARMIRE, E.; TOWNES, C. H. Self-trapping of optical beams. *Phys. Rev. Lett.*, v. 13, p. 479, 1964.

[76] KELLEY, P. L. Self-focusing of optical beams. *Phys. Rev. Lett.*, v. 15, p. 1005–1008, 1965.

[77] BJORKHOLM, J. E.; ASHKIN, A. CW self-focusing and self-trapping of light in sodium vapor. *Phys. Rev. Lett.*, v. 32, p. 129, 1974.

[78] AITCHISON, J. S.; WEINER, A. M.; SILBERBERG, Y.; OLIVER, M. K.; JACKEL, J. L.; LEAIRD, D. E.; VOGEL, E. M.; SMITH, P. W. E. Observation of spatial optical solitons in a nonlinear glass waveguide. *Opt. Lett.*, v. 15, p. 471–473, 1990.

[79] AITCHISON, J. S.; AL-HEMYARI, K.; IRONSIDE, C. N.; GRANT, R. S.; SIBBETT, W. Observation of spatial solitons in AlGaAs waveguides. *Electron. Lett.*, v. 28, p. 1879, 1992.

[80] KHITROVA, G.; GIBBS, H. M.; KAWAMURA, Y.; IWAMURA, H.; IKEGAMI, T.; SIPE, J. E.; MING, L. Spatial solitons in a self-focusing semiconductor gain medium. *Phys. Rev. Lett.*, v. 70, p. 920, 1993.

[81] BARTUCH, U.; PESCHEL, U.; GABLER, T.; WALDHAUS, R.; HORHOLD, H.-H. Experimental investigations and numerical simulations of spatial solitons in planar polymer waveguides. *Opt. Commun.*, v. 134, p. 49, 1997.

[82] AN B. LAWRENCE, W. E. T.; STEGEMAN, G. I. Self-focusing and 2D spatial solitons in PTS. *Electron. Lett.*, v. 32, p. 2092, 1996.

[83] STEGEMAN, G. I.; SEGEV, M. Optical spatial solitons and their interactions: universality and diversity. *Science*, Washington, v. 286, p. 1518, 1999.

[84] KARAMZIN, Y. N.; SUKHORUKOV, A. P. Mutual focusing of high-power light beams in media with quadratic nonlinearity. *Sov. Phys. JETP*, v. 41, p. 414, 1975.

[85] SALVO, R. D.; HAGAN, D. J.; SHEIK-BAHAE, M.; STEGEMAN, G. I.; STRYLAND, E. W. V.; VANHERZEELE, H. Self-focusing and self-defocusing by cascaded second-order effects in KTP. *Opt. Lett.*, v. 17, p. 28, 1992.

[86] TORRUELLAS, W. E.; STRYLAND, E. W. V.; WANG, Z.; HAGAN, D. J.; STEGEMAN, G. I.; TORNER, L.; MENYUK, C. R. Observation of two-dimensional spatial solitary waves in a quadratic medium. *Phys. Rev. Lett.*, v. 74, p. 5036, 1995.

[87] SCHIEK, R.; BAEK, Y.; STEGEMAN, G. I. One-dimensional spatial solitary waves due to cascaded second-order nonlinearities in planar waveguides. *Phys. Rev. E*, v. 53, p. 1138, 1996.

[88] SEGEV, M.; CROSIGNANI, B.; YARIV, A.; FISCHER, B. Spatial solitons in photorefractive media. *Phys. Rev. Lett.*, v. 68, p. 928, 1992.

[89] KRUGLOV, V. I.; LOGVIN, Y. A.; VOLKOV, V. M. The theory of spiral laser beams in nonlinear media. *J. Modern Opt.*, v. 39, p. 2277, 1992.

[90] DESYATNIKOV, A. S.; TORNER, L.; KIVSHAR, Y. S. Optical vortices and vortex solitons. *Prog. Opt.*, v. 47, p. 291, 2005.

[91] SWARTZLANDER, G. A.; LAW, C. T. Optical vortex solitons observed in Kerr nonlinear media. *Phys. Rev. Lett.*, v. 69, p. 2503, 1992.

[92] DUREE, G.; MORIN, M.; SALAMO, G.; SEGEV, M.; CROSIGNANI, B.; PORTO, P. D.; SHARP, E.; YARIV, A. Dark photorefractive spatial solitons and photorefractive vortex solitons. *Phys. Rev. Lett.*, v. 74, p. 1978, 1995.

[93] COUAIRON, A.; MYSYROWICZ, A. Femtosecond filamentation in transparent media. *Phys. Rep.*, v. 441, p. 47–189, 2007.

[94] FEIT, M. D.; J. A. FLECK, J. Beam nonparaxiality, filament formation, and beam breakup in the self-focusing of optical beams. *J. Opt. Soc. Am. B*, v. 5, p. 633–640, 1988.

[95] BESPALOV, V. I.; TALANOV, V. I. Filamentary structure of light beams in nonlinear liquids. *Sov. Phys. JETP*, v. 3, p. 307, 1966.

[96] BLISS, E. S.; SPECK, D. R.; HOLZRICHTER, J. F.; ERKKILA, J. H.; GLASS, A. J. Propagation of a high-intensity laser pulse with small-scale intensity modulation. *Appl. Phys. Lett.*, v. 25, p. 448, 1974.

[97] CHIN, S. L. *Femtosecond laser filamentation*. Springer-Verlag New York, 2010, Chapter 2: "Filamentation Physics".

[98] CHEN, Y.-F.; BECKWITT, K.; WISE, F. W.; AITKEN, B. G.; SANGHERA, J. S.; AGGARWAL, I. D. Measurement of fifth- and seventh-order nonlinearities of glasses. *J. Opt. Soc. Am. B*, v. 23, p. 347–352, 2006.

[99] ZHENG, H.; ZHANG, X.; ZHANG, Z.; TIAN, Y.; CHEN, H.; LI, C.; ZHANG, Y. Parametric amplification and cascaded-nonlinearity processes in common atomic system. *Sci. Rep.*, v. 3, p. 1885, 2013.

[100] SIPE, J. E.; BOYD, R. W. Nonlinear susceptibility of composite optical materials in the Maxwell Garnett model. *Phys. Rev. A*, v. 46, p. 1614–1629, 1992.

[101] SINHA, C.; BHATTACHARYYA, S. *Current topics in atomic, molecular and optical physics*. World Scientific Publishing Co., 2005, Chapter 18: "Third-order optical susceptibility of Metal Nanocluster-glass composites".

[102] ESTEBAN, R.; BORISOV, A. G.; NORDLANDER, P.; AIZPURUA, J. Bridging quantum and classical plasmonics with a quantum-corrected model. *Nature Commun.*, v. 3, p. 825, 2012.

[103] WANG, J.; BLAU, W. J. Inorganic and hybrid nanostructures for optical limiting. *J. Opt. A, Pure Appl. Opt.*, v. 11, p. 024001, 2009.

[104] RIGHINI, M.; GIRARD, C.; QUIDANT, R. Light-induced manipulation with surface plasmons. *J. Opt. A, Pure Appl. Opt.*, v. 10, p. 093001, 2008.

[105] ASADI, R.; MALEK-MOHAMMAD, M.; KHORASANI, S. All optical switch based on Fano resonance in metal nanocomposite photonic crystals. *Opt. Commun.*, v. 284, p. 2230–2235, 2011.

[106] PRABHU, S.; POULOSE, E. K. Silver nanoparticles: mechanism of antimicrobial action, synthesis, medical applications, and toxicity effects. *Int. Nano Lett.*, v. 2, p. 32, 2012.

[107] SAHA, K.; AGASTI, S. S.; KIM, C.; LI, X.; ROTELLO, V. M. Gold nanoparticles in chemical and biological sensing. *Chem. Rev.*, v. 112, p. 2739–2779, 2012.

[108] GUO, S.; WANG, E. Synthesis and electrochemical applications of gold nanoparticles. *Anal. Chem. Acta*, v. 598, p. 181–192, 2007.

[109] CATCHPOLE, K. R.; POLMAN, A. Plasmonic solar cells. *Opt. Express*, v. 16, p. 21793–21800, 2008.

[110] DOMÍNGUEZ-GONZÁLEZ, R.; VARELA, L. G.; BERMEJO-BARRERA, P. Functionalized gold nanoparticles for the detection of arsenic in water. *Talanta*, v. 118, p. 262, 2014.

[111] CHOI, M. J.; MCDONAGH, A. M.; MAYNARD, P.; ROUX, C. Metal-containing nanoparticles and nano-structured particles in fingermark detection. *Forensic Sci. Int.*, v. 179, p. 87–97, 2008.

[112] SCHASFOORT, R. B. M.; TUDOS, A. J. *Handbook of surface plasmon resonance*. Royal Society of Chemistry, 2008, Chapter 2: "Physics of Surface Plasmon Resonance".

[113] RU, E. L.; ETCHEGOIN, P. *Principles of surface enhanced raman spectroscopy and related plasmonic effect*. Elsevier Science Ltd, 2008, Chapter 3: "Introduction to plasmons and plasmonics", p. 124-127.

[114] JOHNSON, P. B.; CHRISTY, R. W. Optical constants of the noble metals. *Phys. Rev. B*, v. 6, p. 4370–4379, 1972.

[115] CHOY, T. C. *Effective medium theory: Principles and applications*. Oxford University Press, 1999, Chapter 1, p.7-10.

[116] XU, Y.; CHEN, X.; ZHU, Y. Modeling of micro-diameter-scale liquid core optical fiber filled with various liquids. *Opt. Express*, v. 16, p. 9205–9212, 2008.

[117] KITTEL, C. *Introduction to solid state physics*. Wiley, 2004, Chapter 14, p. 273.

[118] LI, M.; CUSHING, S. K.; WU, N. Plasmon-enhanced optical sensors: a review. *Analyst*, v. 140, p. 386–406, 2015.

[119] LAKOWICZ, J. R. Plasmonics in biology and plasmon-controlled fluorescence. *Plasmonics*, v. 1, p. 5–33, 2006.

[120] KREIBIG, U.; VOLLMER, M. *Optical properties of metal clusters*. Springer Series in Materials Science, 1995, Chapter 2, p. 23-60.

[121] MAIER, S. A.; ATWATER, H. A. Plasmonics: Localization and guiding of electromagnetic energy in metal/dielectric structures. *J. Appl. Phys.*, v. 98, p. 011101, 2005.

[122] GUO, J.; COOPER, J.; GALLAGHER, A. Selective reflection from a dense atomic vapor. *Phys. Rev. A*, v. 53, p. 1130–1138, 1996.

[123] ONSAGER, L. Electric moments of molecules in liquids. *J. Am. Chem. Soc.*, v. 58, p. 1486–1493, 1936.

[124] GLAUBER, R. J.; LEWENSTEIN, M. Quantum optics of dielectric media. *Phys. Rev. A*, v. 43, p. 467–491, 1991.

[125] DE VRIES, P.; LAGENDIJK, A. Resonant scattering and spontaneous emission in dielectrics: microscopic derivation of local-field effects. *Phys. Rev. Lett.*, v. 81, p. 1381–1384, 1998.

[126] RICARD, D.; ROUSSIGNOL, P.; FLYTZANI, C. Surface-mediated enhancement of optical phase conjugation in metal colloids. *Opt. Lett.*, v. 10, p. 511–513, 1985.

[127] EHRENREICH, H.; PHILIPP, H. R. Optical properties of Ag and Cu. *Phys. Rev.*, v. 128, p. 1622–1629, 1962.

[128] ASPNES, D. E.; KINSBRON, E.; BACON, D. D. Optical properties of Au: Sample effects. *Phys. Rev. B*, v. 21, p. 3290–3299, 1980.

[129] BOHREN, C. F.; HUFFMANN, D. R. *Absorption and scattering of light by small particles*. Wiley-Interscience, 1983, Chapter 3, p. 83-104, 111-114.

[130] MEIER, M.; WOKAUN, A. Enhanced fields on large metal particles: dynamic depolarization. *Opt. Lett.*, v. 8, p. 581–583, 1983.

[131] KELLY, K. L.; CORONADO, E.; ZHAO, L. L.; SCHATZ, G. C. The optical properties of metal nanoparticles: The influence of size, shape, and dielectric environment. *J. Phys. Chem. B*, v. 107, p. 668–677, 2003.

[132] AGNIHOTRI, S.; MUKHERJI, S.; MUKHERJI, S. Size-controlled silver nanoparticles synthesized over the range 5 - 100 nm using the same protocol and their antibacterial efficacy. *RSC Adv.*, v. 4, p. 3974, 2014.

[133] NOGUEZ, C. Surface plasmons on metal nanoparticles: The influence of shape and physical environment. *J. Phys. Chem. C*, v. 111, p. 3806–3819, 2007.

[134] UCHIDA, K.; KANEKO, S.; OMI, S.; HATA, C.; TANJI, H.; ASAHARA, Y.; IKUSHIMA, A. J. Optical nonlinearities of a high concentration of small metal particles dispersed in glass: copper and silver particles. *J. Opt. Soc. Am. B*, v. 11, p. 1236–1243, 1994.

[135] YANG, L.; BECKER, K.; SMITH, F. M.; MAGRUDER, R. H.; HAGLUND, R. F.; YANG, L.; DORSINVILLE, R.; ALFANO, R. R.; ZUHR, R. A. Size dependence of the third-order susceptibility of copper nanoclusters investigated by four-wave mixing. *J. Opt. Soc. Am. B*, v. 11, p. 457–461, 1994.

[136] MA, G.; HE, J.; TANG, S.-H.; SUN, W.; SHEN, Z. Size-dependence of nonlinearity in metal: Dielectric composite system induced by local field enhancement. *J. Nonlinear Optic. Phys. Mat.*, v. 12, p. 149, 2003.

[137] MA, G.; SUN, W.; TANG, S.-H.; ZHANG, H.; SHEN, Z.; QIAN, S. Size and dielectric dependence of the third-order nonlinear optical response of Au nanocrystals embedded in matrices. *Opt. Lett.*, v. 27, p. 1043–1045, 2002.

[138] WANG, K.; LONG, H.; FU, M.; YANG, G.; LU, P. Size-related third-order optical nonlinearities of Au nanoparticle arrays. *Opt. Express*, v. 18, p. 13874–13879, 2010.

[139] SÁNCHEZ-DENA, O.; MOTA-SANTIAGO, P.; TAMAYO-RIVERA, L.; GARCÍA-RAMÍREZ, E. V.; CRESPO-SOSA, A.; OLIVER, A.; REYES-ESQUEDA, J.-A. Size- and shape-dependent nonlinear optical response of Au nanoparticles embedded in sapphire. *Opt. Express*, v. 4, p. 92–100, 2014.

[140] KIM, K.-H.; HUSAKOU, A.; HERRMANN, J. Linear and nonlinear optical characteristics of composites containing metal nanoparticles with different sizes and shapes. *Opt. Express*, v. 18, p. 7488–7496, 2010.

[141] GOVYADINOV, A. A.; PANASYUK, G. Y.; SCHOTLAND, J. C.; MARKEL, V. A. Theoretical and numerical investigation of the size-dependent optical effects in metal nanoparticles. *Phys. Rev. B*, v. 84, p. 155461, 2011.

[142] SATO, R.; OHNUMA, M.; OYOSHI, K.; TAKEDA, Y. Experimental investigation of nonlinear optical properties of Ag nanoparticles: Effects of size quantization. *Phys. Rev. B*, v. 90, p. 125417, 2014.

[143] LEE, Y. H.; YAN, Y.; POLAVARAPU, L.; XU, Q.-H. Nonlinear optical switching behavior of au nanocubes and nano-octahedra investigated by femtosecond Z-scan measurements. *Appl. Phys. Lett.*, v. 95, p. 023105, 2009.

[144] CAN-UC, B.; RANGEL-ROJO, R.; RODRIGUEZ-FERNANDEZ, L.; OLIVER, A. Polarization selectable nonlinearities in elongated silver nanoparticles embedded in silica. *Opt. Mat. Express*, v. 3, p. 2012–2021, 2013.

[145] MOHAN, S.; LANGE, J.; GRAENER, H.; SEIFERT, G. Surface plasmon assisted optical nonlinearities of uniformly oriented metal nano-ellipsoids in glass. *Opt. Express*, v. 20, p. 28655–28663, 2012.

[146] HUA, Y.; CHANDRA, K.; DAM, D. H. M.; WIEDERRECHT, G. P.; ODOM, T. W. Shape-dependent nonlinear optical properties of anisotropic gold nanoparticles. *J. Phys. Chem. Lett.*, v. 6, p. 4904–4908, 2015.

[147] GÓMEZ, L. A.; DE ARAÚJO, C. B.; SILVA, A. M. B.; GALEMBECK, A. Influence of stabilizing agents on the nonlinear susceptibility of silver nanoparticles. *J. Opt. Soc. Am. B*, v. 24, p. 2136–2140, 2007.

[148] GÓMEZ, L. A.; DE ARAÚJO, C. B.; SILVA, A. M. B.; GALEMBECK, A. Solvent effects on the linear and nonlinear optical response of silver nanoparticles. *Appl. Phys. B*, v. 92, p. 61–66, 2008.

[149] LAMPRECHT, B.; LEITNER, A.; AUSSENEGG, F. R. SHG studies of plasmon dephasing in nanoparticles. *Appl. Phys. B*, v. 68, p. 419–423, 1999.

[150] ALMEIDA, E.; MOREIRA, A. C. L.; BRITO-SILVA, A. M.; GALEMBECK, A.; DE MELO, C. P.; DE S. MENEZES, L.; DE ARAÚJO, C. B. Ultrafast dephasing of localized surface plasmons in colloidal silver nanoparticles: the influence of stabilizing agents. *Appl. Phys. B*, v. 108, p. 9–16, 2012.

[151] LINK, S.; EL-SAYED, M. A. Size and temperature dependence of the plasmon absorption of colloidal gold nanoparticles. *J. Phys. Chem. B*, v. 103, p. 4212–4217, 1999.

[152] SÖNNICHSEN, C.; FRANZL, T.; WILK, T.; VON PLESSEN, G.; FELDMANN, J.; WILSON, O.; MULVANEY, P. Drastic reduction of plasmon damping in gold nanorods. *Phys. Rev. Lett.*, v. 88, p. 077402, 2002.

[153] AGARWAL, G. S.; GUPTA, S. D. T-matrix approach to the nonlinear susceptibilities of heterogeneous media. *Phys. Rev. A*, v. 38, p. 5678–5687, 1988.

[154] RATIVA, D.; DE ARAUJO, R. E.; GOMES, A. S. L. One photon nonresonant high-order nonlinear optical properties of silver nanoparticles in aqueous solution. *Opt. Express*, v. 16, p. 19244–19252, 2008.

[155] DOLGALEVA, K.; BOYD, R. W. Local-field effects in nanostructured photonic materials. *Adv. Opt. Photon.*, v. 4, p. 1–77, 2012.

[156] DOLGALEVA, K.; BOYD, R. W.; SIPE, J. E. Cascaded nonlinearity caused by local-field effects in the two-level atom. *Phys. Rev. A*, v. 76, p. 063806, 2007.

[157] BEDEAUX, D.; BLOEMBERGEN, N. On the relation between macroscopic and microscopic nonlinear susceptibilities. *Physica*, v. 69, p. 57–66, 1973.

[158] DOLGALEVA, K.; SHIN, H.; BOYD, R. W. Observation of a microscopic cascaded contribution to the fifth-order nonlinear susceptibility. *Phys. Rev. Lett.*, v. 103, p. 113902, 2009.

[159] STEGEMAN, G. I.; HAGAN, D. J.; TORNER, L. $\chi^{(2)}$ cascading phenomena and their applications to all-optical signal processing, mode-locking, pulse compression and solitons. *Opt. Quantum Electron.*, v. 28, p. 1691–1740, 1996.

[160] YABLONOVITCH, E.; FLYTZANIS, C.; BLOEMBERGEN, N. Anisotropic interference of three-wave and double two-wave frequency mixing in GaAs. *Phys. Rev. Lett.*, v. 29, p. 865–868, 1972.

[161] LU, L.; LUO, Z.; XU, T.; YU, L. Cooperative plasmonic effect of Ag and Au nanoparticles on enhancing performance of polymer solar cells. *Nano. Lett.*, v. 13, p. 59–64, 2013.

[162] GANEEV, R. A.; RYASNYANSKY, A. I. Nonlinear optical characteristics of nanoparticles in suspensions and solid matrices. *Appl. Phys. B*, v. 84, p. 295–302, 2006.

[163] KIM, K.-H.; HUSAKOU, A.; HERRMANN, J. Slow light in dielectric composite materials of metal nanoparticles. *Opt. Express*, v. 20, p. 25790–25797, 2012.

[164] KAURANEN, M.; ZAYATS, A. V. Nonlinear plasmonics. *Nature Photon.*, v. 6, p. 737–748, 2012.

[165] SCHOLL, J. A.; KOH, A. L.; DIONNE, J. A. Quantum plasmon resonances of individual metallic nanoparticles. *Nature*, London, v. 483, p. 421–427, 2012.

[166] GANEEV, R. A.; RYASNYANSKY, A. I.; STEPANOV, A. L.; USMANOV, T. Saturated absorption and nonlinear refraction of silicate glasses doped with silver nanoparticles at 532 nm. *Opt. Quantum Electron.*, v. 36, p. 949–960, 2004.

[167] KIM, K.-H.; HUSAKOU, A.; HERRMANN, J. Saturable absorption in composites doped with metal nanoparticles. *Opt. Express*, v. 18, p. 21918–21925, 2010.

[168] JAYABALAN, J.; SINGH, A.; KHAN, S.; CHARI, R. Third-order nonlinearity of metal nanoparticles: isolation of instantaneous and delayed contributions. *J. Appl. Phys.*, v. 112, p. 103524, 2012.

[169] BONI, L. D.; BARBANO, E. C.; DE ASSUMPÇÃO, T. A.; MISOGUTI, L.; KASSAB, L. R. P.; ZILIO, S. C. Femtosecond third-order nonlinear spectra of lead-germanium oxide glasses containing silver nanoparticles. *Opt. Express*, v. 20, p. 6844–6850, 2012.

[170] DE ARAÚJO, C. B.; OLIVEIRA, T. R.; FALCÃO-FILHO, E. L.; SILVA, D. M.; KASSAB, L. R. P. Nonlinear optical properties of PbO-GeO$_2$ films containing gold nanoparticles. *J. Lumin.*, v. 133, p. 180–183, 2013.

[171] FALCÃO-FILHO, E. L.; DE ARAÚJO, C. B.; GALEMBECK, A.; OLIVEIRA, M. M.; ZARBIN, A. J. G. Nonlinear susceptibility of colloids consisting of silver nanoparticles in carbon disulfide. *J. Opt. Soc. Am. B*, v. 22, p. 2444–2449, 2005.

[172] ZENG, J.; MALOMED, B. A. Stabilization of one-dimensional solitons against the critical collapse by quintic nonlinear lattices. *Phys. Rev. A*, v. 85, p. 023824, 2012.

[173] ZENG, J.; MALOMED, B. A. Bright solitons in defocusing media with spatial modulation of the quintic nonlinearity. *Phys. Rev. E*, v. 86, p. 036607, 2012.

[174] CAPLAN, R. M.; CARRETERO-GONZÁLEZ, R.; KEVREKIDIS, P. G.; A.MALOMED, B. Existence, stability, and scattering of bright vortices in the cubic-quintic nonlinear Schrödinger equation. *Math. Comput. Simul.*, v. 82, p. 1150, 2012.

[175] ROGERS, C.; B.MALOMED; LI, J. H.; CHOW, K. W. Propagating wave patterns in a derivative nonlinear Schrödinger system with quintic nonlinearity. *J. Phys. Soc. Jpn.*, v. 81, p. 094005, 2012.

[176] CROSTA, M.; FRATALOCCHI, A.; TRILLO, S. Bistability and instability of dark-antidark solitons in the cubic-quintic nonlinear Schrödinger equation. *Phys. Rev. A*, v. 84, p. 063809, 2011.

[177] BERGÉ, L.; MEZENTSEV, V. K.; RASMUSSEN, J. J.; CHRISTIANSEN, P. L.; GAIDIDEI, Y. B. Self-guiding light in layered nonlinear media. *Opt. Lett.*, v. 25, p. 1037–1039, 2000.

[178] TOWERS, I.; MALOMED, B. A. Stable (2+1)-dimensional solitons in a layered medium with sign-alternating kerr nonlinearity. *J. Opt. Soc. Am. B*, v. 19, p. 537–543, 2002.

[179] CENTURION, M.; PORTER, M. A.; KEVREKIDIS, P. G.; PSALTIS, D. Nonlinearity management in optics: Experiment, theory, and simulation. *Phys. Rev. Lett.*, v. 97, p. 033903, 2006.

[180] SAITO, H.; UEDA, M. Dynamically stabilized bright solitons in a two-dimensional Bose-Einstein condensate. *Phys. Rev. Lett.*, v. 90, p. 040403, 2003.

[181] MA, H.; GOMES, A. S. L.; DE ARAÚJO, C. B. Measurements of nondegenerate optical nonlinearity using a two color single beam method. *Appl. Phys. Lett.*, v. 59, p. 2666–2668, 1991.

[182] SUTHERLAND, R. L. *Handbook of nonlinear optics*. Dekker, 1996, Chapter 8, p. 512.

[183] LIU, X.; GUO, S.; WANG, H.; MING, N.; HOU, L. Investigation of the influence of finite aperture size on the Z-scan transmittance curve. *J. Nonlinear Opt. Phys. Mater.*, v. 10, p. 431–439, 2001.

[184] CALLEN, W. R.; HUTH, B. G.; PANTELL, R. H. Optical patterns of thermally self-defocused light. *Appl. Phys. Lett.*, v. 11, p. 103–105, 1967.

[185] PILLA, V.; MUNIN, E.; GESUALDI, M. R. R. Measurement of the thermo-optic coefficient in liquids by laser-induced conical diffraction and thermal lens techniques. *J. Opt. A: Pure Appl. Opt.*, v. 11, p. 105201, 2009.

[186] ANVARI, J. Z.; KARIMZADEH, R.; MANSOUR, N. Thermo-optic properties and nonlinear responses of copper nanoparticles in polysiloxane oil. *J. Opt.*, v. 12, p. 035212, 2010.

[187] MAO, Z.; QIAO, L.; HE, F.; LIAO, Y.; WANG, C.; CHENG, Y. Thermal-induced nonlinear optical characteristics of ethanol solution doped with silver nanoparticles. *Chin. Opt. Lett.*, v. 7, p. 949–952, 2009.

[188] NASCIMENTO, C. M.; ALENCAR, M. A. R. C.; CHÁVEZ-CERDA, S.; DA SILVA, M. G. A.; MENEGHETTI, M. R.; HICKMANN, J. M. Experimental demonstration of novel effects on the far-field diffraction patterns of a gaussian beam in a Kerr medium. *J. Opt. A: Pure Appl. Opt.*, v. 8, p. 947–951, 2006.

[189] ARA, M. H. M.; DEHGHANI, Z.; SAHRAEI, R.; DANESHFAR, A.; JAVADI, Z.; DIVSAR, F. Diffraction patterns and nonlinear optical properties of gold nanoparticles. *J. Quant. Spectrosc. Radiat. Transf.*, v. 113, p. 366–372, 2012.

[190] ZAMIRI, R.; ZAKARIA, A.; AHMAD, M. B.; SADROLHOSSEINI, A. R.; SHAMELI, K.; DARROUDI, M.; MAHDI, M. A. Investigation of spatial self-phase modulation of silver nanoparticles in clay suspension. *Optik (Stuttg.)*, v. 122, p. 836–838, 2011.

[191] WAN, W.; JIA, S.; FLEISCHER, J. W. Dispersive superfluid-like shock waves in nonlinear optics. *Nature Phys.*, v. 3, p. 46–51, 2007.

[192] DURBIN, S. D.; ARAKELIAN, S. M.; SHEN, Y. R. Laser-induced diffraction rings from a nematic-liquid-crystal film. *Opt. Lett.*, v. 6, p. 411–413, 1981.

[193] GRISCHKOWSK, D. Self-focusing of light by potassium vapor. *Phys. Rev. Lett.*, v. 24, p. 866, 1970.

[194] MYINT, T.; ALFANO, R. R. Spatial phase modulation from permanent memory in doped glass. *Opt. Lett.*, v. 35, p. 1275–1277, 2010.

[195] WANG, G.; ZHANG, S.; UMRAN, F. A.; CHENG, X.; DONG, N.; COGHLAN, D.; CHENG, Y.; ZHANG, L.; BLAU, W. J.; WANG, J. Tunable effective nonlinear refractive index of graphene dispersions during the distortion of spatial self-phase modulation. *Appl. Phys. Lett.*, v. 104, p. 141909, 2014.

[196] KIVSHAR, Y. S.; ANDERSON, D.; LISAK, M. Modulation instabilities and dark solitons in a generalized nonlinear Schrödinger equation. *Phys. Scr.*, v. 47, p. 679–681, 1993.

[197] ROZANOV, N. N. Modulation instability in a medium with a nonlocal nonlinearity. *Opt. Spectrosc.*, v. 100, p. 609–612, 2006.

[198] ESBENSEN, B. K.; WLOTZKA, A.; BACHE, M.; BANG, O.; KROLIKOWSKI, W. Modulational instability and solitons in nonlocal media with competing nonlinearities. *Phys. Rev. A*, v. 84, p. 053854, 2011.

[199] D. KIP, M.; SOLJACIC; SEGEV, M.; SEARS, S. M.; CHRISTODOULIDES, D. N. (1+1)-dimensional modulation instability of spatially incoherent light. *J. Opt. Soc. Am. B*, v. 19, p. 502–512, 2002.

[200] LIU, Z.; LIU, S.; GUO, R.; GAO, Y.; QI, X.; ZHOU, L.; LI, Y. Modulation instability with incoherent white light in self-defocusing photorefractive crystal. *Opt. Commun.*, v. 281, p. 3171–3176, 2008.

[201] HONG, W.-P. Modulational instability of optical waves in the high dispersive cubic-quintic nonlinear Schrödinger equation. *Opt. Commun.*, v. 213, p. 173–182, 2002.

[202] GUPTA, R.; RAJU, T. S.; KUMAR, C. N.; PANIGRAHI, P. K. Modulational instability of copropagating light beams induced by cubic-quintic nonlinearity in nonlinear negative-index material. *J. Opt. Soc. Am. B*, v. 29, p. 3360–3366, 2012.

[203] SAHA, M.; SARMA, A. K. Modulation instability in nonlinear metamaterials induced by cubic-quintic nonlinearities and higher order dispersive effects. *Opt. Commun.*, v. 291, p. 321–325, 2013.

[204] TAGWO, H.; TIOFACK, C. G. L.; DAFOUNANSOU, O.; MOHAMADOU, A.; KOFANE, T. C. Effect of competing cubic-quintic nonlinearities on the modulational instability in nonlocal Kerr-type media. *J. Modern Opt.*, v. 63, p. 558–565, 2016.

[205] WADA, O. Femtosecond all-optical devices for ultrafast communication and signal processing. *New. J. Phys.*, v. 6, p. 183, 2004.

[206] MIZRAHI, V.; DELONG, K. W.; STEGEMAN, G. I.; SAIFI, M. A.; ANDREJCO, M. J. Two-photon absorption as a limitation to all-optical switching. *Opt. Lett.*, v. 14, p. 1140–1142, 1989.

[207] FRIBERG, S. R.; SMITH, P. W. Nonlinear optical glasses for ultrafast optical switches. *IEEE J. Quantum Electron.*, v. 23, p. 2089–2094, 1987.

[208] STEGEMAN, G. I.; WRIGHT, E. M.; FINLAYSON, N.; ZANONI, R. Third order nonlinear integrated optics. *J. Mater. Sci.*, v. 33, p. 2235–2249, 1998.

[209] REICHERT, M.; HU, H.; FERDINANDUS, M. R.; SEIDEL, M.; ZHAO, P.; ENSLEY, T. R.; PECELI, D.; REED, J. M.; FISHMAN, D. A.; WEBSTER, S.; HAGAN, D. J.; STRYLAND, E. W. V. Temporal, spectral, and polarization dependence of the nonlinear optical response of carbon disulfide. *Optica*, v. 1, p. 436–445, 2014.

[210] ANDERSON, D. Variational approach to nonlinear pulse propagation in optical fibers. *Phys. Rev. A*, v. 27, p. 3135, 1983.

[211] VAKHITOV, N. G.; KOLOKOLOV, A. A. Stationary solutions of the wave equation in a medium with nonlinearity saturation. *Radiophys. Quantum Electron.*, v. 16, p. 783, 1973.

[212] AGRAWAL, G. P. *Nonlinear fiber optics*. Academic Press, 2013, Chapter 6, p. 193-198.

[213] KIVSHAR, Y. Spatial solitons: Bending light at will. *Nature Phys.*, v. 2, p. 729, 2006.

[214] KARTASHOV, Y. V.; MALOMED, B. A.; TORNER, L. Solitons in nonlinear lattices. *Rev. Mod. Phys.*, v. 83, p. 247, 2011.

[215] BANG, O.; RASMUSSEN, J. J.; CHRISTIANSEN, P. L. Subcritical localization in the discrete nonlinear Schrodinger equation with arbitrary power nonlinearity. *Nonlinearity*, v. 7, p. 205, 1994.

[216] CHUNG, Y.; LUSHNIKOV, P. M. Strong collapse turbulence in a quintic nonlinear Schrödinger equation. *Phys. Rev. E*, v. 84, p. 036602, 2011.

[217] RASMUSSEN, J. J.; RYPDAL, K. Blow-up in nonlinear Schroedinger equations-I a general review. *Phys. Scr.*, v. 33, p. 481, 1986.

[218] DAWES, E. L.; MARBURGER, J. H. Computer studies in self-focusing. *Phys. Rev.*, v. 179, p. 862, 1969.

[219] LORIOT, V.; HERTZ, E.; FAUCHER, O.; LAVOREL, B. Measurement of high order Kerr refractive index of major air components. *Opt. Express*, v. 17, p. 13429–13434, 2009.

[220] SCHNEBELIN, C.; CASSAGNE, C.; DE ARAÚJO, C. B.; BOUDEBS, G. Measurements of the third- and fifth-order optical nonlinearities of water at 532 and 1064 nm using the D4σ method. *Opt. Lett.*, v. 39, p. 5046–5049, 2014.

[221] ZUBAIRY, M. S.; MATSKO, A. B.; SCULLY, M. O. Resonant enhancement of high-order optical nonlinearities based on atomic coherence. *Phys. Rev. A*, v. 65, p. 043804, 2002.

[222] SMEKTALA, F.; QUÉMARD, C.; COUDERC, V.; BARTHÉLÉMY, A. Non-linear optical properties of chalcogenide glasses measured by Z-scan. *J. Non-Cryst. Solids*, v. 274, p. 232–237, 2000.

[223] BRÉE, C.; DEMIRCAN, A.; STEINMEYER, G. Saturation of the all-optical Kerr effect. *Phys. Rev. Lett.*, v. 106, p. 183902, 2011.

[224] POINT, G.; BRELET, Y.; HOUARD, A.; JUKNA, V.; MILIÁN, C.; CARBONNEL, J.; LIU, Y.; COUAIRON, A.; MYSYROWICZ, A. Superfilamentation in air. *Phys. Rev. Lett.*, v. 112, p. 223902, 2014.

[225] MOLL, K. D.; HOMOELLE, D.; GAETA, A. L.; BOYD, R. W. Conical harmonic generation in isotropic materials. *Phys. Rev. Lett.*, v. 88, p. 153901, 2002.

[226] PUSHKAROV, K. I.; PUSHKAROV, D. I.; TOMOV, I. V. Self-action of light beams in nonlinear media: soliton solutions. *Opt. Quantum Electron.*, v. 11, p. 471, 1979.

[227] ABDULLAEV, F. K.; GARNIER, J. Dynamical stabilization of solitons in cubic-quintic nonlinear Schrödinger model. *Phys. Rev. E*, v. 72, p. 035603, 2005.

[228] SKARKA, V.; BEREZHIANI, V. I.; MIKLASZEWSKI, R. Spatiotemporal soliton propagation in saturating nonlinear optical media. *Phys. Rev. E*, v. 56, p. 1080, 1997.

[229] VIETHUNG, N.; TRIPPENBACH, M.; INFELD, E.; MALOMED, B. A. Spatial control of the competition between self-focusing and self-defocusing nonlinearities in one- and two-dimensional systems. *Phys. Rev. A*, v. 90, p. 023841, 2014.

[230] CHONG, C.; CARRETERO-GONZÁLEZ, R.; MALOMED, B. A.; KEVREKIDIS, P. G. Multistable solitons in higher-dimensional cubic-quintic nonlinear Schrödinger lattices. *Physica D*, Amsterdam, v. 238, p. 126–136, 2009.

[231] GAIDIDEI, Y. B.; SCHJODT-ERIKSEN, J.; CHRISTIANSEN, P. L. Collapse arresting in an inhomogeneous quintic nonlinear Schrödinger model. *Phys. Rev. E*, v. 60, p. 4877, 1999.

[232] ALFIMOV, G. L.; KONOTOP, V. V.; PACCIANI, P. Stationary localized modes of the quintic nonlinear Schrödinger equation with a periodic potential. *Phys. Rev. A*, v. 75, p. 023624, 2007.

[233] BAIZAKOVA, B. B.; MALOMED, B. A.; SALERNO, M. Multidimensional solitons in periodic potentials. *Europhys. Lett.*, v. 63, p. 642, 2003.

[234] PELINOVSKY, D. E.; KIVSHAR, Y. S.; AFANASJEV, V. V. Internal modes of envelope solitons. *Physica D*, Amsterdam, v. 116, p. 121–142, 1998.

[235] WANG, S.; ZHANG, L. An efficient split-step compact finite difference method for cubic-quintic complex Ginzburg-Landau equations. *Comput. Phys. Commun.*, v. 184, p. 1511–1521, 2013.

[236] LIU, Y.; DURAND, M.; CHEN, S.; HOUARD, A.; PRADE, B.; FORESTIER, B.; MYSYROWICZ, A. Energy exchange between femtosecond laser filaments in air. *Phys. Rev. Lett.*, v. 105, p. 055003, 2010.

[237] KIVSHAR, Y. S.; AGRAWAL, G. P. *Optical solitons: From fibers to photonic crystals*. Academic Press, 2003.

[238] BÉJOT, P.; KASPARIAN, J.; HENIN, S.; LORIOT, V.; VIEILLARD, T.; HERTZ, E.; FAUCHER, O.; LAVOREL, B.; WOLF, J.-P. Higher-order kerr terms allow ionization-free filamentation in gases. *Phys. Rev. Lett.*, v. 104, p. 103903, 2010.

[239] HANG, C.; LI, Y.; MA, L.; HUANG, G. Three-way entanglement and three-qubit phase gate based on a coherent six-level atomic system. *Phys. Rev. A*, v. 74, p. 012319, 2006.

[240] KANG, H.; HERNANDEZ, G.; ZHU, Y. Slow-light six-wave mixing at low light intensities. *Phys. Rev. Lett.*, v. 93, p. 073601, 2004.

[241] ZHANG, Y.; KHADKA, U.; ANDERSON, B.; XIAO, M. Temporal and spatial interference between four-wave mixing and six-wave mixing channels. *Phys. Rev. Lett.*, v. 102, p. 013601, 2009.

[242] DAS, P.; VYAS, M.; PANIGRAHI, P. K. Loss of superfluidity in the bose-einstein condensate in an optical lattice with cubic and quintic nonlinearity. *J. Phys. B: At. Mol. Opt. Phys.*, v. 42, p. 245304, 2009.

[243] HUANG, T.; ZHOU, C. T.; ZHANG, H.; HE, X. T. Effects of higher-order Kerr nonlinearity and plasma diffraction on multiple filamentation of ultrashort laser pulses in air. *Phys. Plasmas*, v. 20, p. 072111, 2013.

[244] KÖHLER, T. Three-body problem in a dilute Bose-Einstein condensate. *Phys. Rev. Lett.*, v. 89, p. 210404, 2002.

[245] BEHESHTI, S.; LAW, K. J. H.; KEVREKIDIS, P. G.; PORTER, M. A. Averaging of nonlinearity management with dissipation. *Phys. Rev. A*, v. 78, p. 025805, 2008.

[246] KEVREKIDIS, P. G.; THEOCHARIS, G.; FRANTZESKAKIS, D. J.; MALOMED, B. A. Feshbach resonance management for Bose-Einstein condensates. *Phys. Rev. Lett.*, v. 90, p. 230401, 2003.

[247] PECCIANTI, M.; CONTI, C.; ASSANTO, G.; DE LUCA, A.; UMETON, C. Routing of anisotropic spatial solitons and modulational instability in liquid crystals. *Nature*, London, v. 432, p. 733–737, 2004.

[248] YANG, J.; ZHANG, P.; YOSHIHARA, M.; HU, Y.; CHEN, Z. Image transmission using stable solitons of arbitrary shapes in photonic lattices. *Opt. Lett.*, v. 36, p. 772–774, 2011.

[249] TIEMANN, M.; HALFMANN, T.; TSCHUDI, T. Photorefractive spatial solitons as waveguiding elements for optical telecommunication. *Opt. Commun.*, v. 282, p. 3612–3619, 2009.

[250] EISENBERG, H. S.; SILBERBERG, Y.; MORANDOTTI, R.; BOYD, A. R.; AITCHISON, J. S. Discrete spatial optical solitons in waveguide arrays. *Phys. Rev. Lett.*, v. 81, p. 3383, 1998.

[251] MARBURGER, J. H. Self-focusing: Theory. *Prog. Quantum Electron.*, v. 4, p. 35–110, 1975.

[252] FIBICH, G.; GAVISH, N.; WANG, X.-P. Singular ring solutions of critical and supercritical nonlinear Schrödinger equations. *PhysicaD*, v. 231, p. 55, 2007.

[253] MAN, W.; FARDAD, S.; ZHANG, Z.; PRAKASH, J.; LAU, M.; ZHANG, P.; HEINRICH, M.; CHRISTODOULIDES, D. N.; CHEN, Z. Optical nonlinearities and enhanced light transmission in soft-matter systems with tunable polarizabilities. *Phys. Rev. Lett.*, v. 111, p. 218302, 2013.

[254] JORGE, K. C.; RIVA, R.; RODRIGUES, N. A. S.; SAKAMOTO, J. M. S.; DESTRO, M. G. Scattered light imaging method (SLIM) for characterization of arbitrary laser beam intensity profiles. *Appl. Opt.*, v. 53, p. 4555–4564, 2014.

[255] JORGE, K. C.; GARCÍA, H. A.; AMARAL, A. M.; REYNA, A. S.; DE S. MENEZES, L.; DE ARAÚJO, C. B. Measurements of the nonlinear refractive index in scattering media using the scattered light imaging method - SLIM. *Opt. Express*, v. 23, p. 19512–19521, 2015.

[256] BERRY, M. V. Optical vortices evolving from helicoidal integer and fractional phase steps. *J. Opt. A: Pure Appl. Opt.*, v. 6, p. 259–268, 2004.

[257] DENNIS, M. R.; O'HOLLERAN, K.; PADGETT, M. J. Singular optics: Optical vortices and polarization singularities. *Prog. Opt.*, v. 53, p. 293–363, 2009.

[258] AMARAL, A. M.; FALCÃO-FILHO, E. L.; DE ARAÚJO, C. B. Characterization of topological charge and orbital angular momentum of shaped optical vortices. *Opt. Express*, v. 22, p. 30315–30324, 2014.

[259] AMARAL, A. M.; FALCÃO-FILHO, E. L.; DE ARAÚJO, C. B. Shaping optical beams with topological charge. *Opt. Lett.*, v. 38, p. 1579–1581, 2013.

[260] SOSKIN, M. S.; VASNETSOV, M. V. Singular optics. *Prog. Opt.*, v. 42, p. 219–276, 2001.

[261] XIN, J.; DAI, K.; ZHONG, L.; NA, Q.; GAO, C. Generation of optical vortices by using spiral phase plates made of polarization dependent devices. *Opt. Lett.*, v. 39, p. 1984–1987, 2014.

[262] ALLEN, L.; PADGETT, M. J.; BABIKER, M. The orbital angular momentum of light. *Prog. Opt.*, v. 39, p. 291–372, 1999.

[263] COURTIAL, J.; PADGETT, M. J. Performance of a cylindrical lens mode converter for producing laguerre-gaussian laser modes. *Opt. Commun.*, v. 159, p. 13–18, 1999.

[264] MASAJADA, J.; DUBIK, B. Optical vortex generation by three plane wave interference. *Opt. Commun.*, v. 198, p. 21–27, 2001.

[265] INDEBETOUW, G.; KORWAN, D. R. Model of vortices nucleation in a photorefractive phase-conjugate resonator. *J. Mod. Opt.*, v. 41, p. 941–950, 1994.

[266] ACKEMANN, T.; KRIEGE, E.; LANGE, W. Phase singularities via nonlinear beam propagation in sodium vapor. *Opt. Commun.*, v. 115, p. 339–346, 1995.

[267] *Angular momentum of light*. IN: Wikipedia, the free encyclopedia 2017. Available in: `http://pt.wikipedia.org/w/index.php?title=Teoria_dos_erros&oldid=1812415`.

[268] GAHAGAN, K. T.; SWARTZLANDER, G. A. Optical vortex trapping of particles. *Opt. Lett.*, v. 21, p. 827–829, 1996.

[269] HE, H.; FRIESE, M. E. J.; HECKENBERG, N. R.; RUBINSZTEIN-DUNLOP, H. Direct observation of transfer of angular momentum to absorptive particles from a laser beam with a phase singularity. *Phys. Rev. Lett.*, v. 75, p. 826, 1995.

[270] SWARTZLANDER, G. A.; FORD, E. L.; ABDUL-MALIK, R. S.; CLOSE, L. M.; PETERS, M. A.; PALACIOS, D. M.; WILSON, D. W. Astronomical demonstration of an optical vortex coronagraph. *Opt. Express*, v. 16, p. 10200–10207, 2008.

[271] TAMBURINI, F.; ANZOLIN, G.; UMBRIACO, G.; BIANCHINI, A.; BARBIERI, C. Overcoming the rayleigh criterion limit with optical vortices. *Phys. Rev. Lett.*, v. 97, p. 163903, 2006.

[272] KIM, H.; PARK, J.; CHO, S.-W.; LEE, S.-Y.; KANG, M.; LEE, B. Synthesis and dynamic switching of surface plasmon vortices with plasmonic vortex lens. *Nano Lett.*, v. 10, p. 529–536, 2010.

[273] GORODETSKI, Y.; DREZET, A.; GENET, C.; EBBESEN, T. W. Generating far-field orbital angular momenta from near-field optical chirality. *Phys. Rev. Lett.*, v. 110, p. 203906, 2013.

[274] GIBSON, G.; COURTIAL, J.; PADGETT, M. J.; VASNETSOV, M.; PASKO, V.; BARNETT, S. M.; FRANKE-ARNOLD, S. Free-space information transfer using light beams carrying orbital angular momentum. *Opt. Express*, v. 12, p. 5448–5456, 2004.

[275] PLICK, W. N.; KRENN, M.; FICKLER, R.; RAMELOW, S.; ZEILINGER, A. Quantum orbital angular momentum of elliptically symmetric light. *Phys. Rev. A*, v. 87, p. 033806, 2013.

[276] FLEISCHER, J. W.; BARTAL, G.; COHEN, O.; MANELA, O.; SEGEV, M.; HUDOCK, J.; CHRISTODOULIDES, D. N. Observation of vortex-ring "discrete" solitons in 2d photonic lattices. *Phys. Rev. Lett.*, v. 92, p. 123904, 2004.

[277] NESHEV, D. N.; ALEXANDER, T. J.; OSTROVSKAYA, E. A.; KIVSHAR, Y. S.; MARTIN, H.; MAKASYUK, I.; CHEN, Z. Observation of discrete vortex solitons in optically induced photonic lattices. *Phys. Rev. Lett.*, v. 92, p. 123903, 2004.

[278] MALOMED, B. A.; MIHALACHE, D.; WISE, F.; TORNER, L. Spatiotemporal optical solitons. *J. Opt. B: Quantum Semiclassical Opt.*, v. 7, p. R53, 2005.

[279] KARTASHOV, Y. V.; VYSLOUKH, V. A.; TORNER, L. Soliton shape and mobility control in optical lattices. *Prog. Opt.*, v. 52, p. 63–148, 2009.

[280] RÜTER, C. E.; MARKRIS, K. G.; ELGANAINY, R.; CHRISTODOULIDES, D. N.; SEGEV, M.; KIP, D. Observation of parity-time symmetry in optics. *Nat. Phys.*, v. 6, p. 192–195, 2010.

[281] MIHALACHE, D.; MAZILU, D.; LEDERER, F.; LEBLOND, H.; MALOMED, B. A. Stability of dissipative optical solitons in the three-dimensional cubic-quintic Ginzburg-Landau equation. *Phys. Rev. A*, v. 75, p. 033811, 2007.

[282] WU, Z.; ZHANG, Y.; YUAN, C.; WEN, F.; ZHENG, H.; ZHANG, Y.; XIAO, M. Cubic-quintic condensate solitons in four-wave mixing. *Phys. Rev. A*, v. 88, p. 063828, 2013.

[283] PASQUAZI, A.; PECCIANTI, M.; CLERICI, M.; CONTI, C.; MORANDOTTI, R. Collapse arrest in instantaneous Kerr media via parametric interactions. *Phys. Rev. Lett.*, v. 113, p. 133901, 2014.

[284] KIVSHAR, Y. S.; LUTHER-DAVIES, B. Dark optical solitons: physics and applications. *Phys. Rep.*, v. 298, p. 81–197, 1998.

[285] TORNER, L.; PETROV, D. Azimuthal instabilities and self-breaking of beams into sets of solitons in bulk second-harmonic generation. *Electron. Lett.*, v. 33, p. 608, 1997.

[286] TORRES, J. P.; SOTO-CRESPO, J. M.; TORNER, L.; PETROV, D. V. Solitary-wave vortices in type II second-harmonic generation. *Opt. Commun.*, v. 149, p. 77–83, 1998.

[287] KIVSHAR, Y. S.; PELINOVSKY, D. E. Self-focusing and transverse instabilities of solitary waves. *Phys. Rep.*, v. 331, p. 117–195, 2000.

[288] VUONG, L. T.; GROW, T. D.; ISHAAYA, A.; GAETA, A. L.; T HOOFT, G. W.; ELIEL, E. R.; FIBICH, G. Collapse of optical vortices. *Phys. Rev. Lett.*, v. 96, p. 133901, 2006.

[289] MINOVICH, A.; NESHEV, D. N.; DESYATNIKOV, A. S.; KROLIKOWSKI, W.; KIVSHAR, Y. S. Observation of optical azimuthons. *Opt. Express*, v. 17, p. 23610–23616, 2009.

[290] ROTSCHILD, C.; COHEN, O.; MANELA, O.; SEGEV, M.; CARMON, T. Solitons in nonlinear media with an infinite range of nonlocality: First observation of coherent elliptic solitons and of vortex-ring solitons. *Phys. Rev. Lett.*, v. 95, p. 213904, 2005.

[291] BRIEDIS, D.; PETERSEN, D. E.; EDMUNDSON, D.; KROLIKOWSKI, W.; BANG, O. Ring vortex solitons in nonlocal nonlinear media. *Opt. Express*, v. 13, p. 435–443, 2005.

[292] KARTASHOV, Y. V.; VYSLOUKH, V. A.; TORNER, L. Stable ring-profile vortex solitons in bessel optical lattices. *Phys. Rev. Lett.*, v. 94, p. 043902, 2005.

[293] YAKIMENKO, A. I.; ZALIZNYAK, Y. A.; KIVSHAR, Y. Stable vortex solitons in nonlocal self-focusing nonlinear media. *Phys. Rev. E*, v. 71, p. 065603, 2005.

[294] MICHINEL, H.; CAMPO-TÁBOAS, J.; QUIROGA-TEIXEIRO, M. L.; SALGUEIRO, J. R.; GARCÍA-FERNÁNDEZ, R. Excitation of stable vortex solitons in nonlinear cubic-quintic materials. *J. Opt. B: Quantum Semiclassical Opt.*, v. 3, p. 314, 2001.

[295] MALOMED, B.; CRASOVAN, L.-C.; MIHALACHE, D. Stability of vortex solitons in the cubic-quintic model. *Physica D*, Amsterdam, v. 161, p. 187–201, 2002.

[296] MIHALACHE, D.; MAZILU, D.; MALOMED, B. A.; LEDERER, F. Stable vortex solitons supported by competing quadratic and cubic nonlinearities. *Phys. Rev. E*, v. 69, p. 066614, 2004.

[297] PEGO, R. L.; WARCHALL, H. A. Spectrally stable encapsulated vortices for nonlinear Schrödinger equations. *J. Nonlinear Sci.*, v. 12, p. 347–394, 2002.

[298] HICKMANN, J. M.; FONSECA, E. J. S.; SOARES, W. C.; CHÁVEZ-CERDA, S. Unveiling a truncated optical lattice associated with a triangular aperture using light's orbital angular momentum. *Phys. Rev. Lett.*, v. 105, p. 053904, 2010.

[299] TZORTZAKIS, S.; SUDRIE, L.; FRANCO, M.; PRADE, B.; MYSYROWICZ, A.; COUAIRON, A.; BERGÉ, L. Self-guided propagation of ultrashort ir laser pulses in fused silica. *Phys. Rev. Lett.*, v. 87, p. 213902, 2001.

[300] NAKAZAWA, M.; YAMAMOTO, T.; TAMURA, K. R. 1.28 Tbit/s-70 km OTDM transmission using third- and fourth-order simultaneous dispersion compensation with a phase modulator. *Electron. Lett.*, v. 36, p. 2027, 2000.

[301] ABB, M.; ALBELLA, P.; AIZPURUA, J.; MUSKENS, O. L. All-optical control of a single plasmonic nanoantenna-ITO hybrid. *Nano Lett.*, v. 11, p. 2457–2463, 2011.

[302] BALLARINI, D.; GIORGI, M. D.; CANCELLIERI, E.; HOUDRÉ, R.; GIACOBINO, E.; CINGOLANI, R.; BRAMATI, A.; GIGLI, G.; SANVITTO, D. All-optical polariton transistor. *Nat. Commun.*, v. 4, p. 1778, 2013.

[303] ABBASI, A.; MORTHIER, G. Optimization of an asymmetric DFB laser used as all-optical flip-flop. *IEEE J. Quantum Electron.*, v. 51, p. 2200106, 2015.

[304] SNYDER, A. W.; LADOUCEUR, F. Light guiding light: Letting light be the master of its own destiny. *Opt. Photonics News*, v. 10, p. 35, 1999.

[305] LIU, X.; BECKWITT, K.; WISE, F. W. Noncollinear generation of optical spatiotemporal solitons and application to ultrafast digital logic. *Phys. Rev. E*, v. 61, p. R4722, 2000.

[306] WU, Y.-D. Nonlinear all-optical switching device by using the spatial soliton collision. *Fiber Integr. Opt.*, v. 23, p. 387–404, 2004.

[307] WU, Y.-D. New all-optical switch based on the spatial soliton repulsion. *Opt. Express*, v. 14, p. 4005–4012, 2006.

[308] LI, S.-M.; LI, Y.; WANG, X.-L.; KONG, L.-J.; LOU, K.; TU, C.; TIAN, Y.; WANG, H.-T. Taming the collapse of optical fields. *Sci. Rep.*, v. 2, p. 1007, 2012.

[309] PETROV, D. V.; TORNER, L.; MARTORELL, J.; VILASECA, R.; TORRES, J. P.; COJOCARU, C. Observation of azimuthal modulational instability and formation of patterns of optical solitons in a quadratic nonlinear crystal. *Opt. Lett.*, v. 23, p. 1444–1446, 1998.

[310] TIKHONENKO, V.; CHRISTOU, J.; LUTHER-DAVES, B. Spiraling bright spatial solitons formed by the breakup of an optical vortex in a saturable self-focusing medium. *J. Opt. Soc. Am. B*, v. 12, p. 2046–2052, 1995.

[311] LUTHER-DAVIES, B.; POWLES, R.; TIKHONENKO, V. Nonlinear rotation of three-dimensional dark spatial solitons in a Gaussian laser beam. *Opt. Lett.*, v. 19, p. 1816–1818, 1994.

[312] CHRISTOU, J.; TIKHONENKO, V.; KIVSHAR, Y. S.; LUTHER-DAVIES, B. Vortex soliton motion and steering. *Opt. Lett.*, v. 21, p. 1649–1651, 1996.

[313] ROZAS, D.; LAW, C. T.; SWARTZLANDER, G. A. Propagation dynamics of optical vortices. *J. Opt. Soc. Am. B*, v. 14, p. 3054–3065, 1997.

[314] SWARTZLANDER, G. A.; ANDERSEN, D. R.; REGAN, J. J.; YIN, H.; KAPLAN, A. E. Spatial dark-soliton stripes and grids in self-defocusing materials. *Phys. Rev. Lett.*, v. 66, p. 1583, 1991.

[315] BOSSHARD, C.; MAMYSHEV, P. V.; STEGEMAN, G. I. All-optical steering of dark spatial soliton arrays and the beams guided by them. *Opt. Lett.*, v. 19, p. 90–92, 1994.

[316] YAO, A. M.; PADGETT, M. J. Orbital angular momentum: origins, behavior and applications. *Adv. Opt. Photon.*, v. 3, p. 161–204, 2011.

[317] LAW, C. T.; ZHANG, X.; SWARTZLANDER, G. A. Waveguiding properties of optical vortex solitons. *Opt. Lett.*, v. 25, p. 55–57, 2000.

[318] LUTHER-DAVIES, B.; XIAOPING, Y. Waveguides and y junctions formed in bulk media by using dark spatial solitons. *Opt. Lett.*, v. 17, p. 496–498, 1992.

[319] TRUSCOTT, A. G.; FRIESE, M. E. J.; HECKENBERG, N. R.; RUBINSZTEIN-DUNLOP, H. Optically written waveguide in an atomic vapor. *Phys. Rev. Lett.*, v. 82, p. 1438, 1999.

[320] CHEN, Z.; SEGEV, M.; CHRISTODOULIDES, D. N.; FEIGELSON, R. S. Waveguides formed by incoherent dark solitons. *Opt. Lett.*, v. 24, p. 1160–1162, 1999.

[321] PASSIER, R.; CHAUVET, M.; WACOGNE, B.; DEVAUX, F. Light-induced waveguide by a finite self-trapped vortex beam in a photorefractive medium. *J. Opt.*, v. 13, p. 085502, 2011.

[322] JAYABALAN, J.; SINGH, A.; CHARI, R.; KHAN, S.; SRIVASTAVA, H.; OAK, S. M. Transient absorption and higher-order nonlinearities in silver nanoplatelets. *Appl. Phys. Lett.*, v. 94, p. 181902, 2009.

[323] STEGEMAN, G.; PAPAZOGLOU, D. G.; BOYD, R.; TZORTZAKIS, S. Nonlinear birefringence due to non-resonant, higher-order Kerr effect in isotropic media. *Opt. Express*, v. 19, p. 6387–6399, 2011.

[324] GLASS, A. M.; GIOVANNI, D. J. D.; STRASSER, T. A.; STENTZ, A. J.; SLUSHER, R. E.; WHITE, A. E.; KORTAN, A. R.; EGGLETON, B. J. Advances in fiber optics. *Bell Labs Tech. J.*, v. 5, p. 168–187, 2000.

[325] DAINO, B.; GREGORI, G.; WABNITZ, S. New all-optical devices based on third-order nonlinearity of birefringent fibers. *Opt. Lett.*, v. 11, p. 42–44, 1986.

[326] PENG, G.-D.; ANKIEWICZ, A. All-optical fibre devices using polarization ellipse rotation. *Opt. Quantum Electron.*, v. 22, p. 343–350, 1990.

[327] LEFORT, L.; BARTHÉLÉMY, A. All-optical transistor action by polarisation rotation during type-II phase-matched second harmonic generation. *Electron Lett.*, v. 31, p. 910–911, 1995.

[328] LEE, J. Y.; YIN, L.; AGRAWAL, G. P.; FAUCHET, P. M. Ultrafast optical switching based on nonlinear polarization rotation in silicon waveguides. *Opt. Express*, v. 18, p. 11514–11523, 2010.

[329] KASHYAP, R.; FINLAYSON, N. Nonlinear polarization coupling and instabilities in single-mode liquid-cored optical fibers. *Opt. Lett.*, v. 17, p. 405–407, 1992.

[330] BESSE, V.; BOUDEBS, G.; LEBLOND, H. Determination of the third- and fifth-order optical nonlinearities: the general case. *Appl. Phys. B*, v. 116, p. 911–917, 2014.

[331] ABOU'OU, M. N. Z.; DINDA, P. T.; NGABIRENG, C. M.; KIBLER, B.; SMEKTALA, F. Impact of the material absorption on the modulational instability spectra of wave propagation in high-index glass fibers. *J. Opt. Soc. Am. B*, v. 28, p. 1518–1528, 2011.

[332] ALAM, M. Z.; LEON, I. D.; BOYD, R. W. Large optical nonlinearity of indium tin oxide in its epsilon-near-zero region. *Science*, Washington, v. 352, p. 795–797, 2016.

[333] YAN, L.; YUE, J.; SI, J.; HOU, X. Influence of self-diffraction effect on femtosecond pump-probe optical Kerr measurements. *Opt. Express*, v. 16, p. 12069–12074, 2008.

[334] LEE, P. C.; MEISEL, D. Adsorption and surface-enhanced raman of dyes on silver and gold sols. *J. Phys. Chem.*, v. 86, p. 3391–3395, 1982.

[335] BRITO-SILVA, A. M.; GÓMEZ, L. A.; DE ARAÚJO, C. B.; GALEMBECK, A. Laser ablated silver nanoparticles with nearly the same size in different carrier media. *J. Nanomater.*, v. 2010, p. 142897, 2010.

[336] TAKAMI, A.; KURITA, H.; KODA, S. Laser-induced size reduction of noble metal particles. *J. Phys. Chem. B*, v. 103, p. 1226–1232, 1999.

[337] PYATENKO, A.; YAMAGUCHI, M.; SUZUKI, M. Laser photolysis of silver colloid prepared by citric acid reduction method. *J. Phys. Chem. B*, v. 109, p. 21608–21611, 2005.

[338] BOUDEBS, G.; BESSE, V.; CASSAGNE, C.; LEBLOND, H.; DE ARAÚJO, C. B. Nonlinear characterization of materials using the D4σ method inside a Z-scan 4f-system. *Opt. Lett.*, v. 38, p. 2206–2208, 2013.

[339] YAN, X.-Q.; LIU, Z.-B.; SHI, S.; ZHOU, W.-Y.; TIAN, J.-G. Analysis on the origin of the ultrafast optical nonlinearity of carbon disulfide around 800 nm. *Opt. Express*, v. 18, p. 26169–26174, 2010.

[340] FALCONIERI, M.; SALVETTI, G. Simultaneous measurement of pure-optical and thermo-optical nonlinearities induced by high-repetition-rate, femtosecond laser pulses: application to cs_2. *Appl. Phys. B*, v. 69, p. 133–136, 1999.

[341] GNOLI, A.; RAZZARI, L.; RIGHINI, M. Z-scan measurements using high repetition rate lasers: how to manage thermal effects. *Opt. Express*, v. 13, p. 7976–7981, 2005.

[342] YU, S.; ZHAO, S.; WEI, G. Local spectral time splitting method for first- and second-order partial differential equations. *J. Comput. Phys.*, v. 206, p. 727–780, 2005.

[343] HIRSH, R. S. Higher order accurate difference solutions of fluid mechanics problems by a compact differencing technique. *J. Comput. Phys.*, v. 19, p. 90–109, 1975.

[344] LIAO, W.; ZHU, J.; KHALIQ, A. Q. M. An efficient high-order algorithm for solving systems of reaction-diffusion equations. *Numer. Meth. Partial Diff. Eq.*, v. 18, p. 340–354, 2002.

[345] WEIDEMAN, J. A. C.; HERBST, B. M. Split-step methods for the solution of the nonlinear Schrödinger equation. *SIAM J. Numer. Anal.*, v. 23, p. 485–507, 1986.

APPENDIX A: NONLINEAR CHARACTERIZATION TECHNIQUES

This appendix describes the characterization techniques that were used to find the NL parameters of the samples used in this thesis.

Z-scan Technique

Z-scan is a simple and accurate technique for measuring the NL refraction index and NL absorption coefficient based on the induced lens effects. This elegant technique introduced by Sheik-Bahae *et al.* [27] is widely used due to the simplicity of the experimental setup, measurement procedures and data acquisition, as well as easy interpretation of results.

The Z-scan technique consists of moving a thin NL sample through the focal region of a well-behaved Gaussian laser beam [1]. The strong interaction of the NL medium with the light beam produces transmittance variations, measured in far-field, because the sample experiences different intensities depending on the sample position (in z-direction) relative to the focus $(z=0)$. The restriction of thin media is necessary because in the Z-scan theory, the propagation effects are neglected [27]. Two configuration corresponding to *closed-aperture* (CA) and *open-aperture* (OA) Z-scan schemes are established for the study of the NL refraction and NL absorption regimes, respectively. For measurements of NL refraction, an small aperture $(S \ll 1)$ is placed in front of the detector, where S represents the light fraction transmitted by the aperture. This optical component produces a more sensitive measure of the beam divergence or focusing, in far field, and is related to a transformation of phase distortion into amplitude distortion. Fig. A.1 illustrates a basic setup of the Z-scan scheme.

A medium displaying NL refraction acts as a lens of variable focal length when it is moved along the z-axis (propagation direction), due to SF or SDF effects [see Section 2.5.1]. Thus, the Z-scan results are due to interplay between the curvature of the wavefront and the positive or negative induced lens effect, which is dependent on the intensity.

In order to understand the operation of the Z-scan technique and be able to interpret the results, a medium with negative NL refraction index (SDF medium) is analyzed. In principle, a SDF medium exhibits negligible NL refraction when it is far from the focal region, due to the low intensity laser in this position. When the sample is moved toward the focus (assuming the starting point before the focus), the wavefront curvature is negative and the SDF medium begins to act as a negative lens collimating the beam and varying the laser beam radius. The result is a smaller, and consequently more intense spot at the aperture placed in front of the detector, producing a higher transmittance after passing through aperture. This effect increases to a maximum when the sample is closer the focus because the intensity is higher. When the sample

---

[1] Laser beams with different shapes can be used in the Z-scan technique since this new profile is considered in the expressions for the analysis of experimental results.

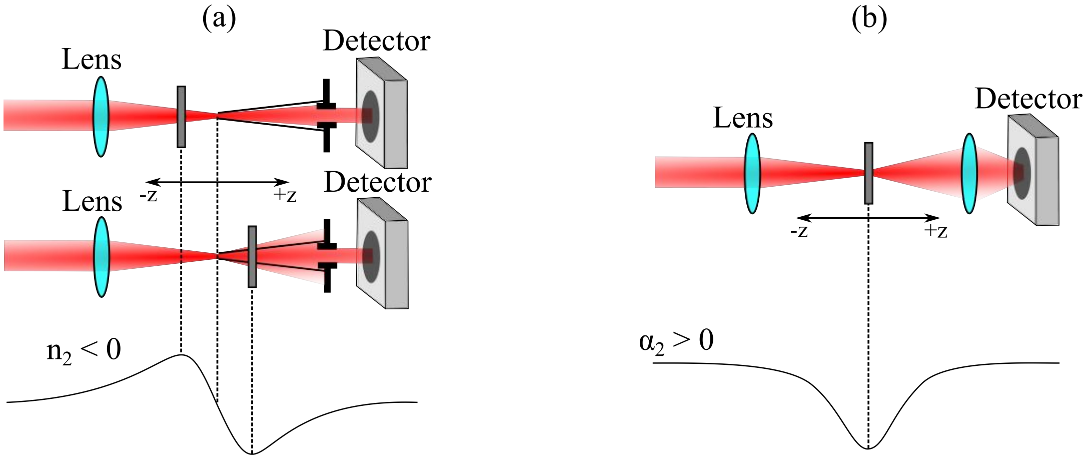

Figure A.1 Basic setup of the (a) *closed-aperture* and (b) *open-aperture* Z-scan technique.

is positioned exactly in the focal plane $(z=0)$, the wavefront curvature is zero and the medium behaves as a thin lens, resulting in a minimal change in the laser beam radius in the far field, and thus, the transmittance assumes the same value that it had in a position far from the focus. After passing through the focus, the behavior is reversed, i. e. the maximum in transmittance (peak) will drop to a minimum (valley). This is because a positive curvature radius plus to the negative induced lens effect produces a larger beam divergence, as a consequence a lower transmittance is detected after the aperture. Finally, the transmittance will return to the linear values when the sample is moved further from the focus. The final result is a curve of transmittance vs position which has a peak followed by a valley, as shown in Fig. A.1(a).

On the other hand, when the sample exhibits a positive NL refraction index (SF medium), the graph is inverted due to positive induced lens effect.

In the OA Z-scan scheme (configuration for measurements of NL absorption), the aperture is removed and the measures correspond to the total power transmitted after the beam passing through the NL sample [Fig. A.1(b)]. If the NL sample presents a decrease in the absorption with increasing intensity, then it is expected an increase in the signal measured by the detector when the sample is located at the focus (where the intensity is the highest). On the contrary, if the absorption effects increase with the intensity, a reduction of the input signal is observed at the focal plane. These behaviors are related to the effects of saturable absorption or multiphoton absorption. Therefore, OA Z-scan curves exhibit a peak or valley in the focus position $(z=0)$ when the NL absorption coefficient is negative or positive, respectively.

In order to describe quantitatively the Z-scan experimental results the following assumptions are made:

- The incident beam is described by a linearly polarized Gaussian electric field of the form:

$$E\left(r,z,t\right)=E_0\left(z,t\right)\frac{w_0}{w\left(z\right)}exp\left[-\frac{r^2}{w^2(z)}-\frac{ikr^2}{2R(z)}\right], \tag{A.1}$$

  where $r=\sqrt{x^2+y^2}$ is the radial coordinate, $E_0\left(z,t\right)$ is the on-axis (for $r=0$) part of amplitude $w\left(z\right)=w_0\sqrt{1+z^2/z_0^2}$ is the beam radius, $R(z)=z\left(1+z_0^2/z^2\right)$ is the curvature radius of the wavefront, $z_0 = \pi w_0^2/\lambda$ is the Rayleigh length, w_0 is the beam waist in the focal plane and λ is the laser wavelength.

- The light propagation in a NL medium is described under the slowly varying envelope and the thin sample approximations. The second assumption obeys the relationship $L < z_0$, where L is the sample length, so both linear diffraction and NL refraction modifications of the beam profile within the NL sample are negligible. Therefore the propagation of the phase, $\triangle\Phi$, and the intensity of the optical beam, $I \propto |E|^2$, inside the NL medium can be separated in two equations:

$$\frac{d\triangle\Phi}{dz'} = -k\left[\triangle n\left(I\right)\right], \tag{A.2}$$

$$\frac{dI}{dz'} = -\left[\alpha\left(I\right)\right]I, \tag{A.3}$$

  where z' is the propagation length inside the medium. For the third-order nonlinearity, we have that $\triangle n\left(I\right) = n_2 I$ and $\alpha\left(I\right) = \alpha_0 + \alpha_2 I$.

For Pure NL Refraction $(\alpha_2 = 0)$***:***
The electric field at the exit face of the sample is given by:

$$E_e\left(r,z,t\right) = E\left(r,z,t\right) exp\left[-\frac{\alpha L}{2}\right] exp\left[i\triangle\Phi\left(r,z,t\right)\right], \tag{A.4}$$

where

$$\triangle\Phi\left(r,z,t\right) = \frac{\triangle\Phi_0^{(3)}\left(t\right)}{1+z^2/z_0^2} exp\left[-\frac{2r^2}{w^2(z)}\right], \tag{A.5}$$

$$\triangle\Phi_0^{(3)}\left(t\right) = kn_2 I_0\left(t\right) L_{eff}, \tag{A.6}$$

with $L_{eff} = \left[1 - exp\left(-\alpha_0 L\right)\right]/\alpha_0$ denoting the effective length of the sample and $I_0\left(t\right)$ is the focal on-axis intensity. Once the amplitude and the phase of the beam at the output of the sample are known, the field distribution at far-field aperture is calculated by using the Gaussian decomposition method [27]. Accordingly, the field at the output face of the sample is decomposed through a series expansion of $exp\left[i\triangle\Phi\left(r,z,t\right)\right]$ and the several Gaussian components propagate in the free space to the aperture plane where they are summed for reconstruction of the beam giving an output electric field, $E_{out}\left(r,z,t\right)$. Finally, the normalized energy transmittance is calculated by integrating spatially and temporally the output intensity

$$T(z) = \frac{\int_{-\infty}^{\infty} dt \int_0^{r_a} dr \left[r\left|E_{out}\left(r,z,t,\triangle\Phi_0^{(3)}\right)\right|^2\right]}{S\int_{-\infty}^{\infty} dt \int_0^{\infty} dr \left[r\left|E_{out}\left(r,z,t,0\right)\right|^2\right]}, \tag{A.7}$$

where $\left|E_{out}\left(r,z,t,0\right)\right|^2$ represents the light irradiance in absence of the nonlinearity, $S = 1 - exp\left(-2r_a^2/w_a^2\right)$, r_a is the aperture radius and w_a is the beam waist in the aperture plane in the linear regime.

The measured normalized energy transmittance in a Z-scan experiment can be fitted numerically to Eq. A.7 in order to find n_2. However, the characterization of NL refraction is usually simplified by applying an analytical solution for the normalized transmittance that can be derived for the on-axis intensity ($S \approx 0$, very small aperture) in the far field condition and for very small steady-state nonlinearity:

$$T(z,S\approx 0) = 1+\frac{4\triangle\Phi_0^{(3)}\,(z/z_0)}{\left[(z/z_0)^2+9\right]\left[(z/z_0)^2+1\right]}. \tag{A.8}$$

Based on the analytical relation expressed in Eq.A.8 it was found numerically that the following expression describes $\triangle T_{p,v}$ within 3% accuracy for $|\triangle\Phi_0| < \pi$:

$$\triangle T_{p,v} \cong 0.406\,(1-S)^{0.25}\left|\triangle\Phi_0^{(3)}\right|. \tag{A.9}$$

For instance, the sensitivity of the measurement for a pinhole aperture $S \approx 0$ is 0.406. Therefore, if the experimental system is able to resolve transmittance changes of about $\triangle T_{p,v} \approx 1\%$ for $S \approx 0$, then the related measurable NL phase shift will be about 25 mrad corresponding to an optical path length of $\Delta nL = \lambda/250$.

NL Refraction with Absorption ($\alpha_2 \neq 0$)**:**

In the presence of NL absorption the solution of Eqs. A.2 and A.3 for the third-order nonlinearity are given by:

$$\triangle\Phi(r,z,t) = \frac{kn_2}{\alpha_2} ln\left[1+q(r,z,t)\right], \tag{A.10}$$

$$I_e(r,z,t) = \frac{I(r,z,t)\,exp\left[-\alpha_0 L\right]}{1+q(r,z,t)}, \tag{A.11}$$

where $q(r,z,t) = \alpha_2 L_{eff} I(r,z,t)$. Since the absorptive and refractive contributions are coupled inside the phase term, NL absorption distort the shape of the Z-scan far-field transmittance. For example, 2PA will enhance the valley and reduce the peak while the saturable absorption will produce an opposite effect. To separate these contributions, we analyze only the OA Z-scan squeme $(S=1)$. In such configuration, the transmittance is insensitive to beam distortion and is only a function of NL absorption. Thus the output energy transmittance can be obtained by integrating spatially and temporally the intensity outgoing from the sample [Eq. A.11] without having to include the free space propagation process. After a spatial integration we get:

$$T(z,t,S=1) = \frac{1+z^2/z_0^2}{q_0}\frac{\int_{-\infty}^{\infty} dt\left[ln\left(1+q_0 f(t)/\left(1+z^2/z_0^2\right)\right)\right]}{\int_{-\infty}^{\infty} dt\left[f(t)\right]}, \tag{A.12}$$

where $f(t)$ is the temporal profile of the laser pulse and $q_0 = \alpha_2 L_{eff} I_0$. By assuming a Gaussian temporal shape, the OA normalized transmittance can be approximated by:

$$T(z,S=1) = \sum_{m=0}^{\infty}\frac{(q_0)^m}{\left(1+z^2/z_0^2\right)^m (m+1)^{3/2}}, \tag{A.13}$$

for $|q_0| < 1$.

If $|q_0| < 1$ and $|\alpha_2| < 2k|n_2|$ a simple division of the CA data by the ones obtained with the OA gives a valley-peak curve where $\triangle T_{p,v}$ closely approximates (within 10%) a purely refractive Z-scan.

Kerr Shutter Technique

Kerr shutter is a pump-probe experiment where the high-intense pump beam is used to induce a birefringence inside the NL medium in order to change the polarization state of weak probe light beam. This technique allows to analyze both the magnitude and the temporal dynamics of the NL response of a Kerr medium. Fig. A.2 shows the experimental configuration for implementation of the Kerr shutter technique. The NL medium is placed between two crossed polarizers so that in absence of the pump beam the linearly polarized probe light can not pass through the system. This configuration is often referred as an optical Kerr cell. In the presence of a strong pump beam an anisotropic refractive index is induced. By spatially and temporally overlapping the two beams a phase difference is "written" by the pump beam and "read" by the probe beam. Consequently, the polarization plane of the probe beam is changed and a small fraction of light is detected after the analyzer. The expression for the intensity outgoing from the Kerr cell is given analytically by [333]

$$I_{Kerr} = I_{probe} sin^2(2\theta)\, sin^2\left(\triangle\Phi^{(3)}/2\right), \tag{A.14}$$

where I_{probe} is the intensity of the incident probe beam, θ is the angle between the polarization planes of the probe and pump beams and $\triangle\Phi^{(3)}$ is the induced NL phase retardation between the ortogonal probe components.

Generally, the Kerr shutter experiment is performed in such way that the pump and a probe beam propagate in nearly collinear direction (with very small angle between them) and their polarization planes are at $\theta = 45°$ with respect to each other in order to maximize I_{Kerr}. In this case, the induced birefringence inside the isotropic medium is described by (see Section 4.2.1

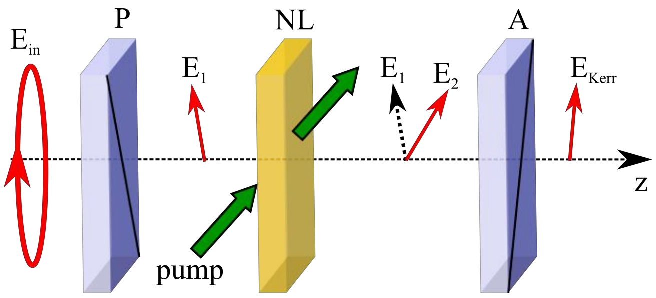

Figure A.2 Basic configuration of the Kerr shutter technique where E_{in} is the input electric field of probe beam with arbitrary polarization, $(E_1)$the incident linearly polarized electric field, (E_2) the nonlinearly rotated electric field, (E_{kerr}) the output electric field, (NL) the NL medium, (P) the polarizer and (A) is the analyzer.

of [21])

$$\delta n = n_{\parallel} - n_{\perp} = \frac{3}{n_0}\left[\chi^{(3)}_{xyyx} + \chi^{(3)}_{xyxy}\right]\left|E_{pump}\right|^2, \tag{A.15}$$

where $n_{\parallel}$ and $n_{\perp}$ are the effective refraction indices experienced by the parallel and the perpendicular components of the probe light with respect to the polarization plane of the pump beam. E_{pump} is the amplitude of the pump electric field. The relative phase difference between the two ortogonal components of the weak field at the exit face of the sample is expressed as:

$$\triangle\Phi^{(3)} = \frac{2\pi}{\lambda_{probe}} L \frac{3}{2n_0^2\varepsilon_0 c}\left[\chi^{(3)}_{xyyx} + \chi^{(3)}_{xyxy}\right] I_{pump}. \tag{A.16}$$

Notice that the term $3\left[\chi^{(3)}_{xyyx} + \chi^{(3)}_{xyxy}\right] / \left(2n_0^2\varepsilon_0 c\right)$ plays the role of the NL refraction. Usually, an induced phase shift is small so that the intensity transmittance of the Kerr cell can be approximated by:

$$T_I = \frac{I_{Kerr}}{I_{probe}} \approx \left(\frac{\triangle\Phi^{(3)}}{2}\right)^2. \tag{A.17}$$

Therefore, a procedure to find the NL refraction index consists in measure the intensity transmittance for the NL sample and compare it with a reference material, maintaining the same intensity of the pump and probe beams.

APPENDIX B: FABRICATION AND CHARACTERIZATION OF MDNCs

In order to conduct the experiments involving MDNCs, two colloids containing silver NPs suspended in acetone and CS_2 were prepared by chemical reduction methods, following the procedures of [334] and [171], respectively.

- **Sample A:** Silver NPs hosted in acetone were obtained by diluting 90 mg of silver nitrate ($AgNO_3$) in 500 ml of water at 100°C. 10 ml of 1% sodium citrate solution ($Na_3C_6H_5O_7$) was added for reduction the Ag^+ ions, and later was boiled and strongly stirred for 1 h. As result, a colloid with Ag NPs of various shapes and sizes was obtained [334].

- **Sample B:** Silver NPs hosted in CS_2 were obtained by adding dropwise 3.75 ml of a 0.03 mol/l $AgNO_3$ aqueous solution to a 0.05 mol/l $N(C_8H_{17})_4Br$ solution in toluene at 100 drops/min. After 10 min, 50 μl of dodecanethiol (dodecanethiol-to-silver molar ratio of 2:1) were introduced in the mixture. Then 3.1 ml of a freshly prepared $NaBH_4$ aqueous solution (0.4 mol/l) was rapidly added to the mixture. The reacting medium was stirred for 3 h, and the organic layer was extracted. The resulting dodecanethiol-stabilized Ag NPs were precipitated by adding ethanol and cooling to −18 °C for 4 h. Finally, the NPs were centrifuged, washed several times with ethanol and redispersed in toluene.

In order to obtain an homogeneous distributions of Ag NPs, the pristine colloids were subjected to a process of laser photofragmentation, under slow stirring, using the second harmonic beam at 532 nm obtained from a Nd: YAG laser (8 ns, 85 mJ/pulse, 10 Hz) for 1 h, according to [335]. The photofragmentation of the NPs is due to their melting and vaporization because of the large absorption of the laser energy by the particles and low heat-transfer for the hosting medium [336, 337]. After photofragmentation, were obtained colloids with homogeneous distributions of spherical NPs with average diameter of (9.0 ± 2.2) nm and (6.0 ± 3.0) nm for sample A and sample B, respectively. Fig. B.1(a) shows the size distribution histogram, for sample A, of the spherical NPs with average diameter of ~9 nm, obtained using a Transmission Electron Microscope (TEM) . While for the sample B, the size distribution histogram was obtained using the Dynamic Ligth Scattering (DLS) technique, as shown in Fig B.1(b). TEM image for sample B is presented in [171].

Colloids with f varying from 0.5×10^{-5} to 2.5×10^{-4} for sample A, and from 0.2×10^{-5} to 4.5×10^{-5} for sample B, were obtained by adding 20 μl to 300 μl of the Ag-water suspension in 1 ml of acetone, and adding 2 μl to 40 μl of the Ag-toluene suspension in 1 ml of CS_2, respectively.

The linear absorption spectra of the samples were measured from 200 nm to 800 nm using a commercial spectrophotometer. Fig. B.2 show the linear absorbance spectra of samples A and B for $f = 4.0 \times 10^{-5}$. Fig. B.2(a) shows the linear absorbance spectra of sample A before (dotted line) and after (solid line) photofragmentation of the original NPs synthesized.

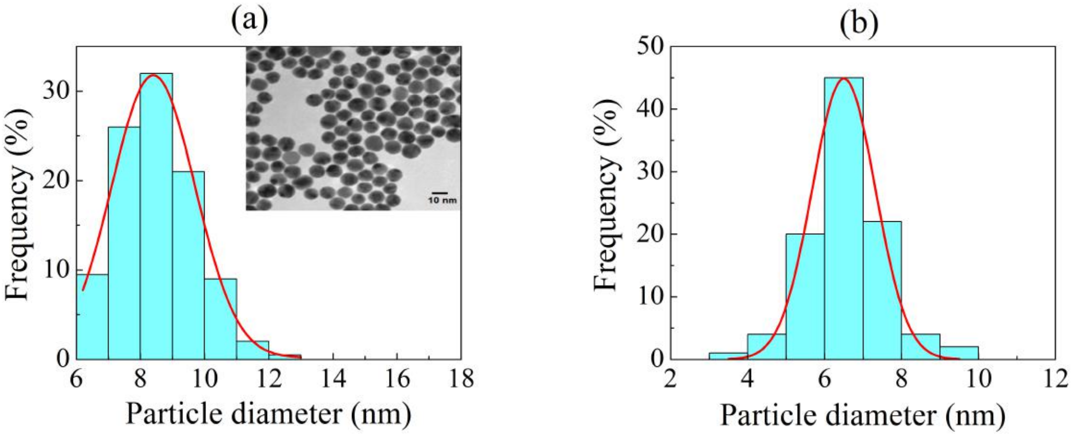

Figure B.1 Size distribution histogram of the NPs after photofragmentation for (a) sample A and (b) sample B.

The smaller LSP resonance linewidth exhibited by the laser-ablated colloid indicates a homogeneous distribution of Ag NPs sizes. The absorbance spectrum of pure acetone (dashed line) presents large transparency window, corroborating that the resonance at ~400 nm is due to the LSP in the Ag NPs. For the case of Ag NPs in CS_2 [Fig. B.2(b)], the LSPR is broader due to the large chemical interaction of sulfur and the Ag surface. CS_2 is also a transparent liquid between 400 and 800 nm.

For sample A, the Ag NPs do not aggregate due to the sodium citrate molecules attached to their surface; the shape and size of the NPs remained unchanged for at least 3 months. However, the sample B is stable for approximately one hour, then begins to precipitate. Nevertheless, after introducing the sample in the ultrasound for a few minutes, it returned to its homogeneous phase.

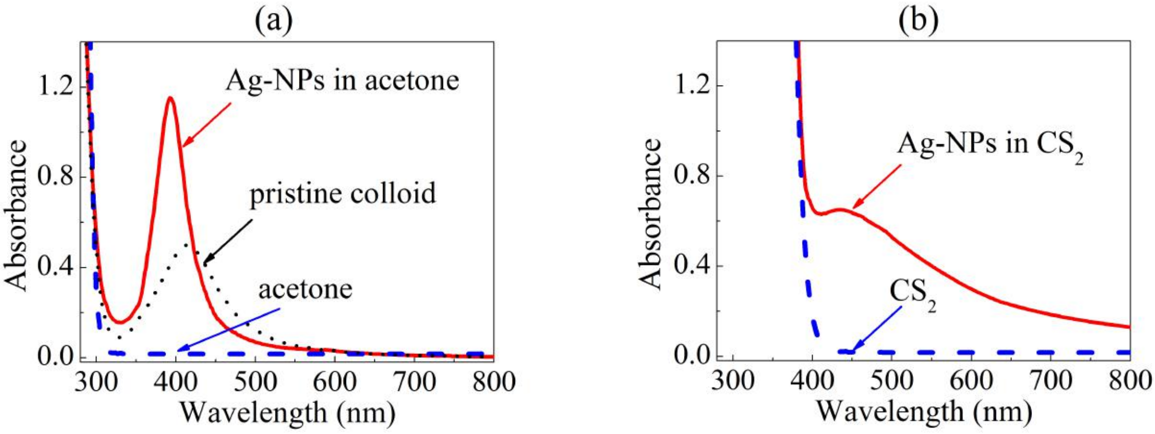

Figure B.2 Linear absorption spectra of the (a) sample A (cell thickness: 1 mm) and (b) sample B (cell thickness: 5 mm), both with $f = 4.0 \times 10^{-5}$.

APPENDIX C: NONLINEAR CHARACTERIZATION OF CARBON DISULFIDE IN THE PICOSECOND AND FEMTOSECOND REGIMES

Carbon disulfide (CS_2) is the NL liquid par excellence. Its high NL behavior has been studied by different characterization techniques, revealing different NL phenomena. Frequently, CS_2 is used as a reference standard for NL optical measurements. However, a variety of results show that the magnitude of the NL response of CS_2 can vary by more than 1 order of magnitude, depending on the characteristics of the incident light beam. Recently, Reichert *et al.* provide a detailed NL characterization of CS_2 by varying the wavelength and pulse duration time of the incident laser [209]. Nevertheless, the study was focused on the third-order nonlinearity only. In this appendix is discussed two models that were adopted to study the evolution of light pulses in (a) 532 nm with duration time of 80 ps and (b) 800 nm with duration time of 100 fs, when propagated inside a cell containing liquid CS_2. Both models were proposed based on the experimental results.

Some discussions in this appendix are focused on the subject of optical vortex beams, because CS_2 was used as a NL medium for experiments with OVSs.

(a) NL behavior of CS_2 at 532 nm and picosecond regime

Besse *et al.* investigated the NL behavior of CS_2 in 532 nm and picosecond regime [26]. The effective third-order refractive index, $n_{2,eff}$, was measured by using the D4σ method, which allows very sensitive measurements for the second moment of the intensity distribution of the transmitted beam [338]. Instead of measuring the variation of the transmitted intensity, as in the Z-scan technique, the D4σ method directly measures changes in the spatial profile of the transmitted beam. Besse noted that $n_{2,eff}$ has a saturated type behavior, as shown by the red points in Fig. 1.5(a), reaching its maximum value $\left(n_{2,eff} = 2.9 \times 10^{-14}\, cm^2/\mathrm{W}\right)$ for an intensity of $\sim$ 17 GW/cm^2. For $I >$ 17 GW/cm^2, $n_{2,eff}$ decreases with increasing intensity. Based on these observations, different types of *Ansatz* were proposed in order to fit the intensity dependence of $n_{2,eff}$. Among these, the *Ansatz* that best fits the experimental results is given by:

$$n_{2,eff}(I) = \frac{aI}{1+b^2I^2}, \tag{C.1}$$

where $a = 3.39 \times 10^{-32}$ m^4/W^2 and $b = 5.76 \times 10^{-15}$ m^2/W. It is important to note that Eq. C.1 does not correspond to the model commonly used to describe the saturation phenomena, which is given by:

$$n'_{2,eff}(I) = \frac{a'}{1+b'I}. \tag{C.2}$$

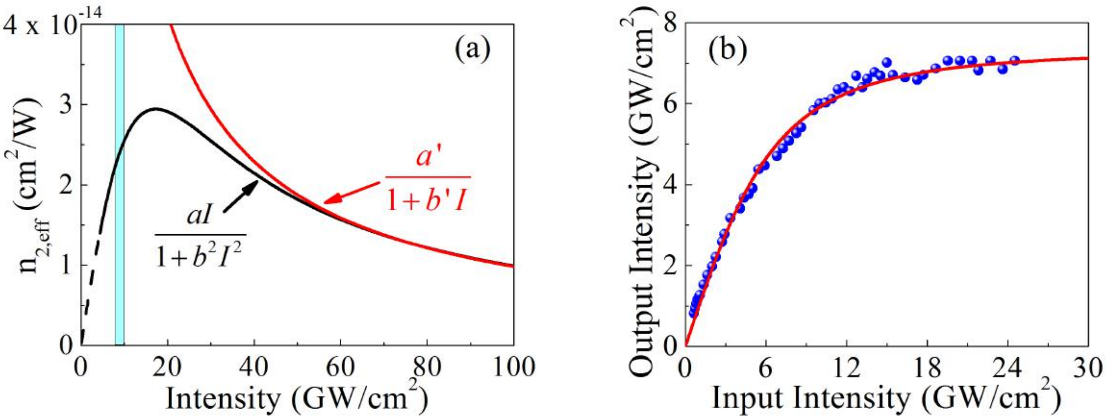

Figure C.1 (a) The effective NL refractive index of CS_2 as a function of the laser intensity in 532 nm and picosecond regime. Red and black lines correspond to the models corresponding to Eqs.C.2 and C.1, respectively. The vertical blue bar indicates the intensity range of the effective stability of the self-trapped vortex beams. (b) Transmittance of CS_2 versus the input laser intensity, in the 1-mm-thick cell. The solid line corresponds to the theoretical fit corresponding to the 3PA effect.

Fig. C.1(a) shows the comparison between Eqs. C.1 (black line) and C.2 (red line), which represent two models of saturable nonlinearity corresponding to the NL refractive index of CS_2 as a function of the laser intensity. To fit the Eq. C.2 to the experimental results reported in [26], we use the values of $a' = 20 \times 10^{-18}$ m^2/W and $b' = 19.3 \times 10^{-15}$ m^2/W. Here, it is possible to note that for high intensities, both models produce similar behavior of $n_{2,eff}$. However, for low intensities the model adopted in Eq. C.2 does not describe the NL behavior observed by the experimental results. This comparison is extremely important to analyze the results of the stable propagation of OVSs in CS_2, discussed in Chapter 7. The shaded section in Fig. C.1(a) represents the stability region of the self-trapped vortex beams in CS_2.

Moreover, it should be added that for very low intensities the model of [26] is no more valid (dashed black line). The measurements published in [26] show a value of $n_2 \sim 1.4 \times 10^{-14}$ cm^2/W for intensities in the range of $1-2$ GW/cm^2, where the measurements were possible. Indeed the signal obtained by using the D4σ method becomes very small at this level [330]. Therefore the growth of $n_{2,eff}$ between 1.4×10^{-14} cm^2/W and $\sim 3 \times 10^{-14}$ cm^2/W at 17 GW/cm^2 can be understood as a contribution of the positive fifth-order nonlinearity. Is worth mentioning that the third-order nonlinearity of CS_2 in the picosecond regime is mainly caused by the molecular reorientation effects. However, for larger intensities, there is plasma formation characterized by NL absorption and negative NL refraction that become more and more dominant, contributing to the reduction of the $n_{2,eff}$ value. This could be understood as the physical explanation of the overall variation shown in Fig. C.1(a).

As concerns the NL absorption, it was reported in [26] that the values of the 2PA and 3PA coefficients for CS_2 at 532 nm, in the picosecond regime, are $\alpha_2 = 0$ and $\alpha_4 = 9.3 \times 10^{-26}$ m^3/W^2, respectively. These value were obtained using the standard open-aperture Z-scan method. The light source was a Nd:YAG laser, operating at wavelength $\lambda = 532$ nm and emitting 12-ps-long linearly polarized pulses with Gaussian temporal and spatial profiles, at the repetition rate of 10 Hz. However, in our experiments, we use a linearly polarized Nd:YAG laser emits 80-ps-long pulses with the Gaussian temporal profile. Nevertheless, the value of α_2 and α_4 are expected to remain the same as measured with 12 ps pulses. To check this expectation, we measured the transmitted intensity through the CS_2 sample versus the incident-beam's intensity.

The blue circles of Fig. C.1(b) represent the experimental data of the output intensity versus the input laser intensity for a vortex beam with topological charge $m = 1$. A quartz cell of thickness 1 mm, filled by liquid CS_2, was used. To analyze the data, we assumed that the transparent liquid $(\alpha_0 = 0)$ exhibits 3PA as reported in [26]. Using the SVEA and considering the sample as an optically thin one, we describe the evolution of the optical intensity, I, along the propagation distance, z, by the differential equation:

$$\frac{\partial I}{\partial z} = -\alpha_4 I^3. \tag{C.3}$$

The red line in Fig. C.1(b) corresponds to the solution of Eq. C.3 using the value that was established in [26].

(b) NL behavior of CS_2 at 800 nm and femtosecond regime

In the femtosecond regime, Kong *et al.* measured the NL behavior of CS_2 by using the Z-scan technique [25]. In the CA scheme, it was identified that CS_2 presents focusing third- and defocusing fifth-order refractive indices for intensities up to hundreds of GW/cm^2. Values of $n_2 = 2.1 \times 10^{-15}$ cm^2/W and $n_4 = -2.0 \times 10^{-27}$ cm^4/W^2 were reported by using a 120 fs pulse laser at a wavelength of 800 nm. These values are very close of the NL refractive indices used to model the stable propagation of two-dimensional spatial solitons in 920 nm ($n_2 = 3.1 \times 10^{-15}$ cm^2/W and $n_4 = -5.2 \times 10^{-27}$ cm^4/W^2) [30]. In both cases, the cubic-quintic refractive nonlinearity of CS_2 has electronic origin.

On the other hand, Kong also concluded, from the OA Z-scan experiments, that NL absorption of CS_2 in 800 nm is attributed only to 3PA, with respective coefficient $\alpha_4 = 1.37 \times 10^{-21}$ cm^3/W^2 [25]. Here arise some controversies with other works reported in the literature. For example, Ganeev *et al.* claims that NL absorption in 795 nm is due to 2PA, with coefficient $\alpha_2 = 5 \times 10^{-11}$ cm/W [34], while Yan *et al.* concluded that the OA Z-scan signal in 800 nm is not due to 2PA nor 3PA, but rather to NL scattering [339]. Thus, to identify the value of NL absorption, to feed in our theoretical models and numerical simulations, we performed an optical limiting experiment, measuring the transmittance of the light beam as a function of the incident intensity. The circles of Fig. C.2(a) show the experimental behavior of the output intensity, I_{out}, versus the input intensity, I_{in}, produced by pass the laser beam (800 nm, 100 fs, 1 KHz) through a cell (thickness: 1 mm) containing liquid CS_2. The green and black lines correspond to fit curves of 2PA $\left(\alpha_2 = 1 \times 10^{-11}\,\text{cm/W}\right)$ and 3PA $\left(\alpha_4 = 1.37 \times 10^{-22}\,cm^3/W^2\right)$, respectively, while the blue line was drawn considering the 2PA and 3PA processes $\left(\alpha_2 = 2.8 \times 10^{-11}\,\text{cm/W and } \alpha_4 = -2.6 \times 10^{-23}\,cm^3/W^2\right)$. Here, it is possible to observe that the models mentioned above do not fit the experimental results, adequately. For this reason, we propose an empirical expression based on the experimental data of Fig. C.2(a), given by:

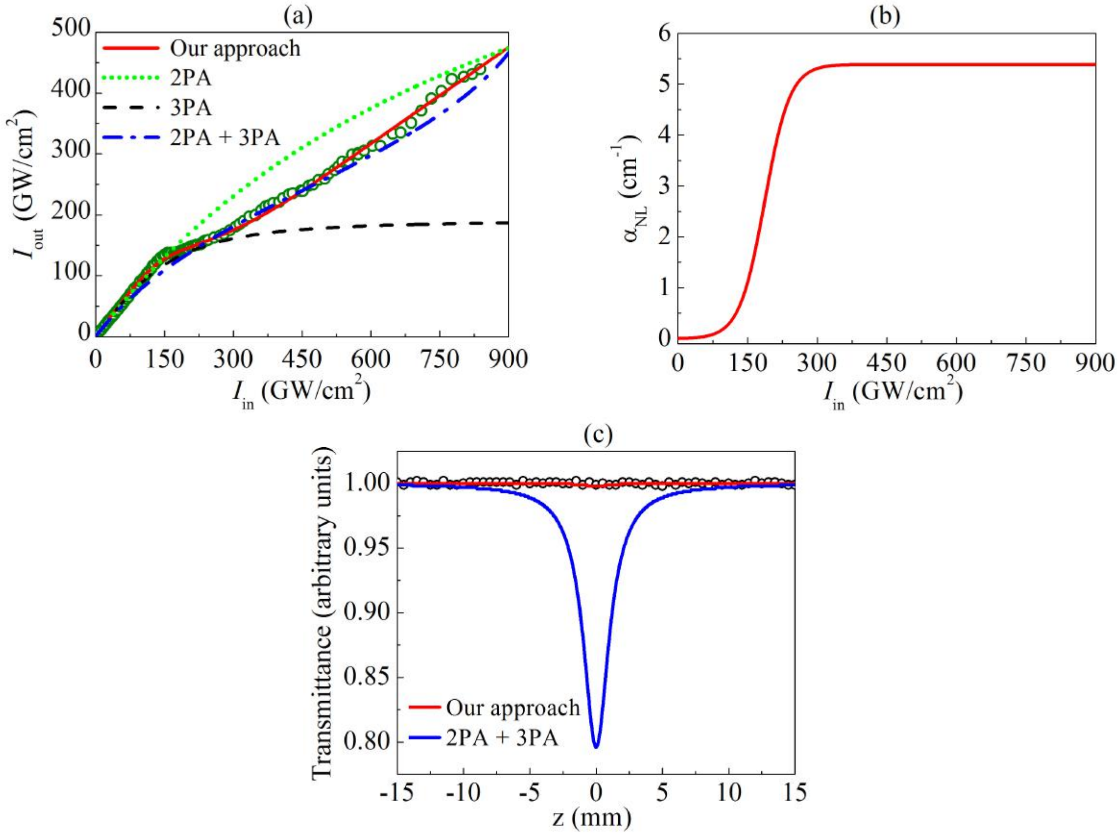

Figure C.2 (a) Transmittance of CS_2 versus laser intensity. Cell length: 0.1 cm. The red line corresponds to best fit by using Eqs. C.4 and C.5. (b) Intensity dependence of α_{NL} for CS_2 in femtosecond regime. (c) *OA* Z-scan curve for CS_2 with laser peak intensity of 30 GW/cm^2.

$$\alpha_{NL}(I) = B\left(\frac{exp\left[\frac{I-C}{D}\right] - exp\left[-\frac{C}{D}\right]}{exp\left[\frac{I-C}{D}\right] + 1}\right), \tag{C.4}$$

with $B = 5.39$ cm^{-1}, $C = 186.7$ GW/cm^2 and $D = 27.16$ GW/cm^2, as shown in Fig. C.2(b). At low intensities, the loss coefficient, $\alpha_{NL}(I)$, has a linear behavior with the intensity, with coefficient $B\left[D\left(1+exp\left(C/D\right)\right)\right]^{-1} = 2.05\times10^{-13}$ cm/W, which is within the range of values of the 2PA coefficients measured by Falconieri *et al.* $\left(4.5\times10^{-13}\text{ cm/W}\right)$ [340] and Gnoli *et al.* $\left(1.2\times10^{-13}\text{ cm/W}\right)$ [341]. A significant increase of α_{NL} is observed for $I > 100$ GW/cm^2, where the NL intensity losses become important. According to Yan [339], for intensities of hundreds of GW/cm^2, intensity loss processes are increased mainly due to the Stokes stimulated Raman scattering and Stokes stimulated Rayleigh-wing scattering. Finally, for $I >$ 350 GW/cm^2, saturation of the loss coefficient is observed. Therefore, several processes contribute to the description of the intensity losses that occurs when a beam passes through a cell filled with CS$_2$. For our case, the contributions of all these processes were condensed in an empirical expression [Eq. C.4], which gives rise to the red line in Fig. C.2(a) obtained by solving the differential equation:

$$\frac{dI}{dz} = -\alpha_{NL}(I)I, \tag{C.5}$$

where α_{NL} [Eq. C.4] is a coefficient which represents all losses of CS_2, i.e. linear and NL absorption, as well as linear and NL scattering.

On the other hand, it can be seen from Fig. C.2(a) that the theoretical fit considering the 2PA and 3PA processes (blue line) is quite close to the experimentally measured values (green circles). However, Fig. C.2(c), corresponding to a measurement using the *OA* Z-scan scheme, shows that for an intensity of 30 GW/cm^2, the absorption coefficients measured (α_2 and α_4) are extremely large and do not fit the experimental results (blue line), contrary to the α_{NL} coefficient proposed in Eq. C.4 (red line). Therefore, we can claim that Eq. C.4 describes adequately the intensity loss processes that occur when a femtosecond pulse propagates inside a cell containing liquid CS_2.

APPENDIX D: RELATIONSHIP BETWEEN THE HON POLARIZATIONS AND HON SUSCEPTIBILITIES

The NL response of matter to optical fields can be described by expressing the induced polarization by a power series of the field with NL susceptibilities, $\chi^{(N)}$, $N = 2, 3, \ldots$, as coefficients of the series. In systems with inversion symmetry all even-order susceptibilities are null and the NL polarization can be expressed, in the convention of [58], by [Eq. 2.76]:

$$\begin{aligned}\tilde{P}_{\mu}^{(2N+1)}(\omega_{2N+2}) = \varepsilon_0 \sum_{\varsigma_1,\varsigma_2,\ldots,\varsigma_{2N+1}} \sum_{\omega} D(\omega_{2N+2};\omega_1,\omega_2,\ldots,\omega_{2N+1}) \\ \times \chi_{\mu\varsigma_1,\varsigma_2,\ldots,\varsigma_{2N+1}}^{(2N+1)}(\omega_{2N+2};\omega_1,\omega_2,\ldots,\omega_{2N+1}) \\ \times \tilde{E}_{\varsigma_1}(\omega_1)\tilde{E}_{\varsigma_2}(\omega_2)\ldots\tilde{E}_{\varsigma_{2N+1}}(\omega_{2N+1}),\end{aligned} \tag{D.1}$$

where $\omega_{2N+2} = \omega_1 + \omega_2 + \ldots + \omega_{2N+1}$ and D is a degeneracy factor given by Eq. 2.11.

For the case of cubic nonlinearity, we can obtain an expression for the third-order NL polarization along the $x-$axis by considering three input fields $E_{1,x}$, $E_{2,x}$ and $E_{3,x}$ (parallel and co-polarized along the x-axis) with frequencies ω_1, ω_2 and ω_3 producing a resultant field with frequency ω_4 via $\chi_{xxxx}^{(3)}(\omega_4;\omega_1,\omega_2,\omega_3)$, given by:

$$P_x^{(3)}(\omega_4) = \varepsilon_0 D^{(3)} \chi_{xxxx}^{(3)}(\omega_4;\omega_1,\omega_2,\omega_3) E_{1,x}E_{2,x}E_{3,x}. \tag{D.2}$$

In an isotropic medium the NL polarization should be independent of the orientation of any axis system used. Thus, in a new axis system (x',y') rotated 45° from the original $x-$axis, the three fields have the following components along the $x'-$axis and $y'-$axis:

$$\left.\begin{aligned} E_{1x'} &= \tfrac{1}{\sqrt{2}}E_{1,x}, & E_{1y'} &= \tfrac{1}{\sqrt{2}}E_{1,x}, \\ E_{2x'} &= \tfrac{1}{\sqrt{2}}E_{2,x}, & E_{2y'} &= \tfrac{1}{\sqrt{2}}E_{2,x}, \\ E_{3x'} &= \tfrac{1}{\sqrt{2}}E_{3,x}, & E_{3y'} &= \tfrac{1}{\sqrt{2}}E_{3,x}. \end{aligned}\right\} \tag{D.3}$$

Also, considering the symmetry properties identified in Eq. 2.14, the nonzero elements of third-order NL susceptibility in the new axis system are given by:

$$\left.\begin{aligned} \chi_{xxxx}^{(3)}(\omega_4;\omega_1,\omega_2,\omega_3) &= \chi_{x'x'x'x'}^{(3)}(\omega_4;\omega_1,\omega_2,\omega_3), \\ \chi_{xxyy}^{(3)}(\omega_4;\omega_1,\omega_2,\omega_3) &= \chi_{x'x'y'y'}^{(3)}(\omega_4;\omega_1,\omega_2,\omega_3), \\ \chi_{xyxy}^{(3)}(\omega_4;\omega_1,\omega_2,\omega_3) &= \chi_{x'y'x'y'}^{(3)}(\omega_4;\omega_1,\omega_2,\omega_3), \\ \chi_{xyyx}^{(3)}(\omega_4;\omega_1,\omega_2,\omega_3) &= \chi_{x'y'y'x'}^{(3)}(\omega_4;\omega_1,\omega_2,\omega_3). \end{aligned}\right\} \tag{D.4}$$

Therefore, the third-order NL polarization induced along the $x'-$axis takes the form:

$$P_{x'}^{(3)} = \varepsilon_0 D^{(3)} \Big[\chi_{x'x'x'x'}^{(3)}(\omega_4;\omega_1,\omega_2,\omega_3)E_{1x'}E_{2x'}E_{3x'} + \chi_{x'x'y'y'}^{(3)}(\omega_4;\omega_1,\omega_2,\omega_3)E_{1x'}E_{2y'}E_{3y'} + \chi_{x'y'x'y'}^{(3)}(\omega_4;\omega_1,\omega_2,\omega_3)E_{1y'}E_{2x'}E_{3y'} + \chi_{x'y'y'x'}^{(3)}(\omega_4;\omega_1,\omega_2,\omega_3)E_{1y'}E_{2y'}E_{3x'}\Big], \quad \text{(D.5)}$$

and substituting Eqs. D.3 and D.4 in Eq. D.5, we have:

$$P_{x'}^{(3)} = \frac{1}{2\sqrt{2}}\varepsilon_0 D^{(3)} \Big[\chi_{xxxx}^{(3)}(\omega_4;\omega_1,\omega_2,\omega_3) + \chi_{xxyy}^{(3)}(\omega_4;\omega_1,\omega_2,\omega_3) + \chi_{xyxy}^{(3)}(\omega_4;\omega_1,\omega_2,\omega_3) + \chi_{xyyx}^{(3)}(\omega_4;\omega_1,\omega_2,\omega_3)\Big] E_{1,x}E_{2,x}E_{3,x}. \quad \text{(D.6)}$$

On the other hand, the third-order NL polarization $P_{x'}^{(3)}(\omega_4;\omega_1,\omega_2,\omega_3)$ in Eq. D.6 can also be obtained by projecting the NL polarization given by Eq. D.2 onto the $x'-$axis of the form:

$$P_{x'}^{(3)} = \frac{1}{\sqrt{2}}\varepsilon_0 D^{(3)} \chi_{xxxx}^{(3)}(\omega_4;\omega_1,\omega_2,\omega_3) E_{1,x}E_{2,x}E_{3,x}. \quad \text{(D.7)}$$

Then, by comparing Eq. D.6 with Eq. D.7, we have:

$$\chi_{xxxx}^{(3)}(\omega_4;\omega_1,\omega_2,\omega_3) = \chi_{xxyy}^{(3)}(\omega_4;\omega_1,\omega_2,\omega_3) + \chi_{xyxy}^{(3)}(\omega_4;\omega_1,\omega_2,\omega_3) + \chi_{xyyx}^{(3)}(\omega_4;\omega_1,\omega_2,\omega_3), \quad \text{(D.8)}$$

where Eq. D.8 can be expressed in a more general and compact form by:

$$\chi_{ijkl}^{(3)}(\omega_4;\omega_1,\omega_2,\omega_3) = \chi_{xxyy}^{(3)}(\omega_4;\omega_1,\omega_2,\omega_3)\delta_{ij}\delta_{kl} + \chi_{xyxy}^{(3)}(\omega_4;\omega_1,\omega_2,\omega_3)\delta_{ik}\delta_{jl} + \chi_{xyyx}^{(3)}(\omega_4;\omega_1,\omega_2,\omega_3)\delta_{il}\delta_{jk}. \quad \text{(D.9)}$$

Of special interest is the case that describes the instantaneous Kerr effect, $\chi_{ijkl}^{(3)}(\omega;\omega,\omega,-\omega)$, mentioned in Table 2.2. Here, by intrinsic permutation symmetry we have that: $\chi_{xxyy}^{(3)}(\omega;\omega,\omega,-\omega) = \chi_{xyxy}^{(3)}(\omega;\omega,\omega,-\omega)$. Thus, Eq. D.9 is rewritten as:

$$\chi_{\mu jkl}^{(3)}(\omega;\omega,\omega,-\omega) = \chi_{xxyy}^{(3)}(\omega;\omega,\omega,-\omega)\left[\delta_{\mu j}\delta_{kl} + \delta_{\mu k}\delta_{jl}\right] + \chi_{xyyx}^{(3)}(\omega;\omega,\omega,-\omega)\delta_{\mu l}\delta_{jk}. \quad \text{(D.10)}$$

By last, Eq. D.10 can be used in the general expression of the third-order NL polarization [Eq. D.1 with $N = 1$]:

$$P_{\mu}^{(3)}(\omega;\omega,\omega,-\omega) = \frac{3}{4}\varepsilon_0 \sum_{jkl} \chi_{\mu jkl}^{(3)}(\omega;\omega,\omega,-\omega) E_j(\omega) E_k(\omega) E_l(-\omega), \quad \text{(D.11)}$$

where the coefficients $D = 3/4$ correspond to the degeneracy factors of the third-order process in the convention of [58], and by using the index notation $\left(\overrightarrow{X} \cdot \overrightarrow{Y} = \sum_{jk} \delta_{j,k} X_j Y_k\right)$, we have that the third-order NL polarization is given by:

$$P_{\mu}^{(3)}(\omega;\omega,\omega,-\omega) = \frac{3}{4}\varepsilon_0 \left\{ 2\chi_{xxyy}^{(3)}(\omega) E_{\mu}(\omega) \left[\overrightarrow{E}(\omega) \cdot \overrightarrow{E}^*(\omega)\right] \right.$$
$$\left. + \chi_{xyyx}^{(3)}(\omega) E_{\mu}^*(\omega) \left[\overrightarrow{E}(\omega) \cdot \overrightarrow{E}(\omega)\right] \right\}. \quad \text{(D.12)}$$

A similar treatment is developed to quintic nonlinearity, where the fifth-order NL polarization along the $x-$axis is given by:

$$P_x^{(5)}(\omega_6) = \varepsilon_0 D^{(5)} \chi_{xxxxxx}^{(5)}(\omega_6;\omega_1,\omega_2,\omega_3,\omega_4,\omega_5) E_{1,x} E_{2,x} E_{3,x} E_{4,x} E_{5,x}, \quad \text{(D.13)}$$

with $\omega_6 = \omega_1 + \omega_2 + \omega_3 + \omega_4 + \omega_5$. In the axis system (x', y'), the fifth-order NL polarization induced along the $x'-$axis, $P_{x'}^{(5)}(\omega_6)$, mixture terms corresponding to $\chi_{x'x'x'x'x'x'}^{(5)}(\omega_6)$, $\chi_{x'x'y'y'x'x'}^{(5)}(\omega_6)$ and $\chi_{x'x'y'y'y'y'}^{(5)}(\omega_6)$. The second term has contributions of 5 fields of which 3 are identical in x' and the 2 others are identical in y', while in the third term 4 field are identical in y' and there is only one field in x'. Thus, considering the number of unique combinations, we have:

$$P_{x'}^{(5)}(\omega_6) = \varepsilon_0 D^{(5)} \left[\chi_{x'x'x'x'x'x'}^{(5)}(\omega_6) E_{1x'} E_{2x'} E_{3x'} E_{4x'} E_{5x'} + \frac{5!}{3!2!} \chi_{x'x'y'y'x'x'}^{(5)}(\omega_6) E_{1x'} E_{2y'} E_{3y'} E_{4x'} E_{5x'} \right.$$
$$\left. + \frac{5!}{4!1!} \chi_{x'x'y'y'y'y'}^{(5)}(\omega_6) E_{1x'} E_{2y'} E_{3y'} E_{4y'} E_{5y'} \right],$$
$$= \frac{1}{4\sqrt{2}} \varepsilon_0 D^{(5)} \left[\chi_{xxxxxx}^{(5)}(\omega_6) + \frac{5!}{3!2!} \chi_{xxyyxx}^{(5)}(\omega_6) + \frac{5!}{4!1!} \chi_{xxyyyy}^{(5)}(\omega_6) \right] E_{1,x} E_{2,x} E_{3,x} E_{4,x} E_{5,x}. \quad \text{(D.14)}$$

Analogously, the fifth-order NL polarization in the $x'-$axis, $P_{x'}^{(5)}(\omega_6;\omega_1,\omega_2,\omega_3,\omega_4,\omega_5)$, can be obtained by projecting the fifth-order NL polarization given by Eq. D.13 onto the $x'-$axis:

$$P_{x'}^{(5)}(\omega_6) = \frac{1}{\sqrt{2}} \varepsilon_0 D^{(5)} \chi_{xxxxxx}^{(5)}(\omega_6) E_{1,x} E_{2,x} E_{3,x} E_{4,x} E_{5,x}, \quad \text{(D.15)}$$

and by comparing the Eqs. D.14 and D.15, we obtain the relationship:

$$\chi_{xxxxxx}^{(5)}(\omega_6) = \frac{10}{3} \chi_{xxyyxx}^{(5)}(\omega_6) + \frac{5}{3} \chi_{xxyyyy}^{(5)}(\omega_6). \quad \text{(D.16)}$$

In particular, for $\chi_{xxxxxx}^{(5)}(\omega;\omega,\omega,\omega,-\omega,-\omega)$, Eq. D.16 can be expressed by:

$$\chi_{\mu jklmn}^{(5)}(\omega) = \frac{10}{3} \chi_{xxyyxx}^{(5)}(\omega)\, \delta_{\mu j} \delta_{kl} \delta_{jm} \delta_{mn} + \frac{5}{3} \chi_{xxyyyy}^{(5)}(\omega)\, \delta_{\mu j} \delta_{kl} \delta_{lm} \delta_{mn}, \quad \text{(D.17)}$$

and by substituting the previous equation in the general expression of the fifth-order NL polarization [Eq. D.1 with $N = 2$]

$$\begin{aligned} P_{\mu}^{(5)}(\omega;\omega,\omega,\omega,-\omega,-\omega) = \frac{5}{8}\varepsilon_0 \sum_{jklmn} \chi_{\mu jklmn}^{(5)}(\omega;\omega,\omega,\omega,-\omega,-\omega) \\ \times E_j(\omega) E_k(\omega) E_l(\omega) E_m(-\omega) E_n(-\omega), \end{aligned} \tag{D.18}$$

with 5/8 being the degeneracy factors of the fifth-order process in the convention of [58], we have the fifth-order NL polarization is given by:

$$\begin{aligned} P_{\mu}^{(5)}(\omega) = \frac{5}{8}\varepsilon_0 \left\{ \frac{10}{3}\chi_{xxyyxx}^{(5)}(\omega) \left|E_{\mu}(\omega)\right|^2 \left[\overrightarrow{E}(\omega)\cdot\overrightarrow{E}(\omega)\right] E_{\mu}^{*}(\omega) \right. \\ \left. + \frac{5}{3}\chi_{xxyyyy}^{(5)}(\omega) \sum_{\sigma=x,y} \left|E_{\sigma}(\omega)\right|^4 E_{\mu}(\omega) \right\}. \end{aligned} \tag{D.19}$$

APPENDIX E: SPLIT-STEP COMPACT FINITE DIFFERENCE METHOD

This appendix is dedicated to discuss the algorithm used to develop the numerical simulations shown in this thesis. An efficient split-step compact finite difference method was used, following the procedure of [235], however adjustments were made to model the NL behavior of the MDNCs and CS_2, in different regimes. We begin expressing the NL equations used in this work in its most general form:

$$i\frac{\partial A}{\partial z}+\frac{1}{2k_0}\nabla_{\perp}A+\frac{i}{2}\alpha_0 A+F\left(|A|\right)A=0, \tag{E.1}$$

where A is the optical field amplitude, $\nabla_{\perp}$ is the transverse Laplacian operator, z is the propagation direction, $k_0 = n_0\omega_0/c$, ω_0 is the laser frequency, c is the speed of light in vacuum, n_0 and α_0 are the linear refractive index and linear absorption coefficient, respectively. $F\left(|A|\right)$ is the function representing the medium nonlinearity, for example:

- For MDNCs: $F(|A|) = \frac{k_0}{2n_0^2}\left[3\chi_{eff}^{(3)}|A|^2+10\chi_{eff}^{(5)}|A|^4+35\chi_{eff}^{(7)}|A|^6\right]$, where $\chi_{eff}^{(2N+1)}$ represent the complex $(2N+1)th$-order susceptibility.
- For CS_2 in the picosecond regime: $F(|A|) = \frac{k_0 a I^2}{1+b^2I^2}+i\frac{\alpha_4 I^2}{2}$, where a and b are constants given by Eq. 5.32, α_4 is the 3PA coefficient and the incident intensity is $I = \frac{1}{2}c\varepsilon_0 n_0|A|$.
- For CS_2 in the femtosecond regime: $F(|A|) = \frac{k_0}{n_0}\left(n_2+n_4 I\right)I+\frac{i}{2}\left[B\left(\frac{exp\left[\frac{I-C}{D}\right]-exp\left[-\frac{C}{D}\right]}{exp\left[\frac{I-C}{D}\right]+1}\right)\right]$, where n_2 and n_4 are the third- and fifth-order refractive indices, B, C and D are constants given Eq. 5.43.

By applying the second-order Strang splitting method [342], we can separate Eq. E.1 into three subproblems, given by:

$$i\frac{\partial A}{\partial z}+\frac{i}{4}\alpha_0 A+\frac{1}{2}F\left(|A|\right)A=0, \tag{E.2}$$

$$i\frac{\partial A}{\partial z}+\frac{1}{2k_0}\nabla_{\perp}A=0, \tag{E.3}$$

$$i\frac{\partial A}{\partial z}+\frac{i}{4}\alpha_0 A+\frac{1}{2}F\left(|A|\right)A=0, \tag{E.4}$$

so that the process of solving Eq. E.1 from z to $z+\triangle z$ can be replaced by solving Eqs. E.2-E.4 within $[z,\, z+\triangle z]$, in sequence.

For one dimensional (1+1)D simulations, as used in Section 6.1.3, Eq. E.3 is given by:

$$i\frac{\partial A}{\partial z}+\frac{1}{2k_0}\frac{\partial^2 A}{\partial x^2}=0. \tag{E.5}$$

However, for (2+1)D simulation, $\nabla_\perp=\left(\partial^2/\partial x^2+\partial^2/\partial y^2\right)$ and by using the first-order Lie formula, we can split Eq. E.3 in two (1+1)D equations, as:

$$i\frac{\partial A}{\partial z}+\frac{1}{2k_0}\frac{\partial^2 A}{\partial x^2}=0, \tag{E.6}$$

$$i\frac{\partial A}{\partial z}+\frac{1}{2k_0}\frac{\partial^2 A}{\partial y^2}=0. \tag{E.7}$$

In the sequence of Eqs. E.2-E.4, we begin to solve the NL equation E.2 by using a second-order Runge-Kutta (RK2) method, as follows:

$$A_1\left(x_j,y_k,z_{n+1}\right)=A\left(x_j,y_k,z_n\right)+\frac{\triangle z}{2}\left(K_1+K_2\right), \tag{E.8}$$

$$K_1=\frac{1}{2}\left[-\frac{\alpha_0}{2}+iF\left(\left|A\left(x_j,y_k,z_n\right)\right|\right)\right]A\left(x_j,y_k,z_n\right), \tag{E.9}$$

$$K_2=\frac{1}{2}\left[-\frac{\alpha_0}{2}+iF\left(\left|A\left(x_j,y_k,z_n\right)+\triangle zK_1\right|\right)\right]\left[A\left(x_j,y_k,z_n\right)+\triangle zK_1\right]. \tag{E.10}$$

Then, the field amplitude $A_1\left(x_j,y_k,z_{n+1}\right)$, obtained by the solution of Eq. E.2 at a distance $\triangle z/2$, is used as an initial condition for solving Eq. E.3 or their analogous Eq. E.5 for (1+1)D and Eqs. E.6-E.7 for (2+1)D. Thus, a compact finite difference (CFD) method [343] is utilized to solve the one-dimensional linear equations. For (1+1)D, applying the Crank–Nicolson scheme for Eq. E.5, one obtains:

$$i\frac{\left[A_2\left(x_j,z_{n+1}\right)-A_1\left(x_j,z_{n+1}\right)\right]}{\triangle z}+\frac{1}{2k_0}\left\{\frac{1}{2\left(\triangle x\right)^2}\left[\delta_x^2A_2\left(x_j,z_{n+1}\right)+\delta_x^2A_1\left(x_j,z_{n+1}\right)\right]\right\}=0, \tag{E.11}$$

where

$$\delta_x^2A_m\left(x_j,z_n\right)=A_m\left(x_{j+1},z_n\right)-2A_m\left(x_j,z_n\right)+A_m\left(x_{j-1},z_n\right). \tag{E.12}$$

However, by using the CFD approximation, which have the advantages of the fourth-order accuracy to approximate the second-order derivatives, we can replace the operator δ_x^2 by the compact one as follows [344]:

$$\delta_x^2\rightarrow\frac{\delta_x^2}{\left(1+\frac{1}{12}\delta_x^2\right)}. \tag{E.13}$$

Therefore, Eq. E.11 is rewritten as:

$$\left[i+\frac{i}{12}\delta_x^2+\frac{1}{4k_0}\frac{\triangle z}{(\triangle x)^2}\delta_x^2\right]A_2\left(x_j,z_{n+1}\right)=\left[i+\frac{i}{12}\delta_x^2-\frac{1}{4k_0}\frac{\triangle z}{(\triangle x)^2}\delta_x^2\right]A_1\left(x_j,z_{n+1}\right),\quad \text{(E.14)}$$

and consequently by using Eq. E.12, we have:

$$\begin{aligned}&\left[\frac{5i}{6}-\frac{1}{2k_0}\frac{\triangle z}{(\triangle x)^2}\right]A_2\left(x_j,z_{n+1}\right)+\left[\frac{i}{12}+\frac{1}{4k_0}\frac{\triangle z}{(\triangle x)^2}\right]\left[A_2\left(x_{j+1},z_{n+1}\right)+A_2\left(x_{j-1},z_{n+1}\right)\right]\\&\quad=\left[\frac{5i}{6}+\frac{1}{2k_0}\frac{\triangle z}{(\triangle x)^2}\right]A_1\left(x_j,z_{n+1}\right)+\left[\frac{i}{12}-\frac{1}{4k_0}\frac{\triangle z}{(\triangle x)^2}\right]\left[A_1\left(x_{j+1},z_{n+1}\right)+A_1\left(x_{j-1},z_{n+1}\right)\right].\end{aligned}\quad \text{(E.15)}$$

Similarly, for (2+1)D, solutions of Eqs. E.6 and E.7 are given by:

$$\begin{aligned}&\left[\frac{5i}{6}-\frac{1}{2k_0}\frac{\triangle z}{(\triangle x)^2}\right]A_2\left(x_j,y_k,z_{n+1}\right)+\left[\frac{i}{12}+\frac{1}{4k_0}\frac{\triangle z}{(\triangle x)^2}\right]\left[A_2\left(x_{j+1},y_k,z_{n+1}\right)+A_2\left(x_{j-1},y_k,z_{n+1}\right)\right]\\&\quad=\left[\frac{5i}{6}+\frac{1}{2k_0}\frac{\triangle z}{(\triangle x)^2}\right]A_1\left(x_j,y_k,z_{n+1}\right)\\&\qquad+\left[\frac{i}{12}-\frac{1}{4k_0}\frac{\triangle z}{(\triangle x)^2}\right]\left[A_1\left(x_{j+1},y_k,z_{n+1}\right)+A_1\left(x_{j-1},y_k,z_{n+1}\right)\right],\end{aligned}\quad \text{(E.16)}$$

$$\begin{aligned}&\left[\frac{5i}{6}-\frac{1}{2k_0}\frac{\triangle z}{(\triangle y)^2}\right]A_3\left(x_j,y_k,z_{n+1}\right)+\left[\frac{i}{12}+\frac{1}{4k_0}\frac{\triangle z}{(\triangle y)^2}\right]\left[A_3\left(x_j,y_{k+1},z_{n+1}\right)+A_3\left(x_j,y_{k-1},z_{n+1}\right)\right]\\&\quad=\left[\frac{5i}{6}+\frac{1}{2k_0}\frac{\triangle z}{(\triangle y)^2}\right]A_2\left(x_j,y_k,z_{n+1}\right)\\&\qquad+\left[\frac{i}{12}-\frac{1}{4k_0}\frac{\triangle z}{(\triangle y)^2}\right]\left[A_2\left(x_j,y_{k+1},z_{n+1}\right)+A_2\left(x_j,y_{k-1},z_{n+1}\right)\right].\end{aligned}\quad \text{(E.17)}$$

Finally, the field amplitude of a beam after crossing a distance $\triangle z$ (step-size in the propagation direction), in a medium with nonlinearity given by $F\left(|A|\right)$, is obtained by using again the RK2 method, with:

$$A\left(x_j,y_k,z_{n+1}\right)=A_m\left(x_j,y_k,z_{n+1}\right)+\frac{\triangle z}{2}\left(K_1'+K_2'\right),\quad \text{(E.18)}$$

$$K_1'=\frac{1}{2}\left[-\frac{\alpha_0}{2}+iF\left(\left|A_m\left(x_j,y_k,z_{n+1}\right)\right|\right)\right]A_m\left(x_j,y_k,z_{n+1}\right),\quad \text{(E.19)}$$

$$K_2'=\frac{1}{2}\left[-\frac{\alpha_0}{2}+iF\left(\left|A_m\left(x_j,y_k,z_{n+1}\right)+\triangle zK_1'\right|\right)\right]\left[A_m\left(x_j,y_k,z_{n+1}\right)+\triangle zK_1'\right],\quad \text{(E.20)}$$

where $m = 2$ or 3 with A_m given by Eq. E.15 or Eq. E.17 for (1+1)D or (2+1)D propagating beam, respectively. The field amplitude of Eq. E.18 is used as initial condition to repeat the sequence of Eqs. E.8 to E.20, a number of times equal to $L/\triangle z$, where L is the sample optical length.

The present method is shown to be convergent of second-order in the propagation direction and fourth-order in transverse directions, which is confirmed numerically. The step-size was determined by using the convergence criterion. First, a value of $\triangle z$, which obey the inequality $\triangle z < 2\left(\triangle x\right)^2/\pi$ [345], was used to propagate an input beam a certain distance L. Then, the step size was halved $(\triangle z' = \triangle z/2)$ and the same input beam was propagated the same distance L, which corresponds to twice the number of steps of $\triangle z$. If the output field, obtained by using $\triangle z'$, converged with the previously obtained by $\triangle z$, then the original step size $(\triangle z)$ is used to perform the numerical simulations. However, if the output field did not converge, a new step size, less than $\triangle z$, was proposed and the convergence process was again verified. This process was repeated for each of the input beam profiles and input powers to ensure that the solution was not spurious. On the other hand, in order to minimize the unphysical results in the simulation, produced when part of the beam going out from the computational window and re-enters on the opposite side interfering with the beam inside the window, we introduce an absorber function given by a super-Gaussian of order 50 with a width defined within 90-95% of the computational window.

APPENDIX F: LIST OF PUBLICATIONS

Published

1. REYNA, A. S.; DE ARAÚJO, C. B. Nonlinearity management of photonic composites and observation of spatial-modulation instability due to quintic nonlinearity, Phys. Rev. A, v. 89, p. 063803, 2014.

2. REYNA, A. S.; DE ARAÚJO, C. B. Spatial phase modulation due to quintic and septic nonlinearities in metal colloids, Opt. Express, v. 22, p. 22456-22469, 2014.

3. REYNA, A. S.; JORGE, K. C.; DE ARAÚJO, C. B. Two-dimensional solitons in a quintic-septimal medium, Phys. Rev. A, v. 90, p. 063835, 2014.

4. REYNA, A. S.; DE ARAÚJO, C. B. An optimization procedure for the design of all-optical switches based on metal-dielectric nanocomposites, Opt. Express, v. 23, p. 7659-7666, 2015.

5. JORGE, K. C.; GARCÍA, H. A.; AMARAL, A. M.; REYNA, A. S.; DE S. MENEZES, L.; DE ARAÚJO, C. B. Measurements of the nonlinear refractive index in scattering media using the scattered light imaging method - SLIM. Opt. Express, v. 23, p. 19512–19521, 2015.

6. DE ARAÚJO, C. B.; KASSAB, L. R. P.; DOMINGUEZ, C. T.; RIBEIRO, S. J. L.; GOMES, A. S. L.; REYNA, A. S. Photoluminescence and nonlinear optical phenomena in plasmonic random media - a review of recent works, J. Lumin., v. 169, p. 492-496, 2016.

7. REYNA, A. S.; BOUDEBS, G.; MALOMED, B. A.; DE ARAÚJO, C. B. Robust self-trapping of vortex beams in a saturable optical medium, Phys. Rev. A, v. 93, p. 013840, 2016.

8. REYNA, A. S.; MALOMED, B. A.; DE ARAÚJO, C. B. Stability conditions for one dimensional optical solitons in cubic-quintic-septimal media, Phys. Rev. A, v. 92, p. 033810, 2016.

9. REYNA, A. S.; DE ARAÚJO, C. B. Taming the emerging beams after the split of optical vortex solitons in a saturable medium, Phys. Rev. A, v. 93, p. 013843, 2016.

10. REYNA, A. S.; DE ARAÚJO, C. B. Guiding and confinement of light induced by optical vortex solitons in a cubic-quintic medium, Opt. Lett., v. 41, p. 191-194, 2016.

Submitted

1. REYNA, A. S.; BERGMANN, E.; BREVET, P.-F.; DE ARAÚJO, C. B. Nonlinear polarization instability in cubic-quintic plasmonic nanocomposites, submitted to Phys. Rev. A.

In Preparation

1. REYNA, A. S.; DE ARAÚJO, C. B. High-order nonlinearities in plasmonic nanocomposites - A review of recent works

APPENDIX G: LIST OF CONFERENCE PAPERS

1. REYNA, A. S.; DE ARAÚJO, C. B. Observation of spatial-modulation instability due to quintic nonlinearity, Frontiers in Optics 2014, Optical Society of America, JTu3A.41.
2. REYNA, A. S.; DE ARAÚJO, C. B. Spatial phase modulation due to quintic nonlinearity in photonic composites, Latin America Optics and Photonics Conference 2014, Optical Society of America, LM4A.19.
3. REYNA, A. S.; DE ARAÚJO, C. B. Stable Optical Vortices Solitons Propagation in CS_2, Frontiers in Optics 2015, Optical Society of America, FM1D.7.
4. DE ARAÚJO, C. B.; REYNA, A. S. Investigation of Stability and Instability Regions of Optical Vortex Solitons in a Saturable Focusing Medium, Latin America Optics and Photonics Conference 2014, Optical Society of America, LTh2D.4.
5. DE ARAÚJO, C. B.; REYNA, A. S. Nonlinear Spectroscopy of Metal-dielectric Nanocomposites, Latin America Optics and Photonics Conference 2014, Optical Society of America, LW2A.4.